COLOUR 85

RAM-JET COMBUSTION BASED ON SHOCK/FLAME INTERACTION

J.A. EDWARDS

DECEMBER 1983

CRANFIELD INSTITUTE OF TECHNOLOGY

COLLEGE OF AERONAUTICS

Ph.D. THESIS

J.A. EDWARDS

Ram-jet Combustion Based on Shock/Flame Interaction

Supervisor: J.L. Stollery

December 1983

"It is the daring, risky hypothesis, the hypothesis that might easily not be true, that gives a special confidence if it stands up to critical examination."

Medawar

ABSTRACT

An experimental investigation into the effects of shock/wake and shock/flame interaction on the base pressure of axisymmetric bodies at Mach 2 has been carried out. This investigation has determined the effects of various forms of shock generator (axisymmetric cowls, two-dimensional wedges and 'delta' wings) on the base pressure. Shock waves generated by over-expanding the airflow in an open-jet wind tunnel have been used to determine the effect of shock strength on the base pressure of an axisymmetric fuel injector. Both peripheral bleed and axial bleed of hydrogen fuel have been examined and the effect of shock compression on the resulting flame has been determined. In the axial bleed case nitrogen and hydrogen bleed without combustion has also been examined. The effect of varying the airflow stagnation temperature has also beeninvestigated.

It is demonstrated herein that there is a distinct shock/wake interaction position that maximises the base pressure, that with interaction at this optimal position the static pressure rise across the shock wave can be communicated in full to the base of the centrebody, and that favourable aerodynamic interference between the wake and a cowl of 5^{o} convergent-divergent internal section can give rise to a net drag reduction. The shock/wake and shock/flame experiments demonstrate that a significant base thrust can be generated, however, the fuel efficiency decreases with increasing shock strength. It is shown that the fuel specific impulse is a function of shock strength, interaction position and bleed mode (peripheral or axial). The onset of boundary layer separation due to the adverse pressure gradient encountered when the base pressure is high appears to limit the useful addition of wake combustion. Finally, it is demonstrated that the base pressure, with and without combustion, is only a weak function of airflow stagnation temperature.

CONTENTS

CHAPTER 1: INTRODUCTION

Over the last 15 years considerable interest has been expressed in the possibility of generating thrust on the base of a projectile by combined external and wake combustion. The flow in the near wake of a bluff body is particularly amenable to modification by wake combustion and experiments have shown that most of the base drag may be eliminated with acceptable fuel specific impulses by such means[1-3]. Initially theoretical appraisals[4-6], of the effects of combining combustion in the free stream with combustion in the wake, generated optimism that such a process could generate a base thrust at acceptable fuel specific impulses. However, more recent theoretical studies[7] have indicated that base pressure control by external burning (with or without wake combustion) may not be attractive from a fuel usage point of view, i.e. high specific fuel consumption. This notwithstanding, some experimental information has been obtained[3,8-10] on the effects of compression waves on bluff body wakes, both with and without wake combustion. This data together with that on shock/wake interaction[11,12] suggests that base pressure enhancement by shock/flame interaction may be a viable basis for air-breathing propulsion or base drag reduction.

The concept of providing areas of increased pressure by shock/flame interaction was described in 1968[13]. A ramjet sustainer configuration utilising shock/flame interaction was proposed by Townend[14] and this idea, as shown in fig. 1.1 is considered (but not tested) here.

The device shown in fig. 1.1 uses a ducted cowl or 'wings' to generate a shock wave - called the 'primary' shock wave - which then interferes with the wake of the centrebody. Fuel is bled at low mass flow rates into the near wake recirculation region and is burnt. Since the evidence indicates that wake combustion alone does not give rise to a base thrust, the purpose of the primary shock wave is to raise the base pressure to an acceptable level. (An 'acceptable level' is discussed in chapter 2.) Similarly a 'secondary' shock wave is generated which then interacts with the wake or rearward face of the cowl or wings and is also combined with wake combustion. This 'secondary' system is proposed to reduce or, hopefully, to eliminate the drag of the primary shock generator. The secondary shock wave is shown in fig. 1.1 as being generated by geometric means. It appears from the results shown in chapter 5 that a strong separation shock exists at the corner of the base of the centrebody when $P_b >> P_\infty$ and that it may be possible to use this shock wave as the secondary system. In other words the possibility of favourable aerodynamic interference could be employed if it can be demonstrated that it exists.

In chapter 2 the drag of a 'typical' artillery rocket is calculated. Trajectory calculations are then performed to determine the required base pressure to effect a sustainer mode in the trajectory of the projectile. For an artillery missile, rocket boosted to Mach 2, it is found that a base pressure ratio, P_b/P_∞, of approximately 1.75 is required to provide a sustain phase of short duration. For a cruise missile of the same geometry as the artillery missile mentioned above, a base pressure ratio, P_b/P_∞, of 1.6 is required to provide thrust = drag.

Chapter 3 comprises a survey of the various methods of base pressure control. For example, geometric modifications to the missile base, aerodynamic modifications to the near wake flow field and thermodynamic modifications to the flow in the base region are discussed. The conclusions drawn from chapter 3; in terms of base pressure control rather than in terms of providing a conventional momentum thrust (as in a full scale ramjet); are that to provide the required base pressure a strong external compression in some form is needed. This is the function of the primary shock system shown in fig. 1.1. It is clear from chapter 3 that little is known, both theoretically and experimentally, about the effect of shock waves on near-wake regions, and therefore it is necessary to collect a certain amount of experimental data.

The experimental programme (chapters 4,5 and 6) was carried out along the following lines:-

a) determine the effect that compression surfaces(of somewhat arbitrary design) have on the base pressure of a centrebody at Mach 2.

b) determine the effect of shock strength on the base pressure of a fuel injector with and without bleed of nitrogen and hydrogen and with wake combustion using hydrogen as the fuel.

c) determine the effect of stagnation temperature on the base pressure of the fuel injector with and without wake combustion for temperatures up to and in excess of those typical of Mach 3 flight at sea level ($300^{o}K \rightarrow 1000^{o}K$).

d) determine the effect of the interference flowfield on the drag of the shock generator hardware.

It is demonstrated that:-

1) there is an optimum position for the shock generator geometry which maximises the base pressure and that at this position a substantial base thrust can be generated, but a phenomenon which we call 'wake buzz' may cause a deterioration in performance, particularly at the lower Reynolds numbers tested.

2) With wake combustion at the mass flow rates tested the base pressure rises almost linearly with increasing incident shock strength until the base pressure is sufficiently high that the approaching boundary layer separates on the afterbody. Also the static pressure increase across the incident shock wave can be communicated to the base and that wake combustion can increase the base pressure further.

3) Sufficient base thrust can be generated to cancel the drag of a projectile at Mach 2 (ignoring any drag induced by the shock generators).

4) Favourable aerodynamic interference exists and may be used to advantage in the design of a sustainer motor.

5) Stagnation temperature only has a minor effect on the base pressure (at least in the range tested, 300°K → 1000°K). The major parameters are incident shock strength and interaction position.

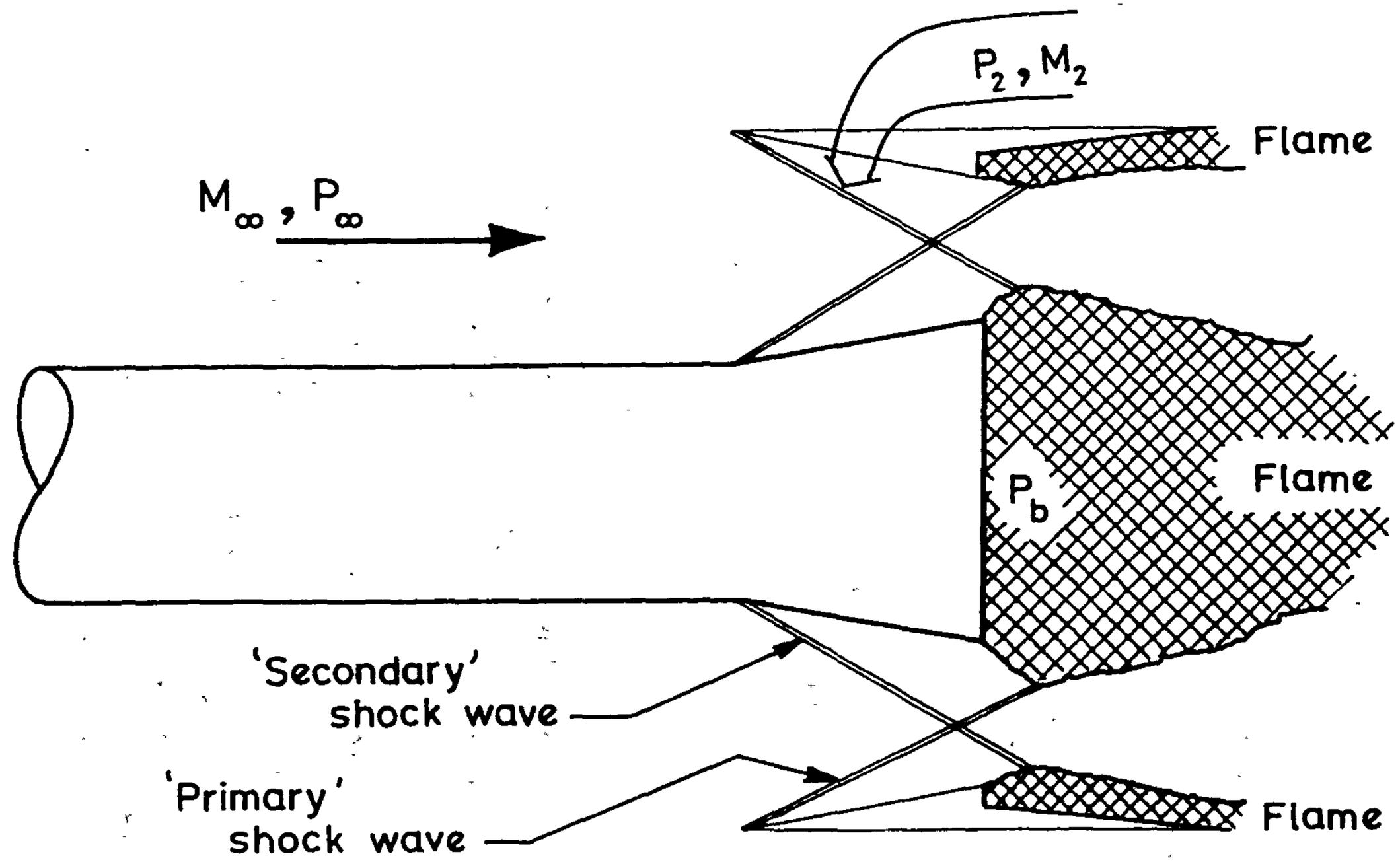

Figure 1.1 Conceptual diagram of ramjet sustainer utilising shock / flame interactions.

CHAPTER 2: TRAJECTORY CALCULATIONS

2.1 Introduction

For a cruise missile it is necessary only to overcome the aerodynamic drag to sustain flight. However, for a ballistic trajectory, this is insufficient, since work has to be done against the earth's gravitational field. The aim in performing trajectory calculations is to establish a rough figure for the base pressure required to sustain a typical artillery rocket at constant Mach number after the termination of the initial boost phase (fig. 2.1).

Townend[14,15] has examined the case of a typical long rod penetrator using kinetic energy as a measure of performance. The effect of fuel specific impulse, with the assumption of Thrust = Drag, was examined for a range of drag coefficients. It was shown that even for low values of specific impulse (200 lbf.sec/lbm) a powered projectile could out-perform the unpowered penetrator since the loss of mass due to fuel consumption was less than the gain in (velocity)^2 at constant range. For a missile of similar dimension to the S.N.I.A. Firos 25 122 mm calibre rocket[16] in cruise flight at Mach 2, the Breguet Range Equation suggests that the range would be proportional to the lift/drag ratio and may extend to approximately 300 km given a lift/drag ratio of 2 and fuel specific impulse of 500 lbf.sec/lbm[15].

The simulation is based upon the Firos 25 122 mm calibre multiple launch rocket system[16]. Details of the numerical method and the drag calculations are given in Appendices A1 and A2. Two series of calculations were made. The first was based on the Firos 25 rocket and the second on a hypothetical Mach 2 rocket.

2.2 Ballistic Trajectories

Fig. 2.2 shows the computed trajectories for the Firos 25 rocket together with the S.N.I.A. data[16]. It can be seen that the agreement is good. The computer simulation overestimates the range by less than 4%.

It should be noted that the length of an artillery rocket is not a sensitive parameter, in the sense that differing length rockets may be fired from the same launcher. This is true at least for the Firos system[16]. However, to allow a new design of rocket to be fired from an existing launcher the calibre should not be changed. The approach adopted here is to allow the ramjet hardware to be deployed at the end of the boost phase. We assume this is done instantaneously, i.e. t_2 in fig. 2.1 is zero, and the rocket boost is followed immediately by ramjet sustain.

The following assumptions in the simulation are made:

1) the projectile may be stretched,

2) any additional weight penalty is due only to the presence of ramjet fuel,

3) during the sustain period (phase 3 in fig. 2.1) the ramjet thrust remains constant,

4) at the end of the sustain phase the ramjet is retracted.

5) If we also assume that the drag of the shock generators can be cancelled by wake combustion combined with the secondary shock system (fig. 1.1), or favourable aerodynamic interference, then the base pressure is directly proportional to the ramjet thrust.

Increasing the length of the basic Firos model by 250 mm from 2.56 m to 2.81 m (i.e. approximately 10%) allows us, by assumption 2, to carry an additional mass of 2.69 kg of kerosene. This increases the launch mass from 52.4 kg to 55.09 kg. It is now unreasonable to compare the increased length rocket with the original Firos model so a 'Stretched Rocket' range was computed. The 'Stretched Rocket' has the same length as the ramjet model but with the additional volume filled with rocket fuel. The launch mass of this projectile was calculated to be 55.64 kg. A comparison of the major parameters for the three rockets is shown in Table 2.1.

Fig. 2.3(a) shows the effect of assuming varying base pressure ratios, P_b/P_∞, for varying sustain times, t_3, on the Mach number at the termination of the sustain phase and the resulting range. To achieve constant Mach number throughout the sustain phase a base pressure ratio of 2.3 is required. If this can be sustained for a period of 8 seconds then the range can be increased to approximately 37.5 km. This implies a fuel specific impulse of approximately 700 lbf.sec/lbm ignoring the drag of the shock generators. The point where the lines of constant P_b/P_∞ converge, at $t_3 = 0$ sec, represents the weight penalty of the ramjet fuel.

Since the experimental facilities available for our use operate at a Mach number of 2, a similar simulation for a hypothetical rocket boosted to Mach 2 was performed. The dimensions of the projectile were as the Firos system. Figure 2.3(b) shows the effects of assuming varying base pressure ratios, P_b/P_∞, for varying sustain times. It can be seen that a base pressure ratio of approximately 1.75 is required to maintain constant flight Mach number. To overcome the aerodynamic drag a base pressure ratio of only 1.6 is required. The additional thrust is required to do work against gravity. Neglecting the drag of the shock generators a base pressure ratio of 1.75 sustained for 10 seconds implies a specific impulse of 500 lbf. sec/lbm. Note that with a 10 second sustain phase an increase in range of about 60% may be achieved.

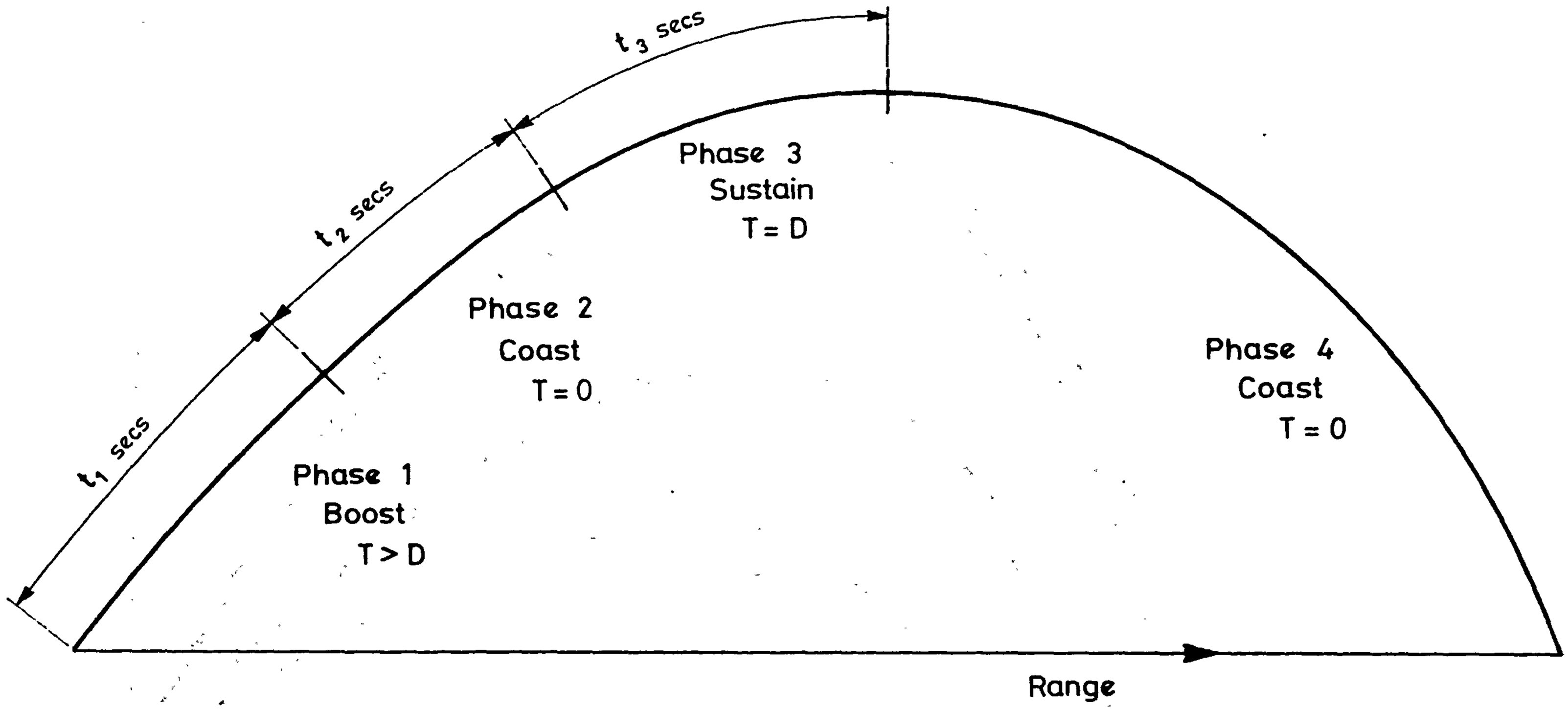

Figure 2.1. Typical boost, coast, sustain trajectory.

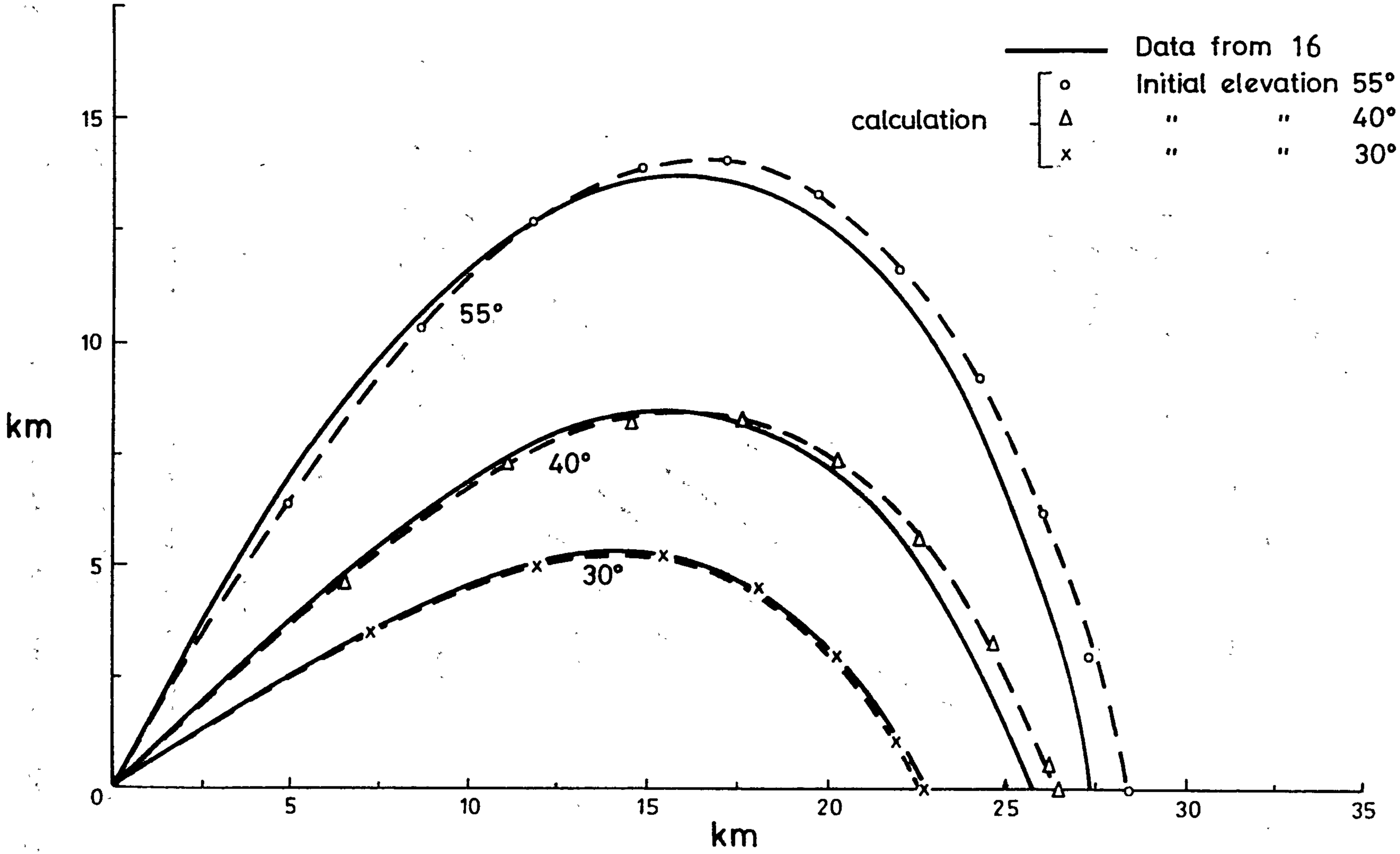

Figure 2.2. Trajectories-comparison of SNIA data (16) with computed trajectories.

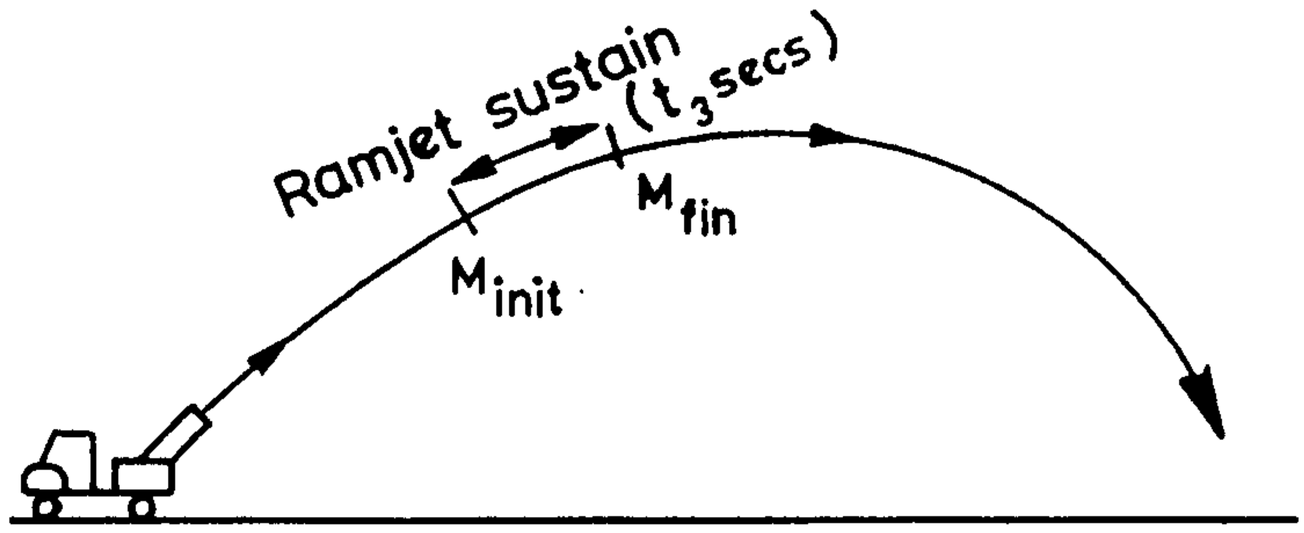

Trajectory (schematic)

M_{init} = Mach number at end of boost.

Launch elevation = 40°

Launch mass = 55.09 kg.

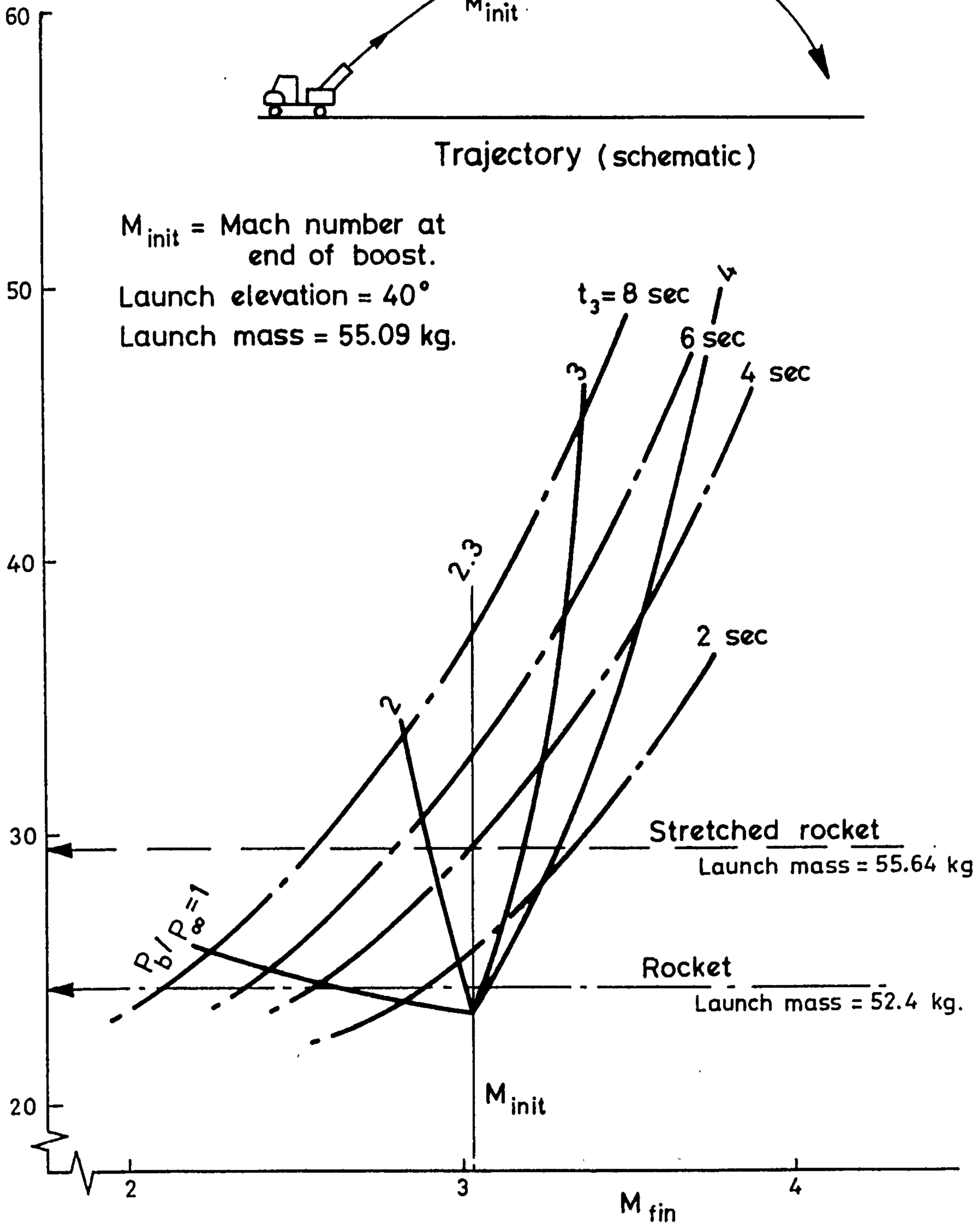

(a) 122mm projectile with rocket boost to Mach No. 3

Figure 2.3. Artillery projectile simulation for varying base pressure ratios (P_{b/P_∞}) and sustain times (t_3).

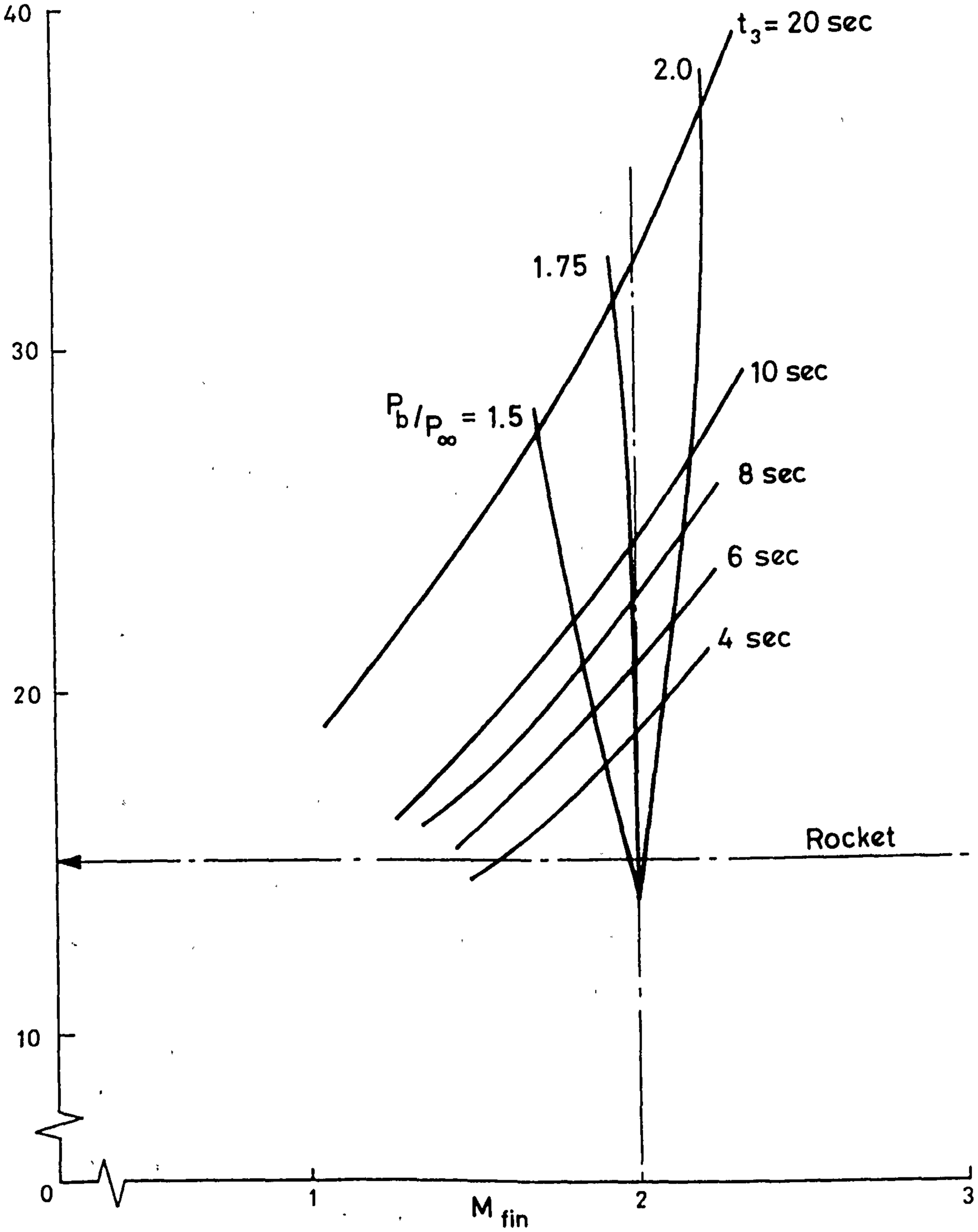

(b) 122 mm projectile with rocket boost to Mach No. 2.

Figure 2.3. (continued)

CHAPTER 3: LITERATURE REVIEW

3.0 Introduction

There is an absence of a rational unified theory which predicts all aspects of the base pressure problem of projectiles (fig. 3.1). The complexity of calculating base pressure for an axisymmetric body even in the absence of complex base geometries, spinning or base injection and/or wake combustion is well known.

Although several aspects of base flow phenomena have been investigated over the past 50 years, experimental results are, in the main, rather meagre. Both in experiment and analysis some of the controversial topics that have persisted over the years are related to the following:

a) the mechanism of separation, expansion and/or compression and shock formation+ in the vicinity of the corner.

b) the structure of the recirculation zone in a closed or open wake.

c) the formation and structure of a mixing layer between the recirculating fluid and the external flow.

d) the effects of base geometry (base recesses, base plates, stings etc.).

e) the upstream effects of the presence of the base corner.

f) the control of base pressure by the distribution of mass, momentum and enthalpy in the near wake region.

g) the nature of the injectants which are most suitable for various applications.

h) the modelling and nature of enthalpy release in the near wake region.

i) the effects of spinning.

j) three-dimensional effects.

It is not the primary purpose of this thesis to attempt to extend the understanding of any of the above listed topics in any fundamental manner. The prime objectives of this investigation are stated in chapter 1. However, all of the above topics (with the possible exception of item i) have some bearing on the project in hand. A number of excellent reviews on the topic of base pressure exist[22-25]. It is the intention in this chapter to update the previous surveys and to briefly scan some of the work included in these for the sake of

---

+ commonly called the 'lip shock' although we prefer the term 'separation shock'

completeness.

There are four basic routes to the reduction of base drag available to the projectile designer:-

i) geometric modifications to the base, e.g. boat-tailing, splitter plates etc.,

ii) boundary layer bleed,

iii) mass injection and

iv) enthalpy addition to the base flow.

Perhaps, since this is the subject of this report, one should also add

v) external compression.

In section 3.1 we discuss some of the early attempts at predicting base pressure by correlations with experimental data. These empirical attempts proved successful only in limited applications. The failure of such correlations is due to the extreme complexity of the base flow as can be seen from the description of the flow field in §3.1.2. In §3.2 we discuss items i), ii) and iii) above under the general heading of 'aerodynamic modifications'. Items iv) and v) are discussed in §3.3 under the heading of 'wake combustion'. In the absence of enthalpy addition external compression may prove to be a useful tool in controlling the base pressure but in practice combustion will be required and we therefore include the topic in §3.3.

3.1 Undisturbed Wake

3.1.1 Early correlations

The first attempts to predict the base pressure of a supersonic projectile took no account of Reynolds number effects. Gabeaud[27,28] obtained a relation between base pressure and Mach number based on what he called a "turbulence theory of residual resistance". The base pressure is given as a function of free stream velocity, q_∞, by the relationship

$$P_b = P_\infty - \tfrac{1}{4}\lambda\rho_\infty q_\infty^2 \qquad 3.1.1$$

where $\lambda = 1$ in supersonic flow. He also gave a relation for the base pressure coefficient in the form

$$C_{P_b} = \frac{2}{\gamma M_\infty^2}\left[\frac{2\gamma M_\infty^2 - (\gamma-1)}{\gamma+1}\left(\frac{2}{\gamma+1}\right)^\gamma \frac{1}{M_\infty^2\gamma} - 1\right] \qquad 3.1.2$$

Hill[30] concluded that the base pressure coefficient varies in a complex manner at low Mach numbers (1→2) depending on model shape, Reynolds number, boundary layer growth etc., however, at higher Mach numbers, he postulates that part of the difference between the limiting case of the assumption of a vacuum behind the projectile and

the actual value of base pressure is directly proportional to dynamic head. Thus, in the range $M_\infty > 2$ he proposed

$$C_{p_b} = \lambda' \frac{2}{\gamma M_\infty^2} \left[1 - \lambda \frac{\gamma-1}{2} M_\infty^2 \right]^{\frac{\gamma}{\gamma-1}} - \frac{2}{\gamma M_\infty^2} \qquad 3.1.3$$

where λ' and λ are empirical constants. Hill recommended that $\lambda = 0.055$ and $\lambda' = 0.5394$.

It is quite clear that, particularly at low supersonic Mach numbers, Reynolds number has a significant effect on base pressure. Probably the first people to attempt to include directly the effects of Reynolds number were Cope[31,32] and Hankins[33].

Cope's model (fig. 3.2) is an extreme simplification but contains some of the essentials of any reasonable model. This model includes a finite thickness of the boundary layer at the corner, the expansion of the boundary layer at the base through an angle ϕ, and the recompression at the section BB'. The freestream turning angle and the boundary layer thickness, δ, together determine the value of the base pressure.

Cope hypothesised that the expansion of the boundary layer fluid from AA' to BB' is isoenergic. Then also applying conservation of mass he obtained

$$\frac{P_b}{P_\infty} = 0.92 \left(\frac{1+\frac{1}{2}(\gamma-1)M_A^2 U_A}{1+\frac{1}{2}(\gamma-1)M_B^2 U_B} \right) \left(1 - \frac{\delta^*}{\delta} \right) \frac{\delta}{\ell} \frac{4K_1}{(1+2K_2 \tan\phi)^2} \qquad 3.1.4$$

where δ^* is the boundary layer displacement thickness at the base corner and K_1 and K_2 are empirical constants defined in fig. 3.2. $(1 - \delta^*/\delta)$ and δ/ℓ are functions of M_∞ for given velocity profiles in the boundary layer. It was found by Cope that for $2 < M_\infty < 3$, $K_2 = 1$ for $Re_\ell \geq 1.5 \times 10^6$, increasing to 1.5 for $Re_\ell \sim 0.5 \times 10^6$. While this method gives acceptable results in the limited Mach number range $2 < M_\infty < 3$ and in the turbulent regime, one unacceptable facet of equation 3.1.4 is that P_b increases linearly with K_1. The method must therefore be restricted in its application.

Kurzweg[34] studied the available data on base pressure with respect to the effects of Mach number, Reynolds number, boat-tailing and base temperature. While both Mach number and Reynolds number play a fundamental role in determining base pressure, once the boundary layer approaching the base is fully turbulent the effect of Reynolds number is practically negligible at a given value of Mach number.

Kurzweg suggested that the base pressure may be calculated by assuming that the velocity of the air which is reduced in the boundary layer approaching the base has to be restored by expansion at the base. Thus he obtained

$$\frac{P_b}{P} = \frac{\int_0^{\delta} \frac{q_y}{q_\infty}\frac{T_\infty}{T_y}\left[\frac{1+\{\frac{1}{2}(\gamma-1)\}\,M_\infty^2\,(1-T_0/T_{y_0})}{1+\{\frac{1}{2}(\gamma-1)\}\,M_\infty^2\,\{1-(T_0/T_{y_0})(q_y^2/q_\infty^2)\}}\right]^{\gamma/(\gamma-1)} y\,dy}{\int_0^{\delta} \frac{q_y}{q_\infty}\frac{T_\infty}{T_y}\,y\,dy} \qquad 3.1.5$$

where q_y is the velocity, T_y is the static temperature and T_{y_0} is the stagnation temperature in the boundary layer at a distance y from the body surface, P is the static pressure of the free stream ahead of the recompression shock, P_y is the static pressure of layer y after expansion of the air if layer y could expand from P_{y_0}, the stagnation pressure of layer y, independently of the other layers to its original velocity, see fig. 3.4.

In order to solve equation 3.1.5 it is necessary to postulate velocity, static temperature and stagnation temperature profiles in the boundary layer. It should be noted that the base pressure calculated represents a pressure value attained after expansion to a chosen velocity. Kurzweg pointed out that the original velocity is regained at some distance from the base (2 → 3 calibres).

These early models do not take account of the essential viscous mechanisms involved in the determination of the flow in the recirculation region. Referring, for instance, to fig. 3.2, the steady-state equilibrium of base pressure and the position of the BB_1 line is reached due to the scavenging effect of the free-stream external flow on the separated region. This reduces the mass of air in the recirculation zone, causing the angle, ϕ, to increase and the pressure in the separated region to decrease. Thus the line BB_1 moves towards the base. However, as this happens the strength of the recompression shock increases, making it more difficult for the scavenged air and the low velocity air in the boundary layer to overcome this pressure rise. These two counter effects serve to establish equilibrium.

3.1.2 Description of the base flow

It should be understood that while one speaks in terms of mean flow properties, the base flow, particularly in the case where there is no physical reattachment surface, is highly time dependent. The current understanding of the base flow at the rear of a slender, bluff based projectile (fig. 3.3), can be summarised in terms of the following phenomena:

a) The boundary layer upstream of the base corner can be characterised by its laminar, turbulent or transitional nature. The detailed description of the boundary layer will be determined by the projectile geometry and the free stream conditions (possibly non-uniform). As the boundary layer approaches the base it faces an acceleration and therefore thins.

b) Both boundary layer and free stream undergo turning and an expansion at the base corner. This turning process is instrumental in defining 1) the separation point, which will in general be on the base surface (fig. 3.3); 2) the possible formation of a separation shock; 3) the initial conditions for the free shear layer leaving the base; and 4) the enthalpy distribution at the base corner, the thermal characteristics of the wall, of course, also being important.

c) The lower edge of the shear layer is the dividing streamline which distinguishes (in a conceptual sense only) the flow in the recirculation zone from the flow arriving from upstream of the corner. Often the assumption is made that the fluid in the base region is stagnant, but in general this fluid recirculates at a low Mach number (< 10% of the external free stream Mach number). A stationary core in the centre of the recirculation zone may appear[23]. One can visualise a boundary layer on the base surface and then it is necessary to balance the work done in overcoming the base wall shear stress with the energy transfer to the base wall in specifying the conditions in the base region.

Above the dividing streamline a shear layer develops from the initial conditions at the corner which connects the base region with the external flow. The entrainment of fluid from the external flow into the base region depends on the conditions at the base corner as well as the conditions along the dividing streamline.

d) The shear layer entrains fluid from the base region also. In the mean this fluid has to remain below the dividing streamline, by definition. Apart from the connection between the recirculating fluid, the shear layer and the external flow through the shear stress and pressure distributions along the dividing streamline, there is also the question of heat transfer. The shear layer develops as a function of the character of the flow (laminar, turbulent or transitional) through the entrainment rate, Mach number and enthalpy distributions in the internal and external regions.

e) Since the flow converges towards the centre line after leaving the base the flow must turn at some point (or in some region) giving rise to a compression followed by a wake. The static pressure in the wake must attain the ambient pressure far downstream. Since, in the absence of mass injection in the recirculation zone, the dividing streamline must 'reattach' and the mass flow in the wake must consist only of the mass flow in the boundary layer at the base corner together with mass entrained in the shear layer from the free stream. The continuity of pressure and shear stress and the requirement that the solution should continue smoothly to downstream ambient conditions constitute the downstream boundary conditions for the base flow problem.

While it would now be possible to examine the attempts of many authors to model the flow in the undisturbed wake and to include a

number of features mentioned above this will not be done. The interested reader is referred to the texts referenced in §3.0.

3.2 Methods of Base Pressure Control - Aerodynamic Modifications

3.2.1 Geometric modifications to the base region

For many years it has been realised that careful afterbody design can reduce base drag. Perhaps the simplest and most obvious geometric modification is the boat-tail. Kurzweg[34] measured the effect of boat-tailing on an axisymmetric cone-cylinder combination at M = 3.24 and found that boat-tailing can significantly reduce base drag. Chapman et al[35] measured the base pressure on fifty-five wings with boat-tailing angles varying from - 2.9° to 20° for varying Mach numbers and Reynolds numbers. They found that for wings the effect of boat-tailing is small.

While for axisymmetric bodies the effects of geometric modifications can give large base drag reductions, this is sometimes at the expense of considerable geometric complexity[38] and offers no possibility of generating base thrust.

3.2.2 Boundary layer bleed and base injection

The basic features of the base flow without injection have been discussed in §3.1. When mass injection is used as a means of base flow control the essential features of the flow remain the same. The base pressure still depends on the interaction between (1) boundary layer growth on the body and the corner expansion process, (2) the development of the separated shear layer as a connection between the base flow and the external flow and, (3) the recompression process of the low pressure fluid to ambient conditions in the wake region.

Base flow control, from the point of view of increased base pressure, can be obtained through mass, momentum, or energy addition to the flow in the base region. When additional mass is injected for base flow control into the base region there are two questions of fundamental importance:

a) for given flow conditions, is there an optimum location where the mass injection is most effective

and

b) when mass is injected, under what conditions will it have a mass input or energy input effect.

Fig. 3.5 shows three typical locations for mass injection. One question of practical importance in regard to mass injection is the means of obtaining the injected mass. In the case shown in fig. 3.5(a) mass is removed from the boundary layer approaching the base by suction. This then modifies the base pressure by its effect on the thinned boundary layer approaching the base and by the effect of the injected mass in the recirculation region. It is clear that boundary layer bleed also offers no possibility of base thrust.

In the cases shown in figs. 3.5(b) and (c) mass has to be carried in the body of the projectile. The peripheral injection arrangement modifies the base pressure by its effect on the afterbody boundary

layer and depending on the injectant velocity, the free stream before, during or after the expansion. On the other hand injection through the base surface (fig. 3.5(c)) introduces changes in the base recirculation region and thereby affects the balance between the recirculation region and the external flow. The orientation of the injection slot and the size and disposition of the injection holes are additional variables in arranging mass injection.

In general, injected fluid introduces mass, momentum and energy effects, however, it is probable that in most cases the momentum and energy addition effects are the most significant. On the other hand mass is entrained into the shear layer from both the inner base region and the external flow and this determines the distribution of pressure and shear stress in the shear layer. The location and shape of the dividing streamline can thus be related to the mass injected into the inner base region and the base pressure can be correlated with respect to the mass injected. When mass is injected through the base it is clear that the fluid that is not entrained in the shear layer has to recirculate or escape through the wake. This means in turn that the dividing line will no longer 'reattach' and the dividing streamline will move outwards, away from the centreline and the recompression region will become directly affected.

The characteristics of the injected fluid that are of interest are (a) temperature, (b) density and (c) molecular weight. A method of obtaining a good combination of these parameters is to obtain combustion of the injectant, either prior to, or in the region of, injection. In the latter case the location of the flame, i.e. the region of enthalpy release, is an important additional parameter.

Cortright and Schroeder[39] investigated the effect of base bleed on partially boat-tailed bodies and cylindrical afterbodies. The injectant was air in all cases, presumably at ambient temperature. The effect of the jet pressure ratio on the base pressure coefficient is shown in fig. 3.6. The most striking feature of these results is that a very small amount of mass injection enhances the base pressure coefficient. Increasing the jet pressure ratio beyond 1 causes a decrease in the pressure coefficient. Other authors[2,40,41,42] have also investigated the effects of base bleed on base pressure. If one defines a non-dimensional mass injection parameter I as $I = \frac{\dot{m}_j}{\rho_\infty U_\infty A}$

where $\dot{m}_j$ is the mass flow rate of injectant, then the effects of mass bleed rate on the base pressure are as shown in fig. 3.7. The results of Reid and Hastings[40] show clearly the effects of the diameter of the bleed hole. At low injection rates the bleed hole diameter is not significant but at high injection rates increasing the bleed hole diameter is beneficial. The results of Townend and Reid[2] indicate the benefits of reducing the molecular weight of the injectant and also the effect of enthalpy release in the wake.

In summary, therefore, it appears that gas ejection becomes more effective with (a) decrease in the molecular weight of the ejected gas, (b) increase in the enthalpy of the ejected gas and (c) decrease in the velocity of the ejected gas.

3.3 Wake Combustion

The two methods of base pressure control introduced in the previous section were 1) geometric design of the base of the projectile (in general, boat-tailing) and 2) mass addition to the near wake region, either into the boundary layer approaching the base or into the recirculation region. However, the results of Townend and Reid[2], fig. 3.7, suggest that a much greater drag reduction can occur when combustion is induced in the wake. (In fact, Townend's results show a value of $P_b/P_\infty > 1$, implying a base thrust, but his experiments suffer to a small extent from wind tunnel interference.)

Two questions then become paramount:

a) Is it possible to establish theoretical and practical limits to the reduction of base drag by the adoption of combustion and boat-tailing separately and in combination?

b) What characteristics of the fuel are significant in choosing the optimal injection of products for combustion?

Optimal injection implies optimal injectant properties (e.g. specific fuel consumption, enthalpy release per unit volume, etc.), mass distribution and enthalpy distribution. Smith[43] has produced an excellent survey of the properties of fuels which may be useful in wake combustion applications.

There are clearly three parameters in addition to those defining the near wake region flowfield already discussed. These are

1) injection mass parameter: for example in the two-dimensional case, Korst[44] uses

$$I_m = \frac{\dot{m}_f T_o}{D P_{o_\infty}} \left(\frac{R}{\gamma g} \right)^{\frac{1}{2}} \qquad 3.3.1$$

where $\dot{m}_f$ is the mass of fuel injected at the base (fuel stagnation properties are assumed to be equal to the airflow stagnation properties), $P_{o\infty}$ = free stream stagnation pressure and T_o = free stream stagnation temperature. D is the height of the base. Other parameters can also be defined, see e.g. fig. 3.7.

2) Injection momentum parameter: for example Collins et al[45] define

$$I_M = I \cdot F(M_e, \gamma_e)$$

$$\text{where } I = \frac{\dot{m}_f}{2\dot{m}_{BL}} \left(\frac{\omega_e}{\omega_f} \right)^{\frac{1}{2}}$$

and $F(M_e, \gamma_e)$ is defined as

$$F(M_e, \gamma_e) = \frac{1}{M_e}\left[\frac{\delta-\delta^*}{\delta-\delta^*-\delta^{**}}\right]\frac{1}{\gamma_e}\frac{T_{o_f}}{T_o}\frac{T_o}{T_e}$$

and $\dot{m}_{BL} = \rho_e U_e(\delta-\delta^*)_e$

where ω is the molecular weight, δ^* is displacement thickness and δ^{**} is momentum thickness, $(\ )_f$ refers to the fuel or injectant and $(\ )_e$ refers to conditions in the external stream.

3) Injection enthalpy parameter[46]:

$$I_h = \frac{\sigma\dot{Q}_b}{DC_pP_{oe}(T_{oe})^{\frac{1}{2}}}\left[\frac{R}{\gamma g}\right]^{\frac{1}{2}}\left[\frac{\gamma+1}{2}\right]^{\frac{\gamma-1}{2(\gamma-1)}}$$

where σ = mixing coefficient, $\dot{Q}_b$ is the total heat addition to the wake and $(\ )_{oe}$ refers to stagnation conditions in the external free stream. The value of σ is determined empirically, for example, Korst and Tripp[47] provide a parameter for compressible flows in the form $\sigma = 12 + 2.76\ M$ where M is the local Mach number in the free stream after expansion at the base corner. An important point of uncertainty is the dependence of σ on the enthalpy of the mixing streams.

Baker et al[1] were among the earliest investigators to examine the reduction of drag of supersonic projectiles by combustion of hydrogen in the wake at a free stream Mach number of 1.9. Scanland and Hebrank[48] investigated the drag reduction of 40 mm projectiles in free flight tests. The fuel used was a pyrotechnic, and they achieved a 65% drag reduction at a specific impulse of 180 lbf.sec/lbm. Other authors have also investigated the application of fumers to base drag reduction [49,50,51] however, the results of Bowman and Clayden[41,42] tend to indicate that 100% drag reduction is an unrealistic goal, at least for Mach numbers less than,say, 4. Davis[52] conducted experiments at M = 1.98 on a two-dimensional model using hydrogen as the fuel.

3.3.1 Base flow models with combustion

An idealised model of the base flow is shown in fig. 3.8. In this model the base region is divided into four zones as follows:

1) Σ_1 is occupied by the returning part of the recirculating fluid i.e. line 1 is the zero velocity line.

2) Σ_2 is the region occupied by the fluid travelling downstream which is recirculated and also contains some of the shear layer fluid.

3) Σ_3 contains the remaining part of the mixing layer.

4) The outer flow.

The region Σ_2 is shown divided into two regions separated by the reattachment streamline (RSL). The portion Σ_{21} incorporates the fluid in forward motion which is recirculated between the reattachment streamline and the dividing streamline (DSL) is displaced, by definition, to allow the passage of an amount of fluid equivalent to the injected fluid mass. It is clear then that Σ_{22} can be identified only if there is injection, and in the absence of injection, the DSL and the RSL coincide and simply become the reattachment streamline. As injection is increased, both the RSL and the DSL are displaced and with the enlargement of the region Σ_{22} the DSL is displaced outwards causing Σ_3 and the outer edge of the mixing layer in turn also to be displaced outwards. In this way changes in the outer stream pressure, the boundaries of the different regions and the base pressure are connected with each other.

If the regions Σ_1 and Σ_{21} are considered together as one region, say Σ_{11}, then Σ_{22} and Σ_3 represent the mixing layer between the vortex pattern at the base in region Σ_{11} and the outer stream. It may be emphasised that the DSL and the concept of a separately identifiable region Σ_{22} are purely for convenience in obtaining mass balance. The injected fluid will also affect the recirculating fluid. Thus, it is only a mathematical convenience to assume that the mass flow in the region Σ_{22} is equal to the injected mass.

One factor of great significance in regard to entrainment in the mixing layer is that the entrainment obviously varies along the mixing layer. This problem is further compounded by the fact that the pressure along the outer edge of the mixing layer also varies as there is expansion at the corner and recompression further downstream. It is difficult to visualize how optimum entrainment (for example, such that the base pressure attains the free stream value) can be arranged by control of the recirculation region through distributed mass injection in the base region. When injection is arranged through the base, apart from a minor adjustment in the angle of injection, one can control only the mass and velocity of injectant. However, if the enthalpy of the injectant can also be controlled, especially through distributed combustion, it is possible to see how the entrainment can be adjusted along the entire length of the mixing layer.

Base combustion provides several extra parameters for controlling the base region flow compared to mass injection. In the most general case, one can control the distribution of mass, enthalpy and molecular weight. In modelling the base flow with combustion, the principal factors are the location and magnitude of enthalpy release. Figure 3.9 illustrates two possible models, the first based on the concept of a stirred reactor at the base and the second based on combustion essentially confined to the mixing layer. In the latter, there is also the possibility of combustion at the axis of the projectile in view of the formation of stagnation zones in the wake neck region and in the vicinity of the base.

The stirred reactor model is applicable to the case where, with an open cavity, either 1) the chemical reaction that has been initiated in the cavity continues after injection (of the initial products of combustion and the un-burned material) into the base region, or 2) the products of combustion in the cavity become mixed with the recirculating fluid after injection. The latter is simply equivalent

to hot gas injection. In either case, the stirred reactor model is based upon the following assumptions:

1) a practically stationary globule of gas located at the base; that is, the recirculating region velocities are assumed to be small, even though there is some type of a vortex in the base region;

2) a single temperature and density assigned to the globule of gas; and

3) an interaction between the wake fluid from the supersonic projectile and the stationary, high temperature globule of gas.

Assumptions 1) and 2) are equivalent to assuming a globule of gas in the base region which is uniform and of a finite volume but a priori unknown shape. Assumption 3) requires modelling the mixing layer between a supersonic flow and a stationary gas under the conditions of (i) the projectile boundary layer and the mixing layer being turbulent, and (ii) a pressure gradient existing along the mixing layer outer edge.

The model with distributed combustion in the mixing layer, and possibly in the vicinity of the axis, is applicable to cases where the injectant undergoes combustion on coming into contact with air. This model assumes that either the injectant is fed into the mixing layer directly or the injectant diffuses into the mixing layer and a diffusion flame is the result. In both cases, a number of other assumptions will be required before the model becomes sufficiently well defined. If the combustible gas is injected directly into the mixing layer, so long as the momentum of the injectant is small, the mixing layer velocity and mass distributions and the mixing layer thickness can be assumed to be unaltered. When the injectant is introduced into the recirculating region and burns in the mixing layer, it is necessary to account for the injectant diffusion into the mixing layer prior to combustion or after ignition.

The model with distributed combustion can be considerably simplified if we assign an enthalpy distribution across the mixing layer and similarity is assumed along the mixing layer. This is the approach adopted by, for example, Broadbent[53-57].

A direct extension of the Korst model[44] for application to reacting wakes in two-dimensional turbulent flow is due to Davis[52]. A fuel (hydrogen) is supposed to be injected through the base over its entire area uniformly. The model is based on two-stream jet mixing with combustion, the latter based on a thin diffusion flame or "flame sheet". The postulates of a jet boundary streamline and the dividing streamline thus complete the essentials of the model.

The mixing region, that is, the free shear layer, is the postulated combustion region; the fuel admitted at the base and the oxygen from the air passing over the body are assumed to diffuse into the reaction zone from opposite sides, and are expected to be completely consumed at a thin flame sheet. Thus the flame sheet is imbedded in the shear

layer.

The free shear layer itself is considered under boundary layer approximations with Lewis and Prandtl numbers equal to unity. Therefore, one can employ Crocco integrals for the element mass fractions and total enthalpy functions as linear functions of the velocity profile.

It should be noted that neither the mixing parameter σ, nor the structure of the shear layer, is in any way affected in this analysis by the injection of the gas or by the reaction of the gas in the base region. The base region enthalpy and the location of the flamesheet are, of course, coupled to the density and velocity profiles in the shear layer.

Some of the experimental data obtained by Davis are presented in fig. 3.10. Davis points out that external combustion of hydrogen was accomplished with little difficulty at values of B larger than 1.3×10^{-5}. Two other observations were (a) at $B > 1.0 \times 10^{-4}$, there was little effect of additional bleeding and (b) at $B > 5.0 \times 10^{-5}$, there was little further effect of combustion. The latter was taken to indicate that the useful energy release had reached a maximum and further increases in P_b were due to base bleed. It should also be noted that Davis obtained specific impulses of the order of 10^4 lbf.sec/lbm.

Temperature related data obtained by Davis are presented in fig. 3.11. The theory seems to underpredict the bulk wake temperature at the lower values of B and overpredict the temperatures at higher values of B. The theory shows that the flamesheet located below the dividing streamline at low values of B shifts to a region above the dividing line at higher values of B. On the other hand, from fig. 3.11(c) it appears that no flamesheet is present at $B = 2.17 \times 10^{-5}$ but that a flamesheet (temperature peak) appears at η equal to zero when B is doubled.

The species concentrations Z_i for two values of B, determined by Davis, are presented in fig. 3.12. Davis notes that the concentration of water vapour, the product, was overpredicted by the theory and also that unreacted oxygen was present in the wake. It should be noted that all of the oxygen was expected in the model to react with the hydrogen on a stoichiometric basis to produce water vapour.

At low mass flow rates the flame sheet concept clearly fails and the significant underprediction of the temperature in the wake indicates the possible presence of a stirred reactor. At the higher mass flow rate shown in fig. 3.11(c) there is distinct evidence that the diffusion flame concept is useful, although the species concentration observed in fig. 3.12 would indicate that reaction was still occurring in the recirculation zone.

Strahle[4] has discussed the control of base flow phenomena with fuel injection normal to the body surface (see fig. 3.13). The principal consideration here is the change one can introduce in the outer inviscid stream and therefore the effect one can produce on one of the parameters governing the "reattachment process". To what

extent this could be practically useful depends upon the coupling between the inviscid and the viscous streams. Earlier investigations of Serafini et al[59] are also of interest here. Strahle's model rests on a clear separation of the flame zone from the recirculation zone and adiabatic assumptions in the reattachment zone. The matching between the viscous and the inviscid regions is carried out using the Lees[60,61] model. The combustion parameter is the energy release and its extent along the direction of flow. Data computed by Strahle on the distribution of pressure and of the viscous zone thickness are presented in fig. 3.14. One question in such computations is the method of taking into account the combustion zone, for example, either by small disturbance theory or by a control volume technique. It appears that the following parameters have a direct influence on the base flow: (a) axial as opposed to peripheral injection, (b) molecular weight of the injectant and (c) the enthalpy of the injected stream.

A number of investigators have been interested in the effects of disturbances in the external stream. Hawkins and Trevett[11] examined the effect on the base pressure of shock waves generated at the lip of an open jet wind-tunnel at M = 1.7 and M = 1.9. Strahle and coworkers[3,9,10] have used compression sections both with and without wake combustion to modify the external flowfield and external combustion has been achieved by Schadow and Chieze[8] on a two-dimensional model and by Hubbartt and Strahle[62] on an axisymmetric model. Both these latter results suffered from wind tunnel interference. Hurdle[12] has investigated the effect on base pressure of a convergent-divergent cowl placed in the free stream. Some of the results obtained by Hurdle[12] are shown in fig. 5.3.

A number of analyses of the effects of external combustion have also been attempted[4-7] using modifications of the Lees model[61]. Initially the results of these analyses proved encouraging, however, Schetz et al[7] suggested that external burning would not be efficient from a fuel usage point of view. This result of Schetz[7] is also in some doubt since it was assumed that the flame extended a considerable distance downstream of the base (fig. 3.15 and 3.16). Significant base pressure rises may be achievable with shorter flame lengths and hence less fuel. The base pressure rises calculated extend P_b/P_∞ from 0.56 to only 1.21 at M = 2, insufficient to cancel the drag of the projectile. One can only conclude that the case for external burning is not proven and can only offer net drag reduction. It appears that to achieve net thrust either fuel must be burnt in a confined space (a ramjet) or a strong external compressive disturbance must be applied (e.g. a shock wave).

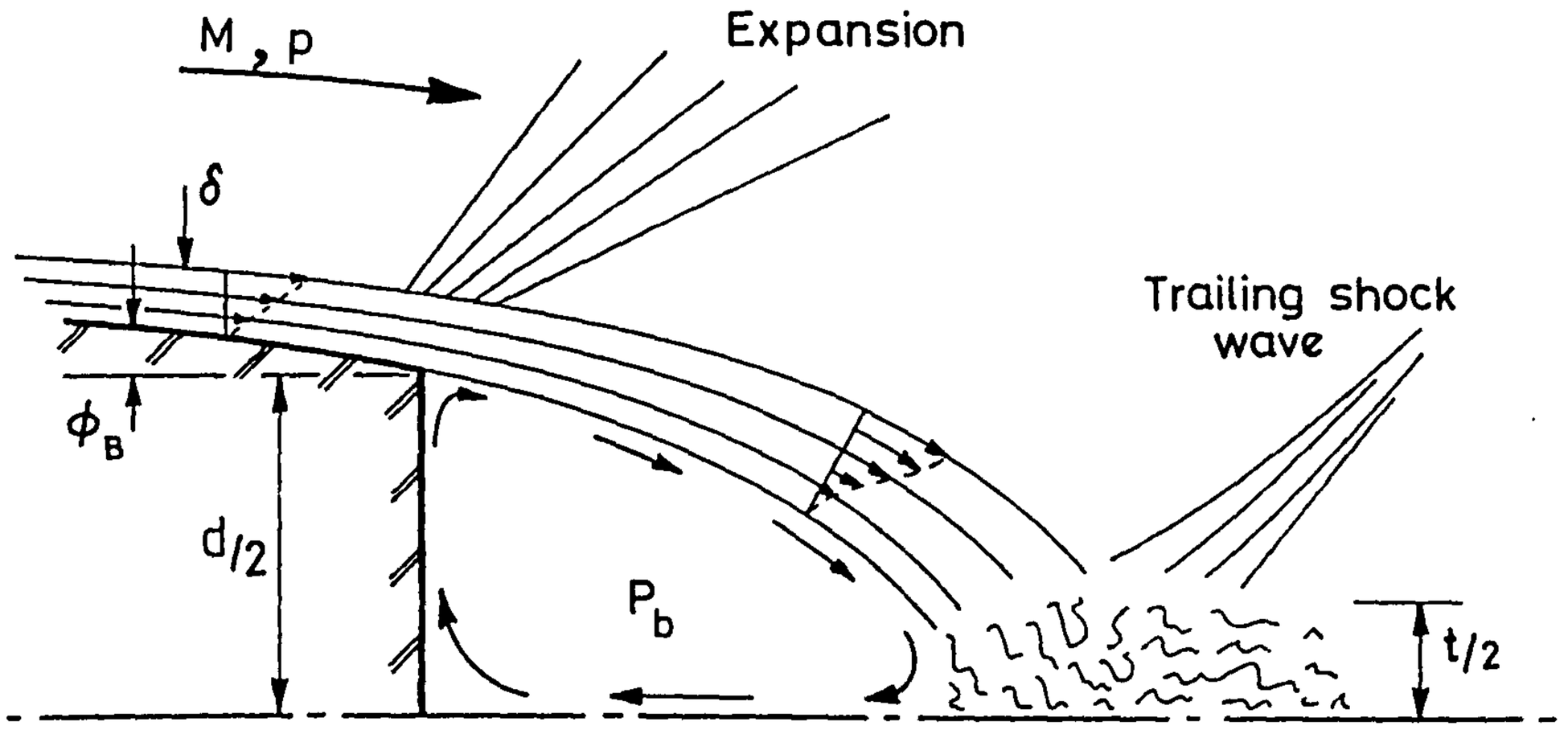

Figure 3.1. Flow at base of a projectile

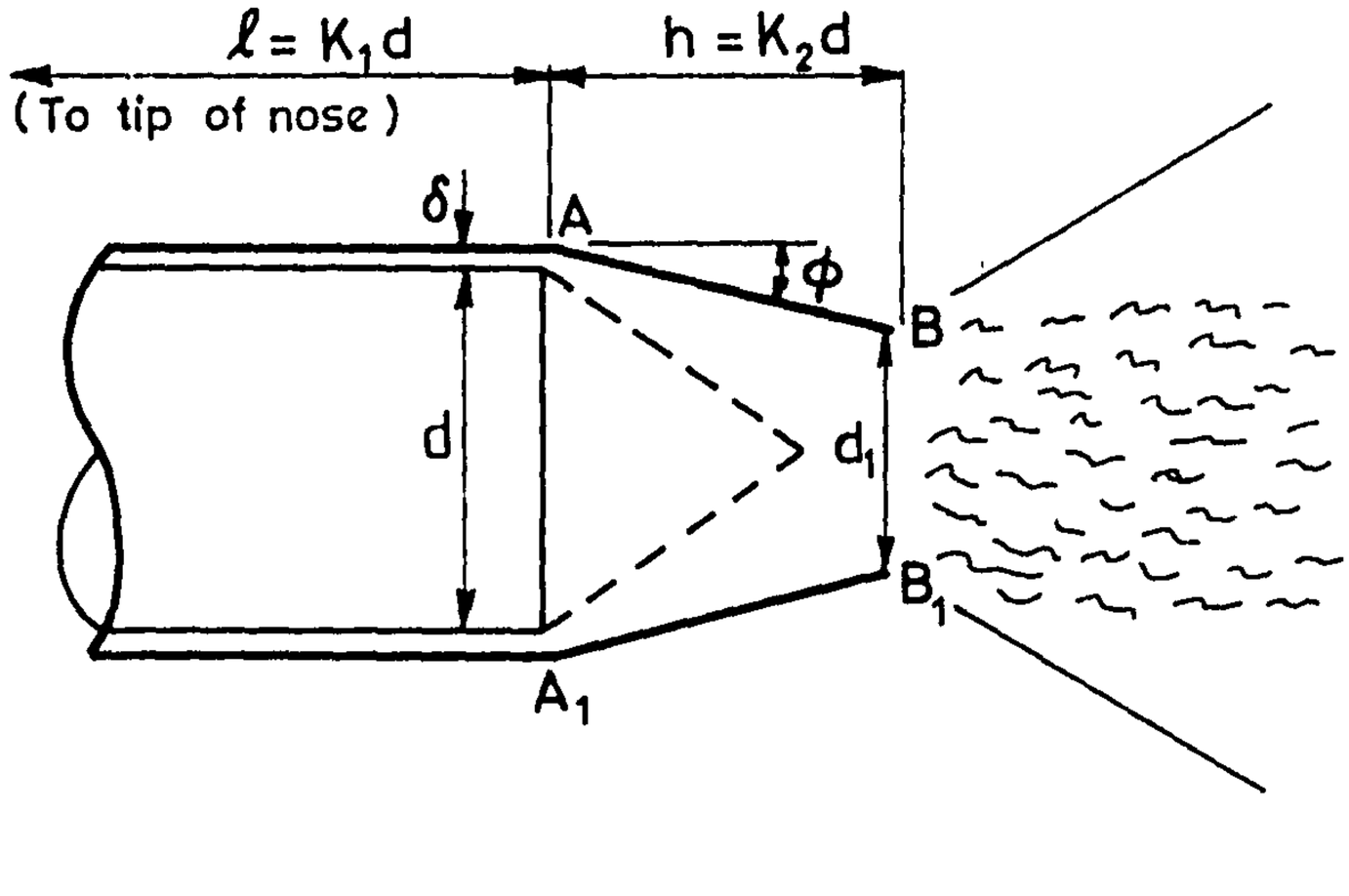

Figure 3.2. Base flow model of Cope[32]

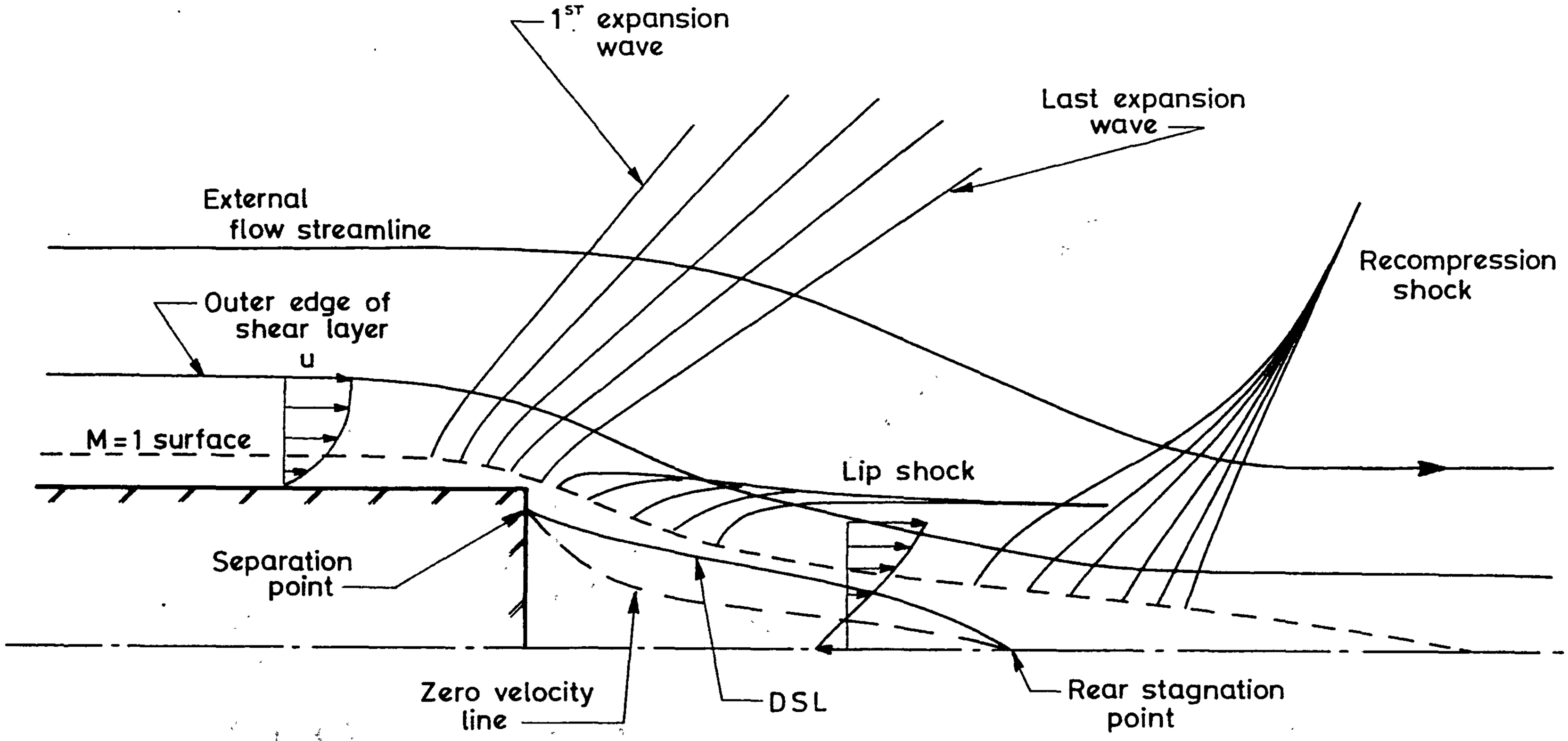

Figure 3.3 Schematic of flow in the base region.

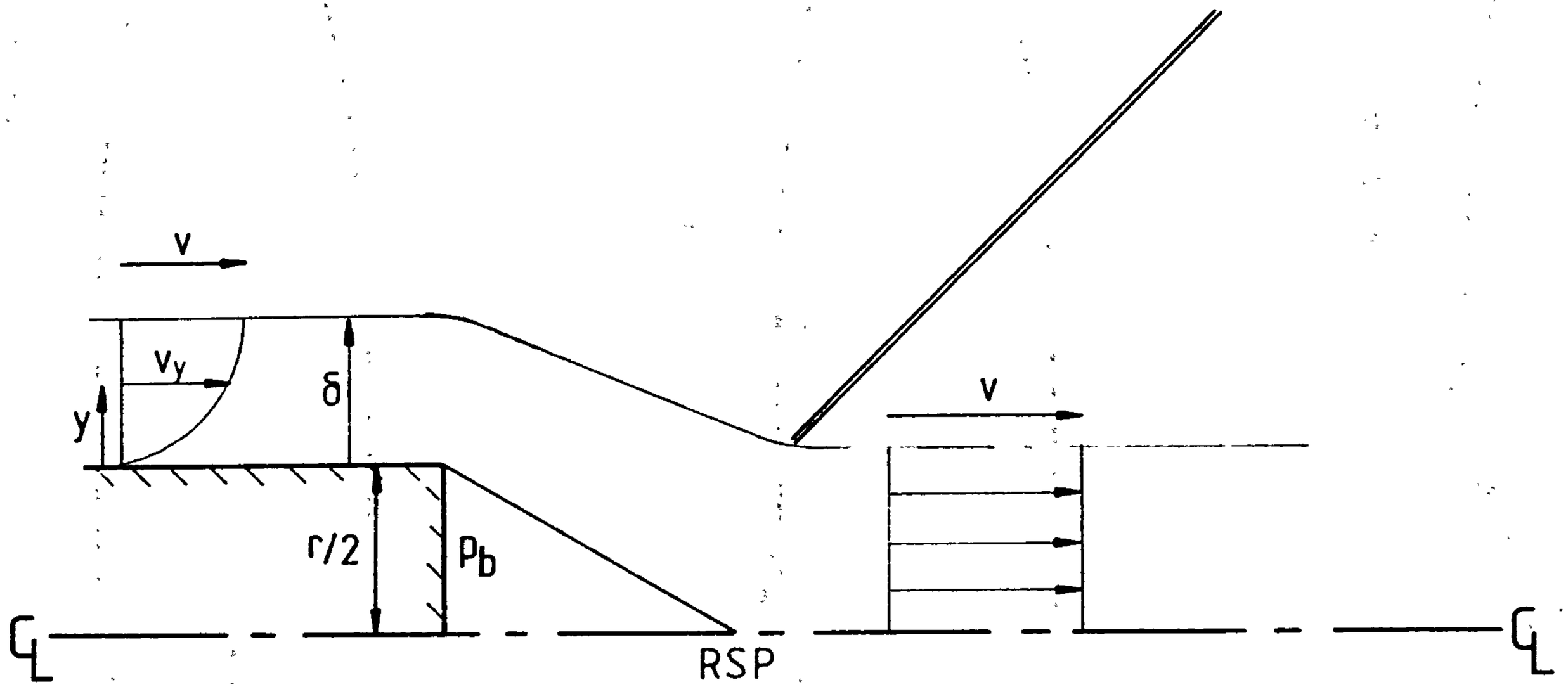

Fig. 3·4: Kurzweg's hypothesis for the calculation of base pressure

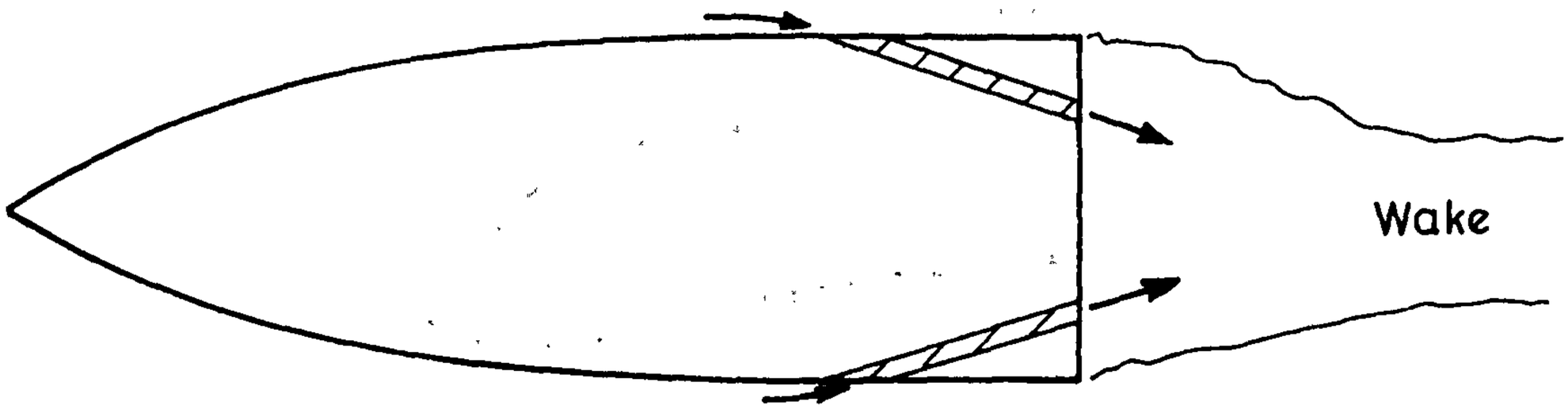

(a) Boundary layer bleed

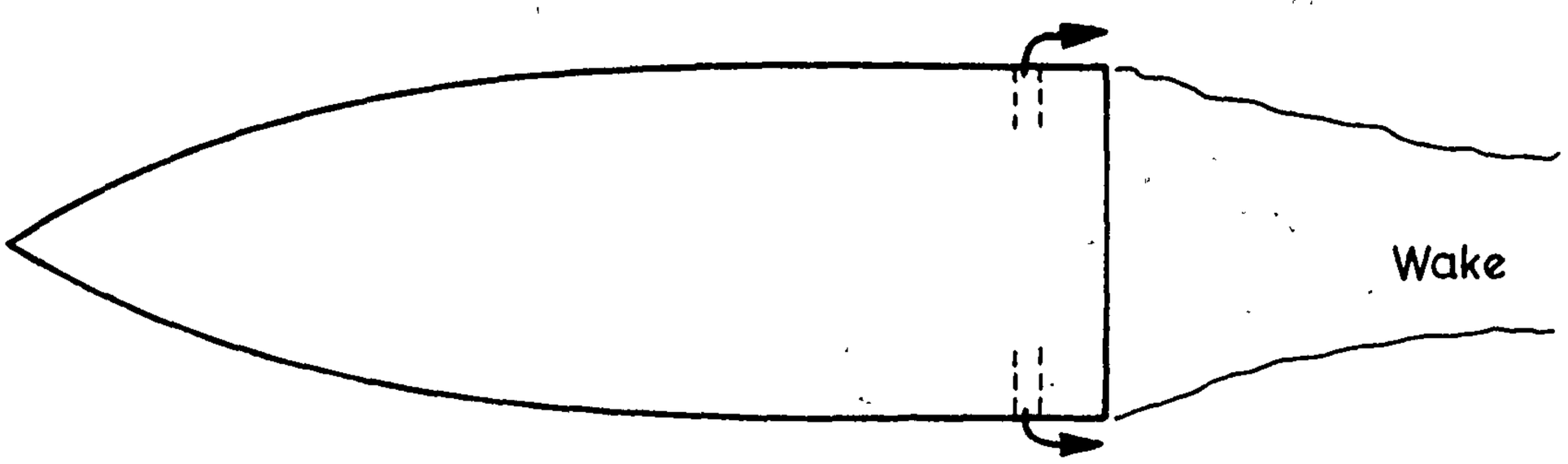

(b) Peripheral injection

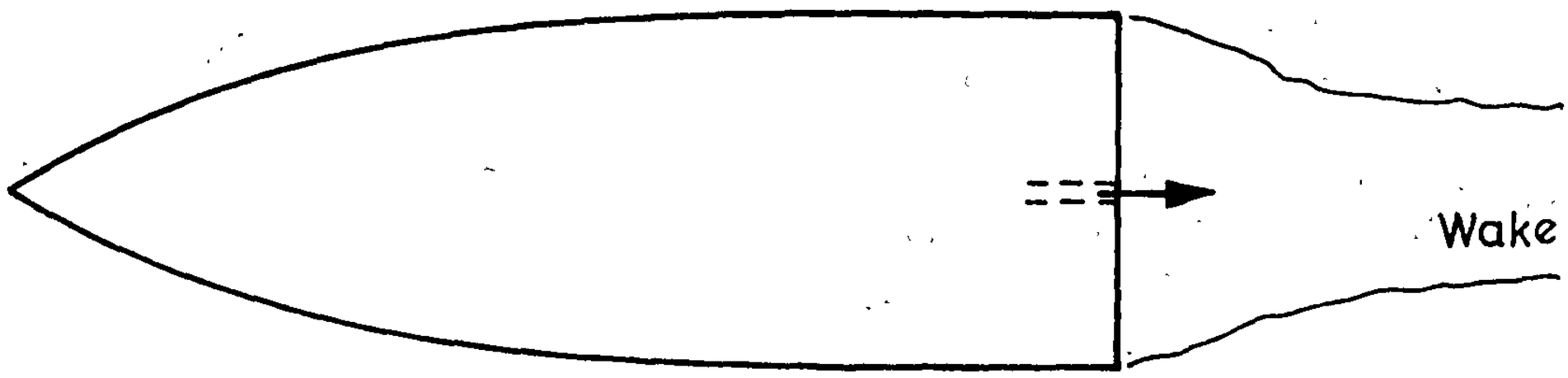

(c) Base injection

Figure 3.5 Typical locations for mass injection.

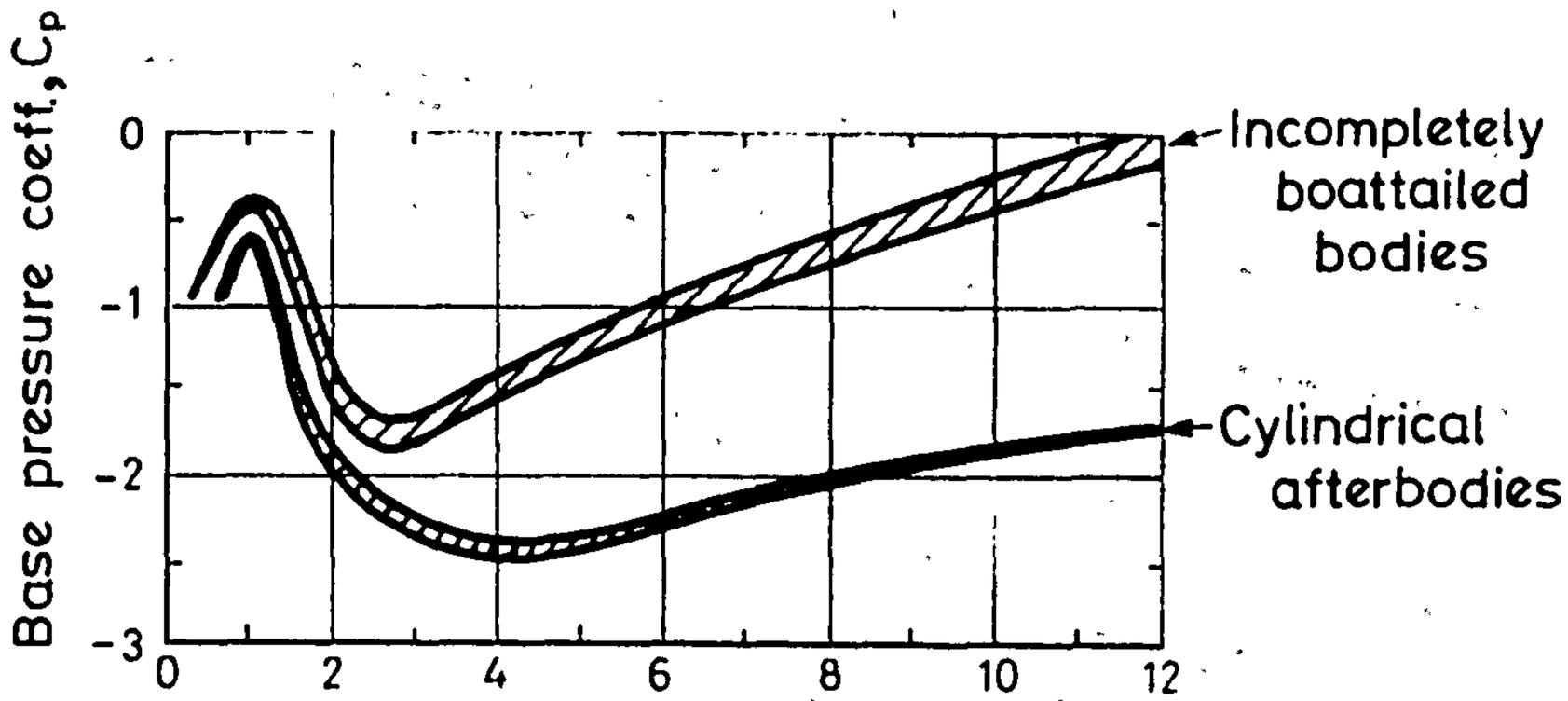

Figure 3.6. Base pressure coefficient Vs injection pressure. (Cortright & Schroeder[39])

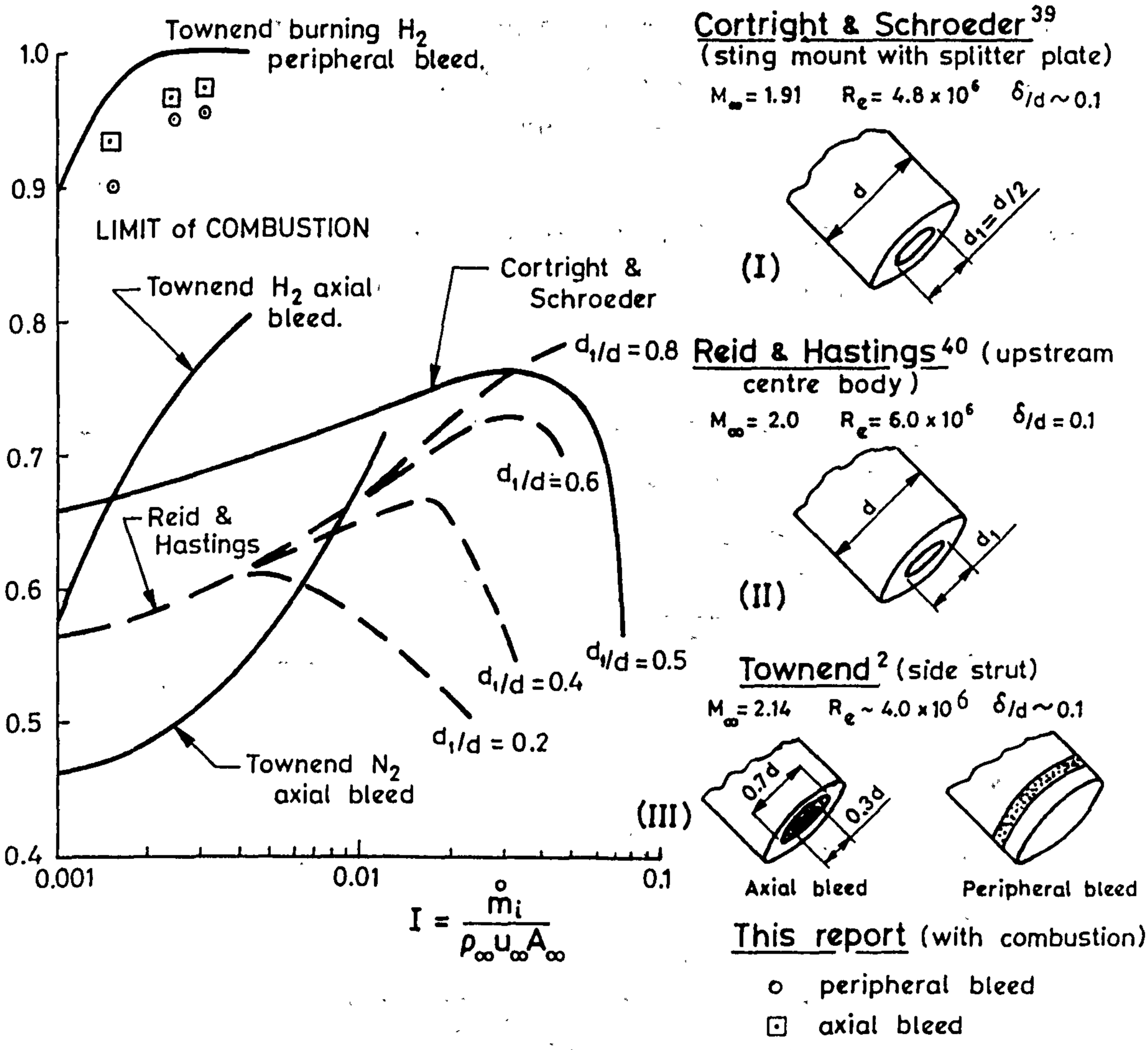

Figure 3.7. Base pressure ratio Vs mass injection parameter.

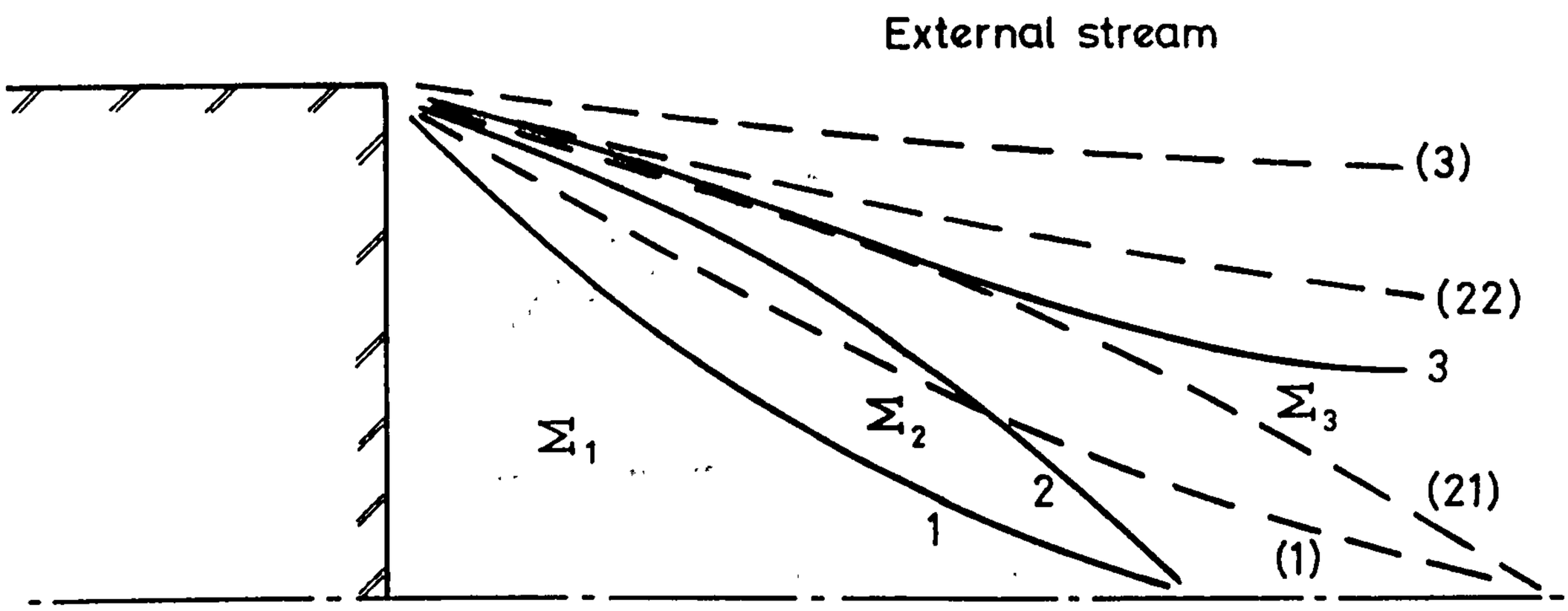

Figure 3.8. Flow zones in the base region.

Key:- —— No injection case . ---( ) With mass injection 1 and (1) zero velocity line. 2 and (21) reattaching streamline. 2 and (22) dividing streamline. 3 and (3) outer edge of shear layer.

Σ_{21} region between (1) and (21). Σ_{22} region between (21) and (22). Σ_3 region between (22) and (3) or 2 and 3.

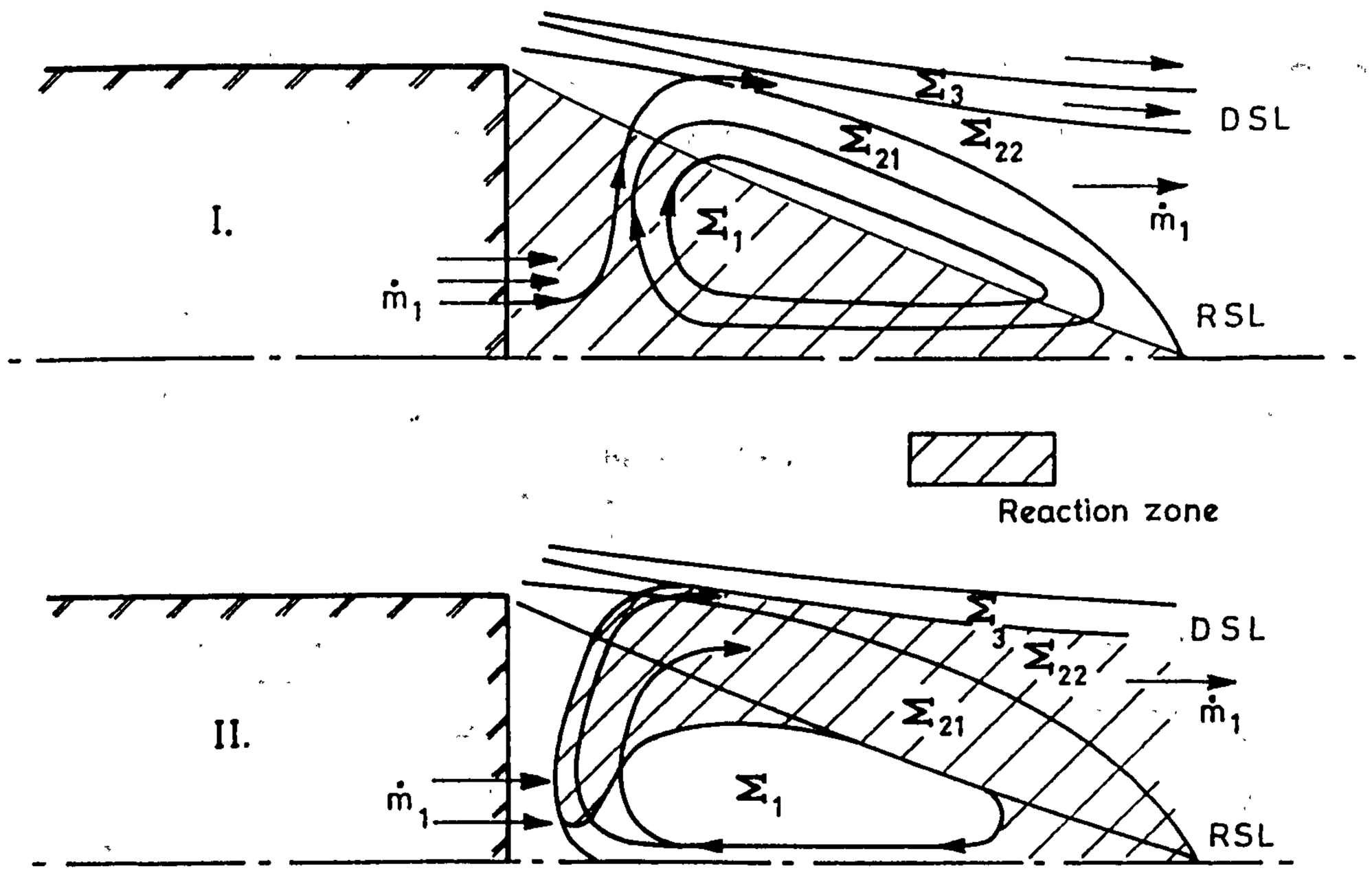

Figure 3.9. Models for enthalpy release in base region.

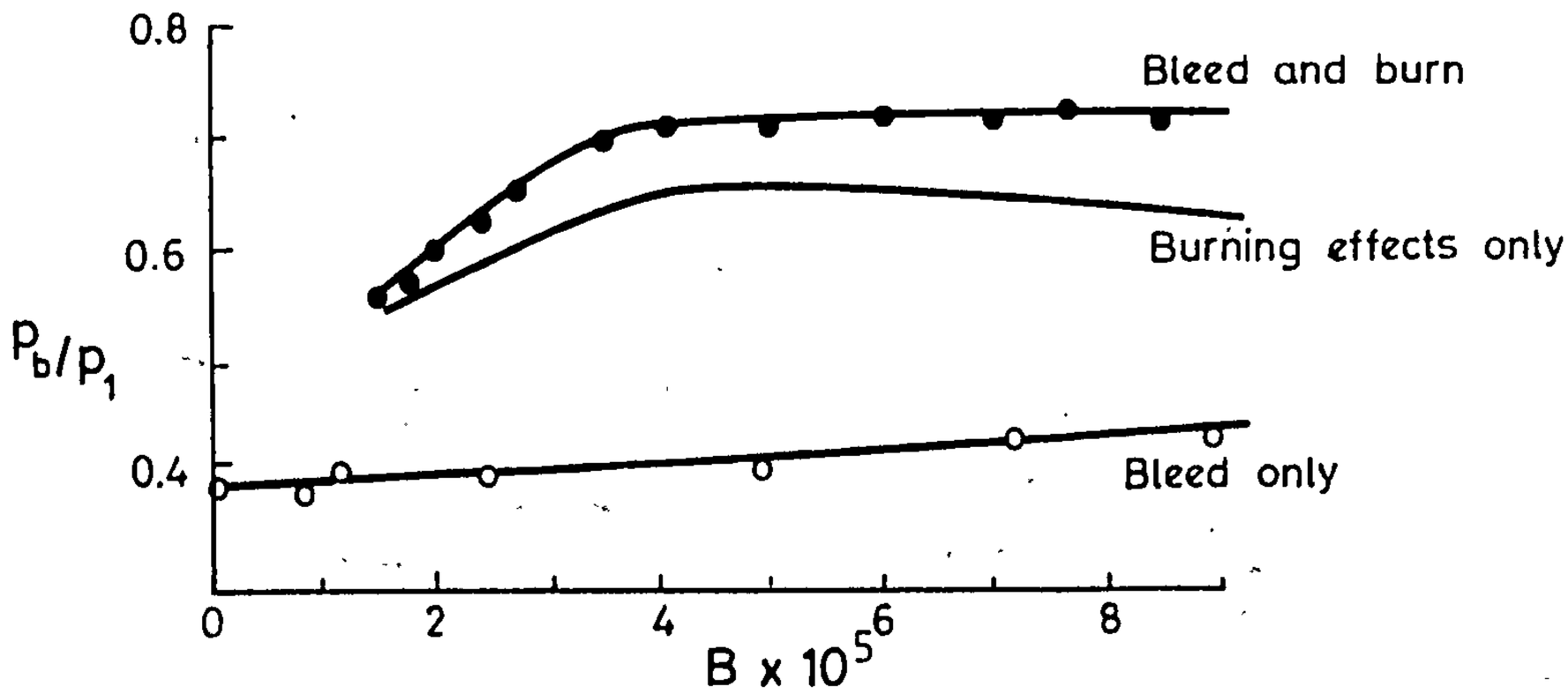

Figure 3.10. Base pressure ratio v^s injection parameter (Davis[52]).

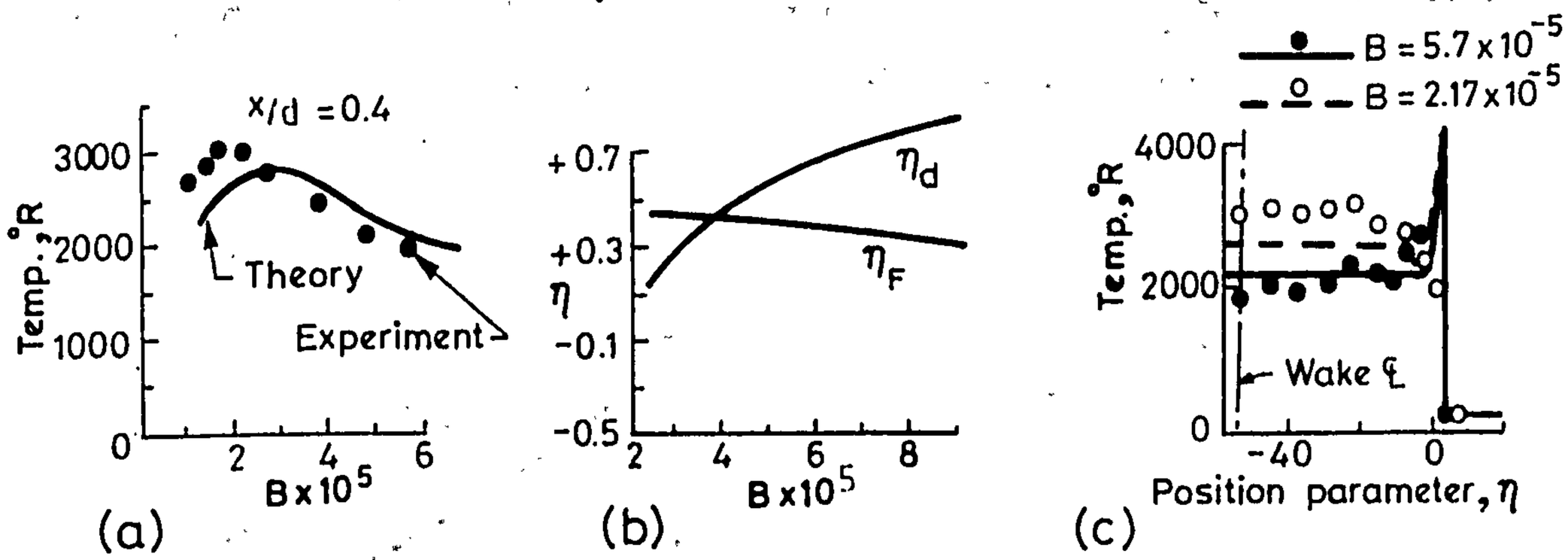

Figure 3.11. Temperature and location of flame in Davis flamesheet model.[52]

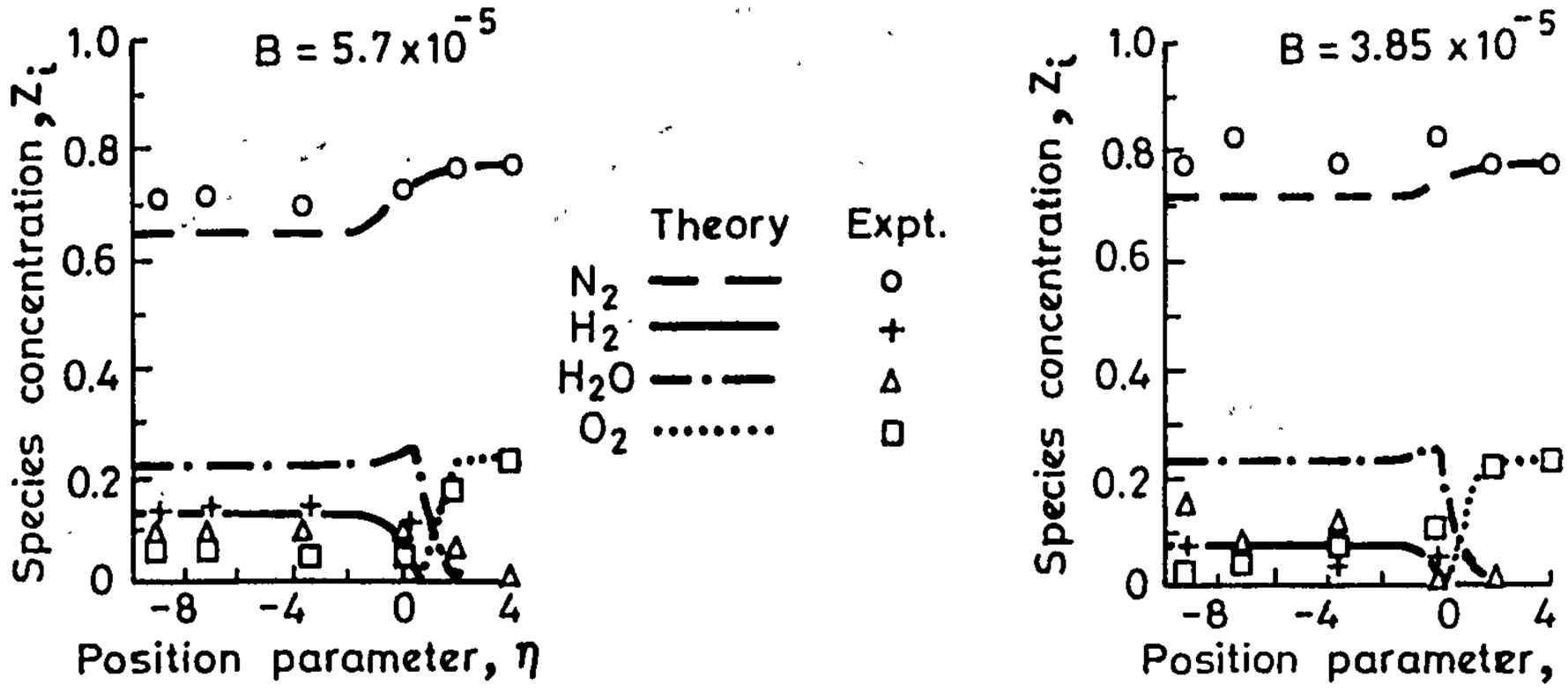

Figure 3.12. Species concentration distribution in Davis flamesheet model.[52]

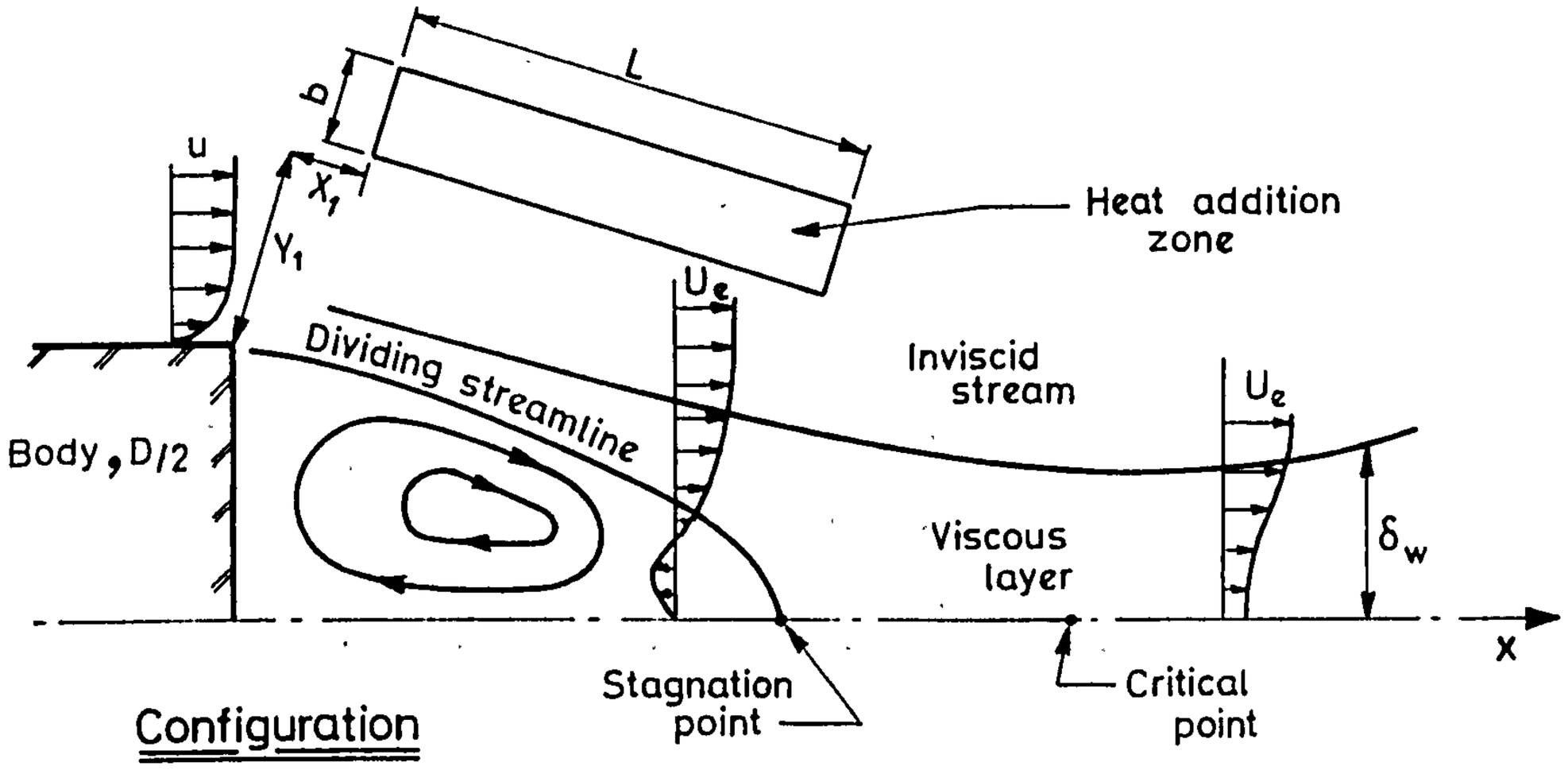

Figure 3.13. Strahle model[4] for body surface injection and combustion.

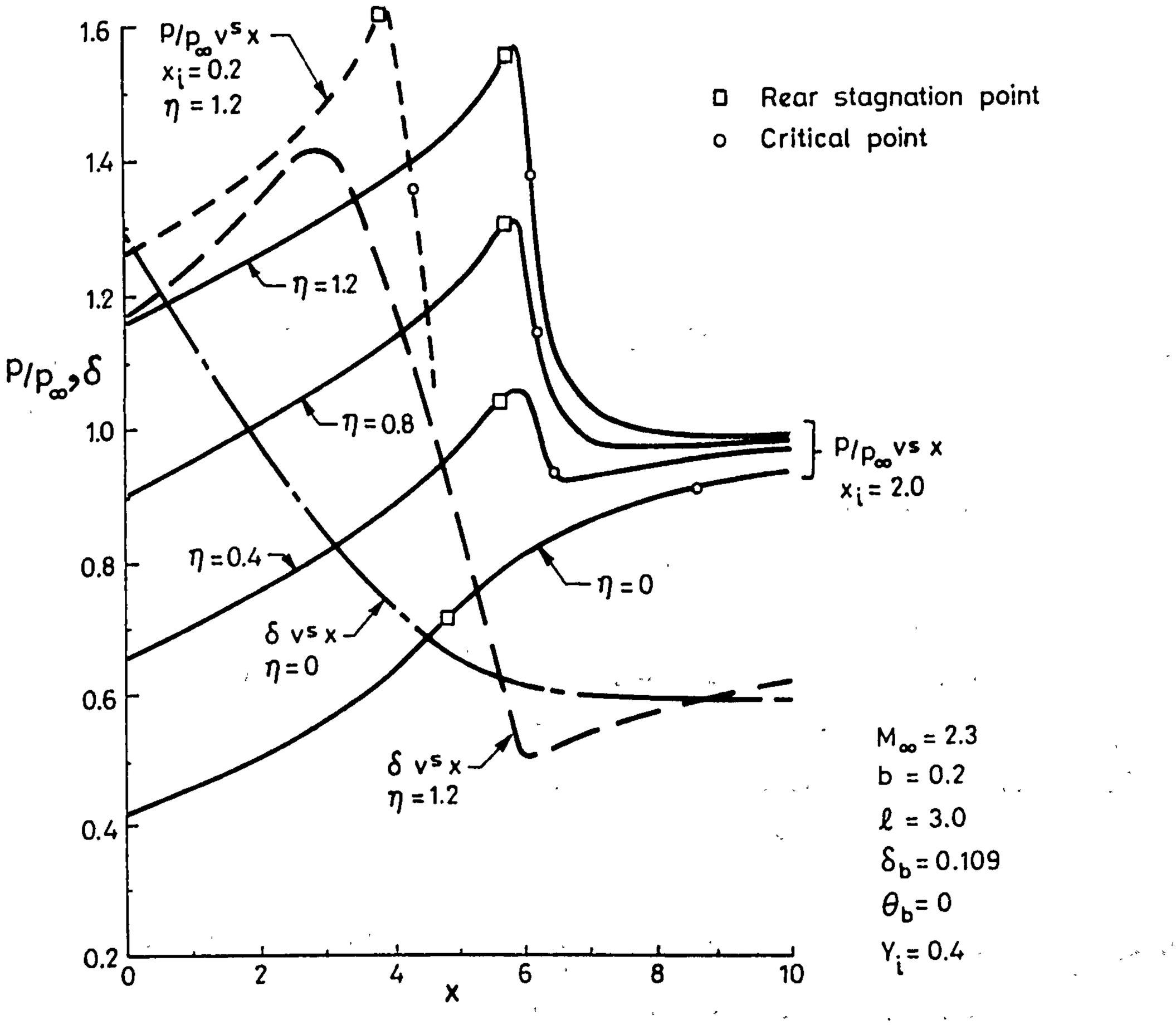

Figure 3.14. Axial pressure distribution and viscous zone thickness. (Strahle[4]).

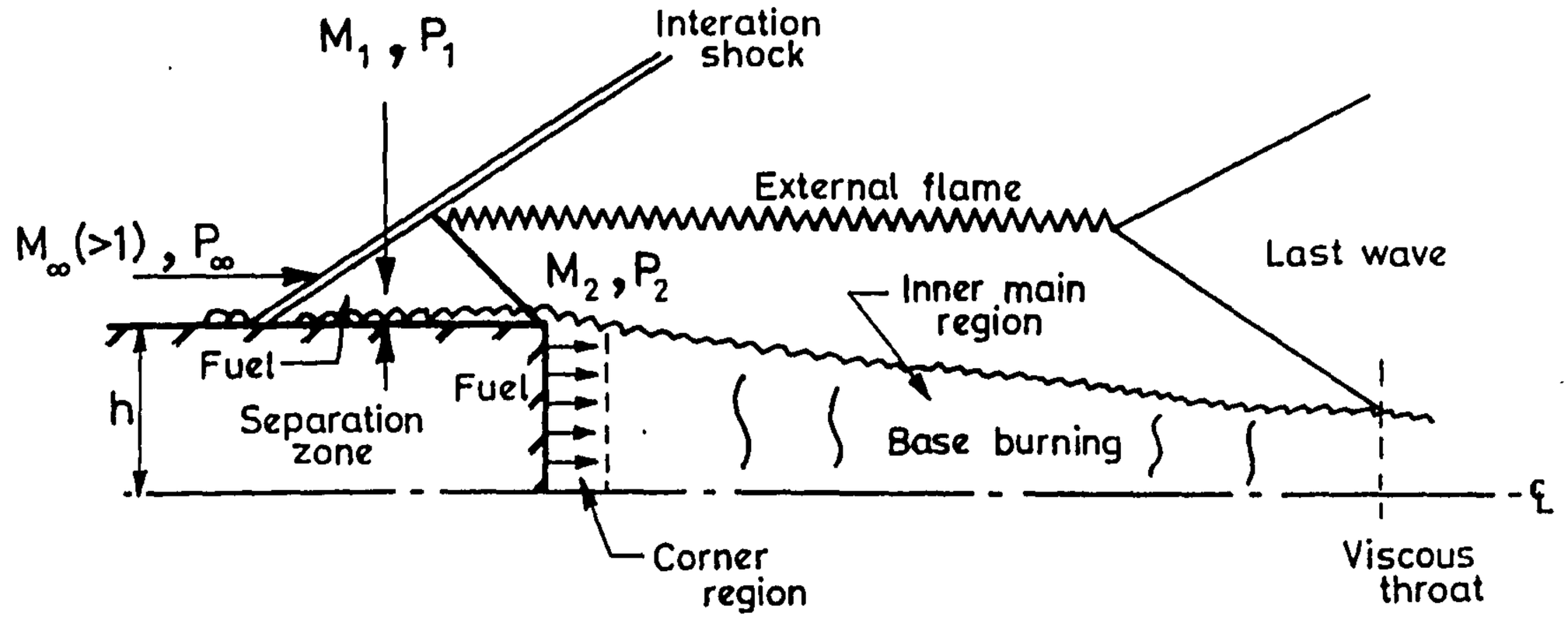

Figure 3.15. Schematic of flow field model with external burning. (Schetz[7])

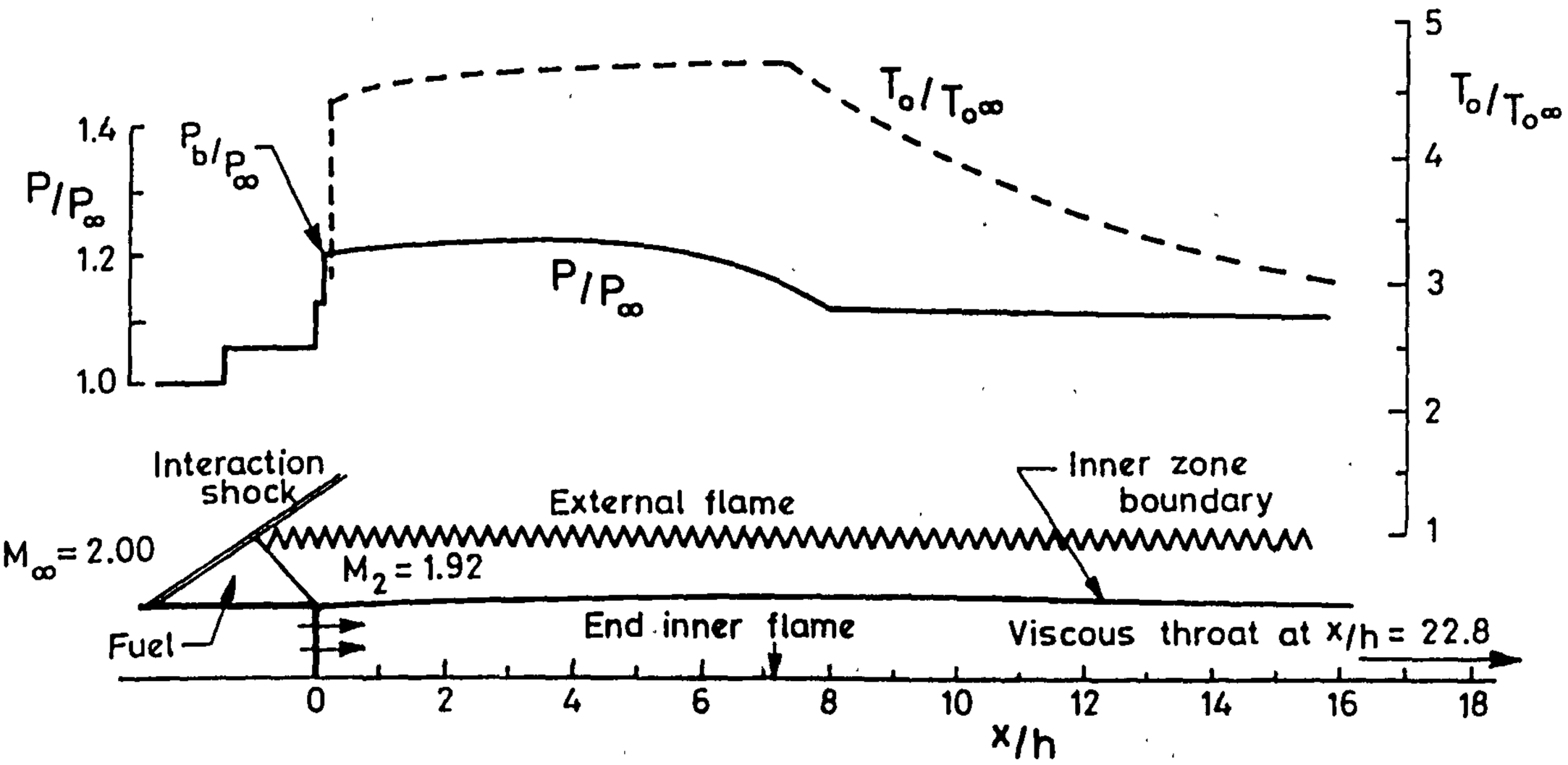

Figure 3.16. Flow field prediction for combined base /external burning. (Schetz[7])

CHAPTER 4: EXPERIMENTAL APPARATUS

4.1 Introduction

Two experimental facilities were used to generate the data presented in this report. The 9 inch x 9 inch continuous running supersonic wind tunnel in the College of Aeronautics was used to perform shock/wake and cowl/wake interference experiments (§4.2). Since this tunnel is a closed return tunnel driven by a centrifugal compressor it is not possible to perform wake combustion experiments in this facility. The Pebble Bed Heater is an open jet regenerative heat exchanger facility, operating continuously and this apparatus was used to perform the base bleed and shock/flame experiments (§4.3).

4.2 The 9" x 9" Wind Tunnel

The tunnel is driven by a centrifugal compressor with two 373 kilowatt electric motors. The tunnel has the capacity of operating at Mach numbers ranging from 1.7 to 2.8 by interchanging two-dimensional, non-symmetric nozzles. A symmetric two-dimensional nozzle operating at a nominal Mach number of 2 was used to generate the data for this report.

The stagnation pressure was automatically maintained at a pre-set value in the range 1.0 - 10.5 psia. The stagnation temperature varied in the range from approximately 0 deg K to 20 deg K above ambient. Control of the stagnation temperature was difficult and would vary by as much as 15 deg K during a run.

During the 'start-up' procedure the tunnel is evacuated to approximately 1.5 psia to minimise starting loads on the compressor. Once the tunnel is up to speed air is admitted over a silica gel drying bed to the required stagnation pressure.

The tunnel has an aerofoil shaped support in the settling chamber which allows models to be positioned through the throat of the tunnel without resorting to a base mounted sting. This support structure has advantages over a sting support when base flows are being studied because it avoids unwanted downstream interference effects which can cause significant modifications to the base pressure[63].

For this test programme the stagnation pressure was varied in the range from 4 psia to 10 psia. A small variation in Mach number (from 1.96 to 1.98, in the mean) was observed due to the changing tunnel boundary layer displacement thickness. The stagnation temperature was monitored continuously using a Chromel-Alumel thermocouple mounted in the tunnel settling chamber. The isentropic flow relations determined the free stream temperature in the working section for the measured stagnation temperature. Sutherlands law was then used to calculate the free stream viscosity, while the equation of state for an assumed perfect diatomic gas provided the free stream air density. Thus after measuring the free stream Mach number the unit free stream Reynolds number was calculated as $3.6 \pm 0.2 \times 10^6$ per m at a nominal stagnation pressure of 4 psia and as $9.4 \pm 0.3 \times 10^6$ per m at 10 psia.

4.2.2 Test configurations

The following tests were made:

a) The interaction between 2-D planar shocks generated by 5^{o} wedges and the wake of the axisymmetric centrebody with a plane base.

b) The interaction between the flowfield generated by a 5^{o} convergent-divergent cowl of 2 calibres diameter and 2 calibres in length and the wake of the centrebody with a plane base.

c) Ditto with the wake of the centrebody with a recessed base.

d) The interaction between the flowfield generated by a 10^{o} convergent-divergent cowl and the wake of the centrebody with a plane base.

e) The interaction between the flowfield generated by a rotationally symmetric array of delta wings placed at 5^{o} incidence with the wake of the centrebody with a plane base.

Pressure measurements (§4.2.3) were made for configurations (a), (b), (d) and (e) and drag force measurements (§4.2.4) were made for configurations (b) and (c).

The two-dimensional shocks were generated by 5^{o} wedges of 9" span and 4½" length mounted on the tunnel roof and floor (fig. 4.1). Both wedges were moveable to allow a traverse of the shock interaction position over a range of approximately 1.5 calibres upstream to 3.5 calibres downstream of the base. The wedges were initially made of softwood but these broke up under running conditions. A second pair of wedges were manufactured of Carp Tufnol, a laminated linen-resin material, which proved successful but is difficult to finish to a smooth surface. Since the wedges were placed in the tunnel boundary layer this was not a significant problem.

The other models were manufactured of brass and machined to a smooth finish. The cowls were supported externally on four faired legs inclined at 30^{o} to the flow direction (fig. 4.2). The legs were supported on a table mounted in a recess in the top and bottom tunnel liners allowing movement in the streamwise direction (fig. 4.3). Care was taken during assembly that the centreline of the cowl coincided with the centreline of the cylindrical afterbody. The centreline positions for both the cowl and afterbody were found to lie within 60 thousandths of an inch, in any radial direction, of the geometrical axis of the tunnel.

The delta wings were placed at a 5^{o} angle of attack mounted in a cowl of cylindrical section with an externally faired leading edge (fig. 4.4). The nose of each wing protruded one half calibre from the leading edge of the support cowl. The wings were mounted in a rotationally symmetric fashion, each wing having anhedral of 45^{o} with an 81^{o} sweep and of length 2 calibres (fig. 4.5).

The recessed base on the centrebody is shown in fig. 4.6. The recess extends to a depth of 1 calibre and at its innermost extent has a diameter of 0.48 calibres, the inner side walls making an angle of 15^{o} with the centreline. No special finishing techniques were used.

The pressureson the internal surface of the 5^{o} cowl were also measured (fig. 4.2). Two sets of pressure tappings were drilled, normal to the internal surface at equal intervals along the length of the cowl. Nine tappings were drilled in each set, positioned diametrically opposite one another, four on the forward face, four on the rearward face and one at the 'throat' of the cowl, making 18 tappings in total.

4.2.3 Pressure measurements

The stagnation pressure was measured by two pitot probes set in the settling chamber. Two pressure tappings set in the top liner of the working section positioned approximately 1 calibre upstream of the base plane were used to measure the free stream static. The centrebody was fully pressure tapped also - six static pressure tappings were drilled on the surface of the cylinder - the first positioned six calibres upstream of the base plane and the remaining five were positioned on the same cylindrical generator being 0.4 calibres apart, the first positioned two calibres upstream of the base plane (fig. 4.1). The base pressure tappings, of which there were nine in all, were arranged in a cruciform arrangement with one at the centre of the base and two on each arm of a cross, one sixth of a calibre apart (fig. 4.7).

In the first instance the nineteen pressure lines were connected to an NPL, 96 port, scanning valve device feeding a diaphragm-type transducer. The transducer calibration curve was found to be linear over the full range of pressures to be measured,but small variations in the slope and intercept were evident due to changing ambient pressures and temperatures. The system was therefore calibrated with the known ambient pressure and a low pressure (typically 0.04 mm Hg) provided by a vacuum pump with a modified Mcleod gauge.

Pressures were read to an accuracy of ± 0.17 mm Hg. At the lower end of the Reynolds number range the base pressures were typically of the order of 20 mm Hg, so the measurements are nominally accurate to ± 1%, however, an individual measurement was only repeatable to approximately ± 5%. A number of measurements were thus made, particularly at the lower end of the Reynolds number range and the mean of these was taken.

The pressure measurements reported in the majority of §5.2 were taken with the NPL device. However, the scanning valve system was updated with an automatic data capturing system controlled by a microprocessor. The results shown in §5.2.7 were obtained with this system.

4.2.4 Drag force measurements

A single component strain gauge balance was designed and manufactured to enable direct base drag force data to be collected. The sketch of the general assembly is shown in fig. 4.8. The balance was designed to be identical, as far as possible, with the existing

pressure tapped support rod (fig. 4.9).

The balance contains a single web on which 4 strain gauges were mounted in a simple Wheatstone bridge arrangement. The gauges were rated at 10 volts and of nominal resistance 100 Ω. Two gauges were placed on the compression side and two were placed on the tension side of the web. The supply voltage of 5 volts was provided by a stabilised power supply and monitored by a Solatron digital voltmeter with an accuracy of ± 2.0 mV. 5 volts was chosen as the supply voltage to minimise thermal drift, however, it was necessary to switch on the supply at least 20 minutes prior to using the balance to allow the zero load reading to stabilise.

The drag web was designed to withstand a total load of 3.5 kg.f. The static calibration curve is shown in fig. 4.10.

A schematic of the forces on the balance is shown in fig. 4.11. The total force measured by the balance, D, is composed of the base drag, P_bA, the skin friction drag, F, and the force on the rod due to the pressure in the web chamber, P_cA, where A is the cross sectional area of the centre support rod. Thus, ignoring friction in the bearings,

$$D = P_cA + F - P_bA \qquad (4.1)$$

It is reasonable to assume that only small differences occur in the friction forces, when compared with the base drag. F is thus considered constant and can be calculated, if necessary, by measuring P_b and P_c.

The procedure eventually adopted for reduction of the data was to relate the readings obtained to the undisturbed base case. Extensive pressure readings with the pressure tapped afterbody had been taken and the repeatability and accuracy of the pressures well established.

Data was collected by cycling the Reynolds number, or stagnation pressure, through the range $4.6 \times 10^4 \leq Re_d \leq 2.5 \times 10^5$, i.e. 2 psi. $\leq P_o \leq$ 10.5 psi., where P_o is the stagnation pressure. In general, for each geometric configuration, 3 cycles were made and readings were taken in steps of approximately 1 psi. Thus for each geometric configuration in excess of 40 drag measurements were taken. The chamber pressure, P_c, was also continually monitored, being measured by a differential manometer to an accuracy of .002 in. Hg., using the stagnation pressure as the reference pressure.

4.2.5 Relationship between drag force and pressure measurements

The force F on the base of the centrebody is given by

$$F = \int_A pdA = \int_0^{d/2} \int_0^{2\pi} prd\theta dr$$

where p is the local pressure acting on an elemental area dA (fig. 4.12).

Assume the base pressure distribution is axisymmetric i.e. p = p(r), then

$$F = 2\pi \int_0^{d/2} p(r)\, r\, dr \qquad (4.2)$$

Now the average base pressure $\overline{P}_b = 1/9 \sum_{i=1}^{9} P_b(i)$ (4.3)

where $P_b(i)$ is the recorded pressure at tapping i so

$$\overline{P}_b = 1/9 \left[p(0) + 4p(d/6) + 4p(d/3) \right] \qquad (4.4)$$

(fig. 4.13).

Then the approximation to the force on the base is

$$F_{approx} = \overline{P}_b A = \frac{\pi d^2}{36} \left[p(0) + 4p(d/6) + 4p(d/3) \right] \qquad (4.5)$$

Now if the base pressure distribution has no local minima in the base region (as is shown in fig. 4.13) then the right hand side of equation 4.5 is greater than the right hand side of equation 4.2. The average base pressure overestimates the base force, or, equivalently, underestimates the base drag. The error is due to the equal weighting given to each of the measured pressures in equation 4.3. That is, there is an implied assumption that each measured pressure acts on an equal base area. This is a false assumption, as can be seen from fig. 4.13.

If one knew, a priori, the true base pressure distribution, p(r), then one could evaluate the error. For example, assuming a parabolic pressure distribution with $P_{bmin} = 0.8\ P_{bmax}$, say, (see fig. 4.13) then

$F_{approx} = 1.056\ F$ i.e. an error of 5.6%

4.3 Pebble Bed Heater

The Pebble Bed Heater is an open jet regenerative heat exchanger[73] (fig. 4.14). The facility consists of a pressure vessel lined with refractory material and a bed of radomly packed alumina pebbles. The pressure vessel, which is a steel shell, is capable of withstanding pressures of up to 250 psia at a temperature of 570°K. The pebble matrix is heated by means of a toroidal burner, which consumes kerosene at between 12 and 18 gallons/hour. The kerosene is burnt in the shell volume above the pebble matrix. Kerosene combustion products are blown through the bed and exhausted to the atmosphere. The heating cycle lasts approximately 6 - 8 hours depending on the required bed temperature. At the end of the heating cycle the heater air is shut off and the high pressure air supply is blown through the pebble matrix in the opposite direction. This air, which is heated during its passage through the matrix, is expanded through a Mach 2, axisymmetric nozzle, thus providing a high enthalpy stream when required. The nozzle, of diameter 2 inches at the jet exit, was surrounded by a water jacket through which water was pumped at high pressure.

An axisymmetric fuel injector (fig. 4.15) of 0.675" diameter, was placed through the throat of the nozzle in a similar manner to that described for the 9" x 9" tunnel. Three test bases were manufactured of silicon nitride (fig. 4.16). Base A was designed to permit peripheral bleed of fuel and comprised a recess of blunted cone section, the cone semi angle making an angle of 15^{o} with the centreline. Base B was designed to permit axial injection, circumferentially around the base of the fuel injector with a bleed gap of 0.1 calibre. The bleed gap was variable on bases A and C. Base C was not tested, but was designed to permit peripheral injection with a bluff base. Bases B and C had 3 pressure tappings drilled in the base plane (see fig. 4.16). Base A had 4 pressure tappings. The pressures were transmitted down stainless steel hypodermic tubing connected to PTFE tube as shown in fig. 4.15.

The fuel mass flow rates were measured on a Fisher Porter $\frac{1}{4}$" flow meter. The hydrogen was ignited when necessary by a 15 kV spark igniter. Shock waves were generated by over expanding the airflow at the lip of the nozzle as shown in fig. 4.17, the shock waves then interfering with the wake of the fuel injector. Spacers of length 0.3125" were manufactured of stainless steel. These could be inserted between the pressure vessel and the nozzle contraction to vary the shock interaction position (see fig. 4.17).

The static pressure on the surface of the fuel injector and the base pressures were measured on mercury manometer banks graduated in one-tenths of an inch. The stagnation pressure in the bed was measured on a Bourdon gauge. The stagnation temperature was measured with a Platinum/Platinum - 10% Rhodium thermocouple mounted in the nozzle contraction.

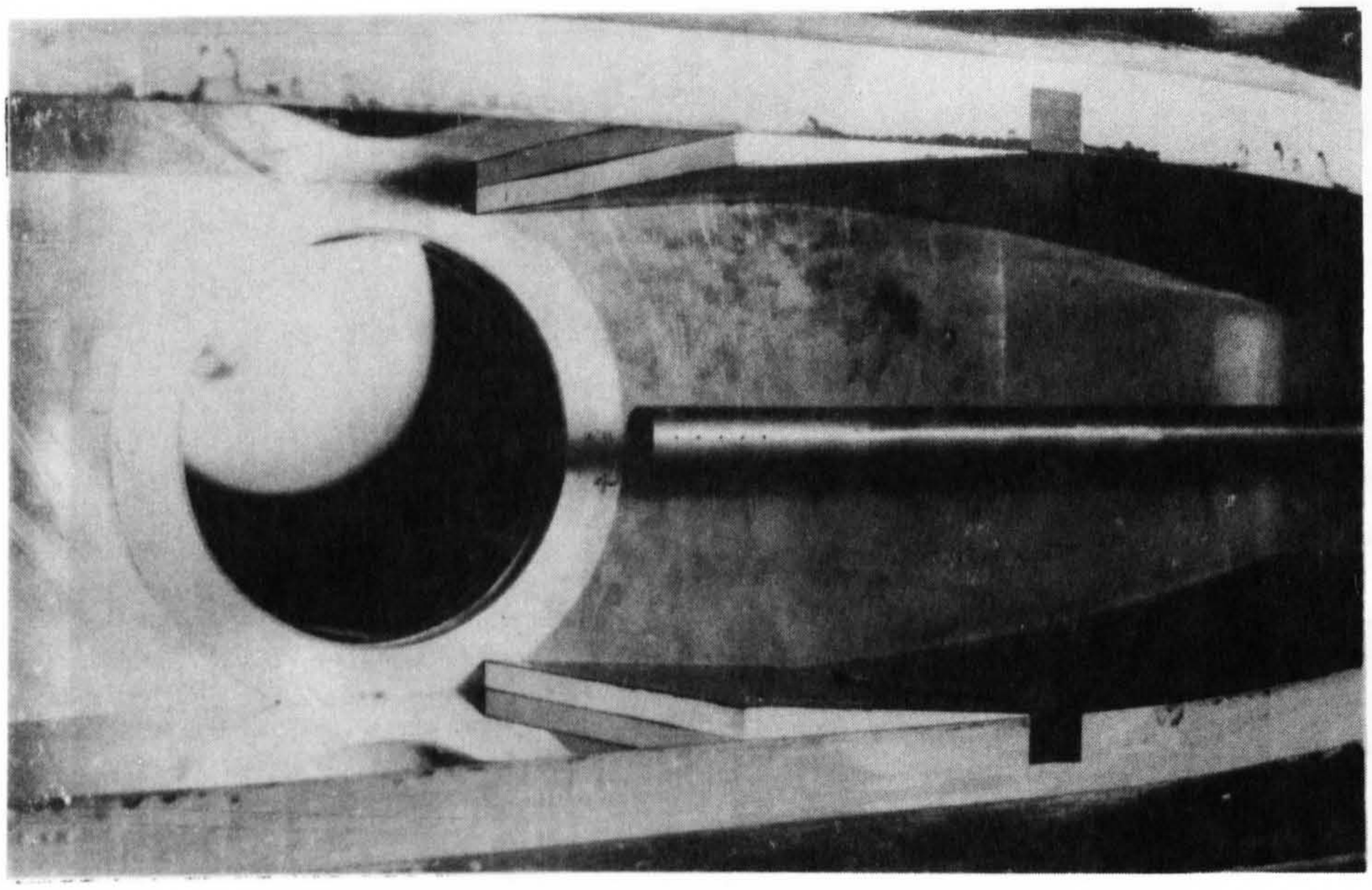

Fig. 4.1 5^{o} Softwood Wedges Mounted in 9" x 9" Tunnel

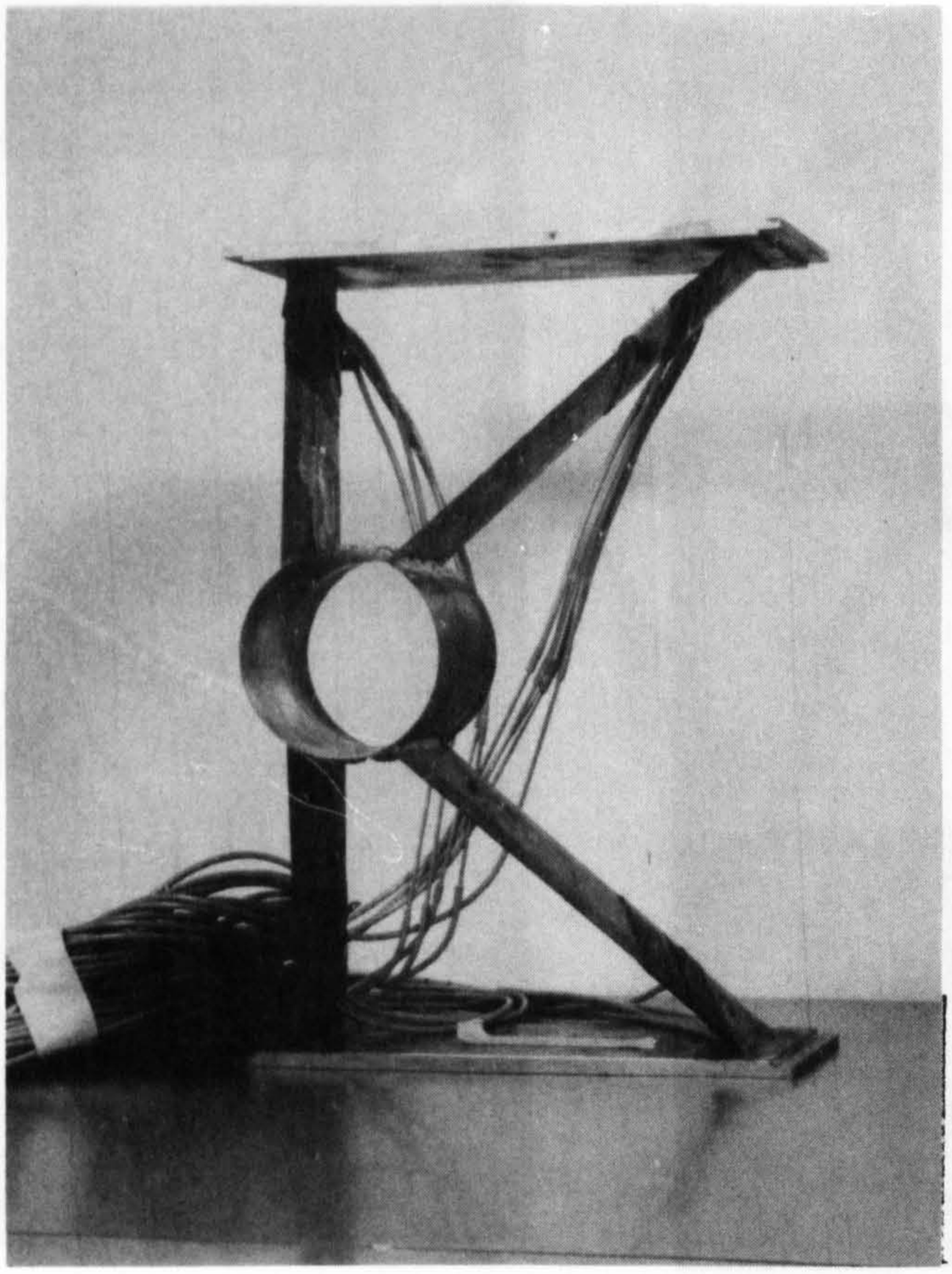

Fig. 4.2 5^{o} Cowl in Mounting

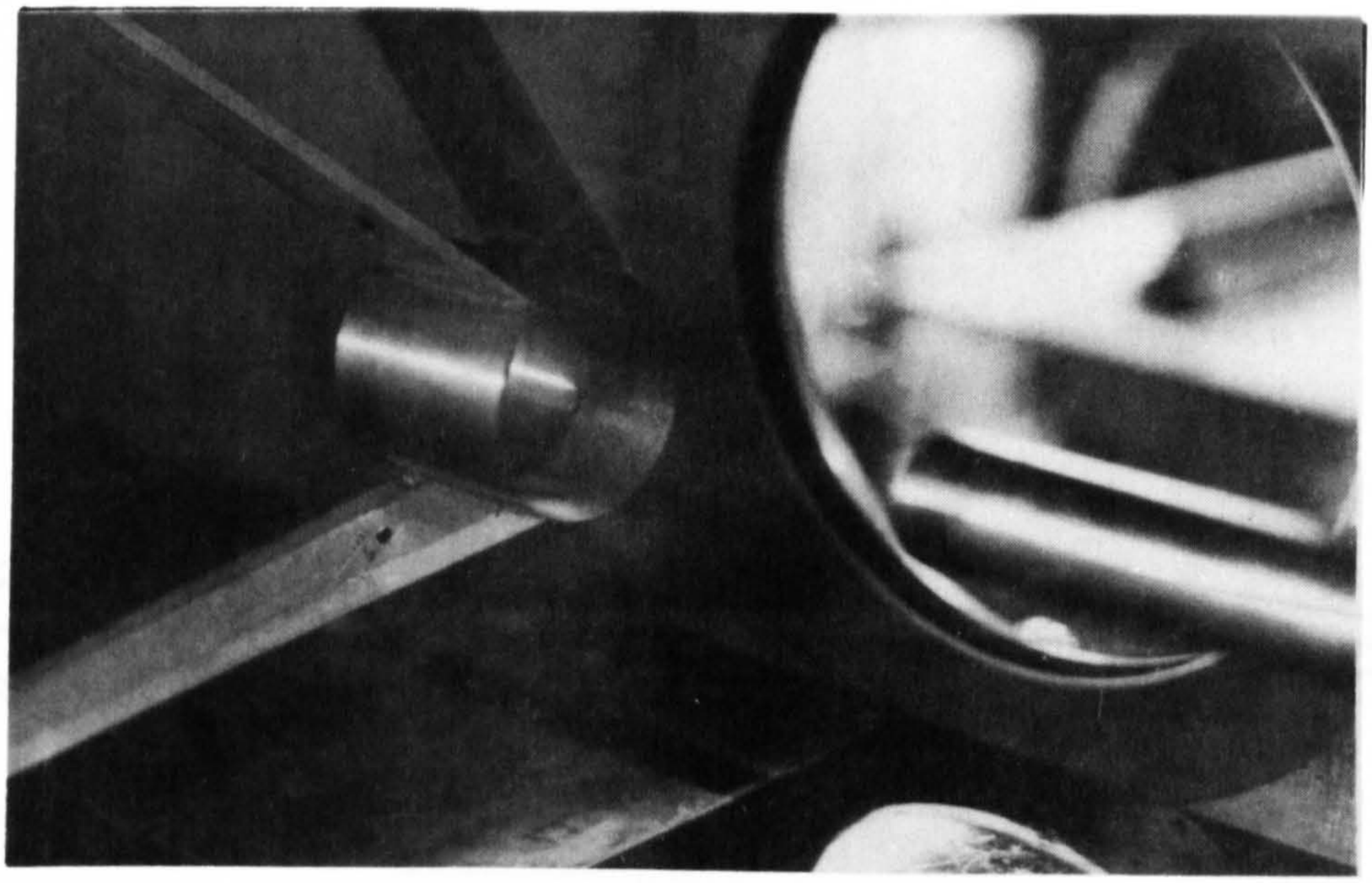

Fig. 4.3 5^{o} Cowl Mounted in 9" x 9" Tunnel

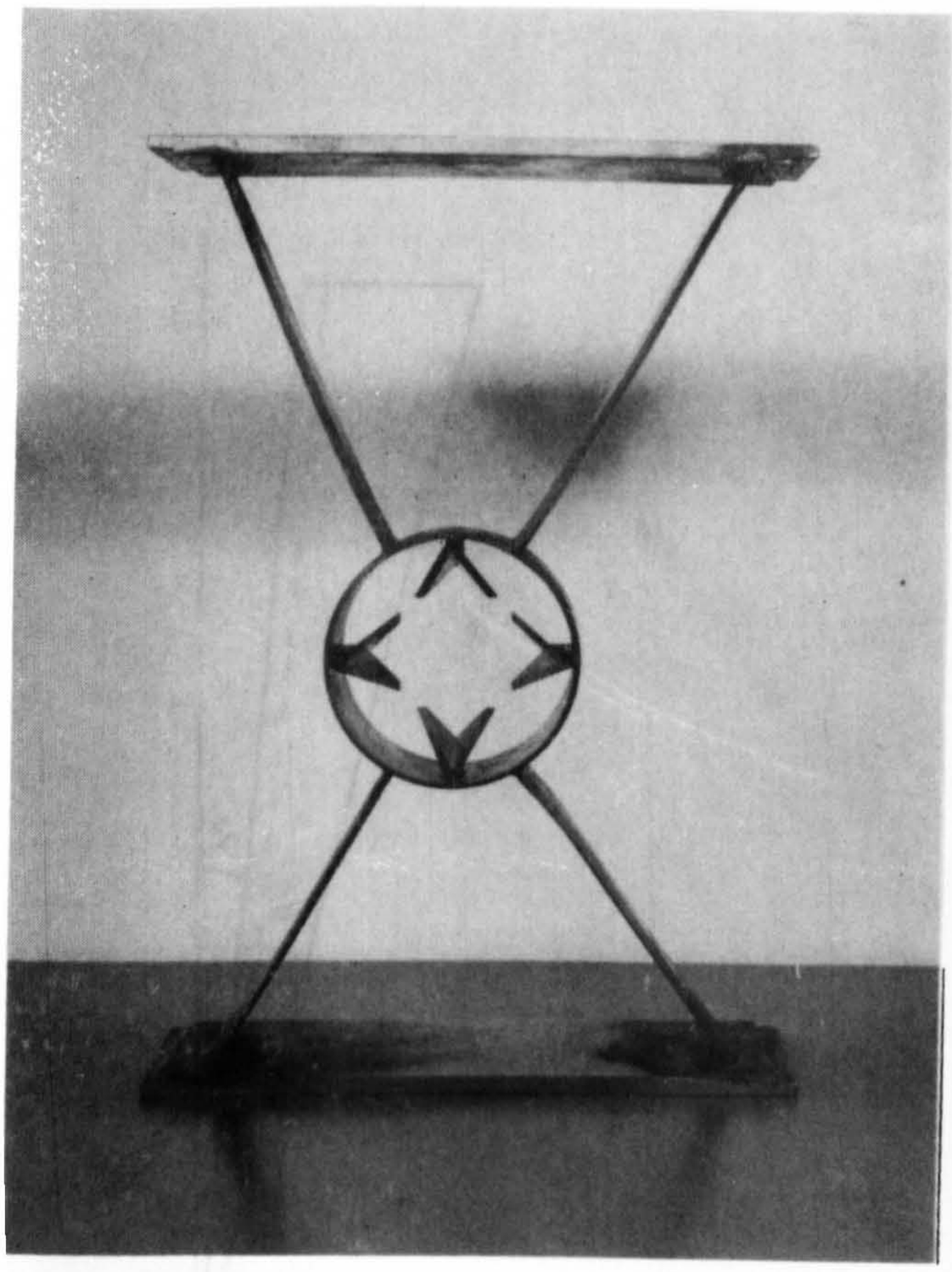

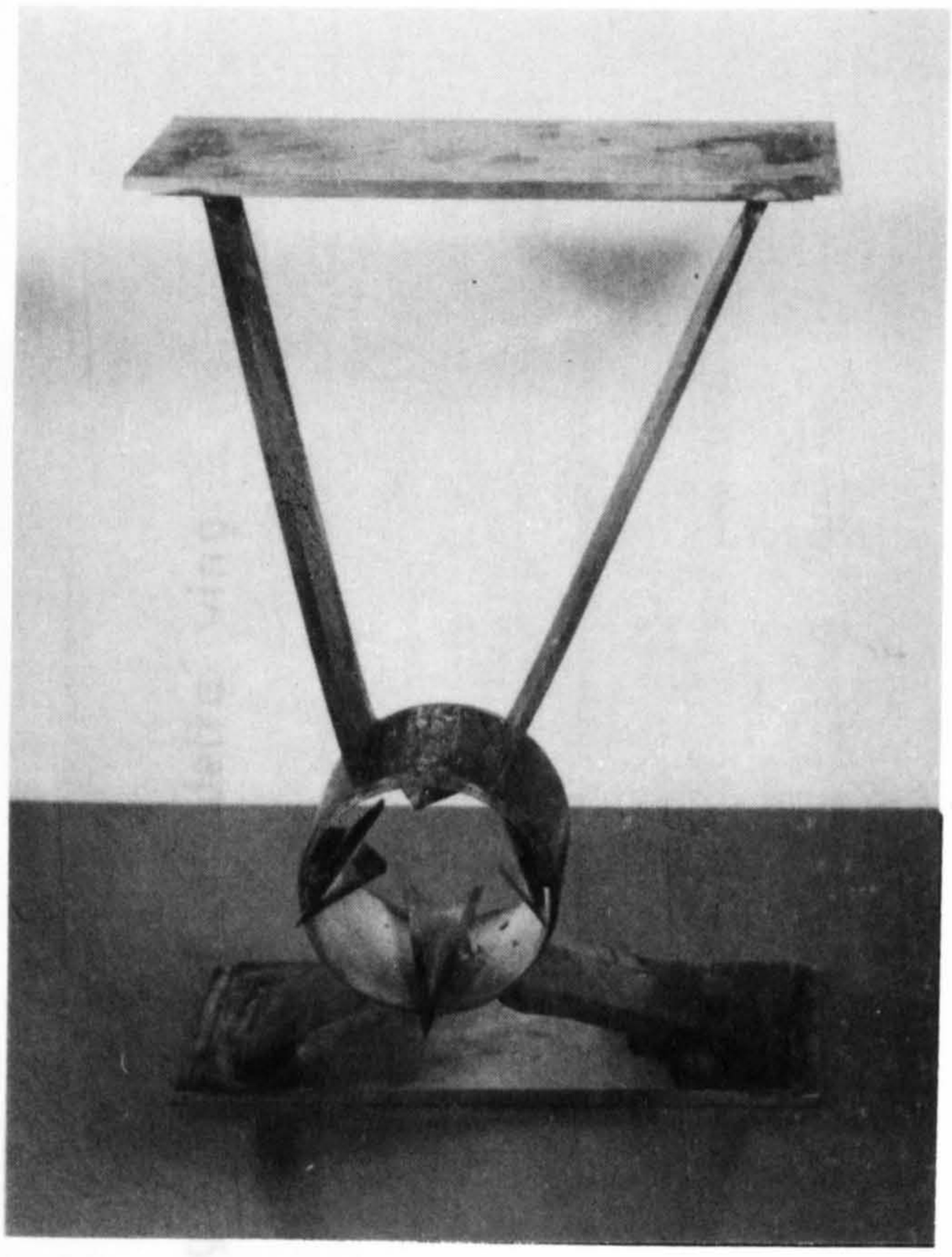

Fig. 4.4 5^{o} Delta Wings in Mounting

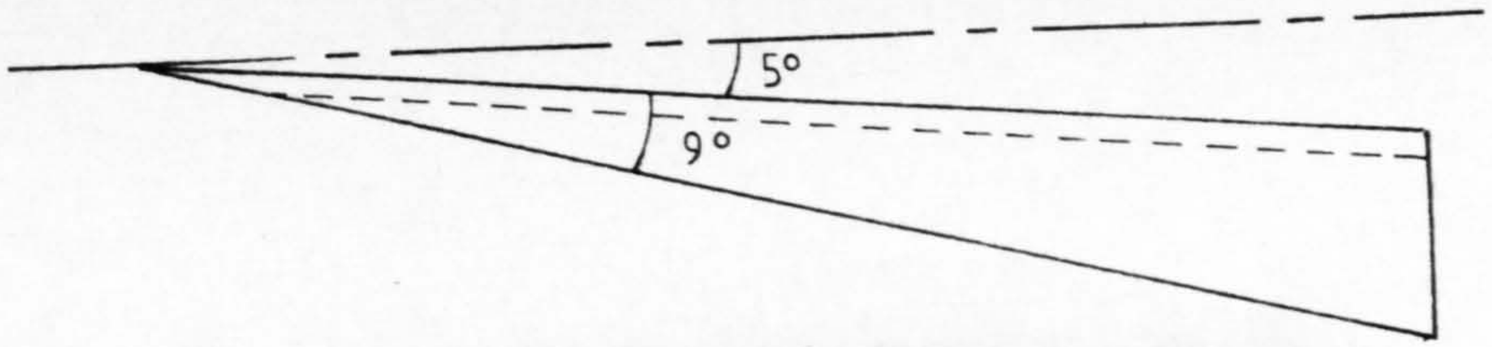

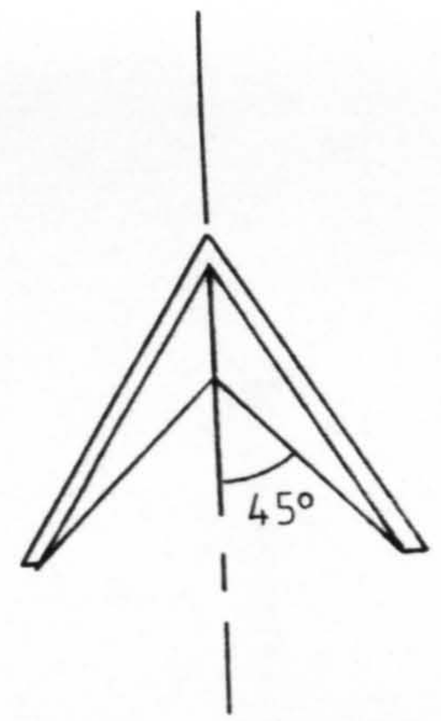

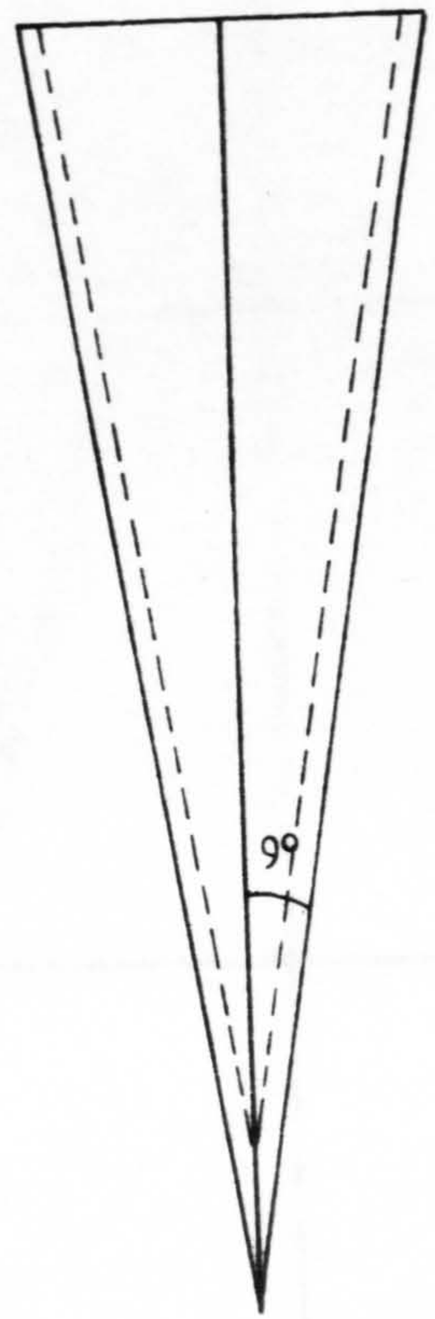

Fig. 4.5 Sketch of `delta´ wing

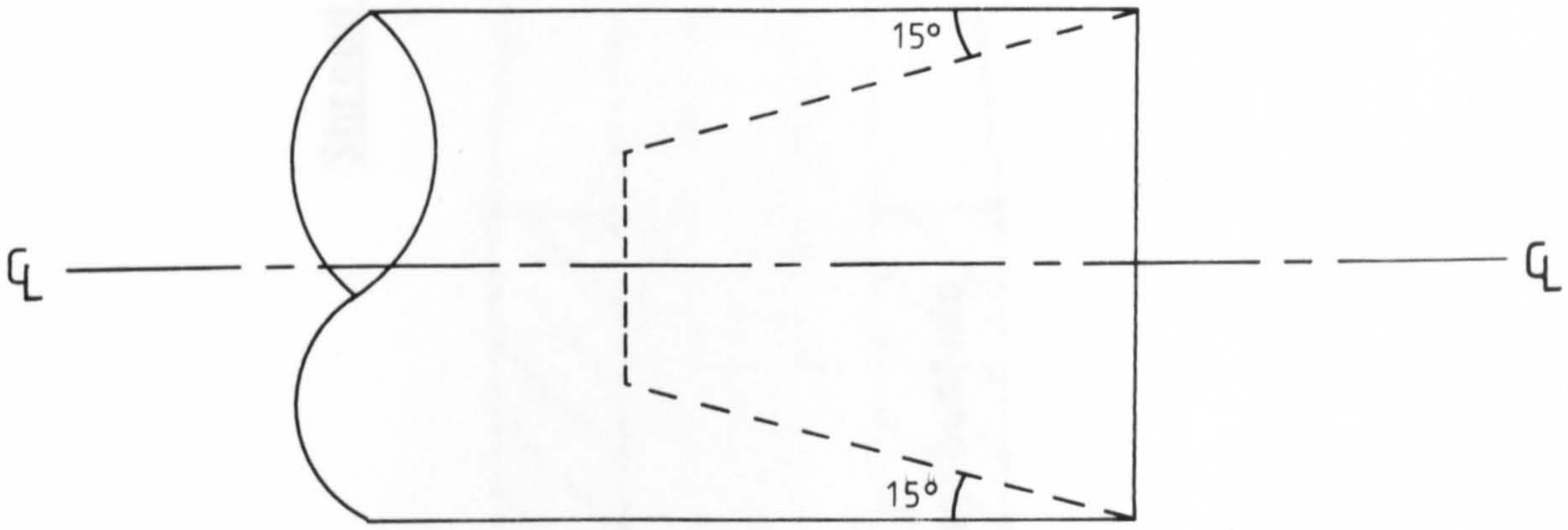

Fig. 4.6 Sketch of recessed base

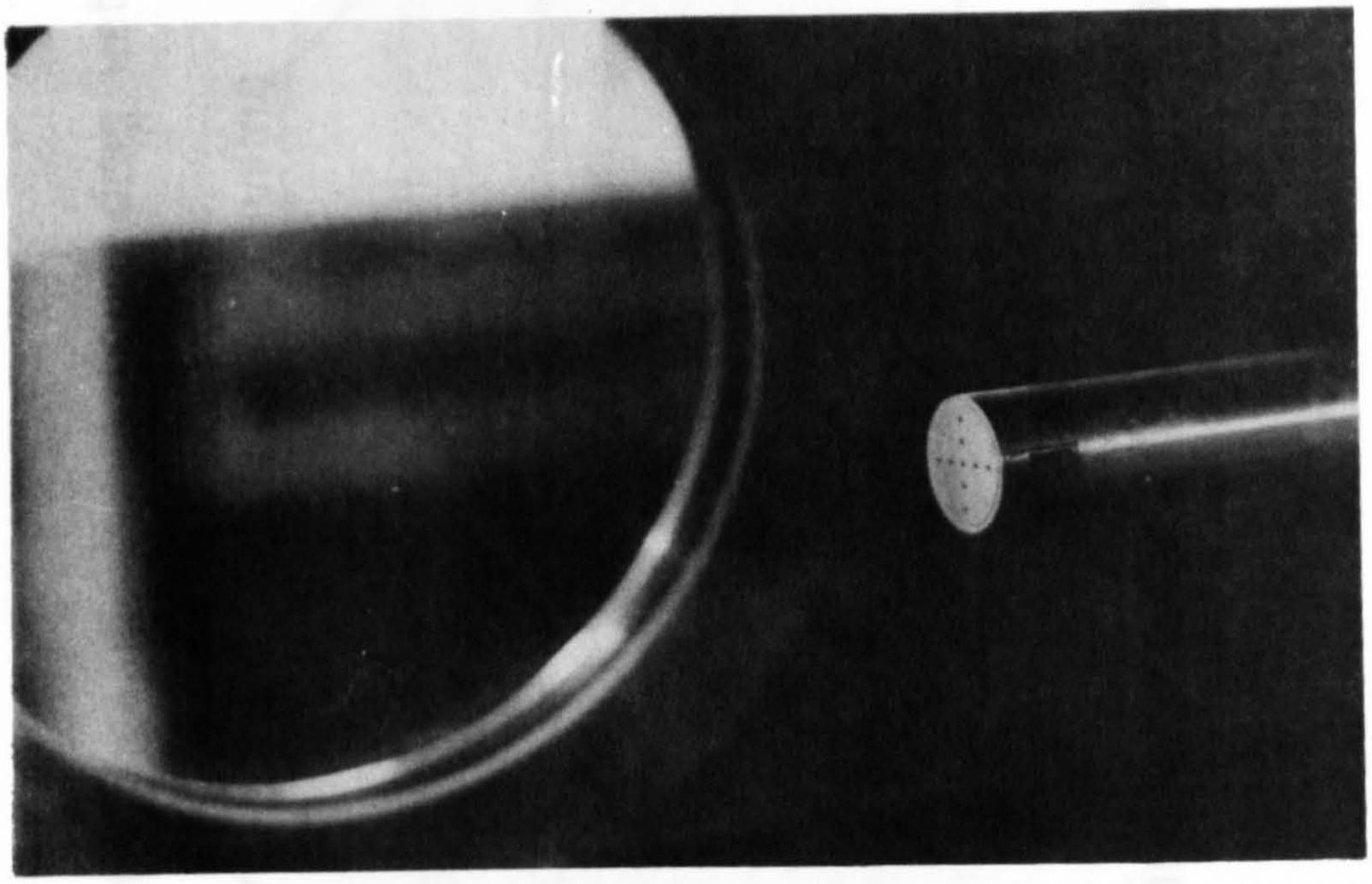

Fig. 4.7 Pressure tapped base mounted in 9" × 9" tunnel

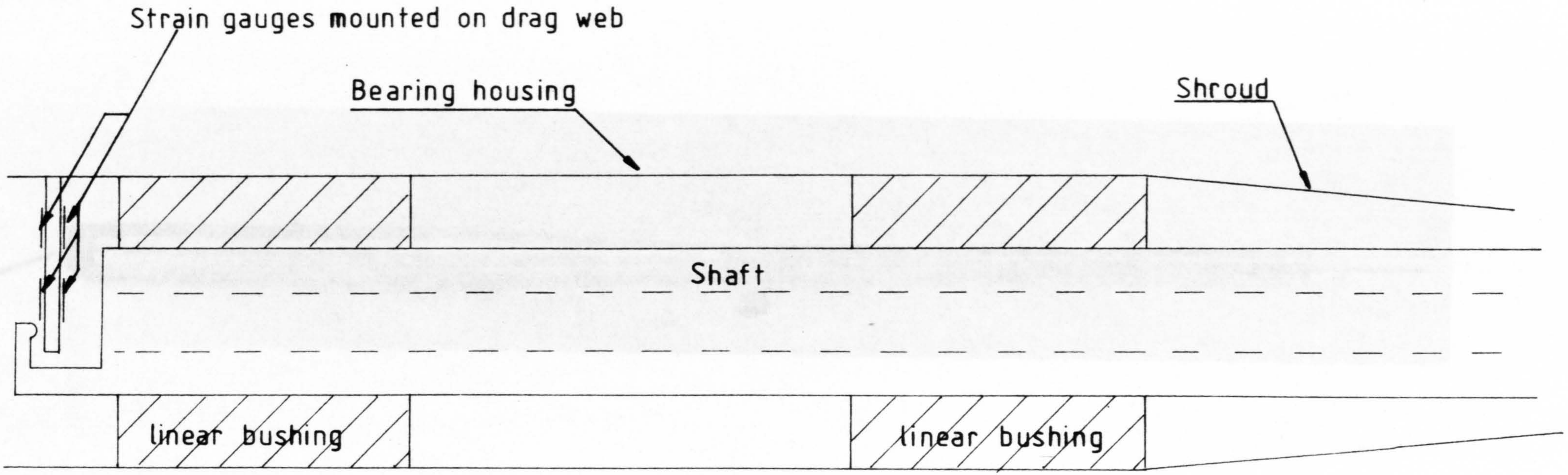

Fig. 4.8 Sketch of Drag Balance Housing

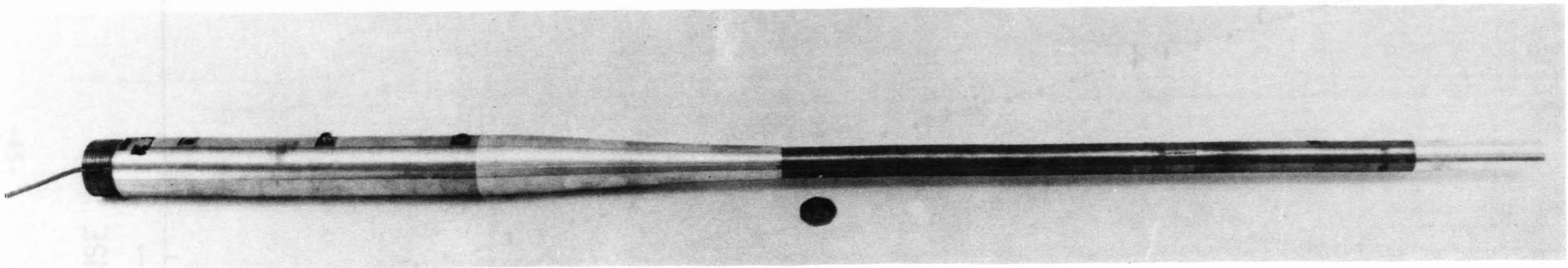

Fig. 4.9 Assembled drag balance

Fig.4.10:DRAG BALANCE CALIBRATION
1ST. FEB. 1982

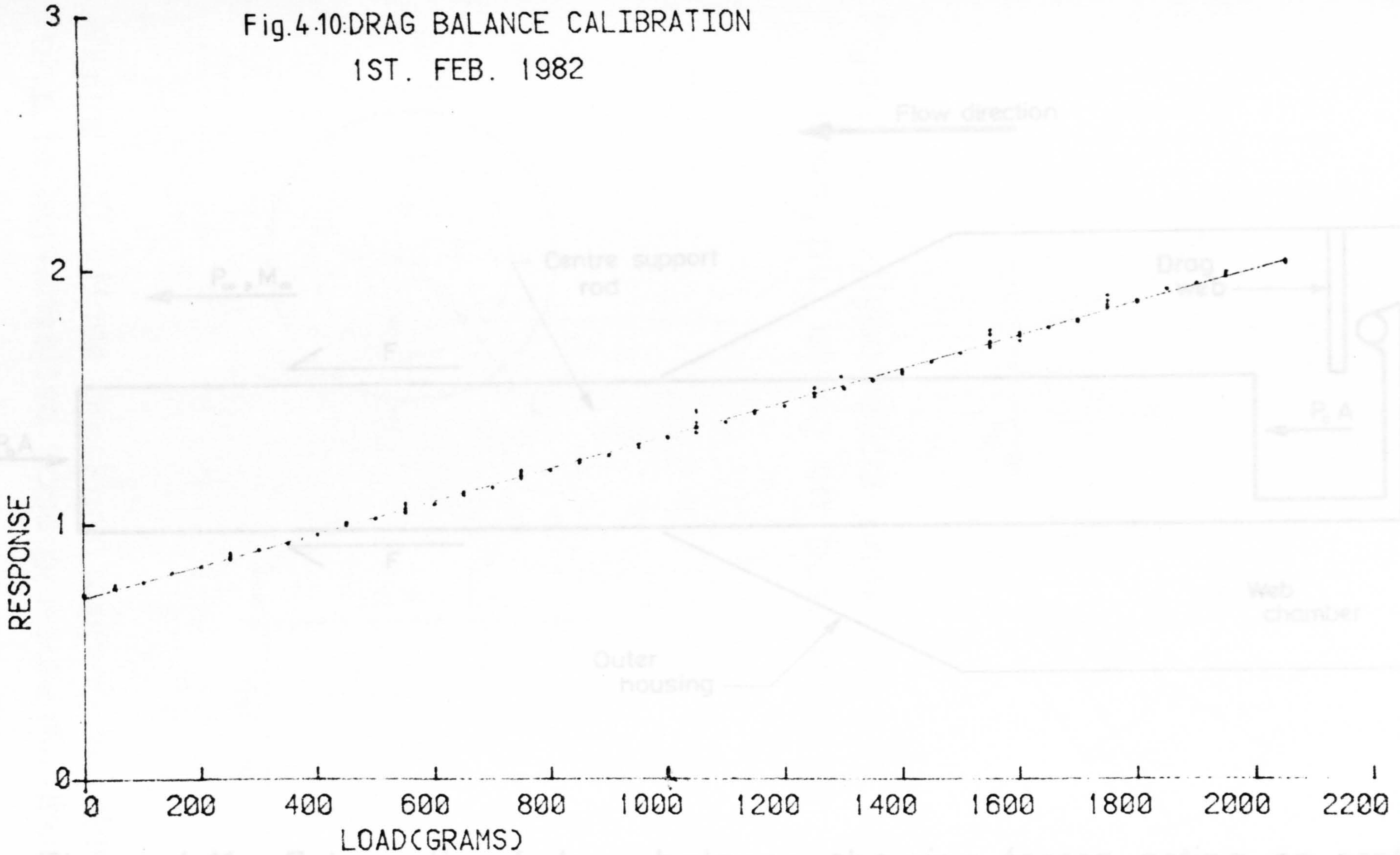

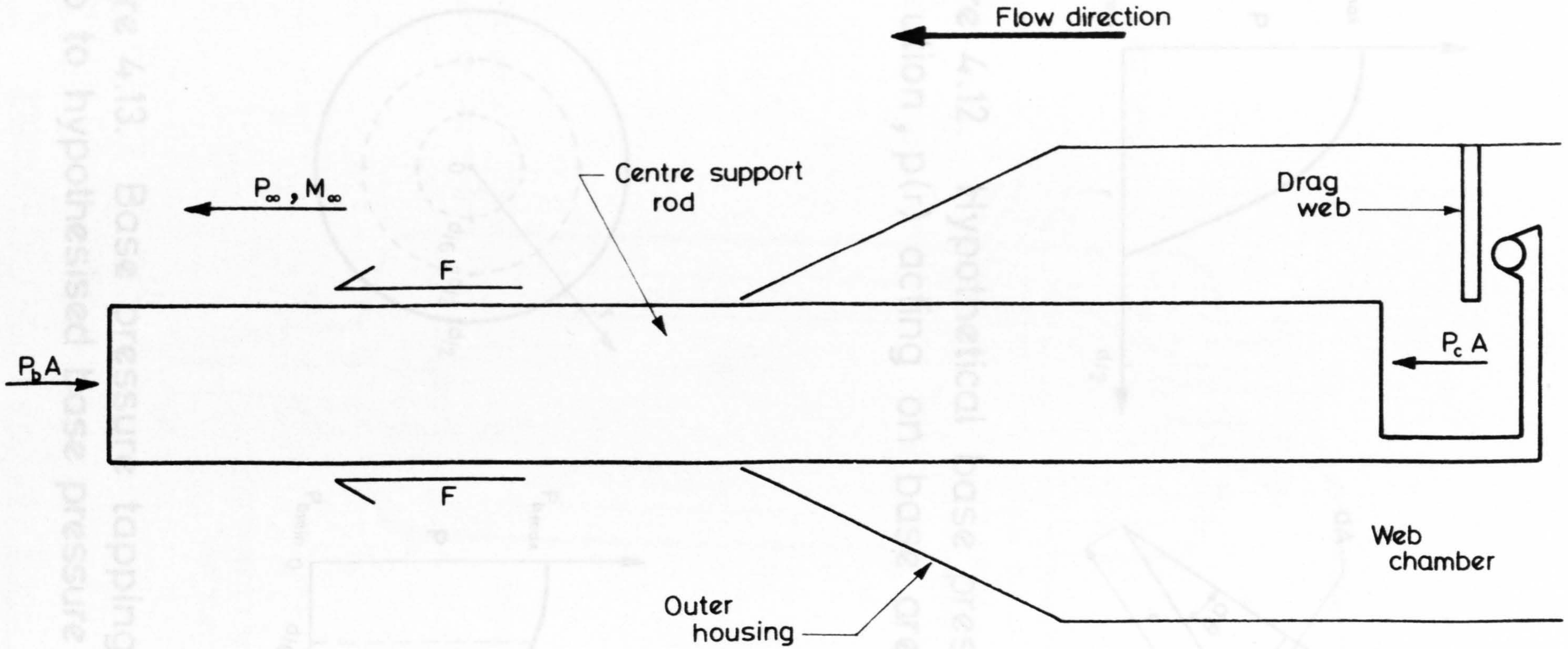

Figure 4.11. Schematic of drag balance showing forces acting on centre support rod.

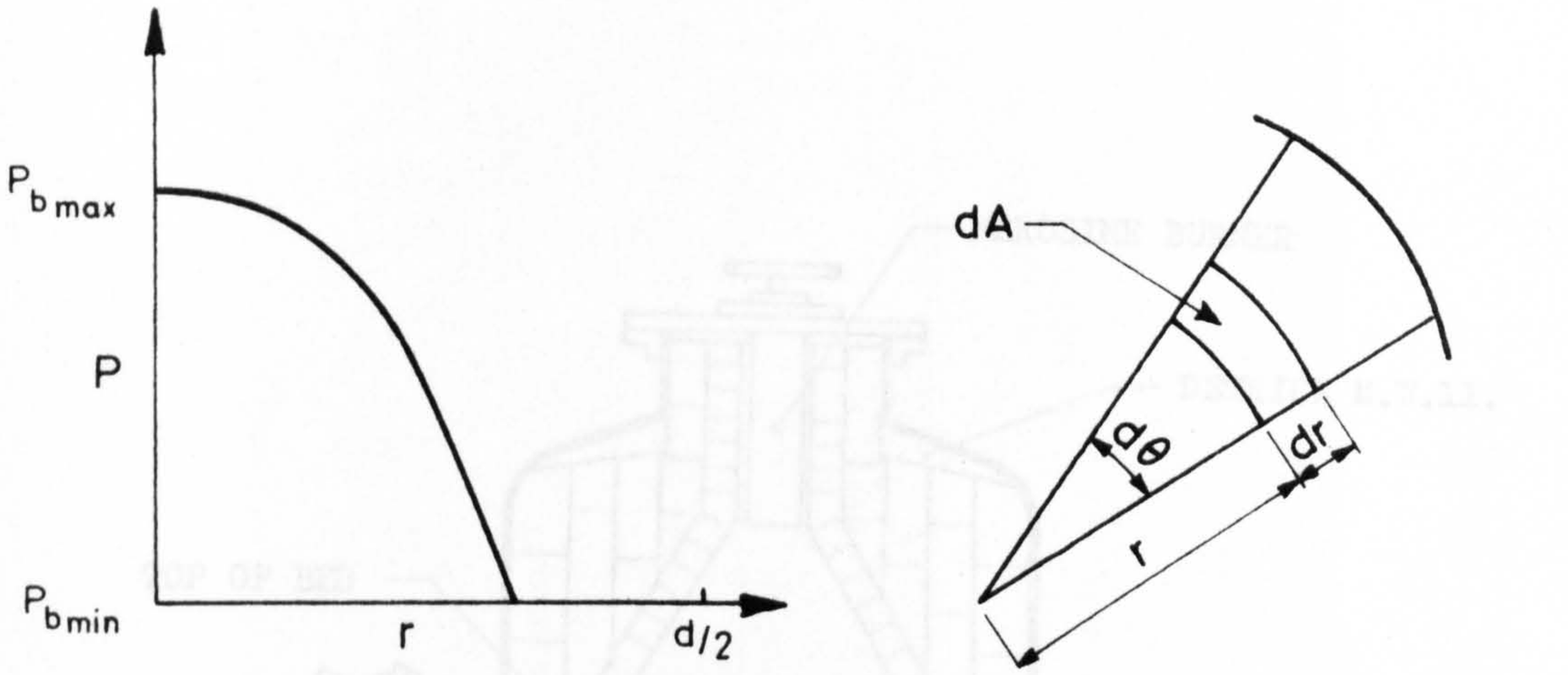

Figure 4.12. Hypothetical base pressure distribution, p(r) acting on base area, dA.

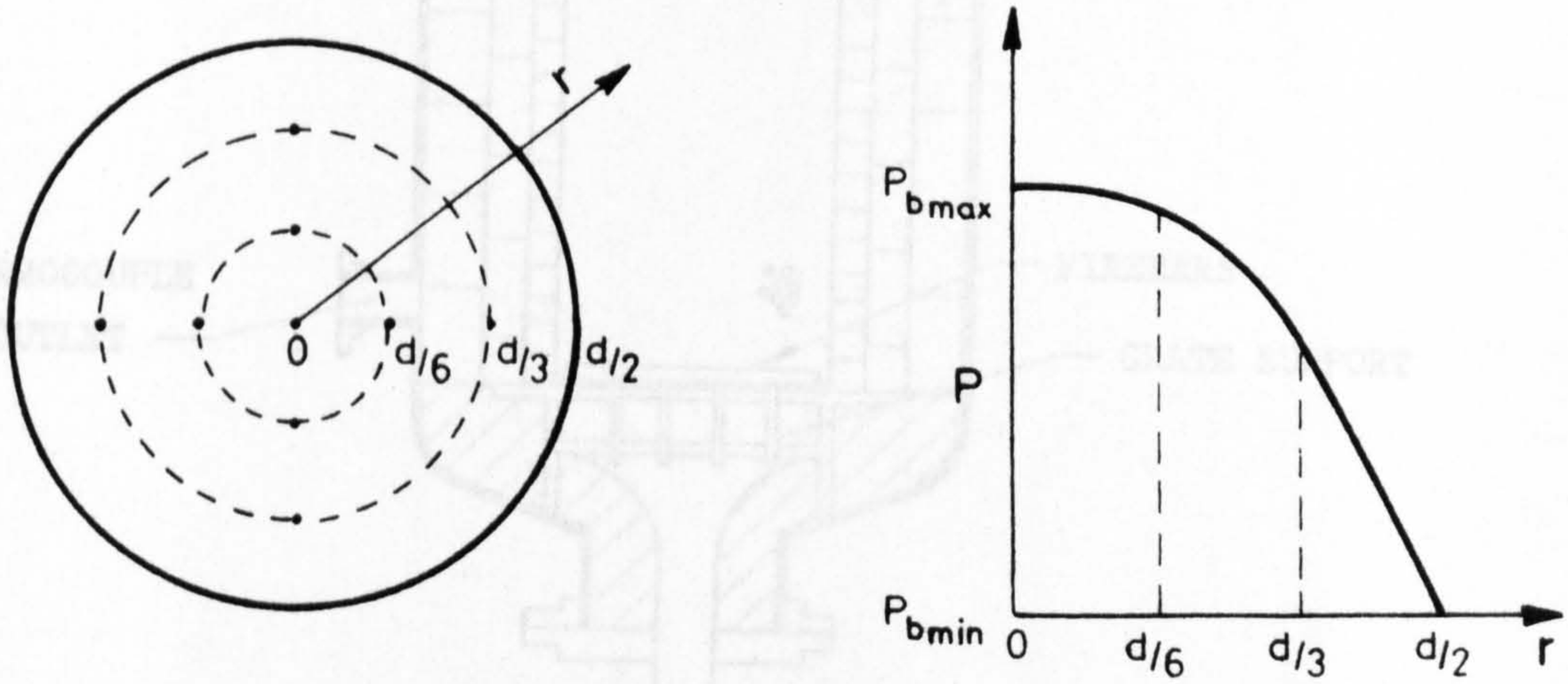

Figure 4.13. Base pressure tapping in relationship to hypothesised base pressure distribution.

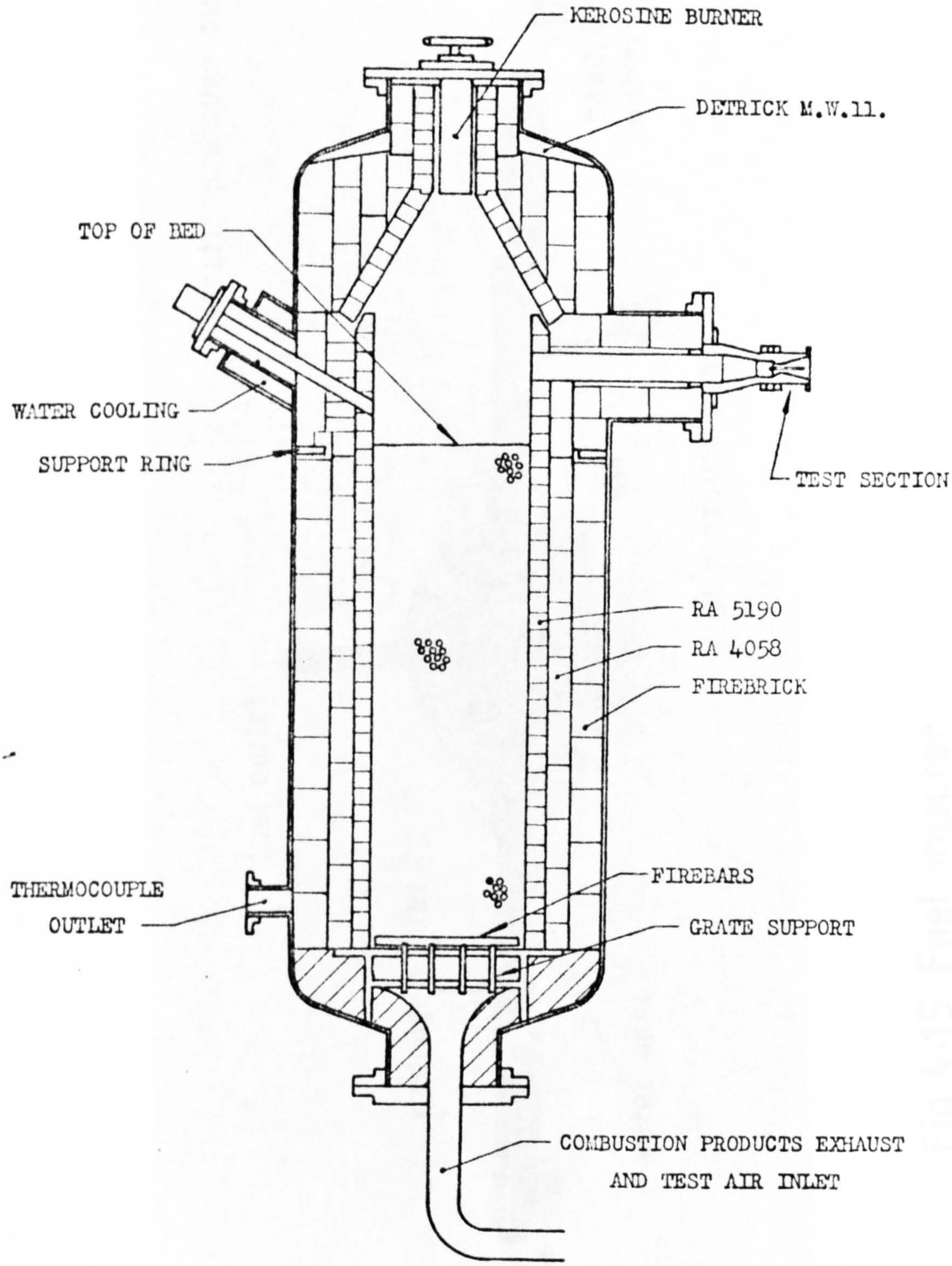

FIGURE 4.14 LAYOUT OF PEBBLE-BED HEATER

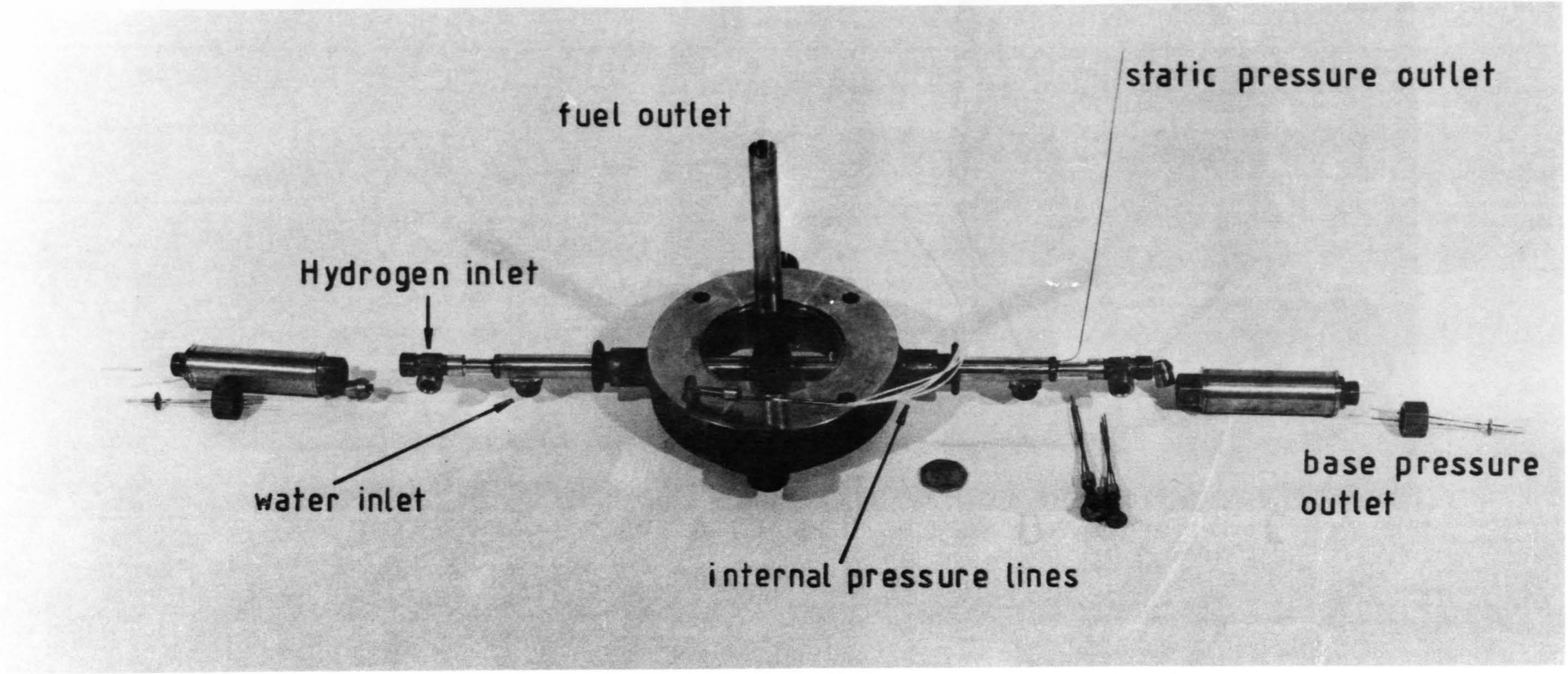

Fig.4.15 Fuel injector

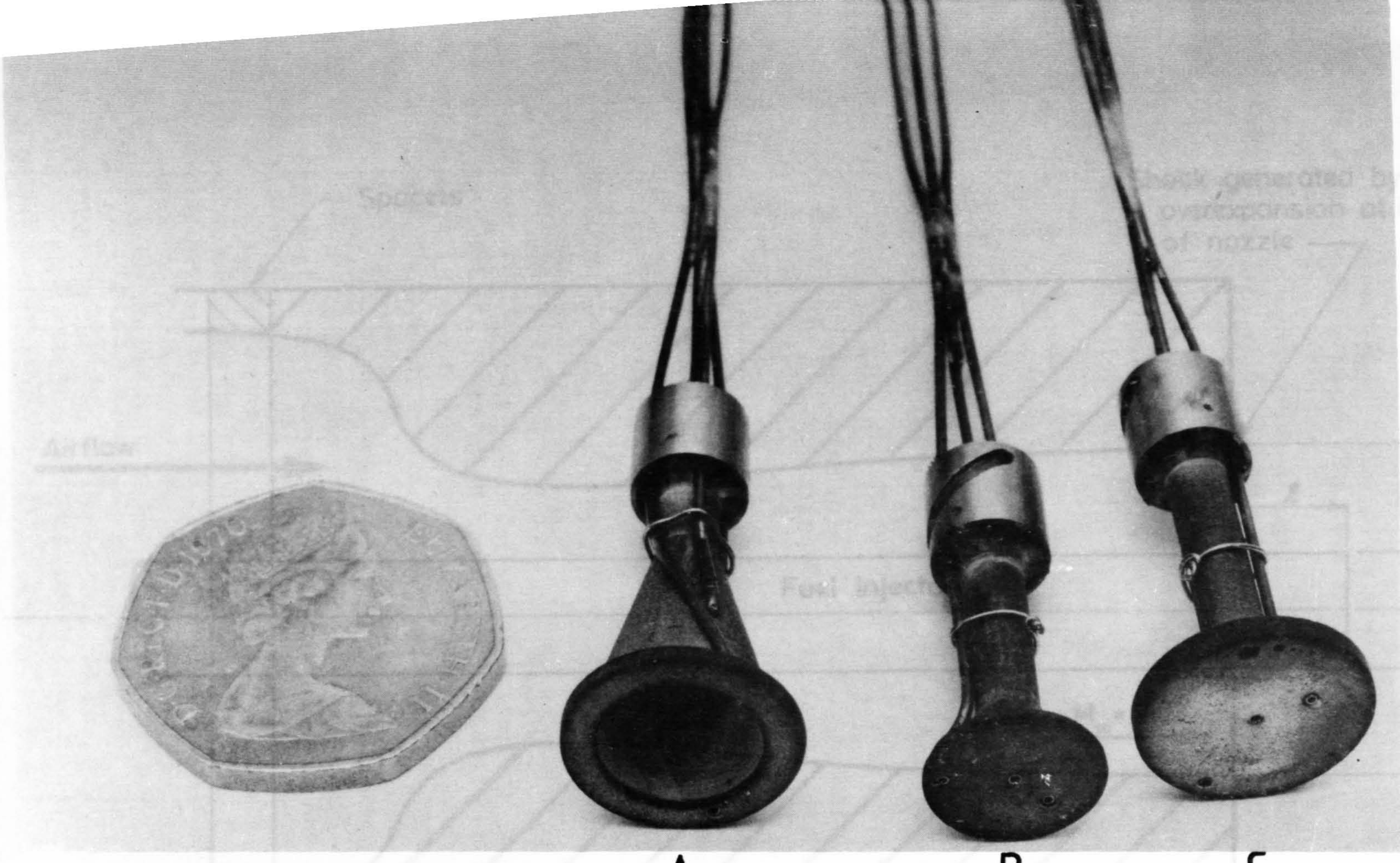

Fig. 4.16 Silicon nitride test bases

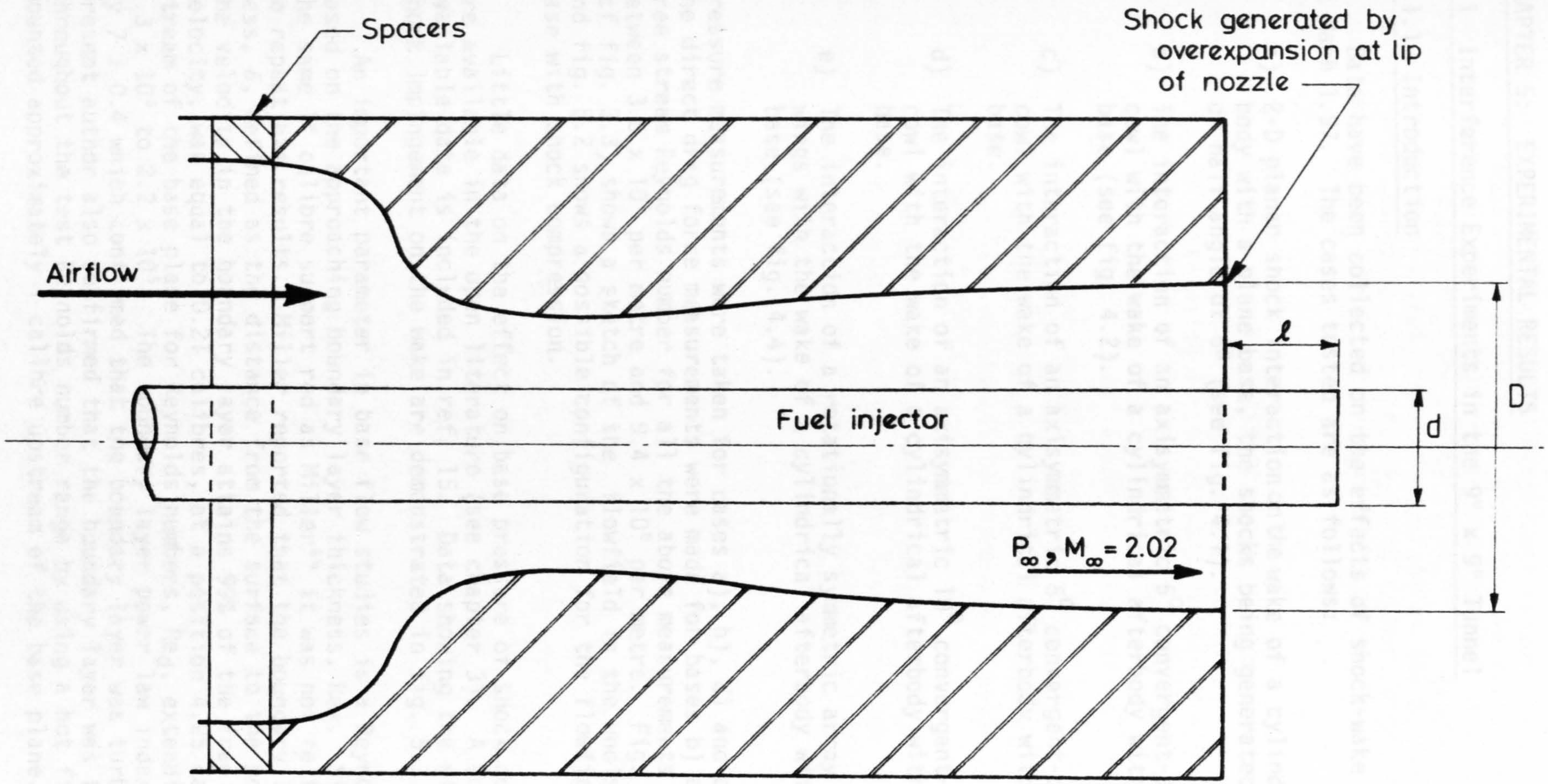

Figure 4.17. Test section of Pebble Bed Heater.

CHAPTER 5: EXPERIMENTAL RESULTS

5.1 Interference Experiments in the 9" x 9" Tunnel

5.1.1 Introduction

Data have been collected on the effects of shock-wake interference at Mach 1.97. The cases tested are as follows:

a) 2-D planar shock interaction on the wake of a cylindrical afterbody with a plane base, the shocks being generated by wedges of half angle of 5^o (see fig. 4.1).

b) The interaction of an axisymmetric 5^o convergent-divergent cowl with the wake of a cylindrical afterbody with a plane base (see fig. 4.2).

c) The interaction of an axisymmetric 5^o convergent-divergent cowl with the wake of a cylindrical afterbody with a recessed base.

d) The interaction of an axisymmetric 10^o convergent-divergent cowl with the wake of a cylindrical afterbody with a plane base.

e) The interaction of a rotationally symmetric array of delta wings with the wake of a cylindrical afterbody with a plane base (see fig. 4.4).

Pressure measurements were taken for cases a), b), d) and e) above and the direct drag force measurements were made for bases b) and c). The free stream Reynolds number for all the above measurements was varied between 3.6×10^6 per metre and 9.4×10^6 per metre. Fig. 5.1 (cf fig. 3.3) shows a sketch of the flowfield in the undisturbed case and fig. 5.2 shows a possible configuration for the flowfield in the case with shock compression.

Little data on the effect on base pressure of shock compression are available in the open literature (see chapter 3). A survey of the available data is included in ref. 15. Data showing the effect of shock impingement on the wake are demonstrated in fig. 5.3.

An important parameter in base flow studies is a Reynolds number based on the approaching boundary layer thickness, Re_δ. Since we used the same 1" calibre support rod as Miller[64] it was not felt necessary to repeat his results. Miller reported that the boundary layer thickness, δ, defined as the distance from the surface to the position where the velocity in the boundary layer attains 99% of the free stream velocity, was equal to 0.21 calibres, at a position 4.25 calibres upstream of the base plane for Reynolds numbers, Re_d, extending from 1.3×10^5 to 2.2×10^5. The boundary layer power law index was given by 7 ± 0.4 which confirmed that the boundary layer was turbulent. The present author also confirmed that the boundary layer was turbulent throughout the test Reynolds number range by using a hot film gauge mounted approximately 1 calibre upstream of the base plane.

Miller reports that his boundary layer traverse was conducted in steps of 20 thousandths of an inch, and thus the variation in boundary layer thickness over the range of Reynolds numbers he tested would be indiscernible assuming that δ/x varies as $Re_x^{-1/5}$. Assuming that the boundary layer thickness, δ, remains constant at the measured value of 0.21 calibres throughout the test Reynolds number range then a Reynolds number $Re = \frac{\rho_\infty U_\infty \delta}{\mu_\infty}$ may be defined with values in the range 1.9×10^4 to 5×10^4.

If it is assumed that a flat plate calculation can give a good approximation to the virtual origin of the turbulent boundary layer on the support rod, then using 1) a recovery factor of 0.90

2) Eckert's reference temperature method

and 3) assuming adiabatic wall conditions

the virtual origin of the boundary layer is found to be 9 calibres upstream of the boundary layer survey point. Defining a fineness ratio as the distance in base calibres from the virtual origin of the boundary layer to the base this configuration represents a projectile of fineness ratio of approximately 13.

The experimental results of the test configurations a) - e) mentioned above are described here. The base pressures, drag measurements where applicable and Schlieren photographs are presented in turn for each configuration. The base pressures observed herein are average base pressures defined as

$$P_b = \frac{1}{n} \sum_{i=1}^{n} P_{b_i}$$

where P_{b_i} is the pressure measured at pressure tapping i on the base and n is the number of tappings on the base (9 in this case). In certain cases difficulties were encountered in achieving a reliable measure of free stream static pressure, because of the feeding forward of shock induced pressure rises through either the tunnel boundary layer or the boundary layer on the afterbody. To circumvent this problem all the results are presented in terms of stagnation pressure measured in the tunnel settling chamber. The free stream static pressure is thus calculated where necessary, assuming $\gamma = 1.4$ and the free stream Mach number, M_∞, = 1.97 unless otherwise stated. The value of the undisturbed base pressure ratio, P_b/P_o, or P_b/P_∞ was first established. The base pressure ratio P_b/P_o was found to be 0.096 ± 0.003 at a Reynolds number, Re_d, of 9.2×10^4 and 0.093 ± 0.002 at a Reynolds number, Re_d, of 2.4×10^5. This corresponds to values of P_b/P_∞ of 0.72 ± 0.02 and 0.69 ± 0.02 respectively. In general the repeatability of the results was in keeping with these error bounds.

Selected schlieren photographs of the flow in the base region are shown. All the photographs shown in this chapter were taken with the knife edge in the horizontal plane. Both long exposure times (10 ms) and short exposure times (8 μs) were used. In general the pictures shown here are for Reynolds numbers, Re_d, of 2.4×10^5 except where the flow varies significantly at different Reynolds numbers (for example in §5.2.8). Fig. 5.4 shows a 10 ms exposure of the

undisturbed wake corresponding to a value of P_b/P_∞ of 0.69.

Some time dependent, and Reynolds number dependent, effects are examined and the results presented in the relevant part of the text. Stability and repeatability of the results are also discussed. Finally, configuration b) above, was re-examined with a pressure tapped cowl to aid the description of the internal flowfield and to determine whether it was possible to achieve a pressure drag reduction without wake combustion.

5.1.2 2-D planar shock interaction

Fig. 5.5 shows the variation in the base pressure ratio, P_b/P_o, with shock interaction distance, for Reynolds numbers, Re_d, of 9.2×10^4 and 2.4×10^5. A sketch of the flowfield generated by the wedges is shown in fig. 5.6. Schlieren photographs of the flow in the base region are shown in fig. 5.7.

In fig. 5.7(a) the initial interaction point is out of shot. The recompression shocks from the wake of the wedges can be clearly seen in the top right hand and bottom right hand corners of fig. 5.7(a), as can the expansion fan from the rear lip of the wedge (cf. fig. 5.6). The incident shocks are clearly curved as they pass through the expansion region. The expansion of the wake as it enters the expansion region and in particular the increase in the turbulent eddy length scale can also be observed. Fig. 5.7(b) is again a short exposure time schlieren photograph, with the shock interaction at 1.1 calibres. The wake diverges as it leaves the afterbody, that is, the shear layer appears to follow a course which takes it away from the centreline, as opposed to the wake converging, as in fig. 5.4, where the shear layer initially travels towards the centreline. A separation shock emanating from the afterbody, slightly ahead of the base, is apparent. Since the flow must be compressed through the separation shock it is reasonable to assume that the base pressure will be greater than the free stream static pressure, and this is confirmed by measurement (see fig. 5.5).

Longer time exposure photographs with interaction at approximately 1.5 calibres downstream of the base are shown in fig. 5.7(c) with $Re_d = 2.4 \times 10^5$ and fig. 5.7(d) with $Re_d = 9.2 \times 10^4$. Fig. 5.7(c) shows the separation shock from the base and the diverging wake, typical of a base pressure greater than free stream static whereas fig. 5.7(d) is consistent with a base pressure slightly less than free stream static (cf. fig. 5.5). Also apparent in fig. 5.7(c) is the reflection of the incident shock as a shock, closely followed by an expansion fan. The interaction region makes a half elliptic section where the shock plane cuts the axisymmetric wake. Since, on a constant pressure surface, the shock will reflect as an expansion, the pressure cannot be considered constant in the interaction region.

A spark photograph and long exposure photograph with the interaction at approximately 2.5 calibres are shown in figs. 5.7(e) and (f). The base pressure measurements show the base pressure to have returned almost to the undisturbed value. The wake recompression or "neck" shock can be seen in both photographs, occurring just before the incident shocks strike the wake, but appears to be slightly downstream of the position in the undisturbed case (fig. 5.4). The apparent thickness of

the incident shocks in fig. 5.7 is due to shock/boundary layer interaction on the side walls.

5.1.3 Plane Base - the interaction of the wake with the flowfield generated by a cowl with 5^{o} convergent-divergent section.

In the previous section the shock interaction distance was defined as the position where the incident shock first strikes the wake. In this and the following sections the variation of base pressure is plotted against the position of the leading edge of the cowl, since it is not possible to observe the point at which the generated shock strikes the wake.

The ratio of base pressure to free stream stagnation pressure has been plotted against the position of the leading edge of the cowl in fig. 5.8 for Reynolds numbers, Re_d, of 9.2×10^4 and 2.4×10^5. Both pressure measurements and the equivalent drag force measurements are shown in fig. 5.8. A distinct maximum base pressure occurs with the leading edge of the cowl positioned close to the base plane. This maximum appears to be slightly in excess of the pressure ratio expected across a two-dimensional oblique shock generated by a 5^{o} wedge (P_b/P_o = 0.176, P_b/P_∞ = 1.31). The drag force measurements show a lower mean base pressure in general because the averaged pressure measurements overestimate the mean base pressure (as discussed in §4.2.5). There is an apparent anomaly in the pressure reading at 1 calibre downstream of the base for $Re_d = 9.2 \times 10^4$. This is discussed in §5.2.8.

Figures 5.9 to 5.13 show long-exposure-time schlieren photographs of the flow at a Reynolds number, Re_d, of 2.4×10^5 as the cowl is moved downstream. These photographs are taken with the drag balance afterbody but there is no discernible difference. Since the pictures are similar there is no necessity to discuss them independently and the following general observations can be made.

The trailing edge shock and the contact discontinuity or slip line separating the internal and external boundary layers can be clearly identified at the rear of the cowl in figs. 5.9 to 5.13. The shocks generated at the leading and trailing edges of the cowl support legs are also easily identified.

The separation shock at the rear of the afterbody is also clearly discernible in figs.5.10, 5.11 and 5.12 and weakens as the cowl is moved downstream. The trailing shock at the rear of the annulus appears to terminate in a Mach disc and reflects as a shock. This feature may not be a true Mach disc. Since the wake approaching the disc may have a subsonic core the normal shock will terminate at the sonic surface giving rise to what one might call a 'Mach annulus'.

Comparison of figs. 5.5 and 5.8 shows that there is a significant qualitative difference between the behaviour of the base pressure ratio with two-dimensional shock interaction and the cowl/wake interaction, upstream of the base plane. This is due to the differing length scales of the shock generators. Comparison of fig. 5.6 with fig. 5.14 shows that, in the case of the cowl, the expansion fan at the throat of the cowl and wave reflections from the internal cowl walls can interact

with the wake in a manner which can significantly modify the base pressure.

5.1.4 Re-entrant Base - the interaction of the wake with the flowfield generated by a cowl with 5^{o} convergent-divergent section.

Pressure measurements were not taken with this configuration. The drag force measurements, converted to base pressure ratios, P_b/P_o, are shown plotted against the position of the leading edge of the cowl in fig.5.15(a)for Reynolds numbers, Re_d, of 9.2×10^4 and 2.4×10^5. Also shown, for comparison, are the results obtained for the plane base. It can be seen from fig.5.15 a that while the undisturbed base pressure for the re-entrant afterbody is approximately 20% lower than that obtained for the plane base, shock compression raises the base pressure to almost the same values as are obtained with the plane base.

No firm reasons for the greater drag of the recessed base in the undisturbed case can be given and in fact, Murthy[23] states (witnout any reference to any particular data) that recessed bases should give less drag. It is known that this is not necessarily true in subsonic flow (e.g. Morel[74]).

5.1.5 Plane Base - the interaction of the wake with the flowfield generated by a cowl with 10^{o} convergent-divergent section

Drag force measurements were not taken with this configuration. Since the results of §5.1.3 and §5.1.4 suggested that an optimal cowl position existed (with the leading edge of the cowl close to tbe base plane) it was not felt necessary to examine more than three cowl positions. The ratio of the average base pressure to the stagnation pressure at the three cowl positions tested is shown in fig. 5.15(b). For comparison, the curve shown in fig. 5.8 obtained with the 5^{o} cowl is also shown. It can be seen from fig.5.15b that the base thrust generated by the 10^{o} cowl is greater than twice that generated by the 5^{o} cowl. As it was surmised, the maximum base pressure was observed with the leading edge of the cowl positioned close to the base plane.

Long-time-exposure (10 ms) schlieren photographs with the leading edge of the cowl positioned in the base plane and one calibre downstream of the base are shown in fig. 5.16. It can be seen from fig. 5.16 that in both cases shown a normal shock occupies the plane of the inlet. From fig. 5.16(a) it can be clearly seen that the boundary layer on the centrebody separates some distance upstream of the base. While the boundary layer appears to enter the cowl, some flow spillage must occur. The same is true of fig. 5.16(b). Dust deposition on the centrebody suggests that the boundary layer separates approximately 0.15 calibres upstream of the base.

In both cases shown in fig. 5.16 the flow inside the cowl, (at least that part outside the wake), must be accelerated to supersonic speeds since the trailing flow configuration, with a clearly defined oblique shock, must be supersonic.

5.1.6 Plane Base - Interaction with rotationally symmetric 'delta' wings inclined at 5^{o} to the free stream

It was suggested by Townend[14] that caret wings with a sweep greater than that required to hold the two-dimensional generated shock-wave may prove beneficial due to the generation of leading edge vortices which may enhance fuel mixing. The experimental configuration is described in §4.2.2 and is shown in figs. 4.4 and 4.5. A sketch of the flowfield expected over a single wing is shown in fig. 5.17. Since the flowfields generated by each wing interact, even without considering the three-dimensional interaction with the wake, it is clear that the flowfield will be extremely complex.

As in the previous section, drag force measurements were not taken. The base pressure ratios, P_b/P_o, obtained at the four wing positions tested are shown in fig. 5.18. There appears to be some similarity with the results obtained with the two-dimensional wedges (fig. 5.5) in that the distinct peaking of the base pressure is not evident.

Schlieren photographs of the flow at a Reynolds number, Re_d, of 2.4×10^5 for each position tested are shown in fig. 5.19. The bow shock generated by each wing can be observed as can the extremely complex flowfield at the rear of the support cowl. The wake can be observed in figs. 5.19(c) and 5.19(d) and is typical of a wake structure with a base pressure less than, but close to, free stream static.

5.1.7 Cowl Pressures - Plane base with 5^{o} convergent-divergent cowl

In terms of chronology these tests were among the last to be performed. It was suggested by a two-dimensional drag calculation, together with the shock/wake interaction results obtained in the Pebble Bed Heater (§5.2), that some benefit, in terms of pressure drag reduction, may be available by using a cowl of small angle. It seems apt to discuss these experiments here, before moving on to a description of the unsteady phenomena.

The cowl (of 2 base calibres in length and 2 base calibres in diameter) which was used to obtain the results in sections 5.1.3 and 5.1.4 was pressure tapped on the internal surface (see §4.2.2 and fig. 4.2). Four positions of the cowl, with the leading edge close to the base plane, were tested. The pressures obtained on the internal surface of the cowl are shown in fig. 5.20. Since the pressures obtained on the opposite surfaces of the cowl differed somewhat these are plotted independently and the mean of the surface values is also shown. No schlieren photographs were taken since the flowfield was not expected to vary from that already shown in §5.1.3. It can be seen from fig. 5.20 that the static pressures on the surface of the cowl differ considerably from the two-dimensional calculation, particularly on the upstream face. There are two major reasons for this:

(a) there are areas of the flowfield in the inlet where the quasi-one-dimensional approximations apply, i.e. isentropic compression can take place on the upstream surface.

(b) the interaction with the wake flowfield (fig. 5.21). The separation shock interacts with the incident shock generated at the lip of the cowl and after this interaction impinges on the cowl surface. It can be seen from figs. 5.20 (a) - (d), that as the cowl is moved rearward the maximum pressure observed on the cowl surface moves towards the leading edge. Fig. 5.21 shows possible flowfield configurations for the cases with the leading edge of the cowl 0.6 calibres upstream of the base and 0.1 calibres upstream of the base.

The pressure distributions shown in fig. 5.20 were then integrated to obtain the drag coefficients,

$$C_D = \frac{D}{\frac{1}{2}\gamma P_\infty M_\infty^2 A}$$

where D is the drag force and A is the base area. The drag coefficient of the cowl, C_{DC}, the base drag coefficient, C_{DB}, and the net drag coefficient, C_{DN}, for each cowl position tested, are shown in fig.5.22. The base drag coefficient is, of course, negative, implying a base thrust (compare fig. 5.22 with fig. 5.8). It can be seen that the net drag coefficient can be less than the undisturbed base drag coefficient (approximately 30% less with the cowl leading edge in the region 0.6 calibres to 0.35 calibres upstream of the base plane). A zone of favourable interference therefore exists with the cowl leading edge positioned between 0.6 calibres and 0.2 calibres upstream of the base plane. Furthermore, the point of minimum drag coeffficient does not coincide with the point of maximum base thrust.

It should be pointed out that only pressure drag has been taken into account here.

5.1.8 Time dependent, Reynolds number and unsteady effects

No discussion has been made of the anomaly in the pressure readings in fig. 5.8, where at $Re_d = 9.4 \times 10^4$ the base pressures with the leading edge of the cowl positioned 1 calibre downstream of the base plane, as observed by direct pressure measurements and as implied by drag force measurement, do not agree. The mean and range of the pressure readings at this position are shown. The large range of pressures obtained, varying by +7% and -3%, suggests an unsteadiness or fluctuation in the base pressure. The mean base pressure is substantially lower than that implied by the drag balance at the same Reynolds number. The spark photographs shown in fig. 5.23 confirm that there is a substantial difference in the flow in the base region at the different Reynolds numbers shown.

Fig. 5.23(b) at a Reynolds number of 2.4×10^5 shows a wake configuration corresponding to a base pressure greater than free stream static pressure and is consistent with the pressures measured (see fig. 5.8). However, fig. 5.23(a) shows the edge of wake leaving the base parallel to the centreline, a configuration which implies that

the base pressure is approximately equal to the free stream static pressure and which conflicts with the measurements made.

The manner in which the flow structure changes is also of interest. As the Reynolds number decreases there comes a point at which the wake shows an instability, oscillating between the configuration shown in fig. 5.23(b), which is presumably a limiting flow configuration, and some other limiting flow configuration. The wake flow configuration presumably passes through that shown in fig. 5.23(a) to some other limiting flow representative of a lower base pressure.

Pressure measurements through the Reynolds number range are shown in fig. 5.24. The large range of measured pressures at 4 and 6 psi is shown. This variation is not evident at the higher Reynolds numbers, and is confirmed to be due to an instability or oscillation in the near wake region by fig. 5.25. This oscillation was not observable with the naked eye, being at too high a frequency. No further measurements were taken and the frequency of the oscillations remains unknown.

A similar effect was evident with the cowl positioned 2.5 calibres behind the base plane. However, in this case, the oscillations were under some circumstances visible with the naked eye but were at too high a frequency to count, and this suggested that the frequency must be of the order of 10 Hz(i.e. $\frac{\omega L}{U_\infty} \simeq 1.6 \times 10^{-2}$ where L is the distance between the base and the cowl leading edge). Fig. 5.26 shows 10 ms exposures of the flow at a Reynolds number, Re_d, of 9.2×10^4. The visual observations suggested that the flow configuration shown in fig. 5.26(b) was stable in the sense that once the flow was firmly established in this mode, varying the Reynolds number appeared to fail in re-establishing the oscillations.

In fig. 5.27 spark schlieren photographs of the oscillatory flow are shown. Fig. 5.27(a) shows the wake in a configuration which is close to the undisturbed case (see fig. 5.4) and thus probably represents the limiting case mentioned above. The subsequent photographs, i.e. figs. 5.27(b), (c) and (d) represent base flow patterns representative of higher base pressures.

5.2 Shock/Wake and Shock/Flame Interaction

5.2.1 Introduction

The experiments reported in this section were carried out in the Pebble Bed Heater (see §4.3 and fig. 4.14). An axisymmetric Mach 2 nozzle was used with a cylindrical fuel injector mounted through the throat (see figs. 4.17 and 5.25). After assembly of the nozzle and injector it was observed that the injector was angularly displaced in the horizontal plane from the true centreline of the working section by approximately $1\frac{1}{2}^o$. It was decided to centre the injector at the nozzle lip and this implied that the injector would be displaced from the centreline at the throat and a non-uniform Mach number distribution across the working section would result. It was therefore felt necessary to survey the working section to determine the extent of any non-uniformity in the flow conditions. The results

of a pitot survey in the horizontal plane are shown in fig. 5.29. The mean Mach number was evaluated as $M_\infty = 2.02 \pm 0.05$. There was no discernible variation in Mach number with stagnation pressure in the range tested (50 psig - 113 psig corresponding to values of P_2/P_∞ (see fig. 5.28) in the range 1.83 - 0.90 respectively). Measuring the Mach angle at the nozzle lip from schlieren and shadowgraph photographs gave $M_\infty = 2.06 \pm 0.06$.

There are significant disadvantages in performing shock interference experiments by overexpanding the airflow:

1) the Reynolds number, Re_d, varies with stagnation pressure (for example at a stagnation temperature of 300°K, Re_d was calculated to vary downwards from 1.7×10^6 for the fully expanded jet† to 9.5×10^5 at a stagnation pressure of 64.7 psia).

2) the position of shock interaction varies with the degree of overexpansion.

3) the reference pressure, P_∞, varies, decreasing with increasing degree of overexpansion. However, these disadvantages were considered acceptable since this form of experiment makes it possible to visualise the flow and to obtain useful scientific and design information. Shadowgraph, schlieren and direct luminosity photographs are shown in the text.

Only two of the three test bases shown in fig. 4.16 were tested due to time and economic limitations. In §5.2.2 the results are shown for the recessed base with peripheral bleed of fuel. Axial bleed results are shown in §5.2.3 and §5.2.4. Since it has been shown quite clearly in §5.1 that the interaction position has a significant effect on base pressure spacers of length 0.46 d were manufactured and could be placed in the subsonic portion of the nozzle, as shown in fig. 5.28. The effect of varying the position of the shock interaction is described in §5.2.3.

The effect of stagnation temperature on the base pressure, both with and without combustion, is examined in §5.2.4. A discussion of the effects of wind tunnel interference is included in §5.2.5 and this chapter concludes with a description of the effects of shock compression on fuel efficiency in §5.2.6.

5.2.2 Peripheral bleed (recessed base) at a stagnation temperature, $T_0 \sim 300^oK$

The test base used to obtain the results in this section was designed to permit peripheral bleed with fuel injection 0.1 inches upstream of the base plane. The base itself was recessed, as shown in fig. 5.30. Since Townend and Reid[2] had shown that gap size is not an important parameter in wake combustion experiments the bleed gap was

---

† The terminology 'fully expanded' is used here to denote that the jet exit static pressure is equal to atmospheric, i.e. $P_\infty = P_2$, e.g. fig. 5.41(a) comes close to this condition.

set arbitrarily at 0.06 inches (approximately 0.1 calibres). Hydrogen gas, at a stagnation temperature of approximately 300°K, was used as the fuel and was bled subsonically into the boundary layer.

Fig. 5.30 shows the effect on the base pressure ratio of the shock generated at the lip of the nozzle for varying degrees of over-expansion in the nozzle. The no bleed case and hydrogen combustion at three mass flow rates are shown. The wake combustion results and the no bleed results indicate that the base pressure increases in an approximately linear manner when $P_b/P_\infty > 1$ at least until $P_2/P_\infty \simeq 1.7$. Also the effect of adding combustion in the wake diminishes with increasing incident shock strength. It was not possible to reduce the hydrogen mass flow rate much below 0.15 gm/sec since the weak extinction limit was found to be 0.13 gm/sec (with the jet fully expanded). This agrees reasonably well with that observed by Townend and Reid[2] though their models had bluff and conical bases.

For the case with no bleed three runs are shown (tagged differently) as an indication of the repeatability. The repeatability of the results can be seen to be adequate (better than ± 5%) and was continually improved as experience was gained with the apparatus (to better than ± 2%). Shadowgraph photographs of the flow are shown in figs. 5.31 - 5.34.

The flowfield in the near wake region without bleed is shown in fig. 5.31. With only weak shock interaction, as is shown in fig. 5.31(a) the wake initially converges towards the centreline, as is expected with $P_b/P_\infty = 0.65$. Some asymmetry is evident, both in the flowfield (as was mentioned in §5.2.1) and in positioning of the base with respect to the centreline of the injector. The bleed gap can be clearly seen and a disturbance at the gap is evident, due partly to the geometrical asymmetries.

As the shock strength is increased the shock/wake interaction position moves upstream (fig. 5.31(a) - (f)) and the wake responds to the increasing base pressure by converging towards the centreline more slowly (fig. 5.31(a) and (b)), until, with $P_b/P_\infty \simeq 1$, the shear layer leaves the injector parallel to the centreline (fig. 5.31(c)). As the base pressure increases further, the wake initially diverges from the centreline, figs. 5.31(d) - (f)). With $P_b/P_\infty = 1.80$ (fig. 5.31(f)) the approaching boundary layer separates from the injector at, or slightly in front of, the leading edge of the bleed gap.

Shadowgraph photographs with combustion in the wake are shown in figs. 5.32 to 5.34 for the three hydrogen mass flow rates tested, 0.15 gm/sec, 0.23 gm/sec and 0.3 gm/sec, respectively. With a weak disturbance in the wake, ($P_2/P_\infty = 1.03$), as the mass flow rate rises, see fig. 5.30, figs. 5.32(a), 5.33(a) and 5.34(a), the base pressure rises from $P_b/P_\infty = 0.97$ and the shear layer responds appropriately. The angle the shear layer makes with the horizontal decreases as the mass flow rate (and the base pressure) increases until in fig. 5.34(a) it can be seen that the shear layer leaves the base approximately parallel to the centreline. It is interesting to note that with incident shock strengths of $P_2/P_\infty = 1.82$ (figs. 5.32(f), 5.33(f) and 5.34(f)) the scale of the separated zone on the centrebody is increased in comparison with the case with no combustion, fig. 5.31(f).

It should be observed that there is no evidence of significant second derivatives of the density inside the wake. A direct luminosity photograph of the flame at a mass flow rate of 0.3 gm/sec is shown in fig. 5.35. The flame was an orange-yellow colour presumably due to entrainment of impurities from the silicon nitride base. This flame structure is superimposed on a shadowgraph photograph of the same flow in fig. 5.36. The flame lies inside the shear layer. A tungsten wire was placed diametrically through the combustion zone (see e.g. fig. 5.46) and this appeared to confirm that the zone bounded by the luminous front was hot. It was not possible to photograph the probe as the wire melted quite rapidly.

It was previously noted, in connection with fig. 5.30, that the effect of combustion in the wake diminishes with increasing incident shock strength. In the case of the fully expanded jet, i.e. $P_2 = P_\infty$, the addition of wake combustion is clearly effective in reducing the base drag, however, little benefit is obtained by increasing the hydrogen mass flow rate above, say, 0.23 gm/sec. These effects are quantified in §5.2.6.

Finally in this section we compare the effects of variations in the non-dimensional bleed parameter, H, (as used by Townend and Reid[2]) on the base pressure ratio for varying incident shock strength (fig. 5.37). It is apparent from fig. 5.37 that little or no benefit accrues in increasing H at high incident shock strengths.

An attempt was made to test this configuration at high stagnation temperature (T_0 = 1450°K). The ceramic base unfortunately broke up after more than 10 minutes of run time and approximately 5 minutes with wake combustion. It is probable that failure was due to impact with a fragment of fire brick but it is possible that thermal failure occurred. In practice since flight times are expected to be much less than five minutes in duration it is clear that silicon nitride is a suitable material for use at high stagnation temperature (at least up to 1450°K) and with hydrogen combustion in the wake.

5.2.3 Axial bleed at a stagnation temperature $T_0 \approx 300^oK$

The test base used in these experiments was designed to provide axial bleed, circumferentially around the base of the injector and the gap size was set at 0.07 inches, i.e. 0.1 calibres. Nitrogen bleed, hydrogen bleed without combustion, and hydrogen bleed with combustion were examined. The effect of varying the shock interaction position by inserting spacers in the nozzle (see fig. 5.28) was also examined. Initially, the apparatus was set to give a value for ℓ/D of 0.11.

The effects of shock/wake interaction on the base pressure of the injector are shown in figs. 5.38 and 5.39. The effects of nitrogen bleed at bleed mass flow rates of 0.88 gm/sec and 1.98 gm/sec are shown in fig. 5.38. An intermediate mass flow rate of 1.54 gm/sec was also tested but the results were identical with those obtained at a mass flow rate of 1.96 gm/sec. Fig. 5.39 shows the effect of hydrogen bleed without combustion at the three mass flow rates tested, i.e. 0.15, 0.23 and 0.3 gm/sec. Clearly the effects of nitrogen bleed are relatively insignificant. In the fully expanded jet, drag reduction of less than 8% is observed with a nitrogen mass flow rate of 1.96 gm/sec. The

effects of hydrogen bleed are more pronounced. A drag reduction of 16% is achieved with a mass flow rate of 0.3 gm/sec. No benefit is observed when increasing the nitrogen mass flow rate above the intermediate mass flow rate of 1.54 gm/sec and little benefit is obtained by increasing the hydrogen mass flow rate above, say, 0.23 gm/sec. However, the benefits of mass bleed are insignificant (at least in percentage terms) at large shock strengths. For example, at an incident shock strength of 1.37, hydrogen bleed at a mass flow rate of 0.3 gm/sec increases the base pressure by approximately 3%.

The effect of igniting the hydrogen at the same bleed rates as mentioned above is shown in fig. 5.40. For comparison the effects of nitrogen bleed at a mass flow rate of 0.88 gm/sec and hydrogen bleed at a mass flow rate of 0.3 gm/sec are also shown in fig. 5.40. The effect of enthalpy addition is clearly significant, at least for shock strengths of less than, say, 1.8. Wake combustion of hydrogen at a mass flow rate of 0.3 and 0.23 gm/sec increases the base pressure by over 50% in the fully expanded jet, almost eliminating the base drag.

The behaviour of both peripheral and axial bleed with shock compression is similar (compare fig. 5.30 with fig. 5.40). Axial bleed with combustion is more effective than peripheral bleed in raising the base pressure in the case with $P_2/P_\infty = 1$, as is discussed in §5.2.6.

Selected schlieren photographs of the near wake flowfield with and without combustion are shown in fig. 5.41. These photographs were taken with a dual cut-off (i.e. a double knife edge was used with cut-off on both top and bottom of the light beam) in an attempt to obtain uniform colour of the shocks (e.g. black) and expansions (e.g. white). This was not particularly successful because the noise from the jet tended to cause vibration which moved the knife edge positions. This notwithstanding, the main features in the flow can be clearly identified. The behaviour of the wake is similar to that described earlier for peripheral bleed (§5.2.2). However, at the same shock strengths, the shock/wake interaction point is further downstream (compare fig. 5.41 with figs. 5.31 and 5.34). This is the primary cause of the slightly lower base pressure ratios observed at large shock strengths (compare fig. 5.40 with fig. 5.30). Fig. 5.41(e) shows, without bleed, the approaching boundary layer on the centrebody close to the point of incipient separation. Fig.5.41 (f), at a marginally higher incident shock strength with combustion in the wake, shows clearly that the approaching boundary layer has separated well upstream of the base.

The lettering in figs. 5.41(a) and (d) is referred to in the discussion on wind tunnel interference (§5.2.5).

Streaks in the near wake flowfield can be clearly observed in figs. 5.41(b) and (d). Comparison also with the direct luminosity photographs shown in fig. 5.45 shows that there is some non-uniformity in the injection process and/or in the inviscid free stream.

The effect of removing one spacer to obtain $\ell/D = 0.27$ is shown by comparing figs. 5.42 and 5.43 with 5.40 and 5.41. Shock impingement now occurs closer to the base. The line representing $P_b/P_\infty = P_2/P_\infty$ is shown in fig. 5.42. The curve showing the effect of shock/wake interaction rises steadily towards the $P_b/P_\infty = P_2/P_\infty$ line appearing to

cross this line when $P_2/P_\infty \simeq 1.48$. At an incident shock strength of 1.79 the curve has again crossed the $P_b/P_\infty = P_2/P_\infty$ line and, as can be seen from fig. 5.43(f), the approaching boundary layer has separated upstream of the base plane. At an incident shock strength of 1.55 P_b/P_∞ is 4.5% greater than P_2/P_∞. The reason for P_b/P_∞ appearing to be greater than the incident shock strength is due to the assumption of constant P_2 (atmospheric) behind the shock, inherent in the calculation of P_2/P_∞. In practice, since the flow is axisymmetric, the strength of the incident shock will increase towards the centreline. It is not suggested that without wake combustion, P_b/P_∞ can be greater than the incident shock strength at the impingement position. It can be seen from fig. 5.43(e) that the approaching boundary layer remains attached and that the shock impingement point is close to the optimum (see figs. 5.3 and 5.8).

The addition of wake combustion has a similar effect to that shown in fig. 5.40, however the base pressures obtained are consistently higher. An interesting feature is that once the approaching boundary layer has separated, reducing the hydrogen mass flow rate appears to be beneficial. This is thought to be due to a reduction in the scale of the separated zone on the afterbody, leading to an increase in pressure at the base. In practice, boundary layer separation ahead of the base would normally be avoided.

A direct comparison of the effects of nozzle position, and thereby shock interaction position, is shown in fig. 5.44. At given shock strengths the nominal shock interaction position shifts by less than 0.5 calibres, yet the effects on base pressure are significant. The case shown with $\ell/D = 0.27$ without combustion, at shock strengths greater than 1.55, gives slightly higher base pressures than the case with $\ell/D = 0.11$ including the effects of wake combustion.

Schlieren and direct luminosity photographs with a hydrogen mass flow rate of 0.15 gm/sec are shown in fig. 5.45. It was decided to display the direct luminosity photographs at this mass flow rate purely because of the increased contrast observed. At higher fuel mass flow rates, e.g. 0.3 gm/sec, the hydrogen burns, apparently as a turbulent diffusion flame, with a typical low luminosity blue flame.

The effect of increasing the mass flow rate above, say, 0.23 gm/sec appears only to increase the length of the flame with little apparent change in base pressure. Since no wake probing has been undertaken to determine the wake pressures and temperature a tungsten wire of 0.01 inches diameter was stretched diametrically through the near wake region in an attempt to determine the regions of greatest heat release. This kind of probing is, of course, highly intrusive and must be taken as qualitative in nature. Fig. 5.46 shows direct luminosity photographs with the jet at close to the fully expanded condition for probe positions of approximately 0.5 calibres and 1 calibre downstream of the base plane. The luminous region extends to approximately 5 calibres downstream of the base plane. A sketch of the hot wake region determined by this method is shown in fig. 5.47.

As was mentioned in §5.2.2 the tungsten wire melted rapidly in the peripheral bleed case. This indicates that the wake core temperature

in the axial bleed case is lower than that with peripheral bleed. Another significant difference in the behaviour of axial bleed and peripheral bleed is in the weak extinction limit. With axial bleed the weak extinction limit was too low to measure on our apparatus (< 0.03 gm/sec) while with peripheral bleed weak extinction occurred at a mass flow rate of 0.13 gm/sec.

A hypothetical configuration of the near wake flowfield in the case with axial bleed is shown in fig. 5.48. Postulated static temperature profiles are shown in fig. 5.49. The major difference in the streamline patterns hypothesised for axial bleed (fig. 5.48) and peripheral bleed (fig. 5.50) is in the dividing streamline (DSL). In fig. 5.50 (peripheral bleed) the DSL reattaches whereas in fig. 5.48 (axial bleed) it does not.

5.2.4 Shock/wake and shock/flame interaction at 'high' stagnation temperature ($550^{o}K < T_o < 1370^{o}K$)

Both the peripheral bleed and axial bleed cases were tested. As previously mentioned the recessed base broke after approximately five minutes with wake combustion with airflow stagnation temperatures in the range $1350^{o}K \leq T_o \leq 1450^{o}K$. The hydrogen fuel self-ignited at this stagnation temperature. No pressure measurements were made although a direct luminosity movie film of the initial stages of the experiment was taken.

The tests with axial bleed were more successful. Two spacers were placed upstream of the nozzle to give a value for ℓ/D (see fig. 5.28) of 0.11. This value was chosen since the tests at $T_o = 300^{o}K$ had been more extensive (§5.2.3). Because of the experiences with the peripheral bleed case (see above) schlieren movie film was employed. (This required the base to be exposed to the high temperature for a shorter period of time.) Unfortunately the relative movement of the pebble bed (due to thermal expansion) with respect to the water cooling supply to the injector caused a torque on the injector and consequently the injector yawed. This was not observed until after the completion of filming. The results shown in fig. 5.51 should therefore be treated with reservation. It was not possible to repeat these in this programme.

The values of P_∞ used in the calculation of P_b/P_∞ shown in fig. 5.51 were calculated using the isentropic flow equation[68]

$$P_\infty = P_o \left(1 + \frac{\gamma-1}{2} M_\infty^2 \right)^{-\frac{\gamma}{\gamma-1}} \qquad 5.2.1$$

Since $\gamma = \gamma(T)$ and $M_\infty = M_\infty(\gamma)$ the relevant values of γ and M_∞ were found from figs. B.2 and B.3. It should be noted that the difference in calculated static pressure between the assumption of constant γ and M_∞ and $\gamma = \gamma(T)$, $M_\infty = M_\infty(\gamma)$ is significant for stagnation temperatures above, say, $T_o = 750^{o}K$ notwithstanding that the variation in $M_\infty(\gamma)$ is less than the local variation in the working section (§5.2.3). It should be pointed out that there is also a significant Reynolds number variation with stagnation temperature. At $890^{o}K$, $Re_d = 3.1 \times 10^5$ [69]

at the fully expanded jet condition.

Due to the difficulties involved in integrating the isentropic flow equations from stagnation conditions to free stream conditions the remainder of the results in this section are presented in terms of a base pressure ratio, P_b/P_o, and, for want of a better term 'compression ratio', P_2/P_o. Fig. 5.52 shows the effect of compression ratio on base pressure ratio for varying stagnation temperature. Only small differences with stagnation temperature are apparent and the behaviour is qualitatively the same as shown in fig. 5.40. The effects of stagnation temperature on the base pressure ratio are shown for constant compression ratios in fig. 5.53.

It can be seen from fig. 5.53 that, in general, the base pressure ratio decreases slightly with stagnation temperature at constant compression ratio. The maximum observed decrease in base pressure ratio is 6.7% without combustion at a compression ratio of 0.14 over a stagnation temperature range of 300°K to 950°K. With combustion, the maximum decrease is 6.3% at the same compression ratio over a stagnation temperature range of 300°K to 890°K.

It should be pointed out that two effects mentioned in the preceding paragraphs tend to reduce the base pressure ratio with increasing stagnation temperature.

1) The analysis in Appendix B indicates that the shock strength decreases with increasing stagnation temperature. This effect can account for a decrease in base pressure ratio of the order of 2% by estimating the decrease in shock strength using equation 5.2.1 and table B.1.

2) Since the Reynolds number decreases we would also expect the base pressure ratio to decrease slightly (particularly when $P_b/P_\infty > 1$). The extent of this effect is difficult to estimate. Fig. 5.8 shows a decrease in base pressure ratio of about 4% at the optimal interaction position with a decrease in Reynolds number by a factor of about 2.5.

If this effect carries over to the higher Reynolds numbers experienced in this facility then the two factors can account for a substantial proportion of the variation in base pressure ratio.

In conclusion it can be stated that the base pressure ratio is a weakly decreasing (almost constant) function of stagnation temperature.

One further point should be made from the observations recorded in fig. 5.53. The base pressure ratio increases with stagnation temperature at a constant compression ratio of 0.22 and with hydrogen combustion in the wake. This is due to the effects of water cooling in the fuel injector on the boundary layer approaching the base. The boundary layer is subjected initially to heated wall conditions, (i.e. $T_\infty/T_W < 1$) and moves with increasing stagnation temperature to cooled wall conditions (i.e. $T_\infty/T_W > 1$). This inhibits the onset of separation and thus enhances the base pressure at high incident shock strengths.

5.2.5 Wind tunnel interference effects

Wind tunnel interference effects are a common problem in base flow studies (see Chapter 3). Some of the cases tested in §5.2 undoubtedly suffer from unwanted interference. The extent of the effects have not been systematically examined but a description of the effects and some general comments are included here. As an example, fig. 5.41 has been chosen to demonstrate the extent of the interference flowfield.

Fig. 5.41(a) shows the near wake flow with the jet close to the fully expanded condition. The expansion fan from the corner of the base (point A in fig. 5.41(a)) reflects from the edge of the jet (at point B) as a compression because the edge of the jet is a constant pressure (atmospheric) surface. This compression interacts with the wake approximately 3 calibres downstream of the base (at point C), sufficiently close to affect the base pressure, tending to give a falsely high reading. With wake combustion, fig. 5.41(b), the expansion fan is weakened and little interference is expected. Fig. 5.41(c) shows the effects of an incident shock of strength, P_2/P_∞, of 1.24. The wake is responding almost as if the length of the afterbody had been increased by approximately 1.2 calibres (c.f. fig. 5.41(a)) and the reflection of the expansion fan interacts approximately 3.5 calibres downstream of the incident shock interaction point. We are unaware if this is significant.

Once P_b becomes greater than P_∞, as is shown in figs. 5.4(d), (e) and (f), a shock is observed at the base, due to the divergence of the wake (point A on fig. 5.41(d)). This shock reflects as an expansion from the edge of the jet (point B on fig. 5.4(d)), which will tend to reduce the base pressure[67]. The reflected expansion fan from the incident shock interaction (point C on fig. 5.4(d)) then reflects as a compression from the edge of the jet (point D). The wake responds to both these interference effects (points E and F on fig. 5.41(d)). However, one would expect that the incident expansion at point E, being closer to the base, would have the greater effect, leading to reduced base pressure. There may be some 'shielding' effect due to the strong disturbance at the shock interaction position.

One may therefore surmise that any interference effects will tend to increase the base pressure when $P_b/P_\infty < 1$ and decrease the base pressure when $P_b/P_\infty > 1$.

5.2.6 Fuel efficiency

As a measure of the efficiency of the combustion and bleed processes we use specific impulse. Specific impulse in this context is defined as (base force rise)/(fuel mass flow rate),

$$\text{i.e. specific impulse, } \sigma_0, = \left(\frac{P_b}{P_\infty} - \frac{P_{b_1}}{P_\infty} \right) P_\infty \frac{A}{\dot{m}_f} \qquad 5.2.2$$

where P_b/P_∞ is the base pressure ratio with bleed or wake combustion at some incident shock strength, P_2/P_∞ and P_{b1}/P_∞ is the base pressure ratio without bleed but at the same incident shock strength, P_2/P_∞. That is P_b/P_∞ is a function of fuel mass flow rate and incident shock strength, $P_b/P_\infty = P_b/P_\infty\ (\dot{m}_f,\ P_2/P_\infty)$, whereas P_{b1}/P_∞ is a function of incident shock strength only, $P_{b1}/P_\infty = P_{b1}/P_\infty\ (\dot{m}_f \equiv 0,\ P_2/P_\infty)$.

The specific impulse, σ_0, defined as in equation 5.2.2, for the peripheral bleed case discussed in §5.2.2, is plotted as a function of incident shock strength in fig. 5.54. The major feature demonstrated in fig. 5.54 is the rapid decline in σ_0 with increasing incident shock strength.

In the form expressed in equation 5.2.2 σ_0 is a direct function of P_∞. In practice, we would prefer the experimental data to be expressed not as a function of P_∞, but of P_2. This is because in the design process the variation in P_2/P_∞ would be effected by geometric means with (at constant altitude) constant P_∞. It is valid, therefore, to define a specific impulse, σ_1, by

$$\sigma_1 = \left(\frac{P_b}{P_\infty} - \frac{P_{b_1}}{P_\infty} \right) P_\infty \frac{P_2}{P_\infty} \frac{A}{\dot{m}_f} \qquad 5.2.3$$

σ_1 is a specific impulse referred to atmospheric pressure and in the context of these experiments is a useful measure if the base pressure ratios P_b/P_∞ and P_{b1}/P_∞ are essentially independent of Reynolds number (an assumption which is justified over the small range of Reynolds number tested here by the results of §5.1, fig. 5.8). Clearly, since $\sigma_1 = \sigma_0 \times P_2/P_\infty$, any decrease in σ_1 with increasing shock strength will be less than that observed in σ_0 (fig. 5.54). The variation in σ_1 with shock strength is shown in fig. 5.55.

The specific impulses σ_0 and σ_1 calculated for the axial bleed case with $\ell/D = 0.11$ are shown in figs. 5.56 and 5.57. σ_0 and σ_1 for the axial bleed case with $\ell/D = 0.27$ are shown in fig. 5.58. In the undisturbed jet, axial bleed gives greater specific impulses (however defined) than peripheral bleed at the same mass flow rates (approximately 25% greater). This is due to the effect of mass addition directly into the base recirculation zone with axial bleed, rather than into the boundary layer, as is the case with peripheral bleed.

It was noted in §2.2 that to sustain a Mach 2 projectile for a period of approximately 10 seconds a specific impulse of approximately 500 lbf.sec/lbm is required. This calculation assumed that kerosene was the fuel used. It was observed in Townend[14,15] that, for conventional

ramjets, the specific impulse of hydrogen is approximately three times that of kerosene. For hydrogen bleed at a mass flow rate of 0.3 gm/sec (not the optimum in terms of both base pressure ratio and specific impulse) σ_0 exceeds 500 lbf.sec/lbm for all cases up to incident shock strengths of between 1.6 and 1.7. σ_0 exceeds 1500 lbf.sec/lbm only up to shock strengths of about 1.2 with $\dot{m}_f$ = 0.3 gm/sec with axial bleed, however, σ_1 exceeds 1500 lbf.sec/lbm up to shock strengths of 1.4 (1.6 in the case of axial bleed with ℓ/D = 0.11).

In all the cases shown in figs. 5.54 to 5.58 the effect of shock compression is seen to reduce the efficiency of wake combustion. It is clear that the specific impulses obtained are functions of:

1) Shock strength

2) Shock interaction position, and

3) Bleed mode.

Fig. 5·1 Streamline Sketch. For Undisturbed Base Flow

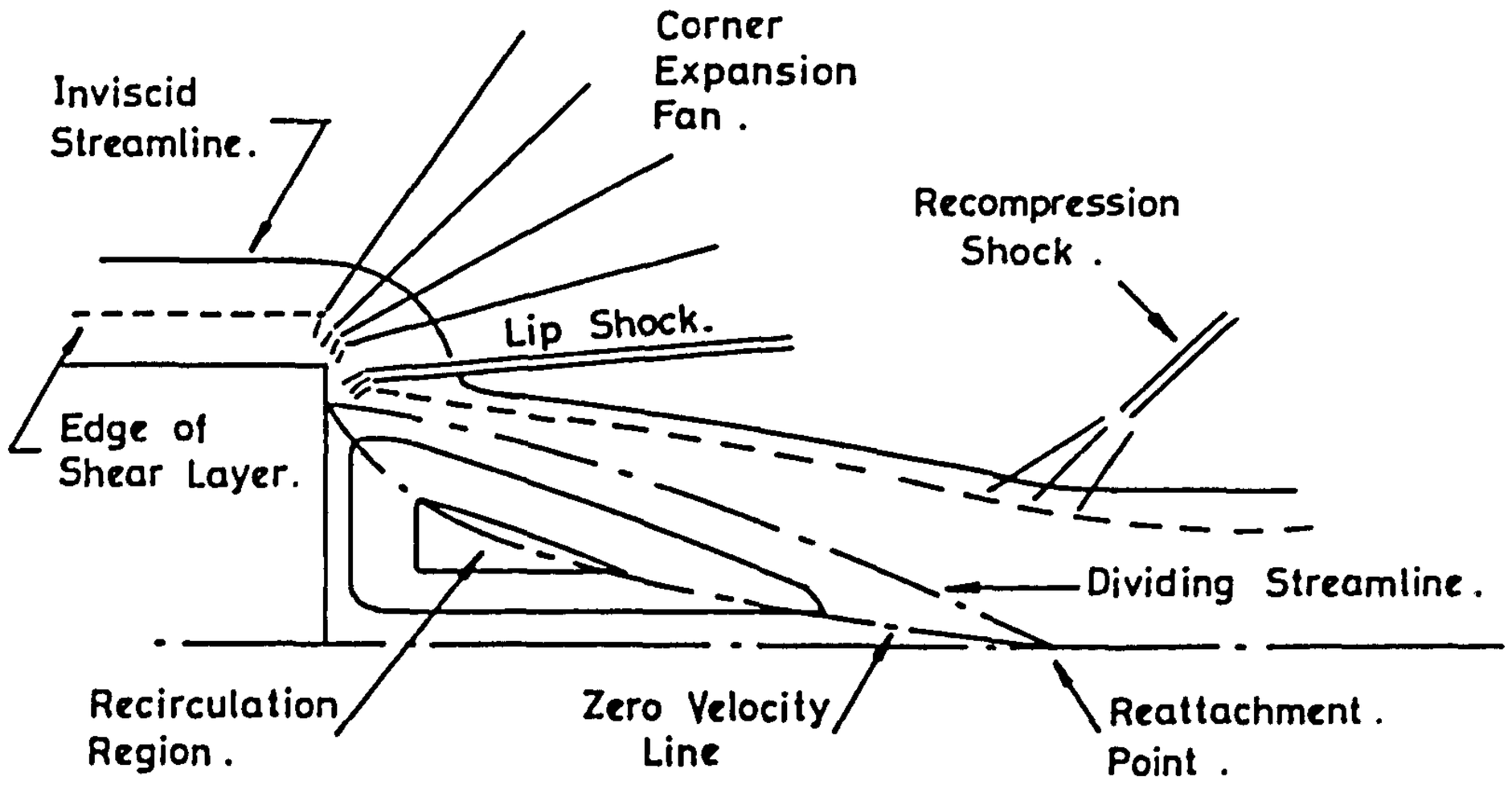

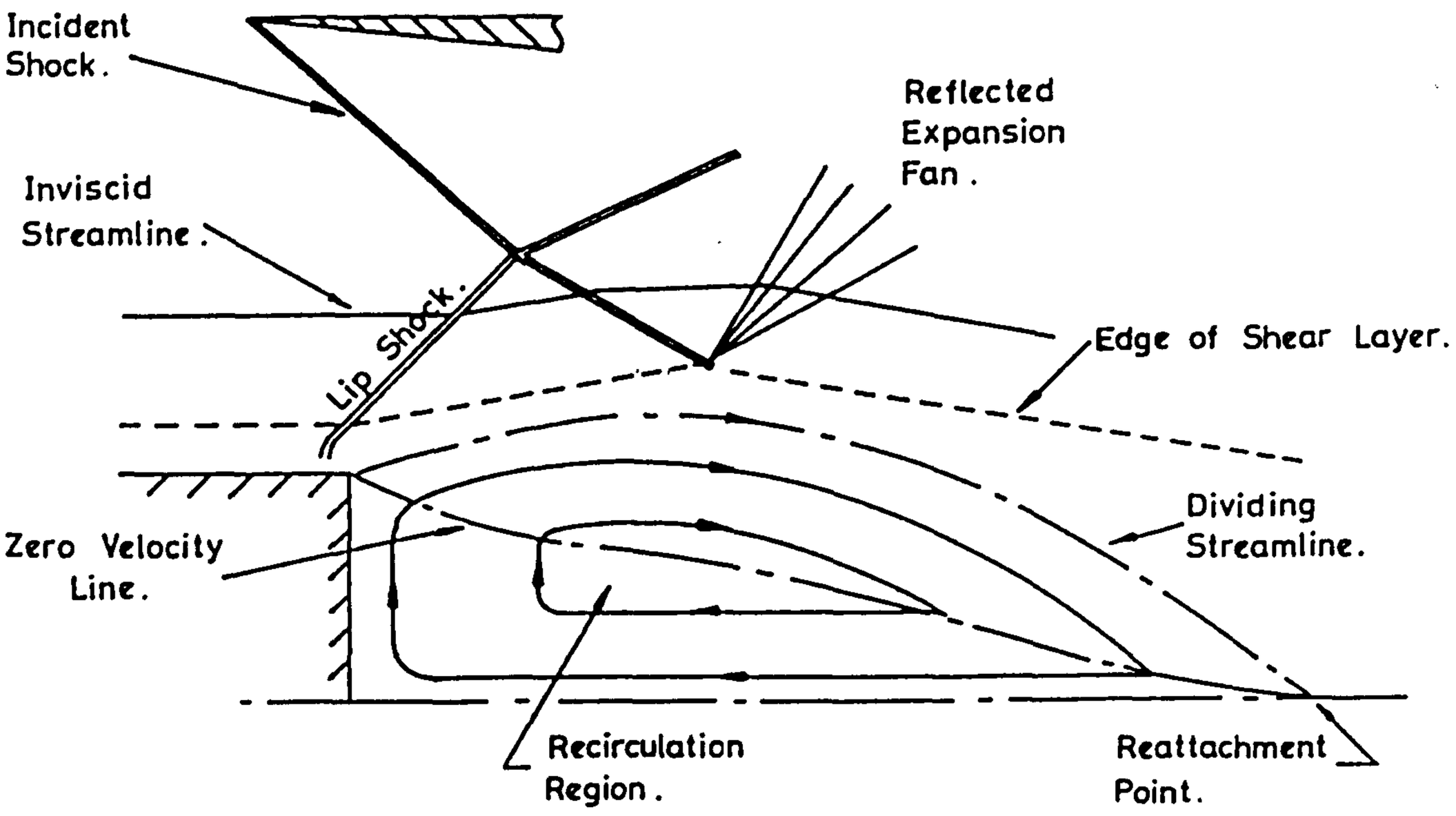

Fig. 5-2 Streamline sketch of compressed base flow

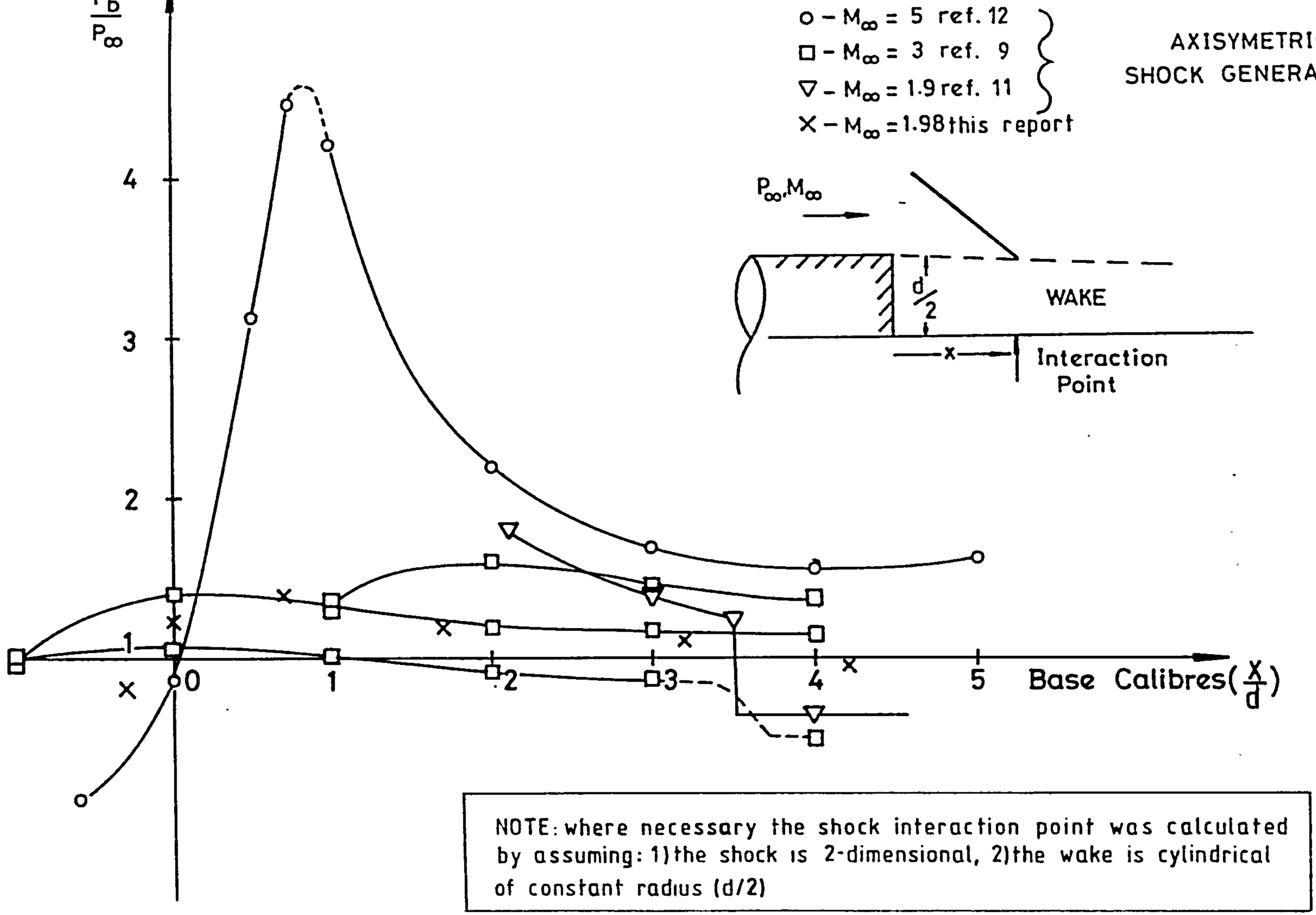

NOTE: where necessary the shock interaction point was calculated by assuming: 1) the shock is 2-dimensional, 2) the wake is cylindrical of constant radius (d/2)

Fig.5.3 Base Pressure Ratio vs Shock Interaction Distance (X/d).

[Where necessary P_∞ was calculated as $P_o \left(1 + \frac{\gamma-1}{2} M\right)^{\frac{-\gamma}{\gamma-1}}$]

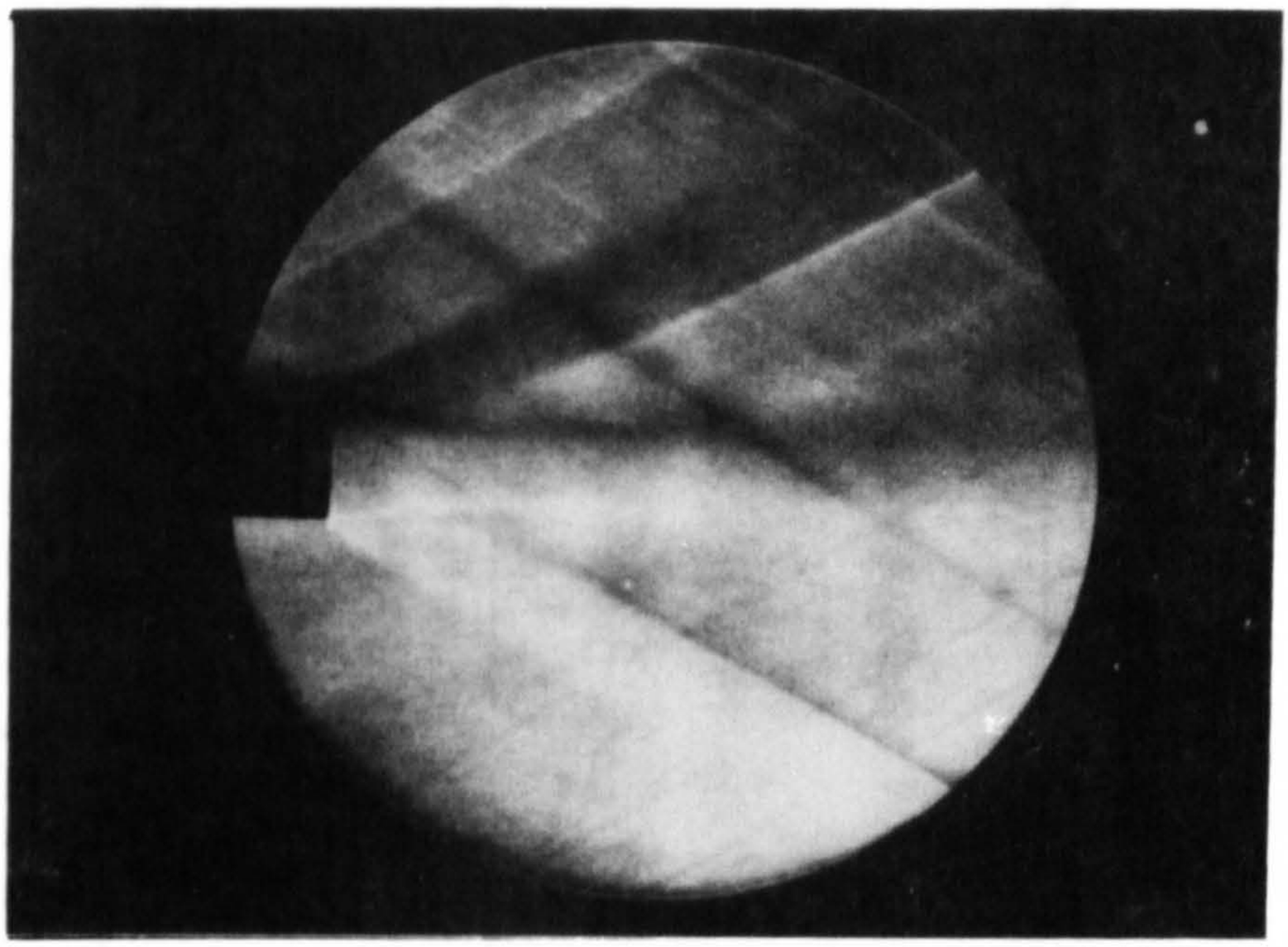

Fig. 5.4 Undisturbed Wake, $Re_d = 2.4 \times 10^5$, 10 ms exposure

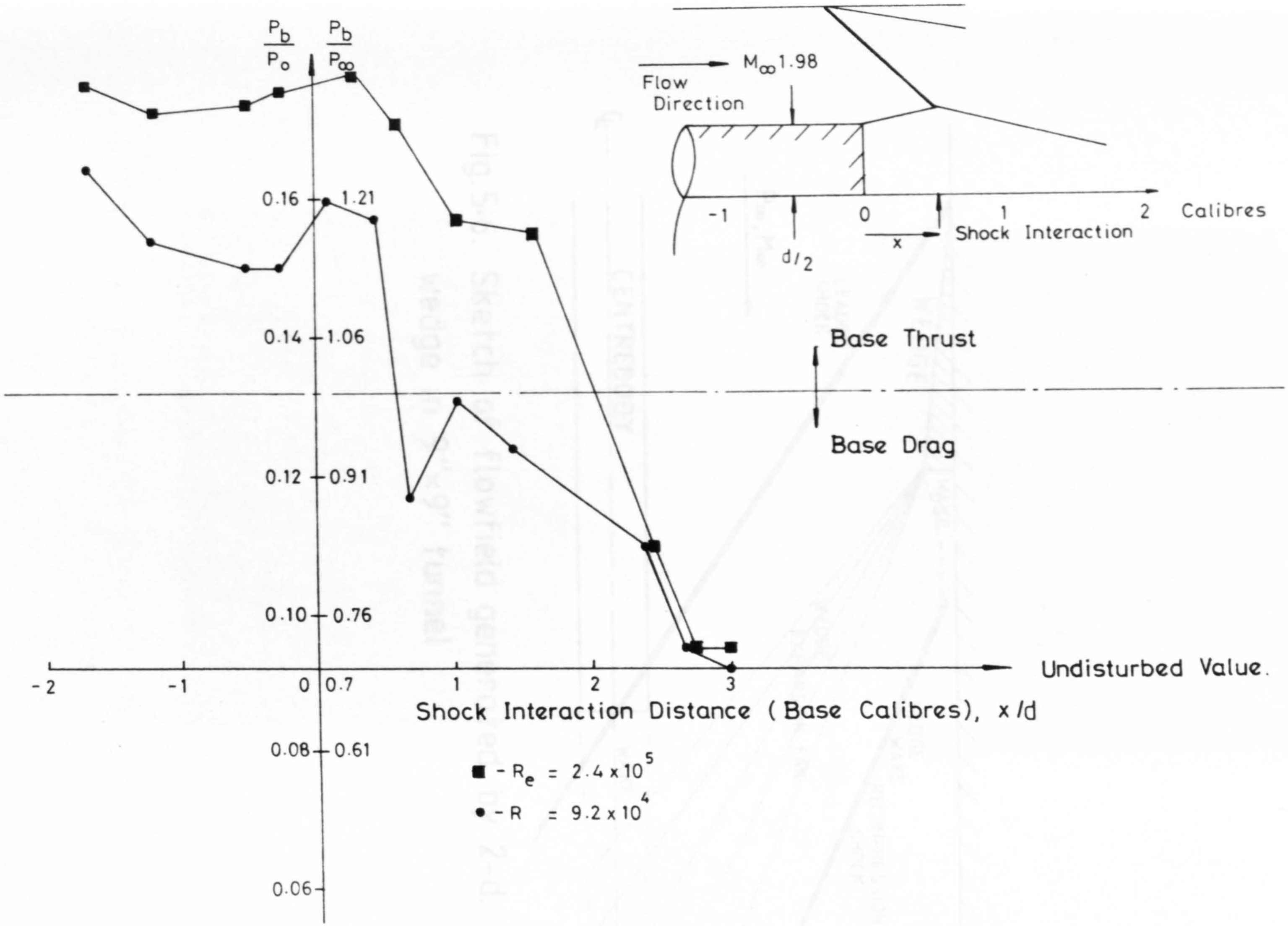

Fig. 5.5:
Base Pressure Ratio vs Shock Interaction Distance for 2-D Planar Shock Generators.

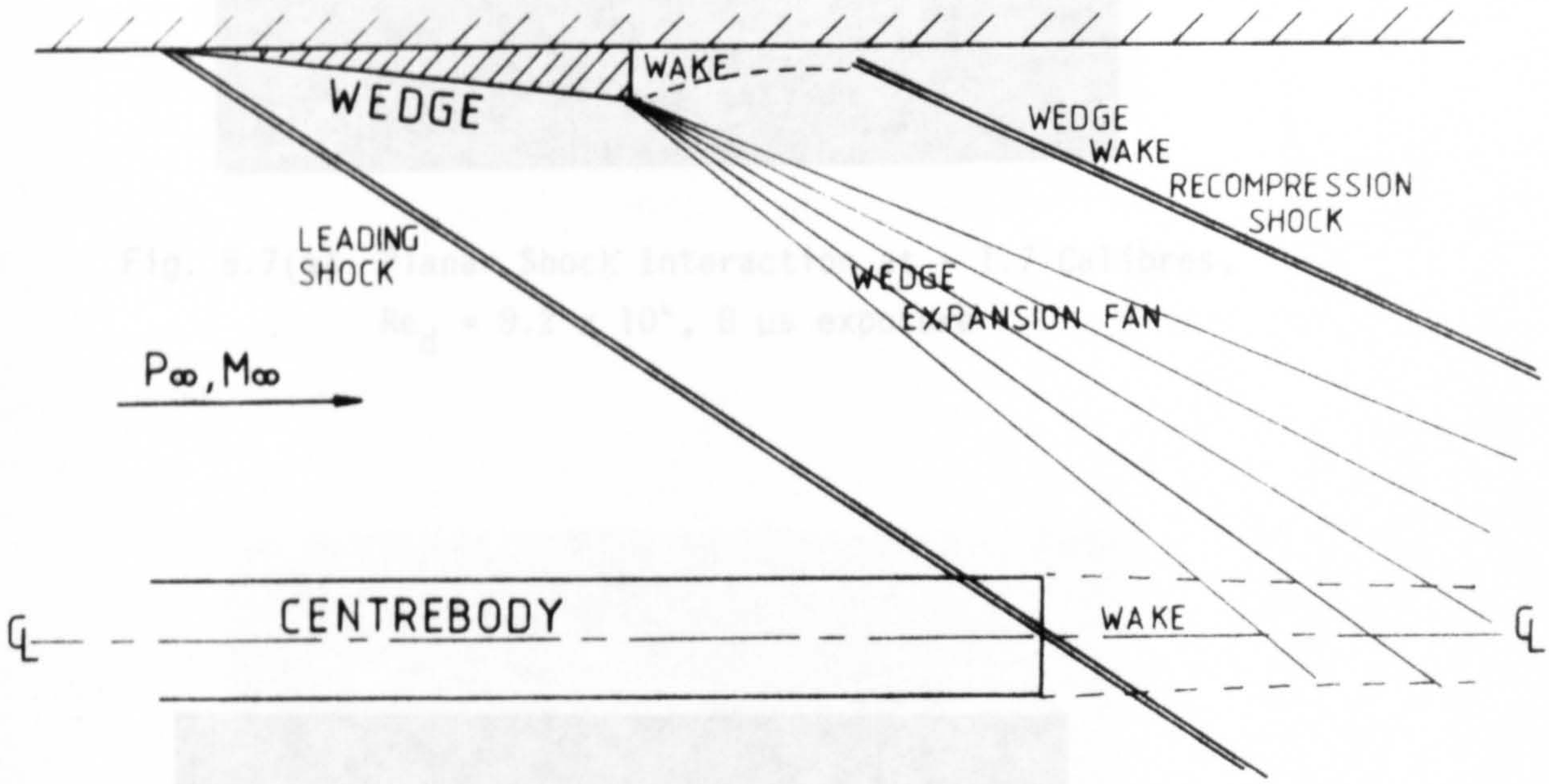

Fig. 5.6. Sketch of flowfield generated by 2-d. wedge in 9"×9" tunnel

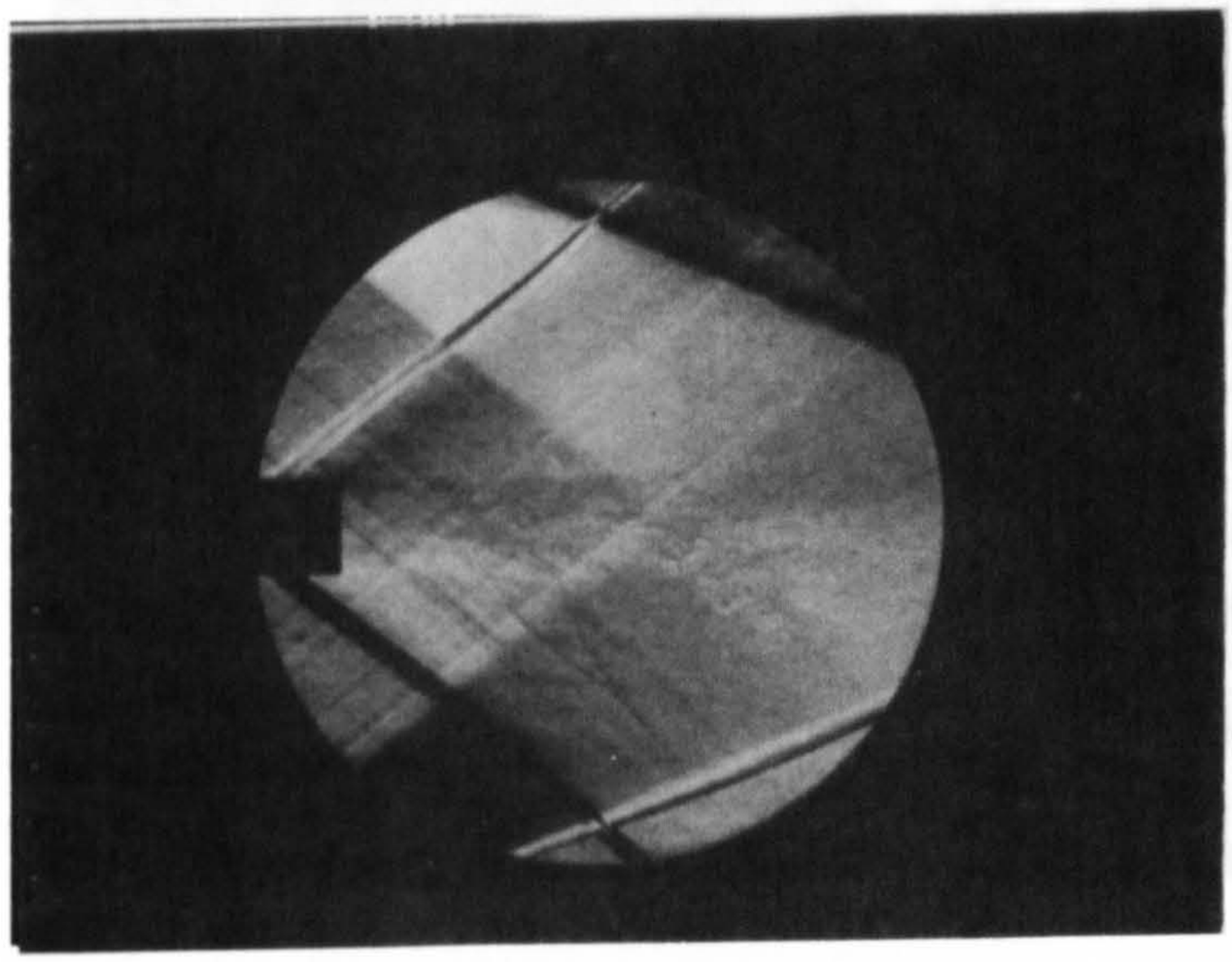

Fig. 5.7(a) Planar Shock Interaction at - 1.7 Calibres,
$Re_d = 9.2 \times 10^4$, 8 μs exposure

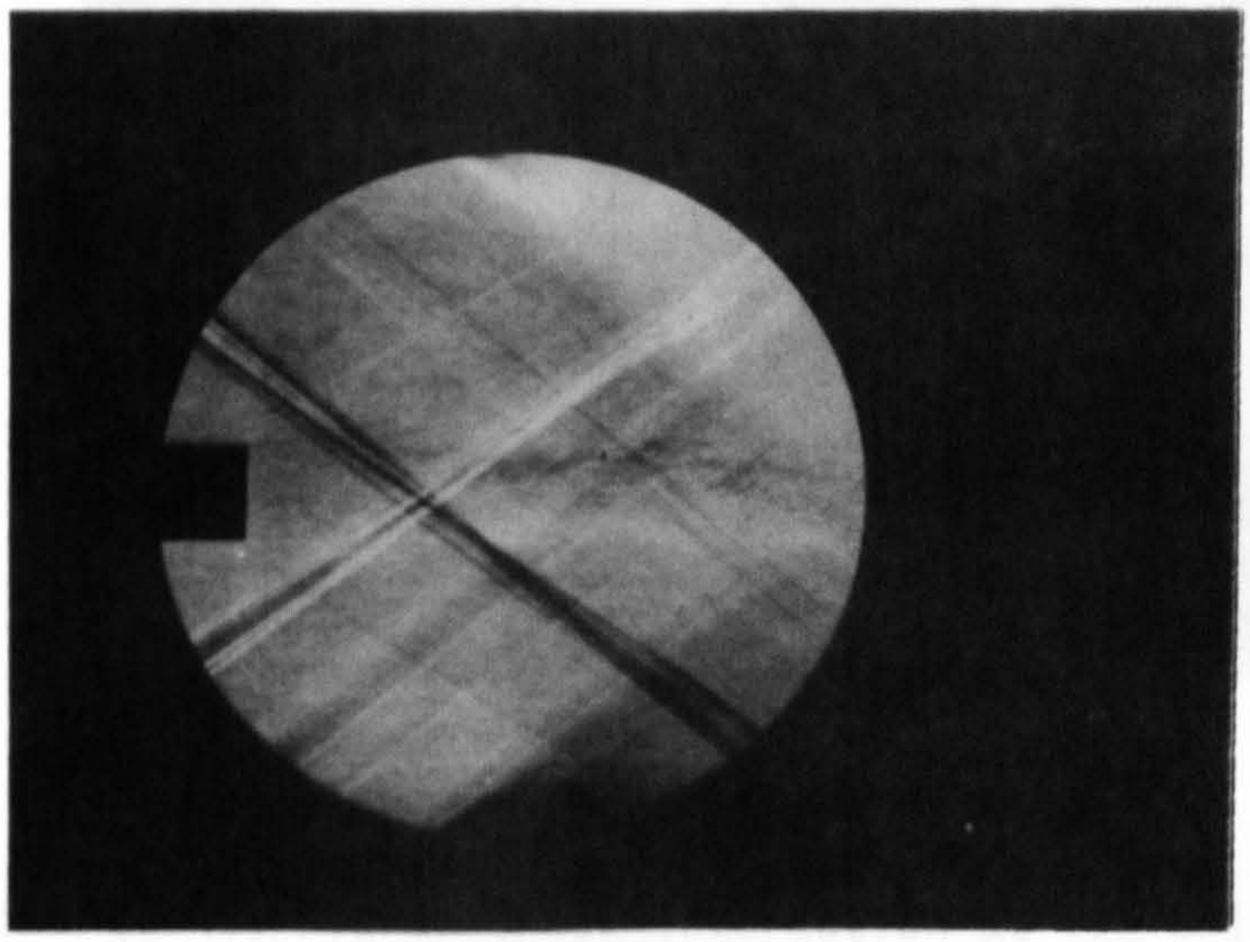

Fig. 5.7(b) Planar Shock Interaction at 1 Calibre,
$Re_d = 9.2 \times 10^4$, 8 μs exposure

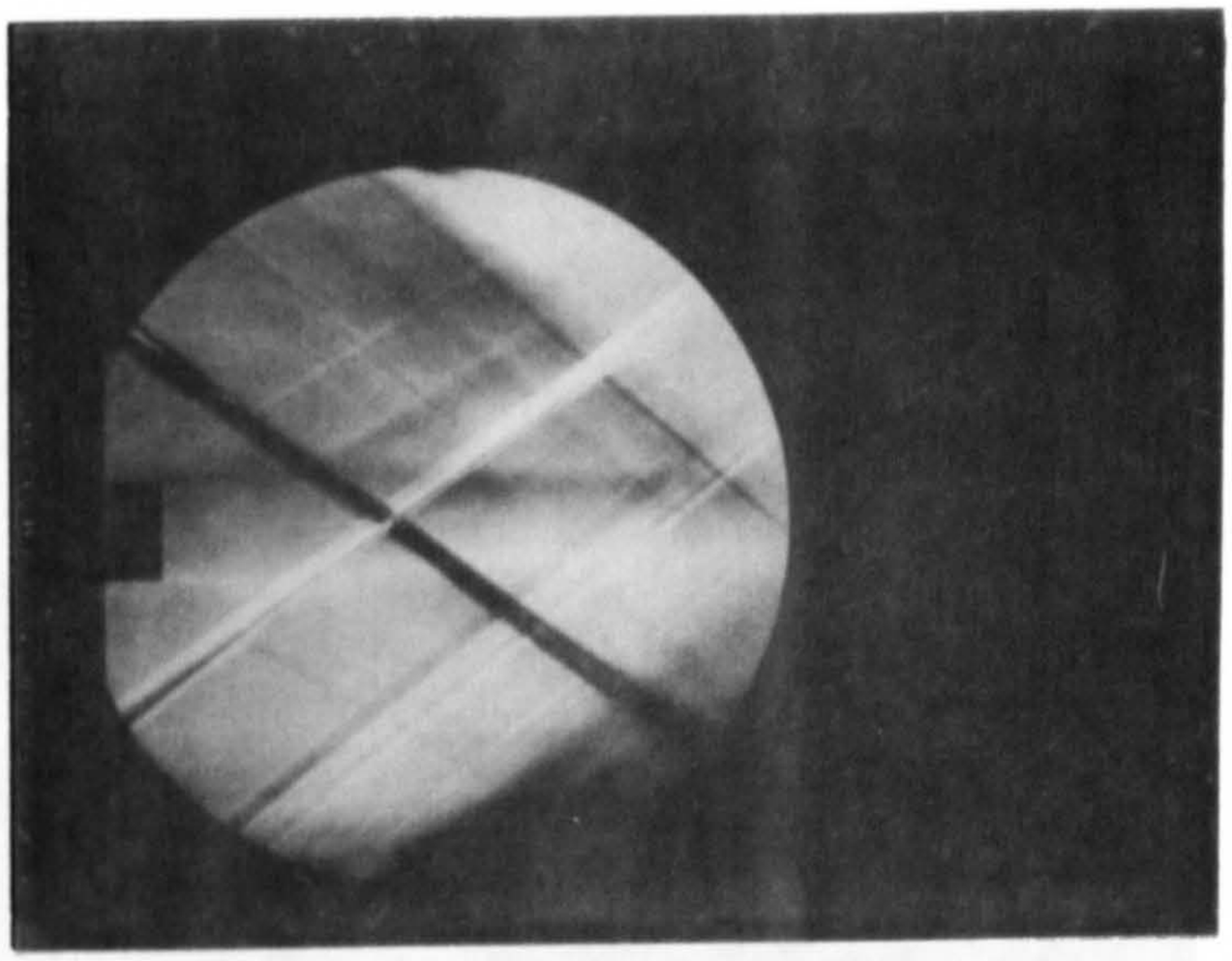

(c) $Re_d = 2.4 \times 10^5$, 10 ms exposure

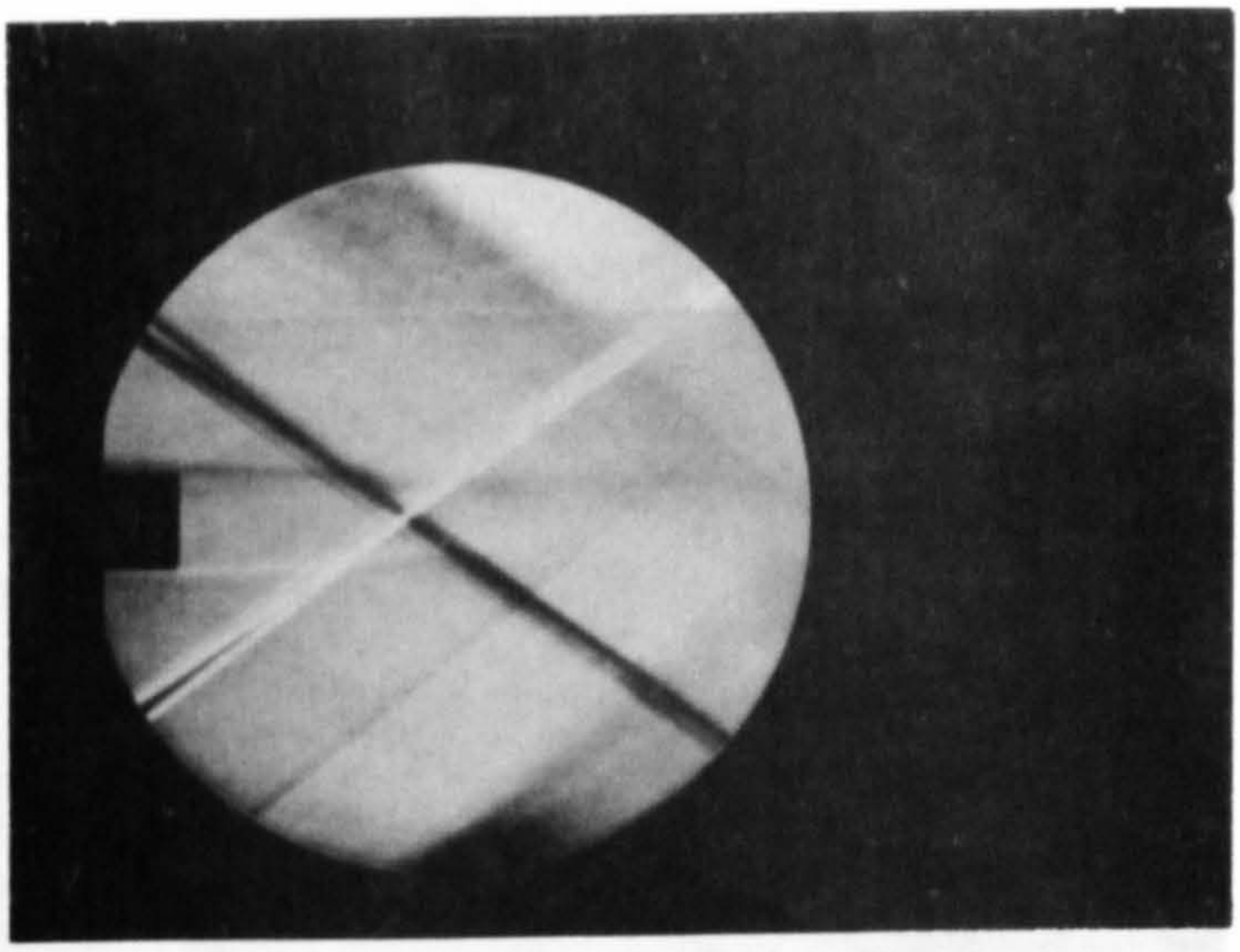

(d) $Re_d = 9.2 \times 10^4$, 10 ms exposure

Fig. 5.7 (Cont) Planar Shock Interaction at 1.5 Calibres

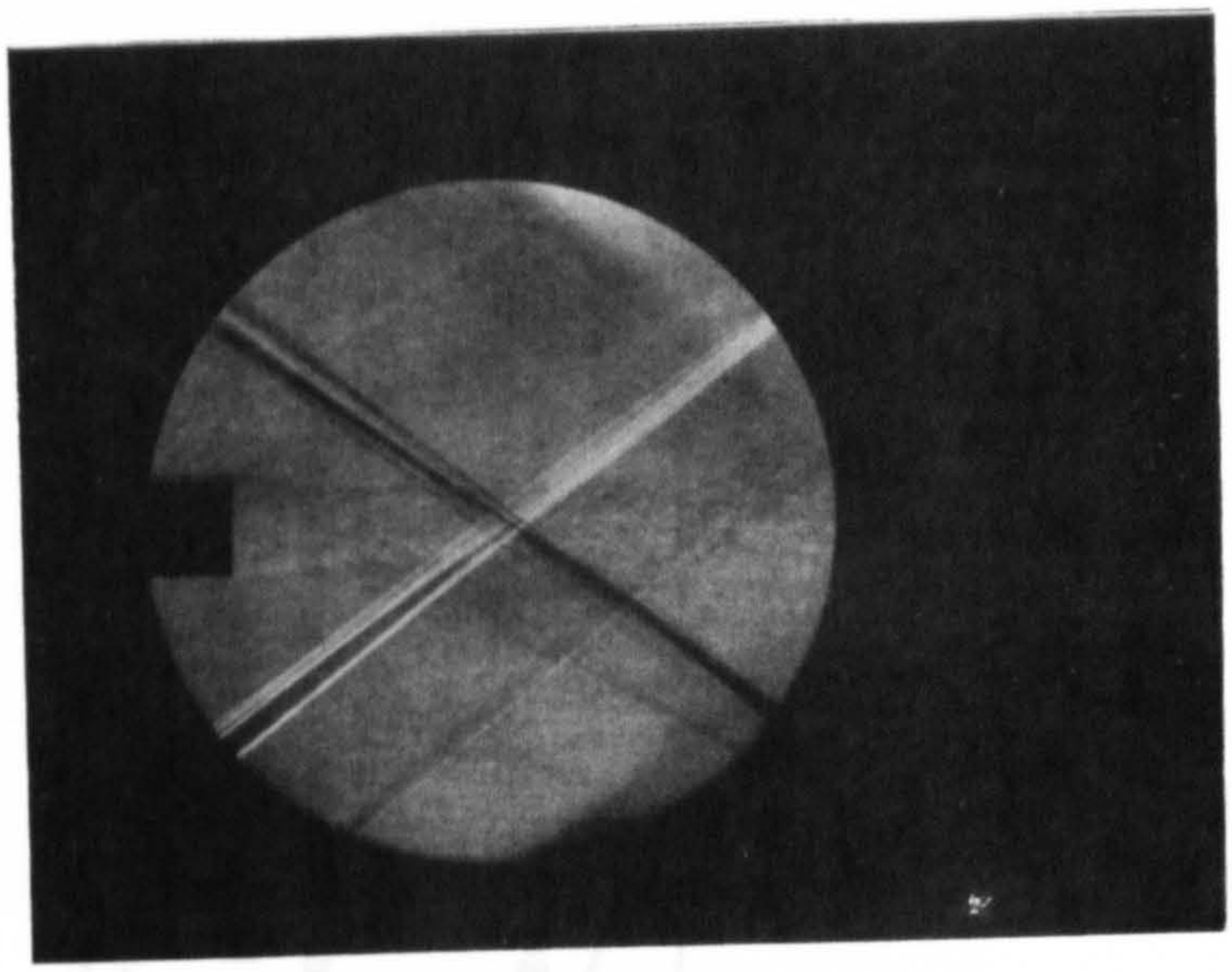

(e) 8 μs exposure

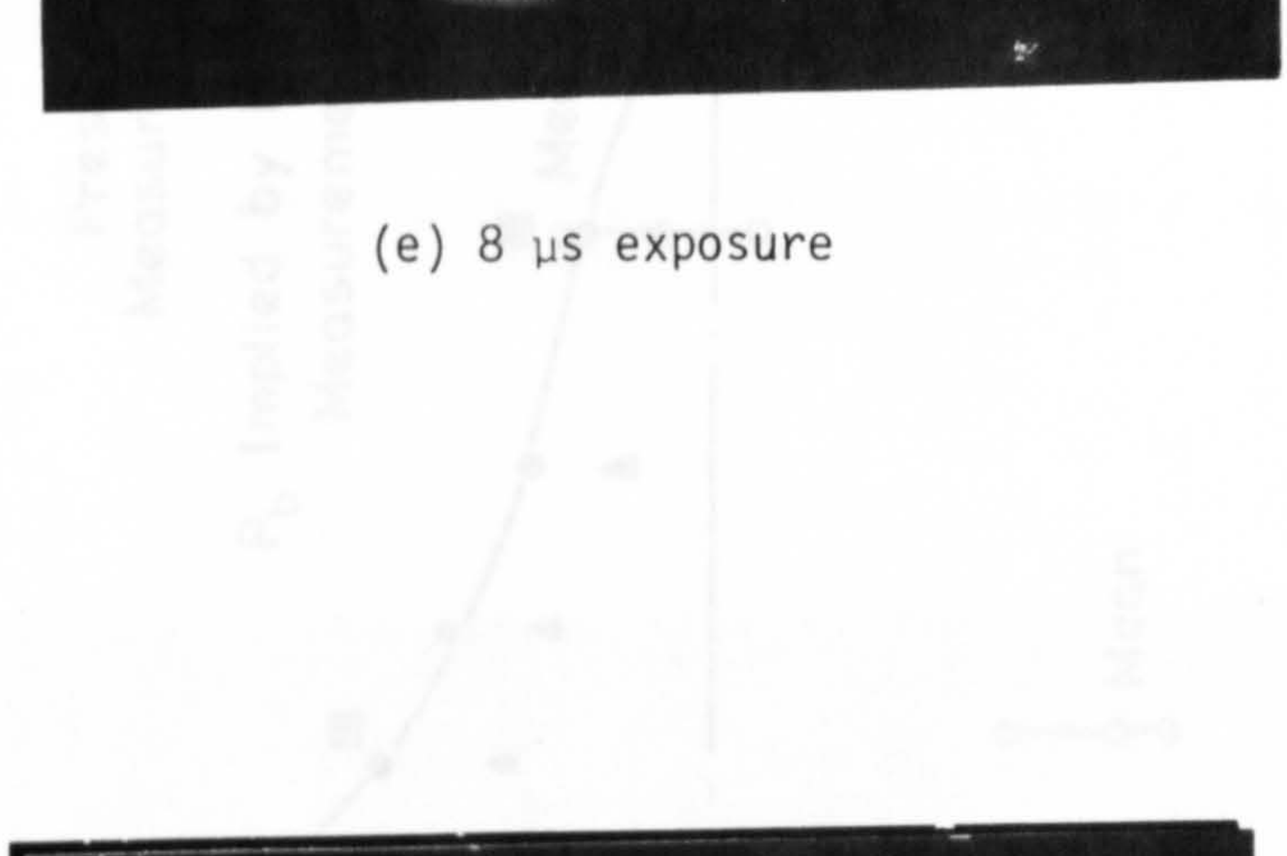

(f) 10 ms exposure

Fig. 5.7 (cont) Planar Shock Interaction at 2.5 Calibres

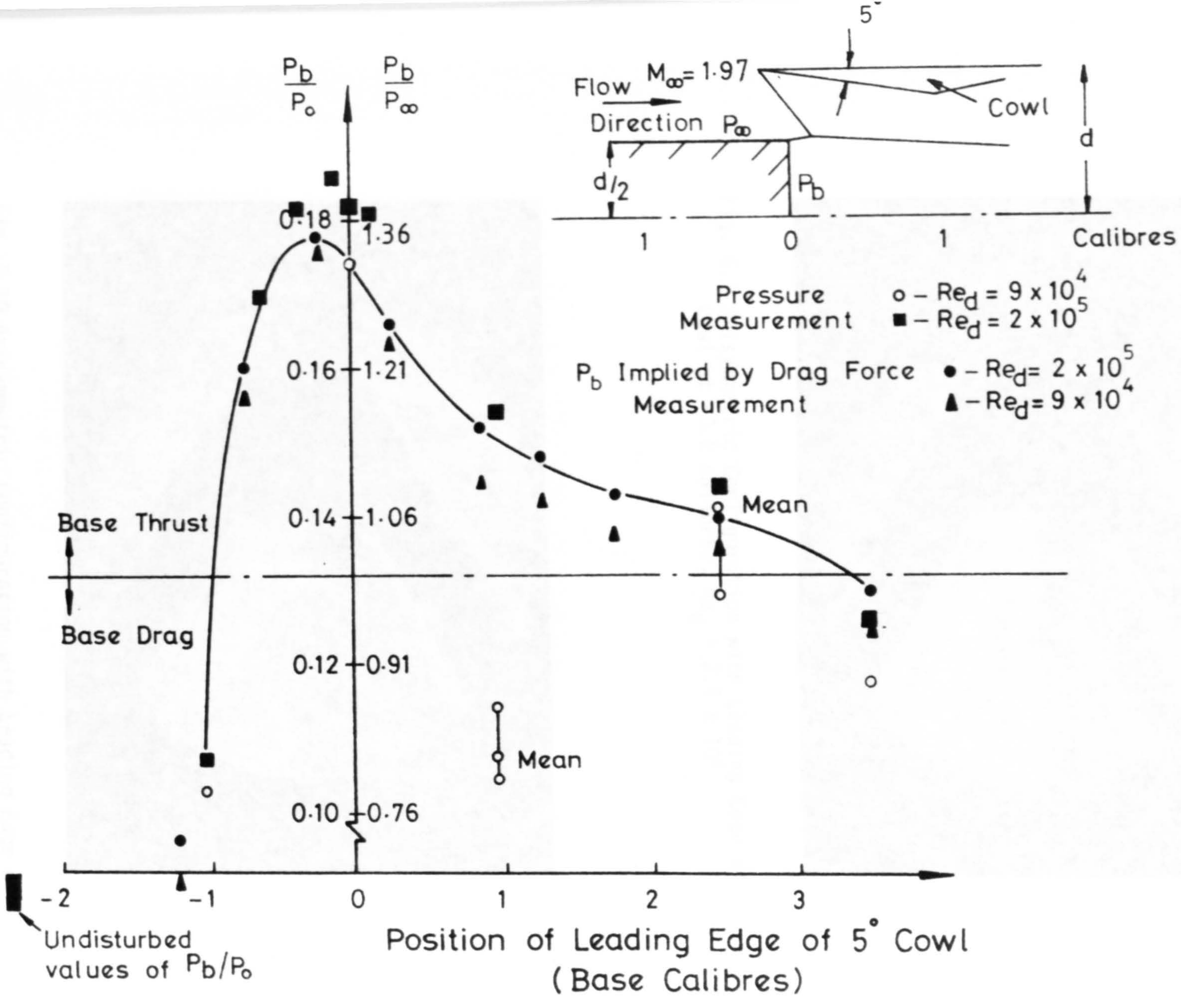

Figure 5·8. Base pressure ratio vs shock interaction distance (axisymmetric cowl)

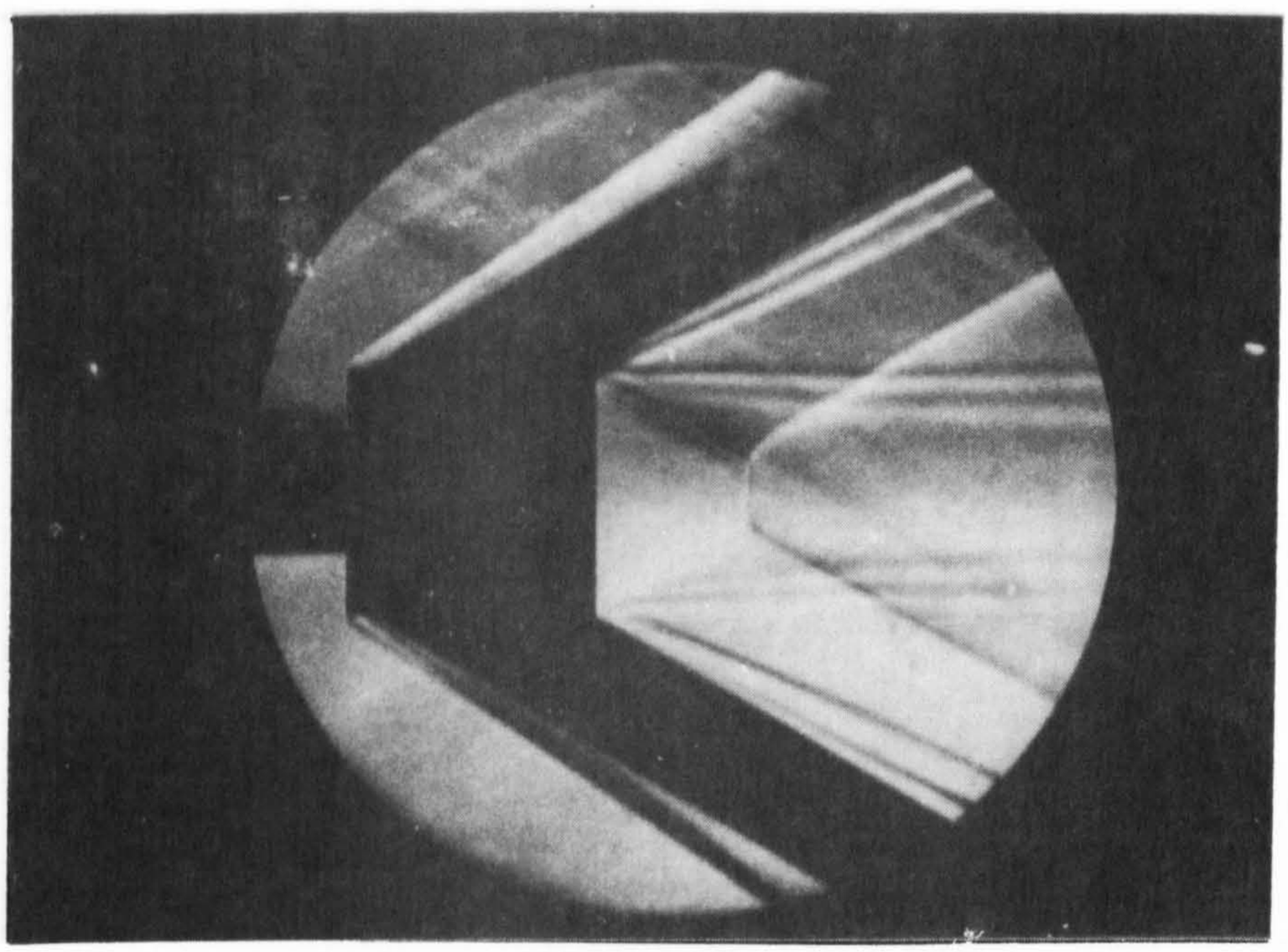

Fig. 5.9 Axisymmetric Configuration with Leading Edge of Cowl at -0.2 calibres, $Re_d = 2.4 \times 10^5$

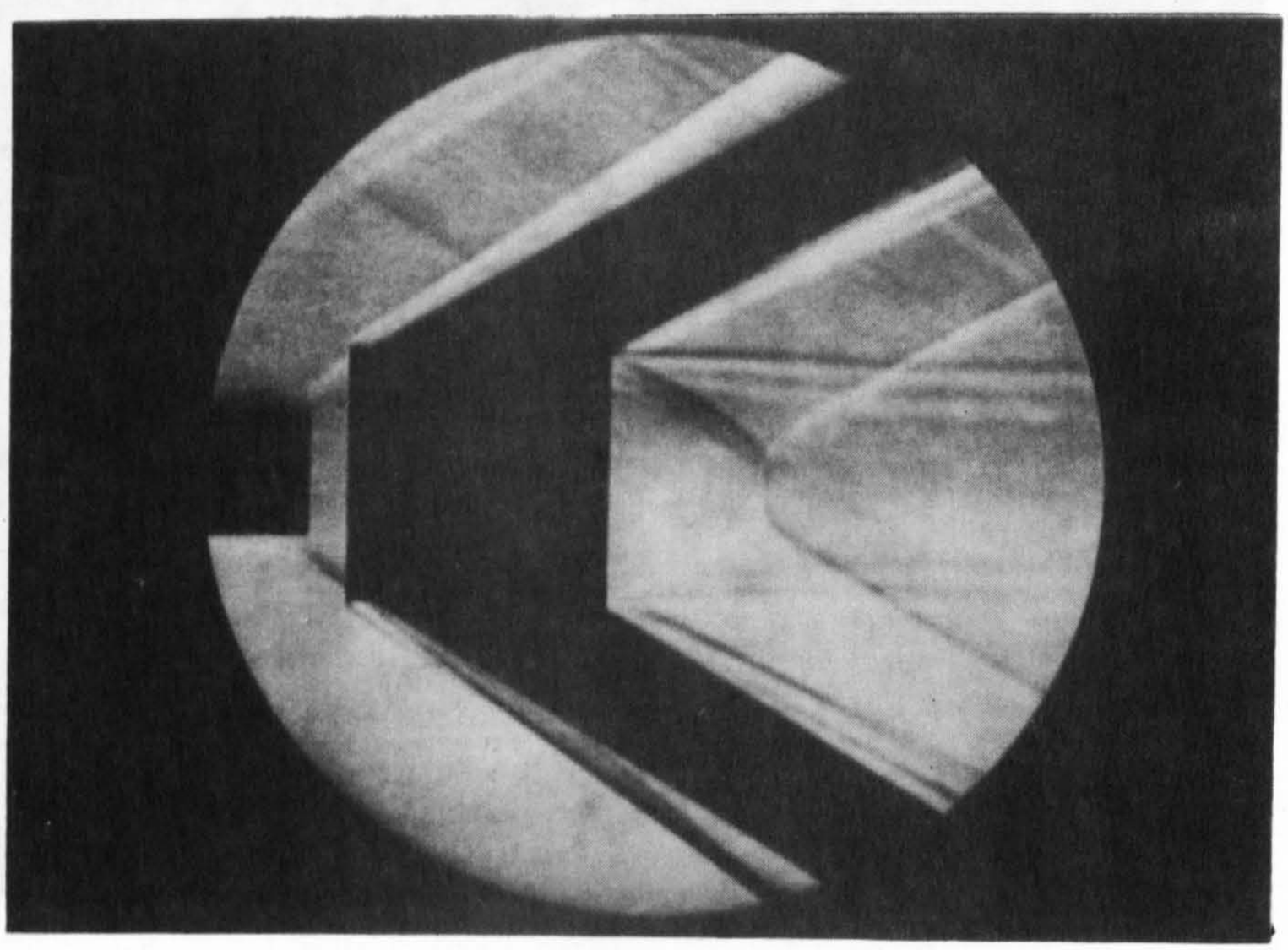

Fig. 5.10 Axisymmetric Configuration with Leading Edge of Cowl at 0.3 calibres, $Re_d = 2.4 \times 10^5$

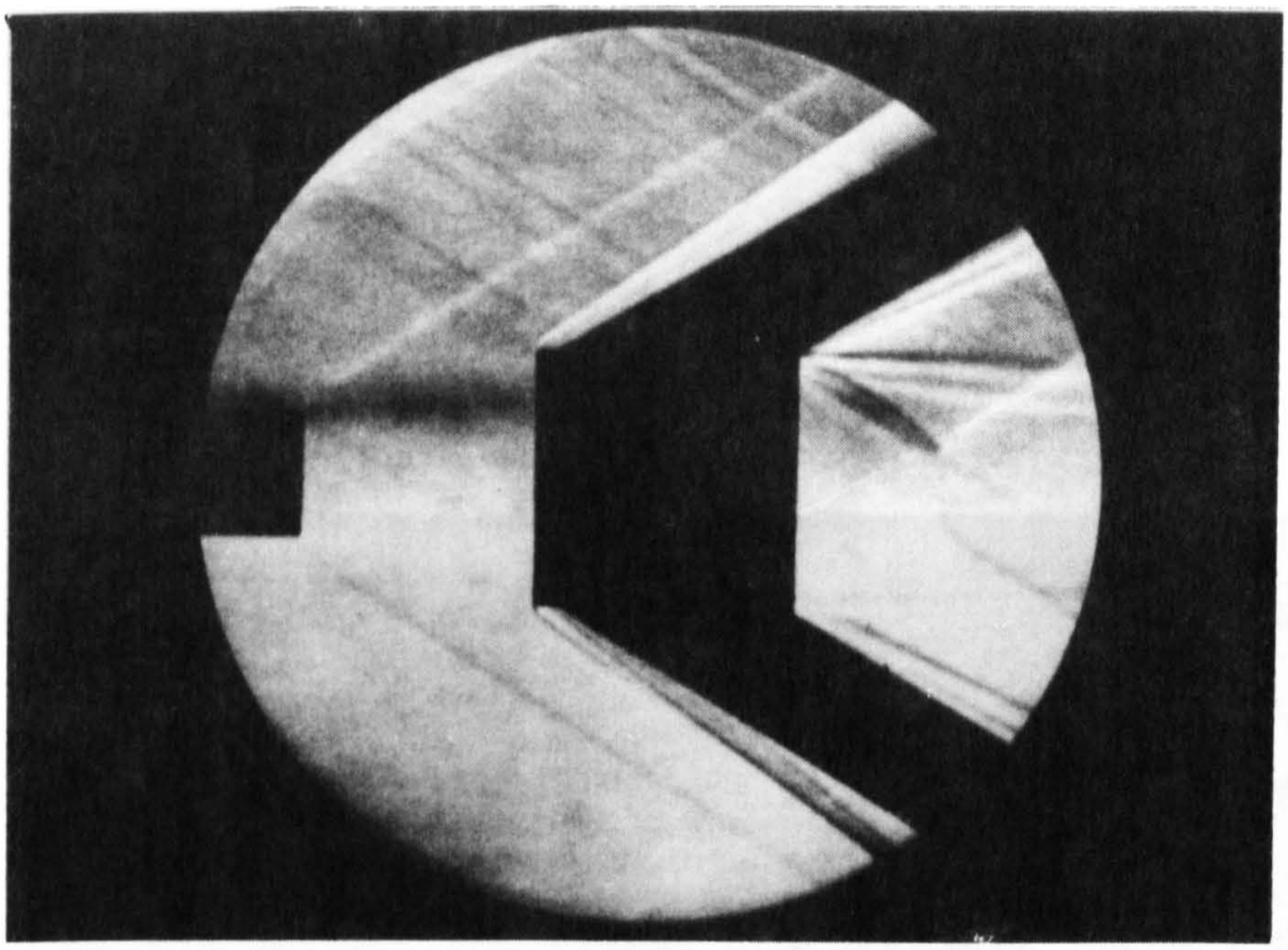

Fig. 5.11 Axisymmetric Configuration with Leading Edge of Cowl at 1.8 calibres, $Re_d = 2.4 \times 10^5$

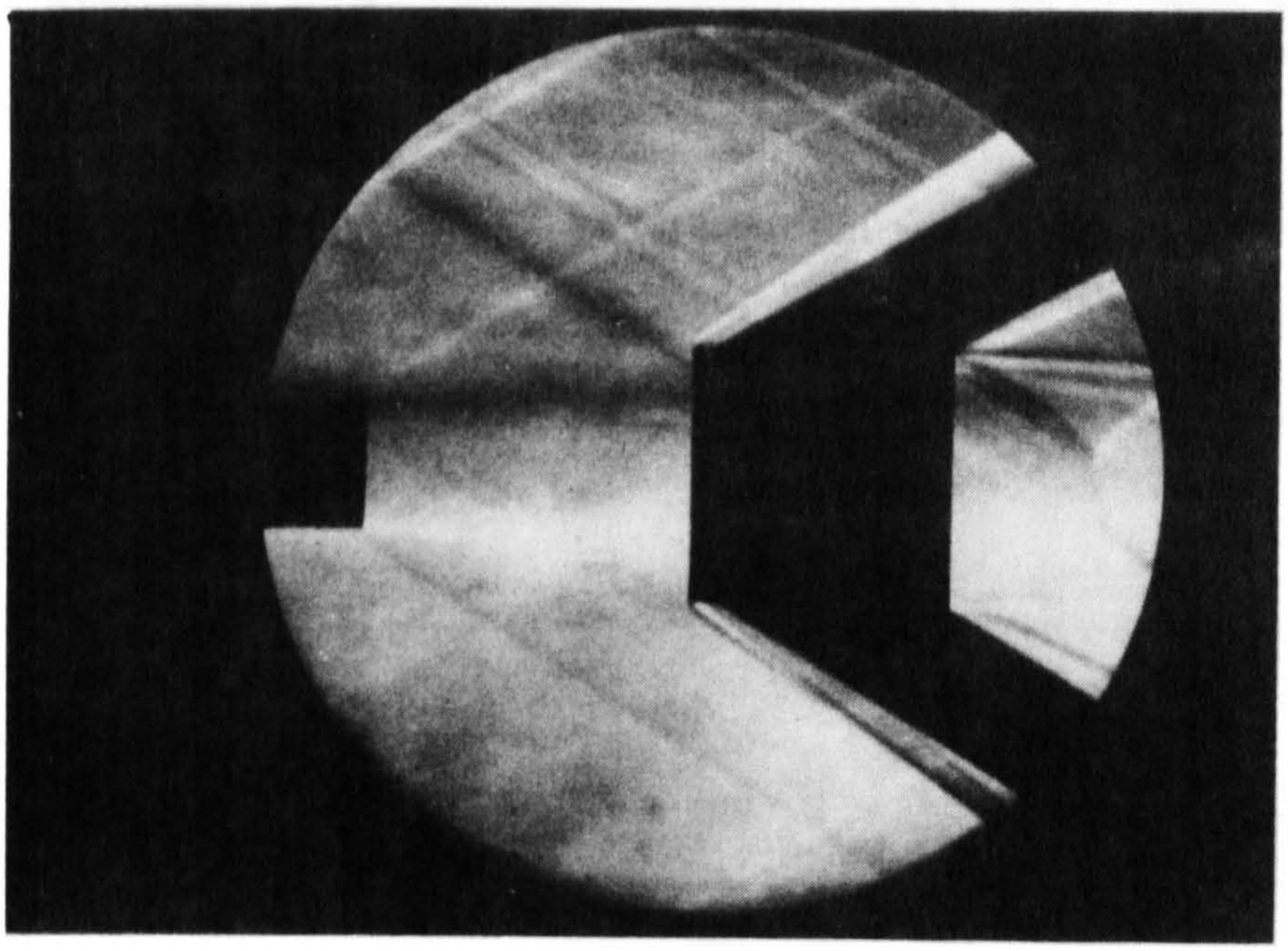

Fig. 5.12 Axisymmetric Configuration with Leading Edge of Cowl at 2.5 calibres, $Re_d = 2.4 \times 10^5$

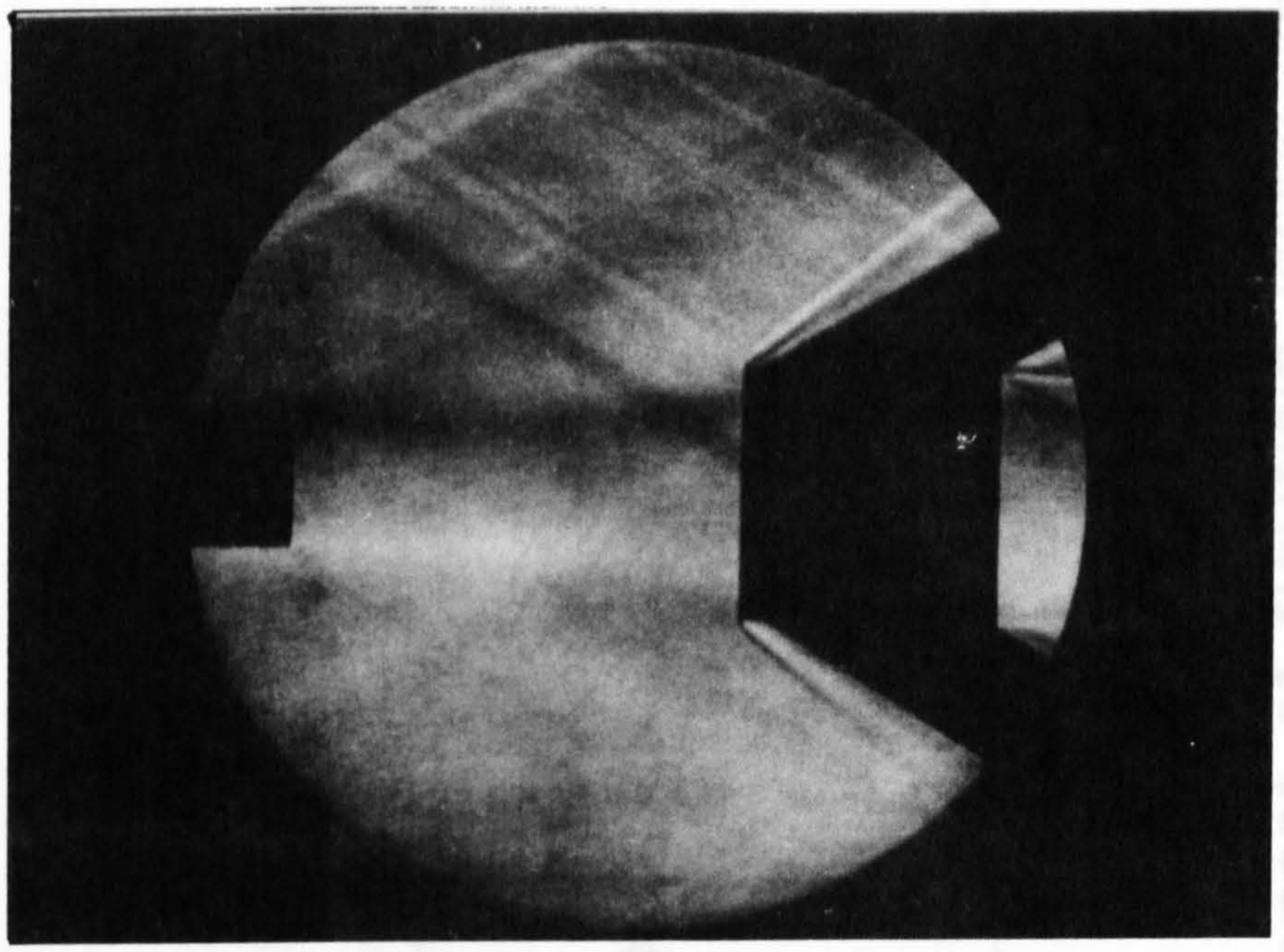

Fig. 5.13 Axisymmetric Configuration with Leading Edge of Cowl at 3.5 Calibres, $Re_d = 2.4 \times 10^5$

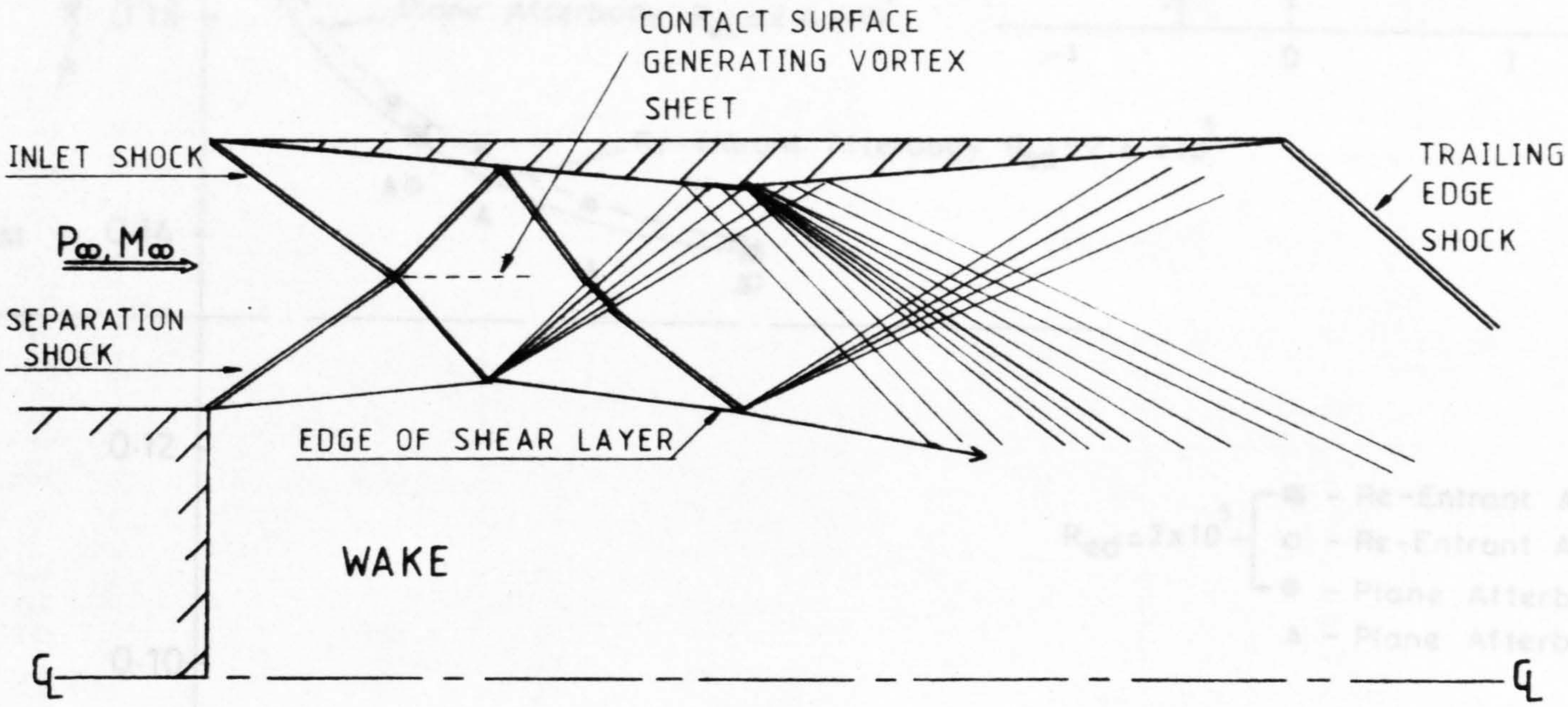

Fig. 5.14. Sketch of development of flowfield inside cowl

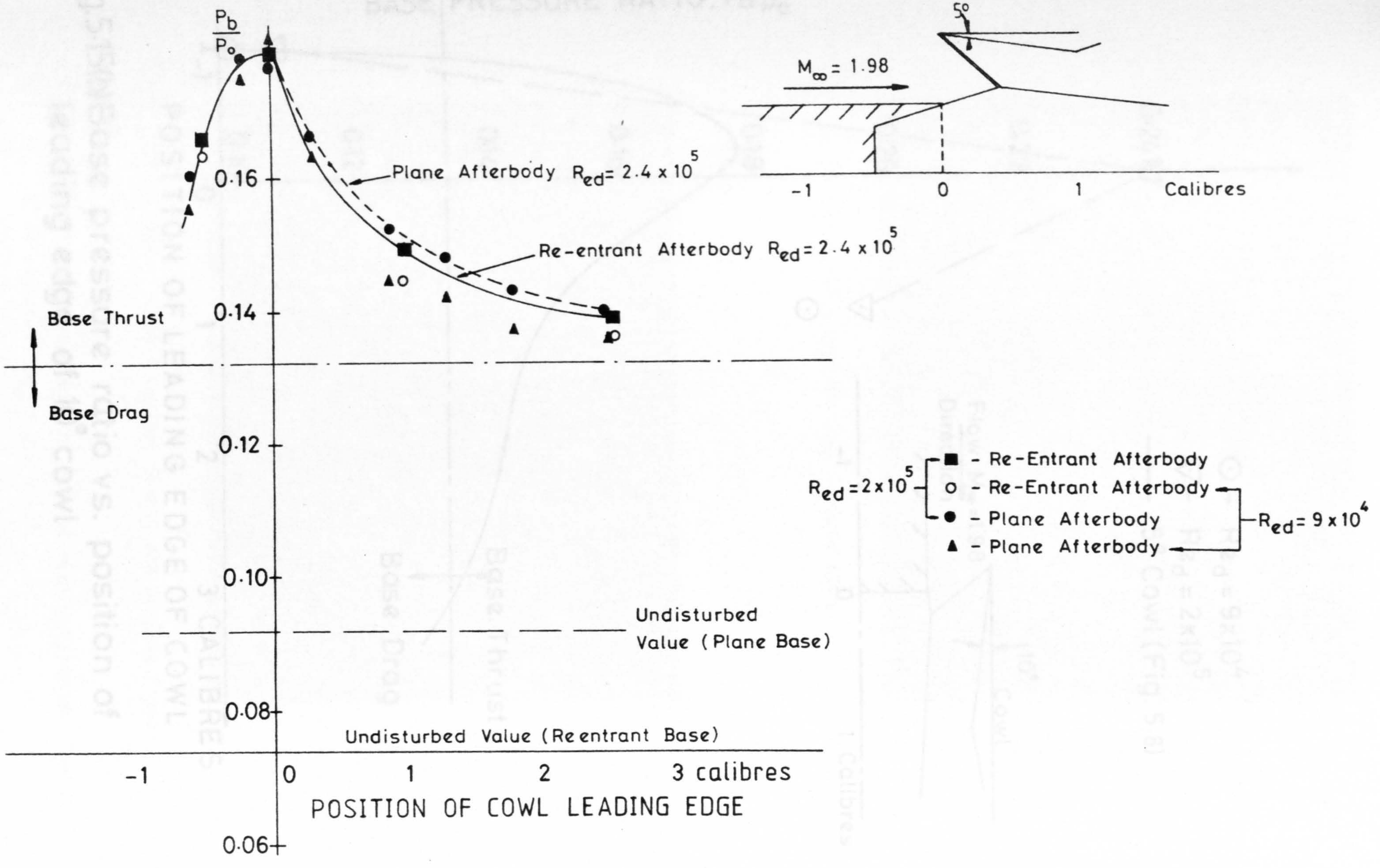

Fig. 5·15(a). Base pressure ratio vs. cowl position (5°cowl, recessed base)

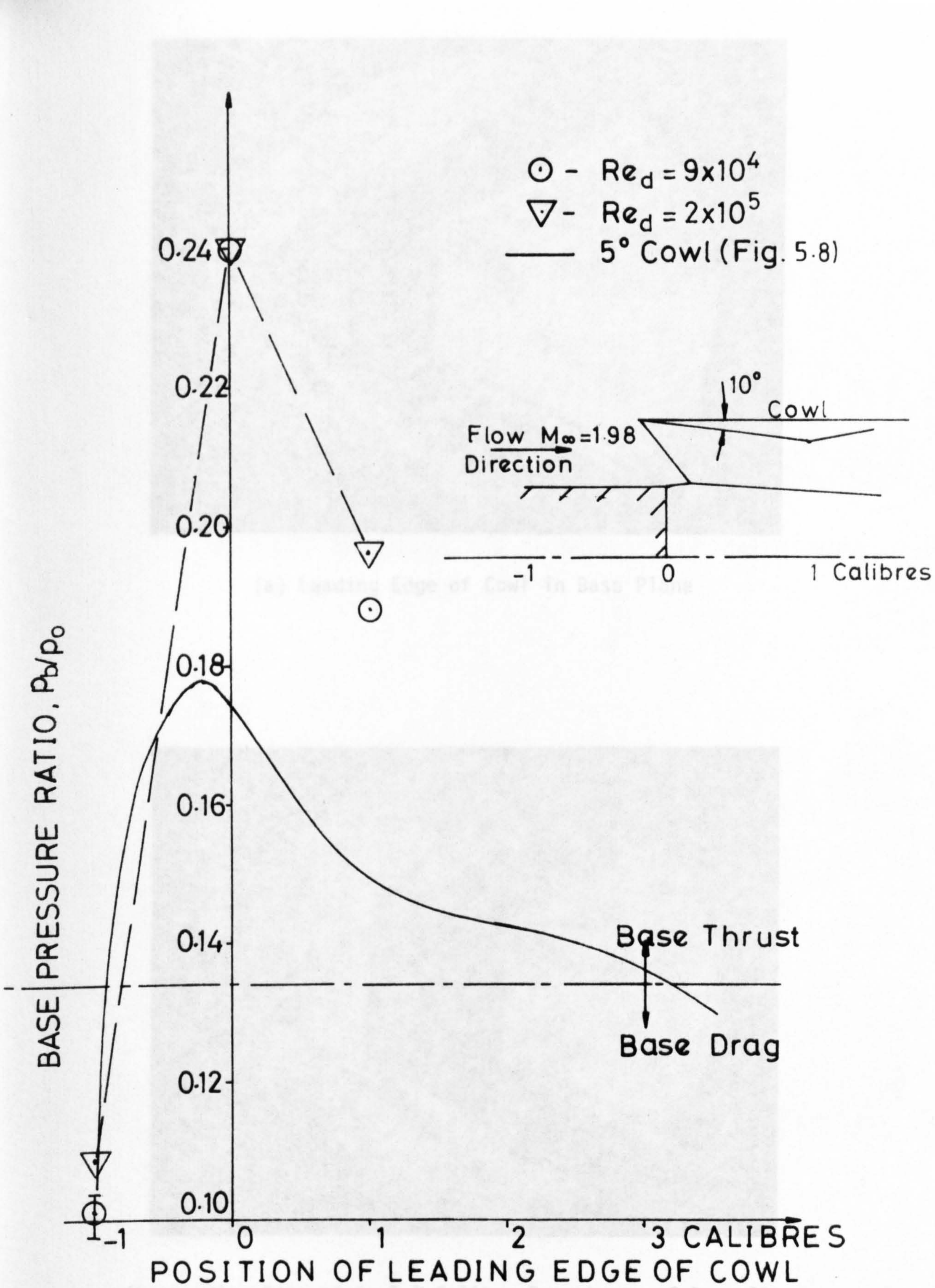

Fig.5.15(b) Base pressure ratio vs. position of leading edge of 10° cowl

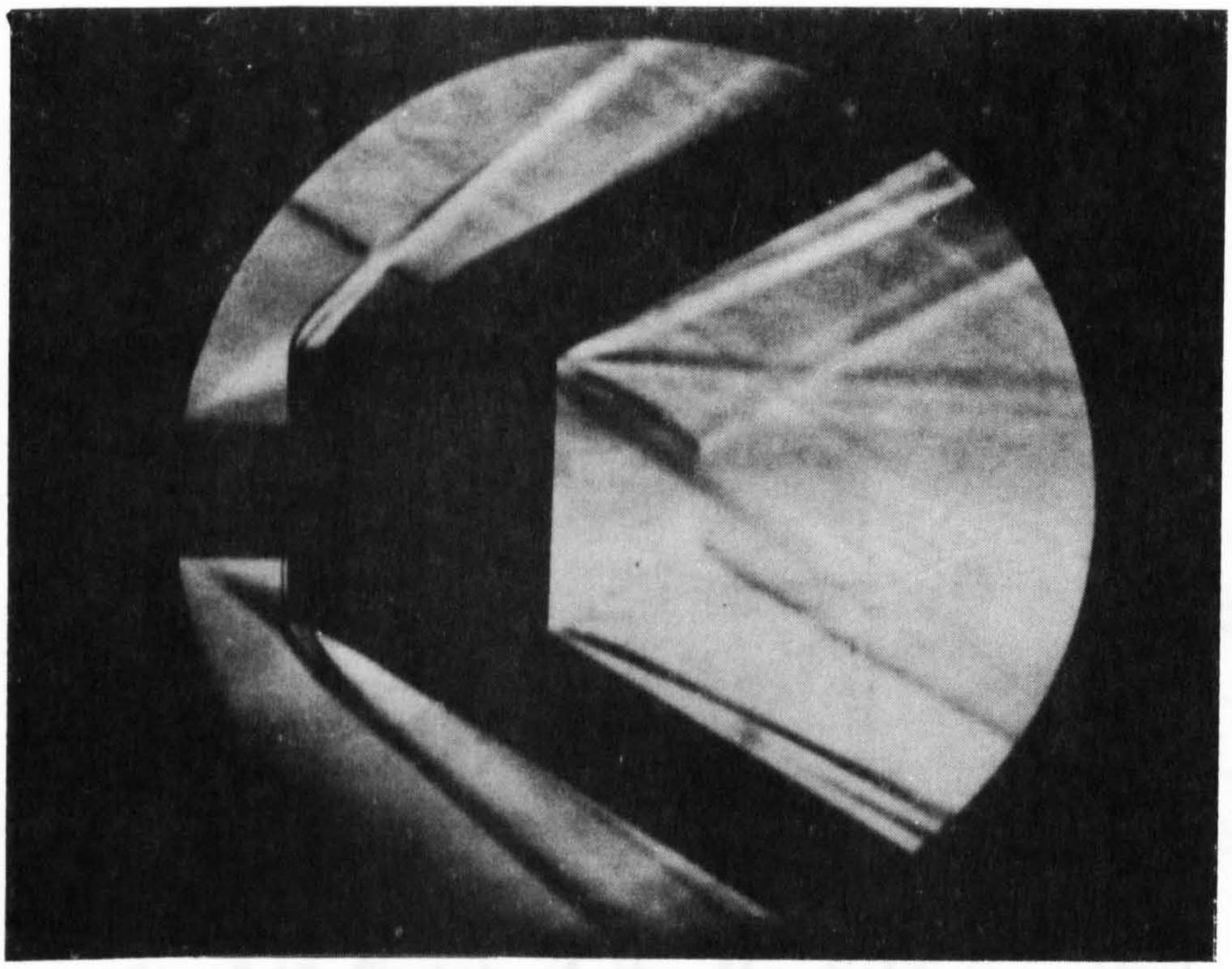

(a) Leading Edge of Cowl in Base Plane

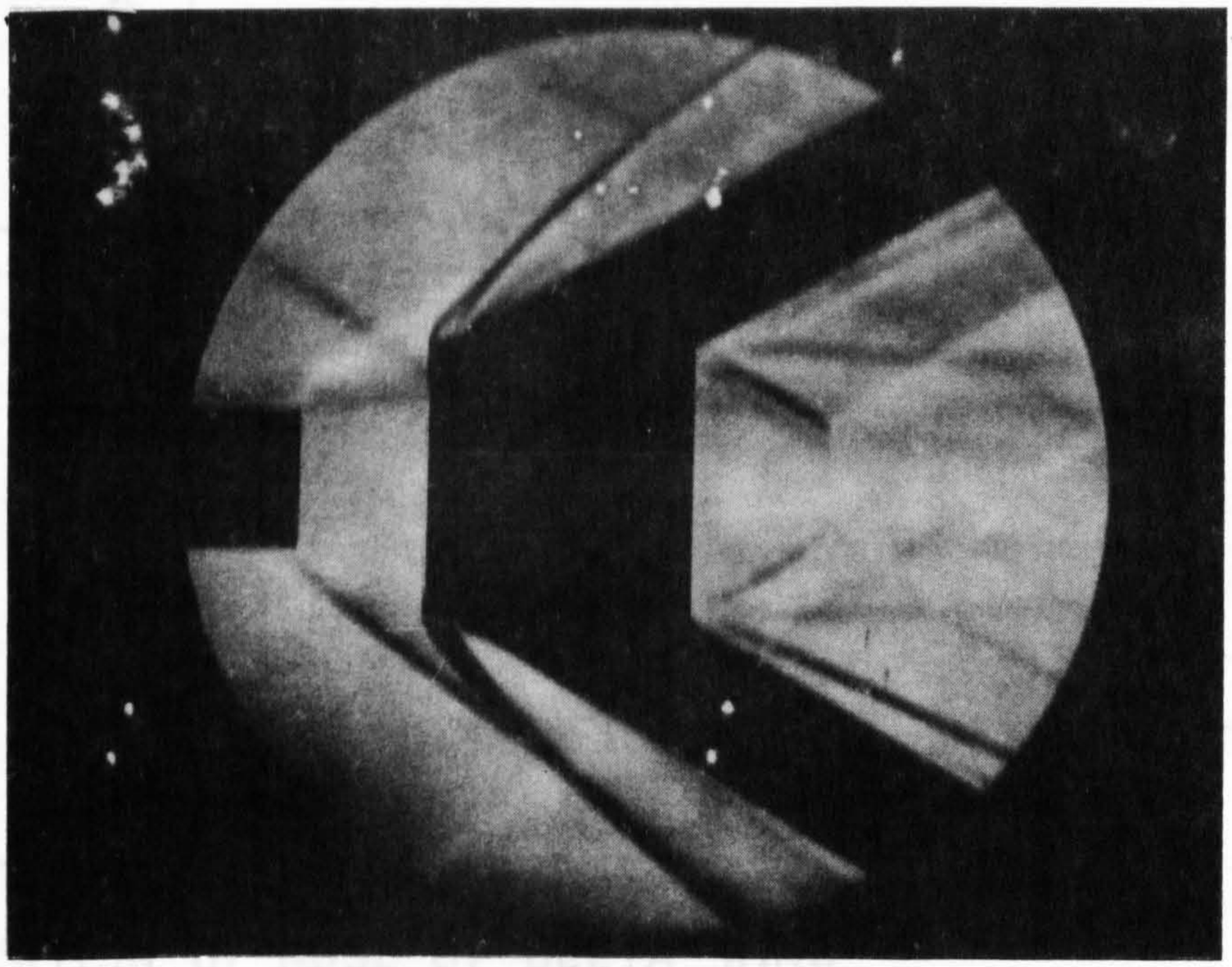

(b) Leading Edge of Cowl 1 Calibre Downstream of Base Plane

Fig. 5.16 Schlieren Photographs of 10^{o} Convergent-Divergent Cowl.
10 ms exposure. $Re_d = 2.4 \times 10^5$

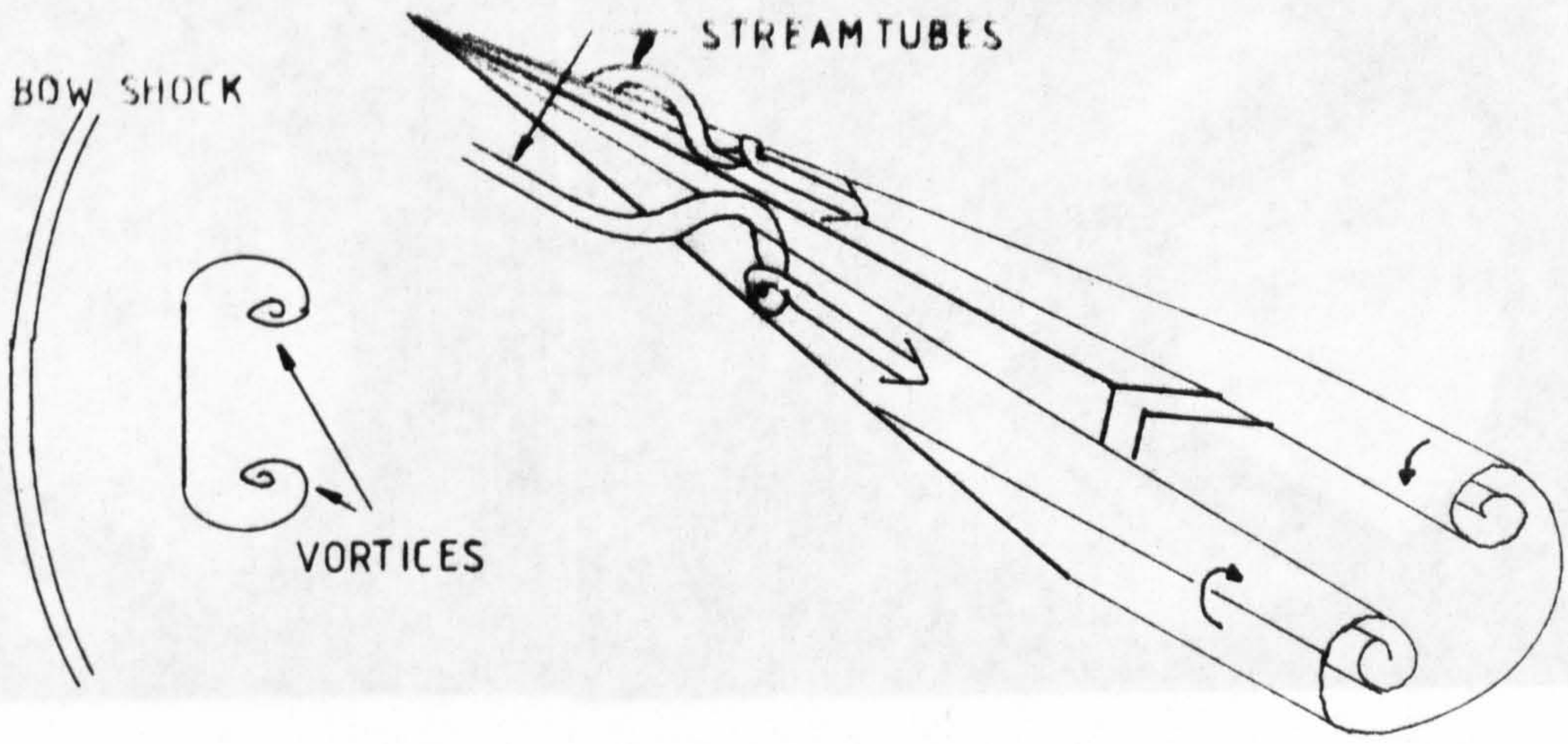

Fig. 5.17 Sketch of the flowfield over `delta´ wing

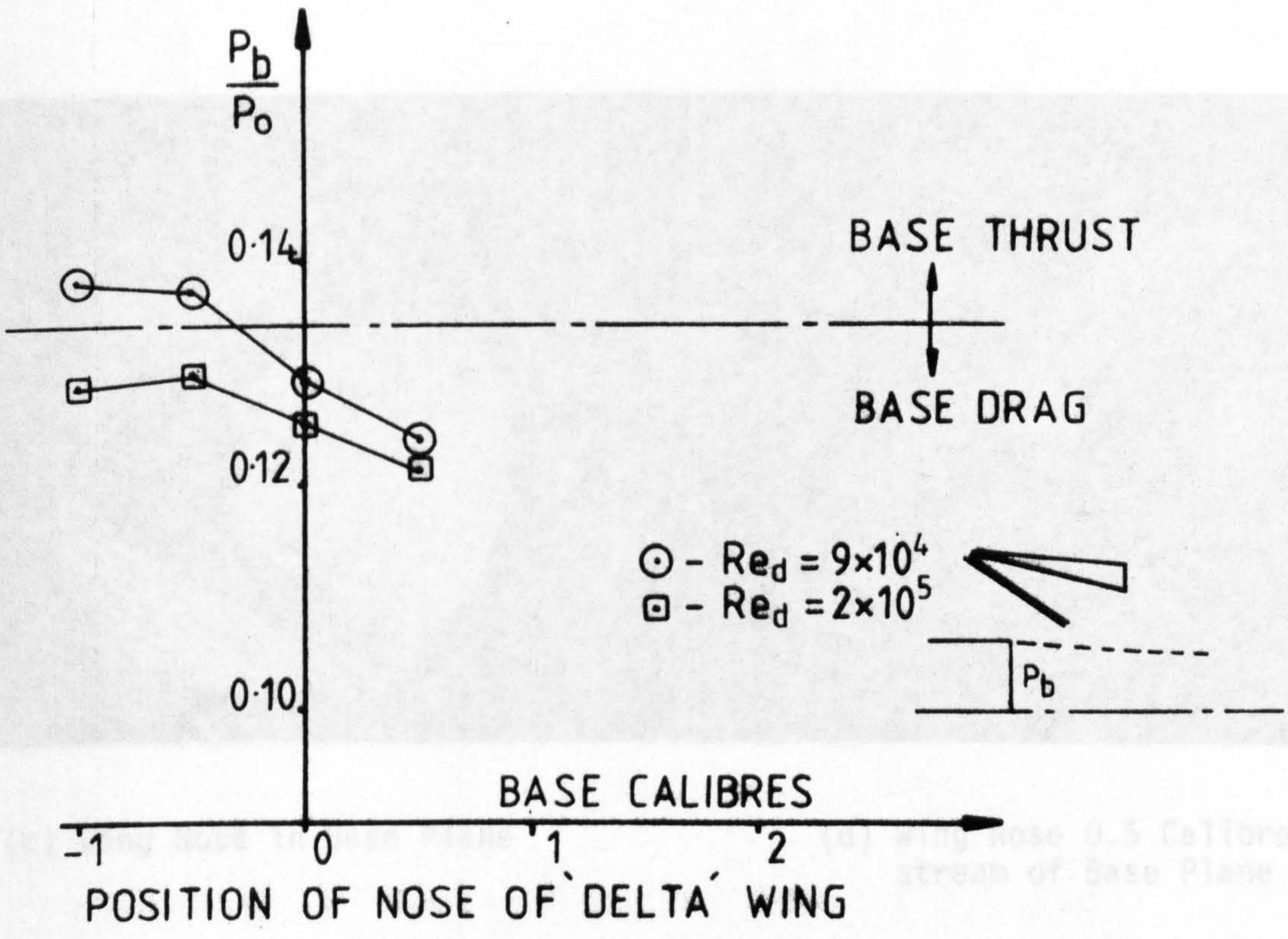

Fig. 5·18 Base pressure ratio vs. position of nose of delta wing

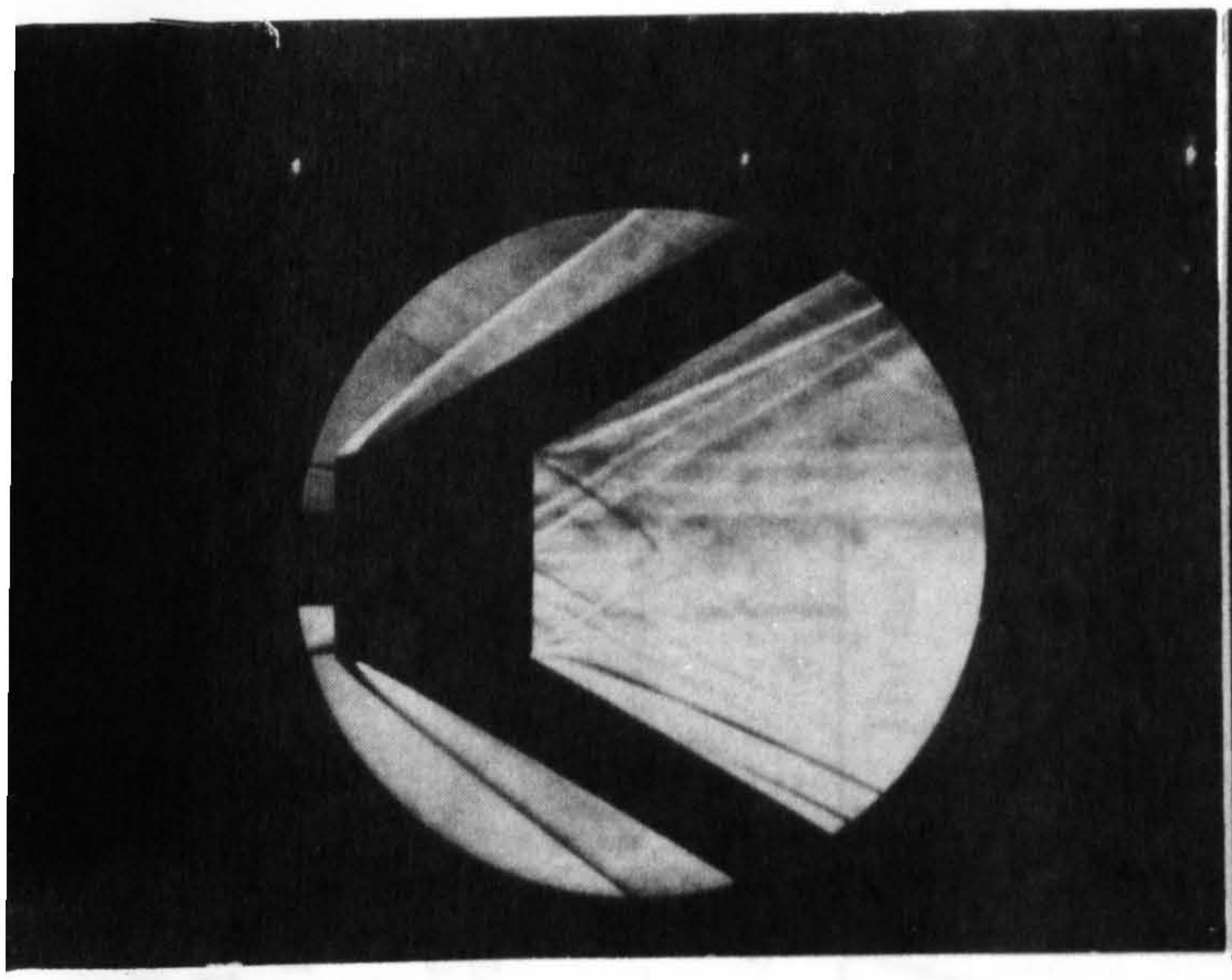

(a) Wing Nose 1 Calibre Upstream of Base Plane

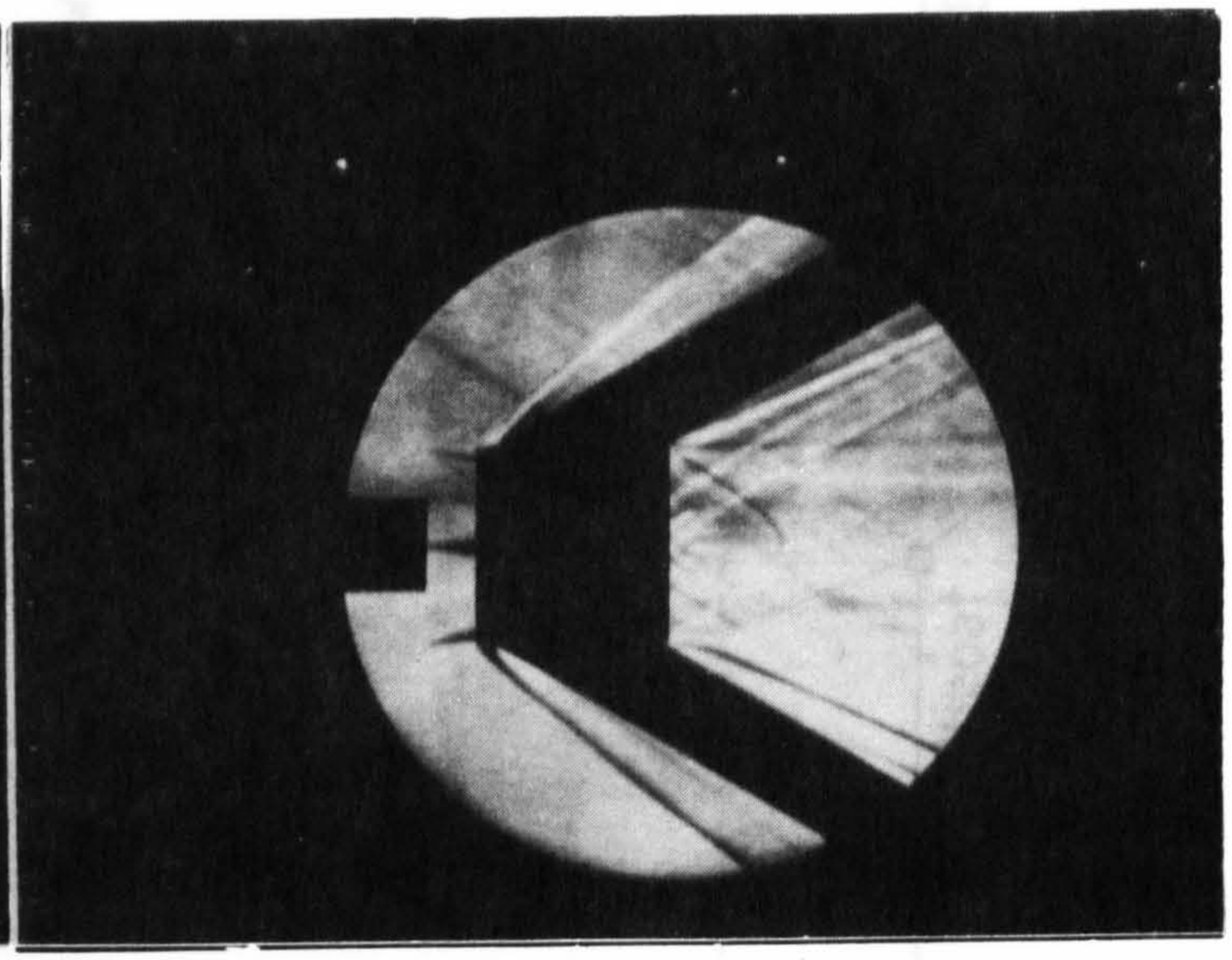

(b) Wing Nose 0.5 Calibres Upstream of Base Plane

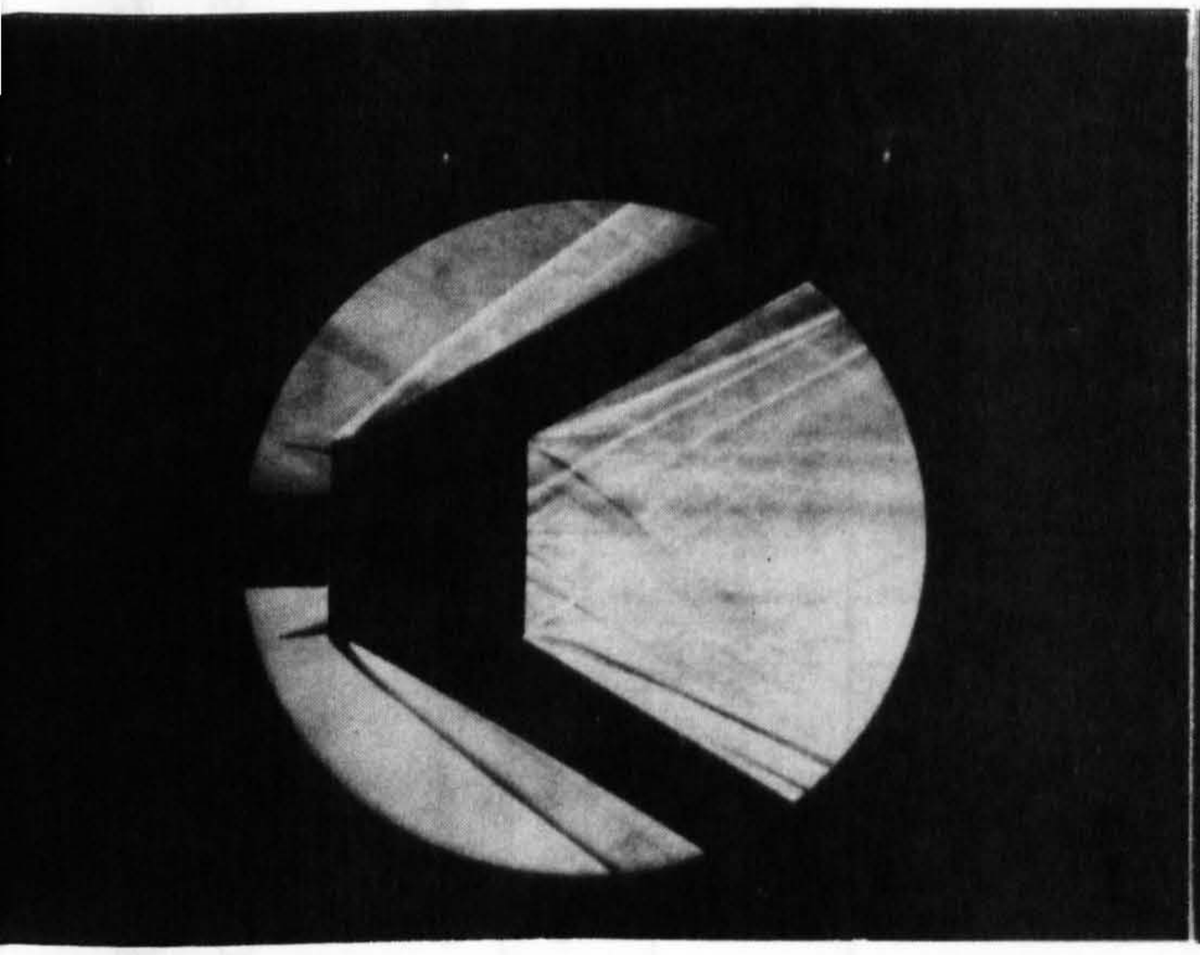

(c) Wing Nose in Base Plane

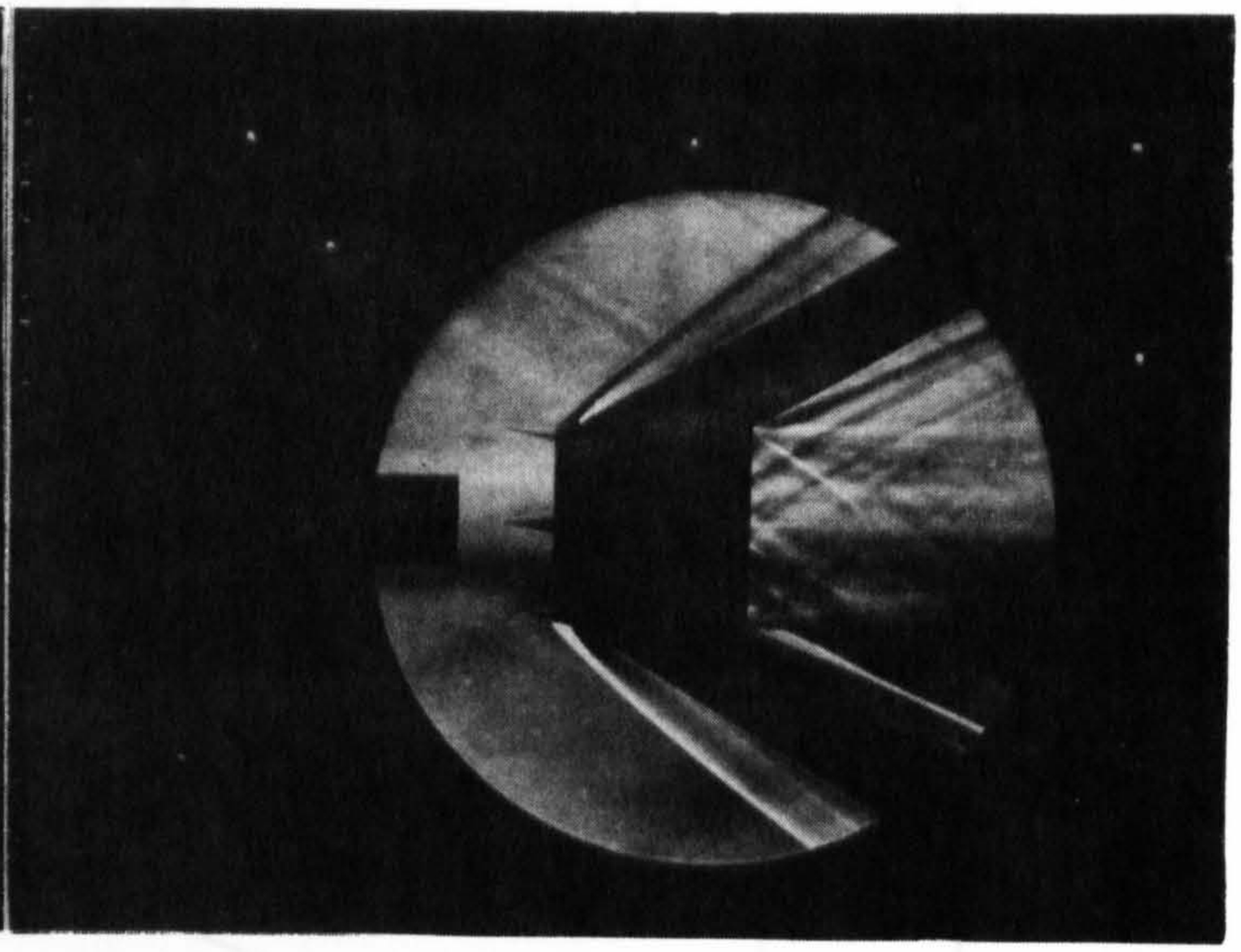

(d) Wing Nose 0.5 Calibres Downstream of Base Plane

Fig. 5.19 10 ms Exposure Schlieren Photographs of 'Delta' Wing Interaction with Flowfield. $Re_d = 2.4 \times 10^5$

Fig. 5.20 Pressure ratio on cowl internal surface: $Re_d = 2.4 \times 10^5$, $M_\infty = 1.96$

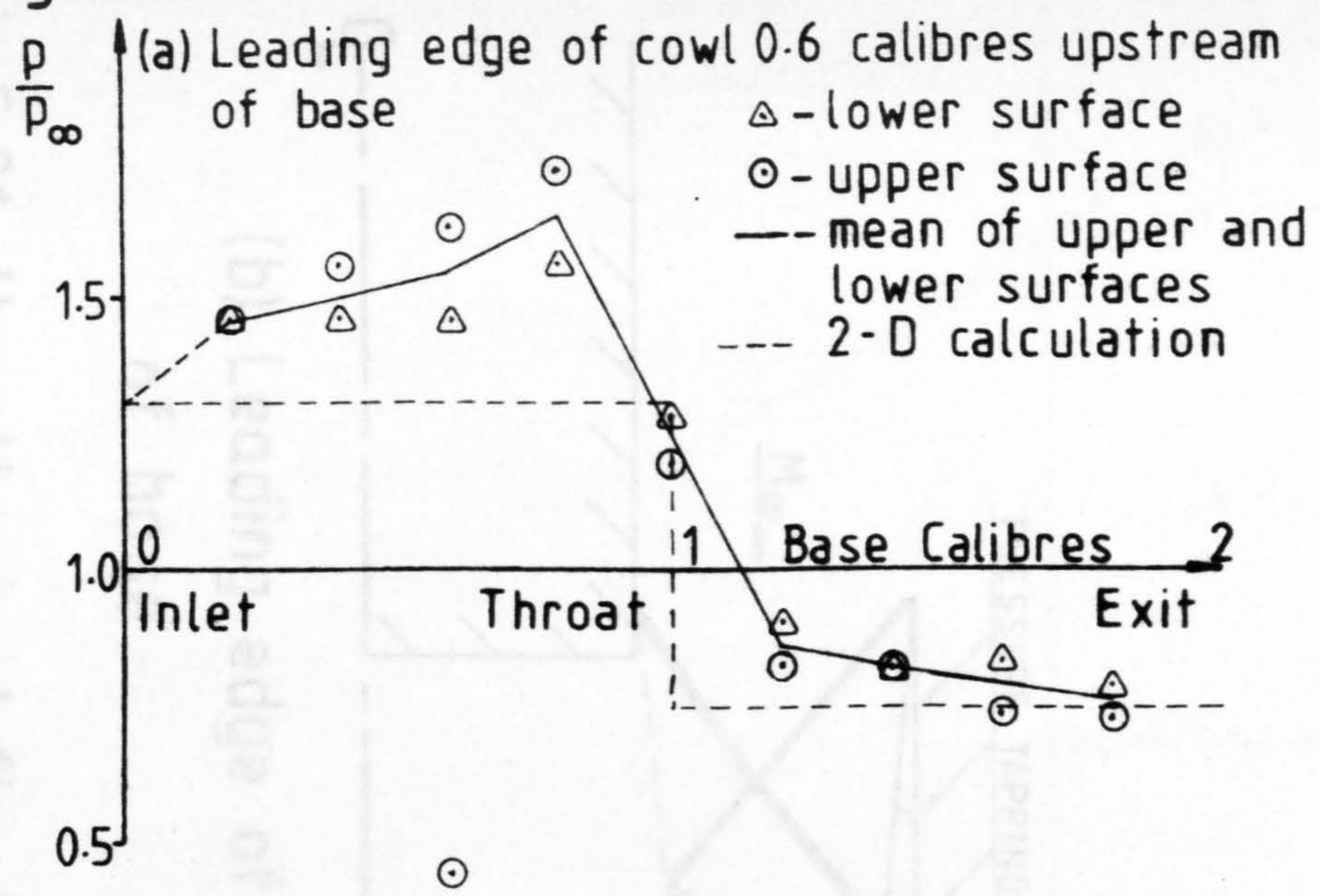

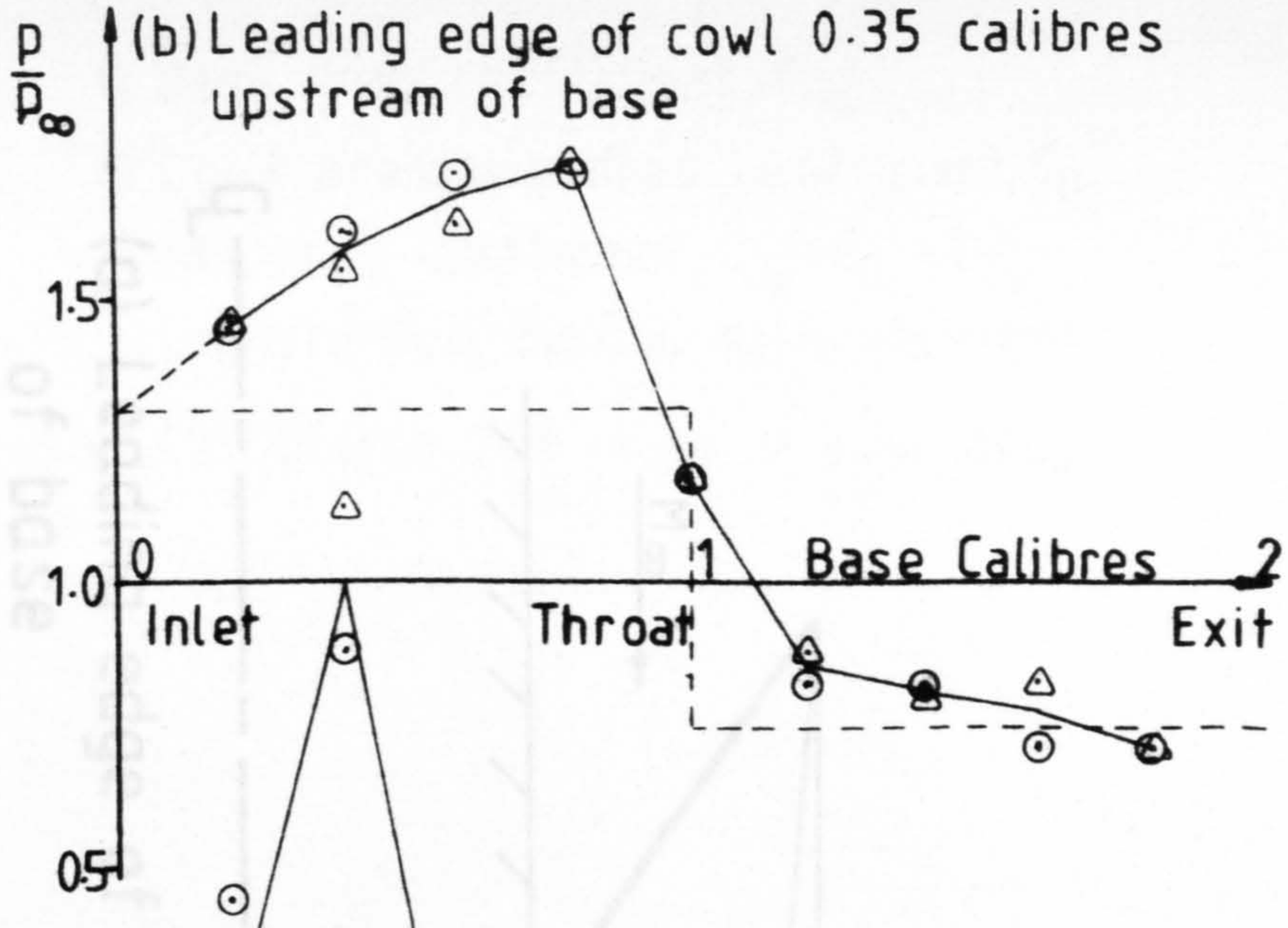

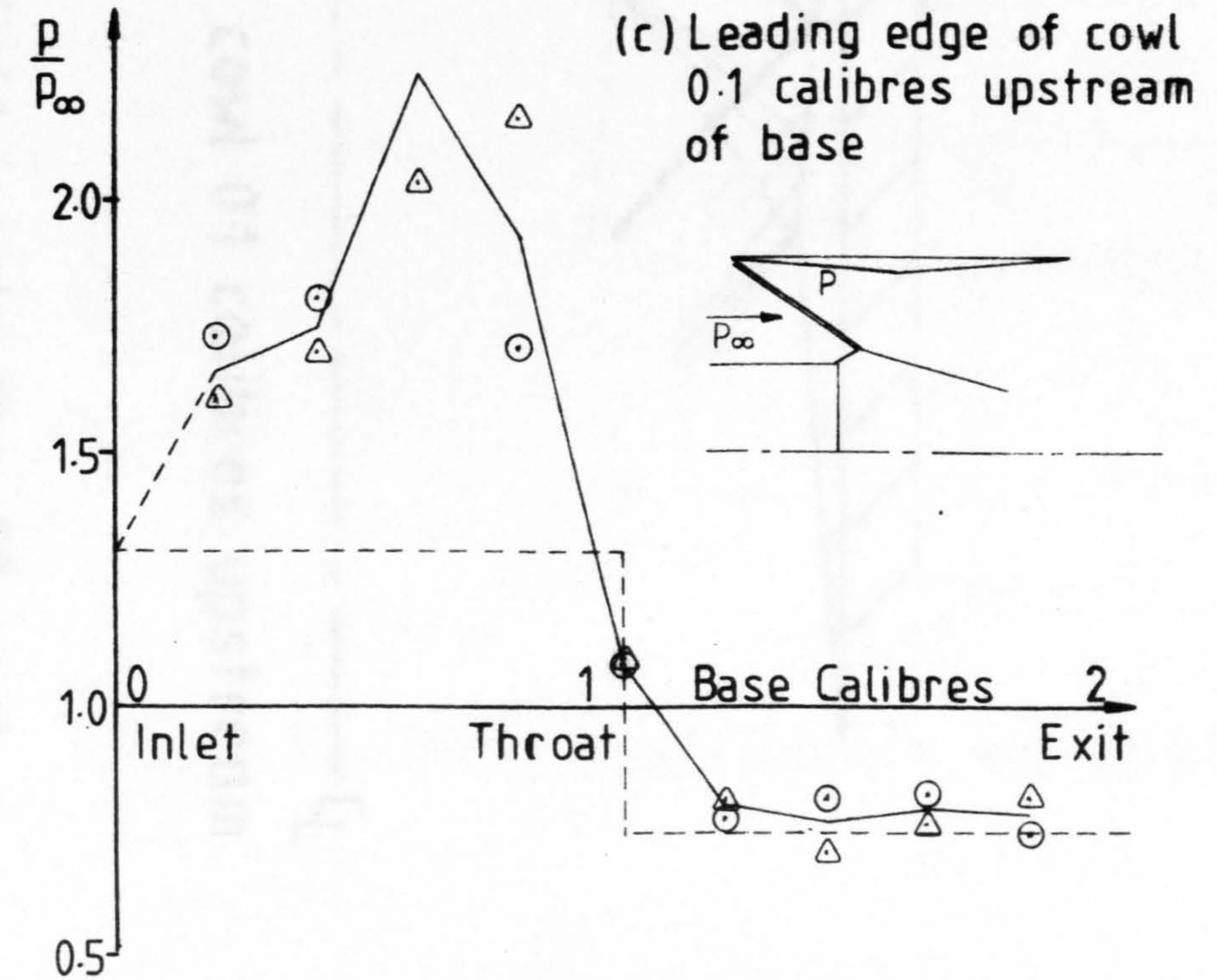

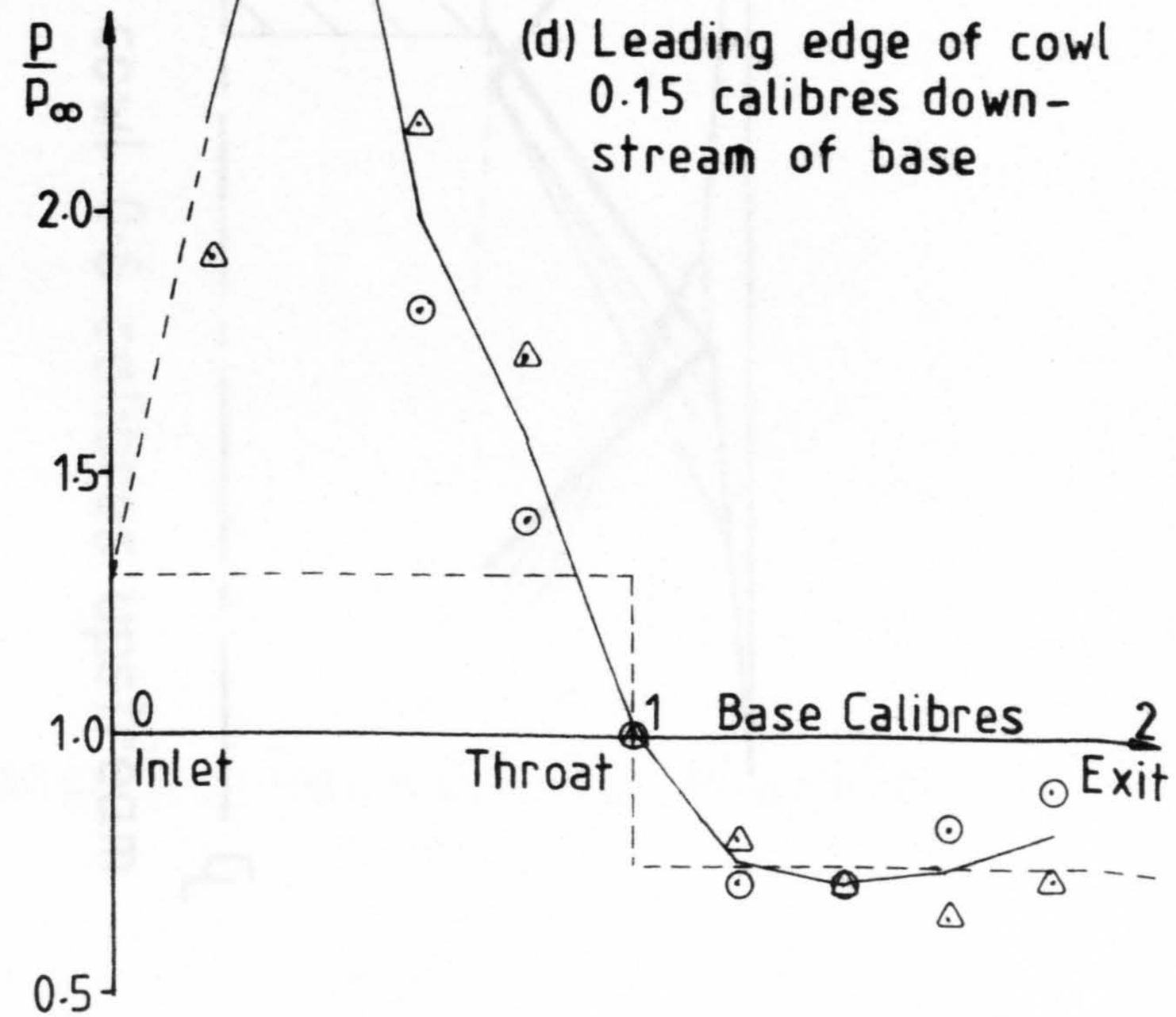

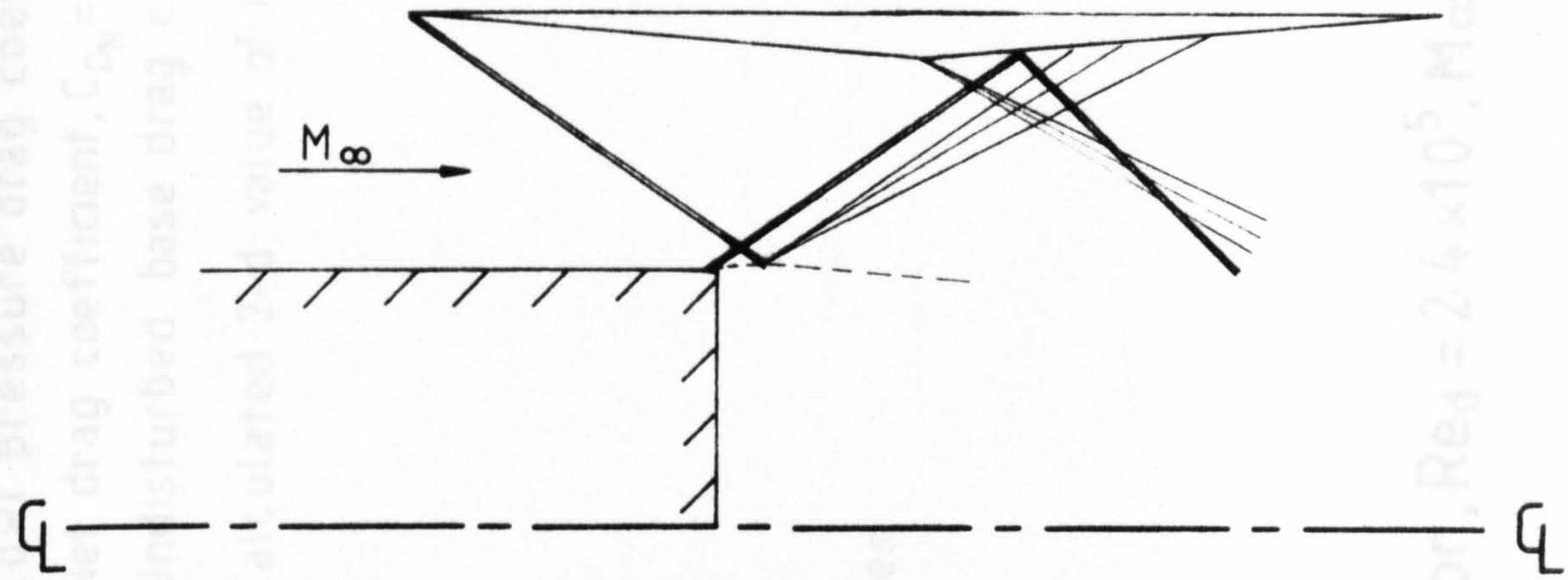

(a) Leading edge of cowl 0·6 calibres upstream of base

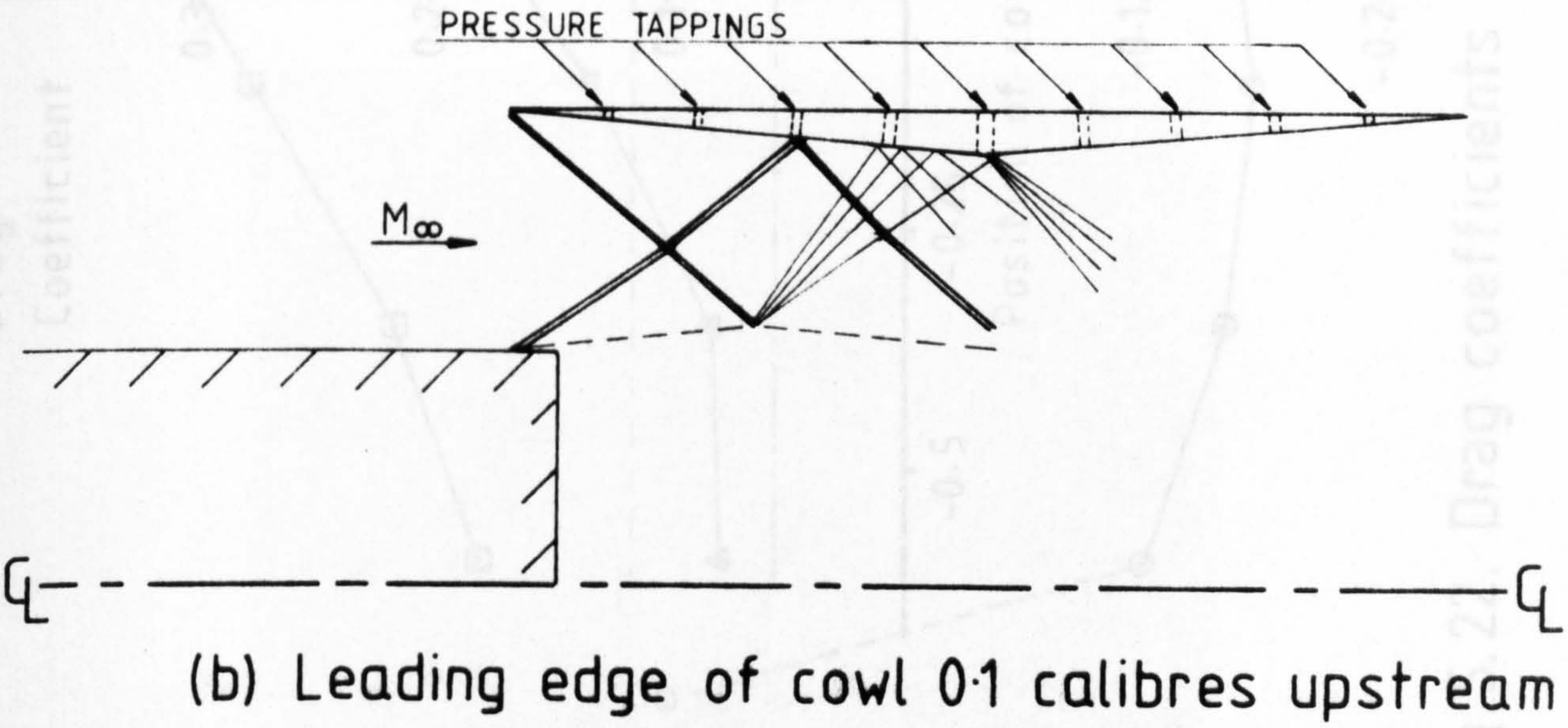

(b) Leading edge of cowl 0·1 calibres upstream of base

Fig.5·21. Hypothesised flowfield inside the 5° cowl (cf. fig.5·20), $M_\infty = 1{\cdot}96$.

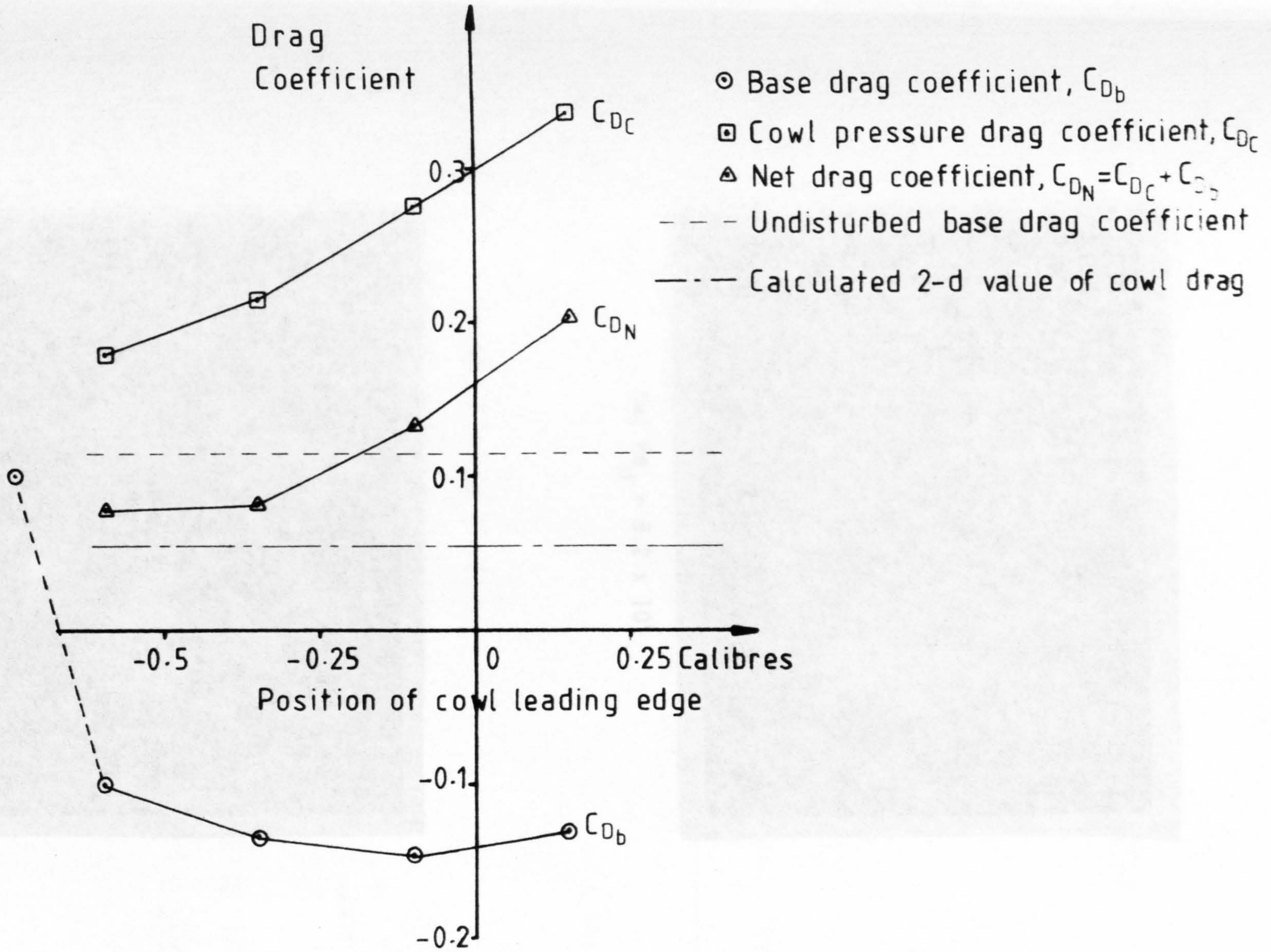

Fig. 5.22. Drag coefficients vs. cowl position, $Re_d = 2{\cdot}4\times10^5$, $M_\infty = 1{\cdot}96$

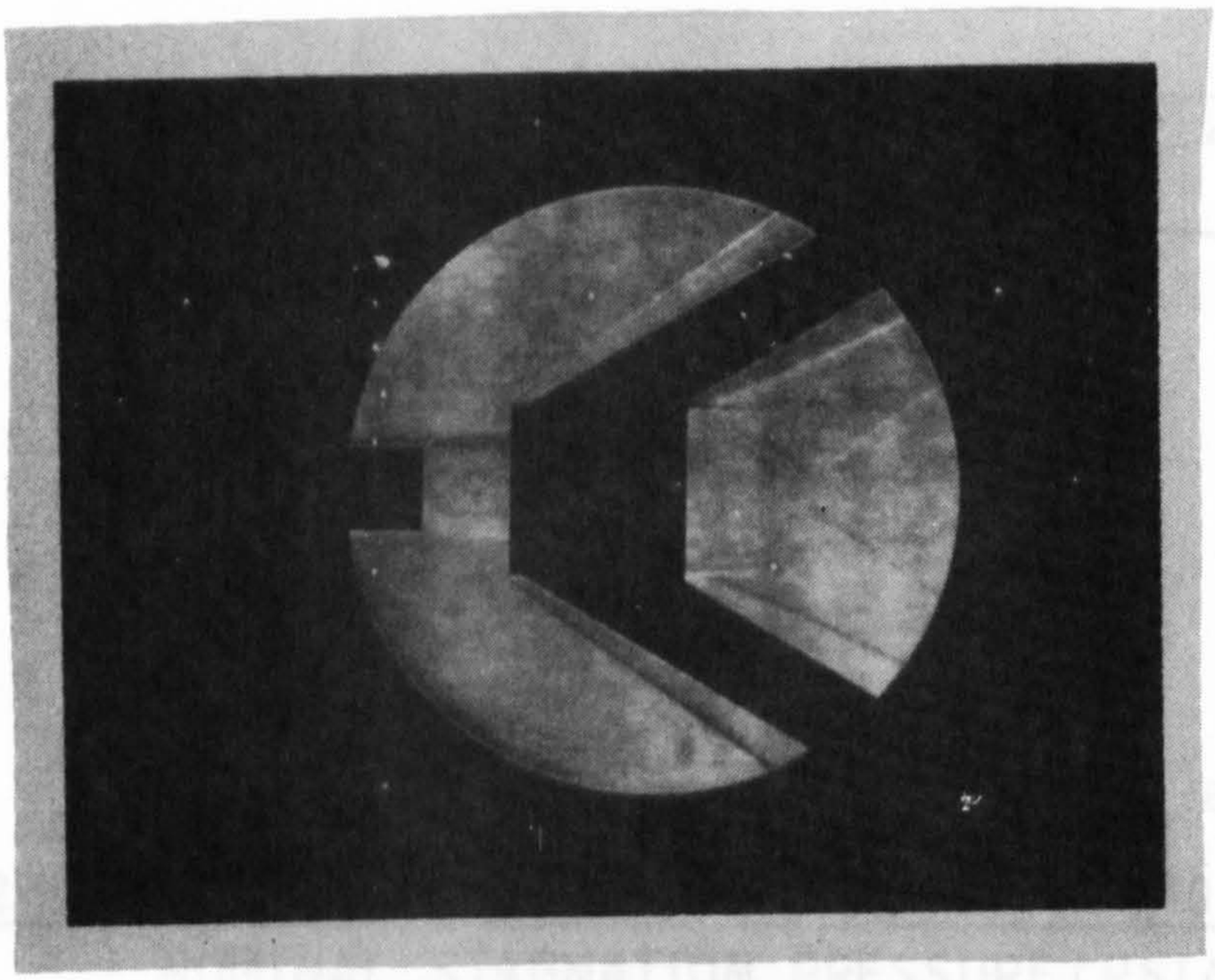

(a) $Re_d = 9.2 \times 10^4$

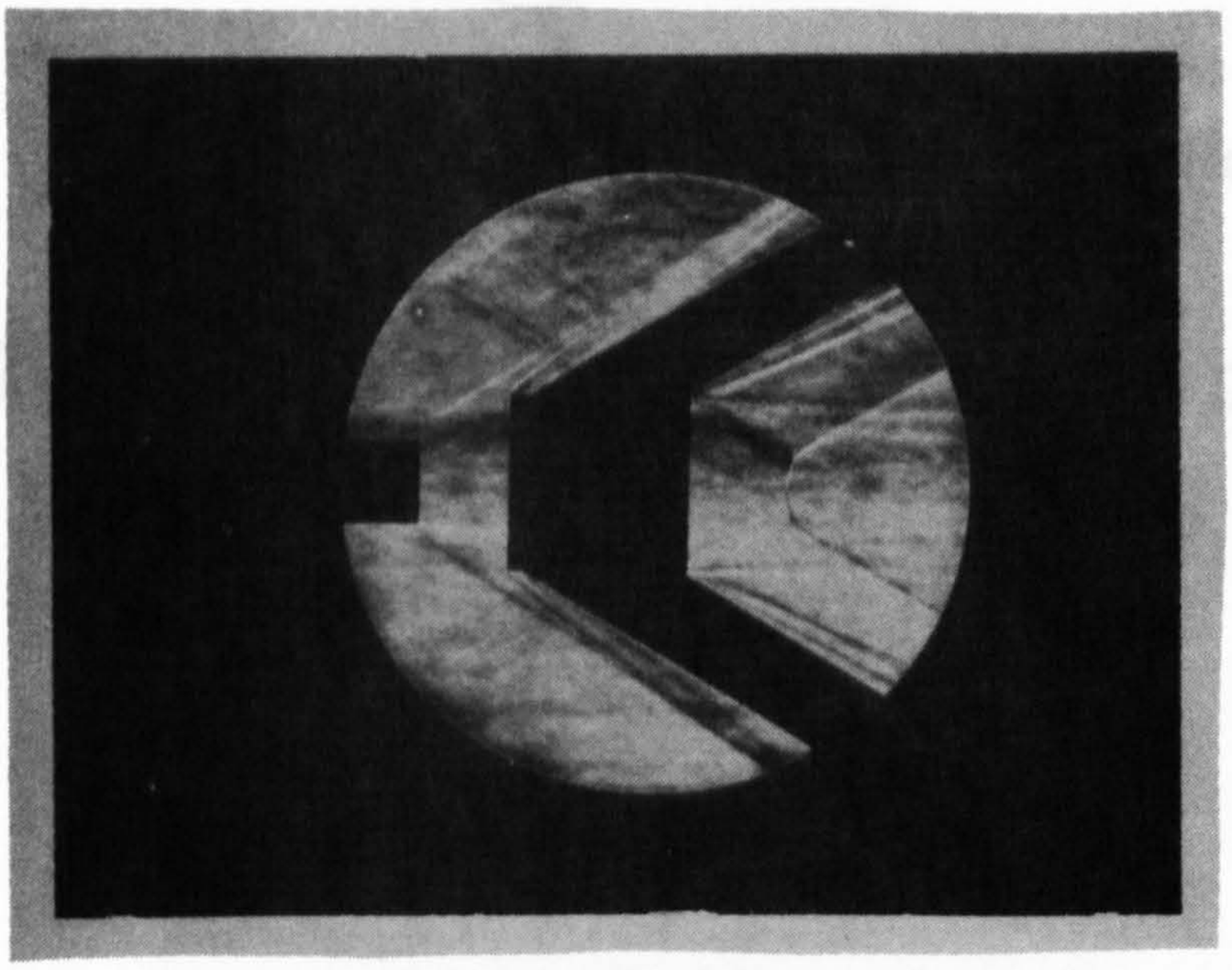

(b) $Re_d = 2.4 \times 10^5$

Fig. 5.23 Axisymmetric Configuration with Leading Edge of Cowl at 1 Calibre, 8 μs exposure

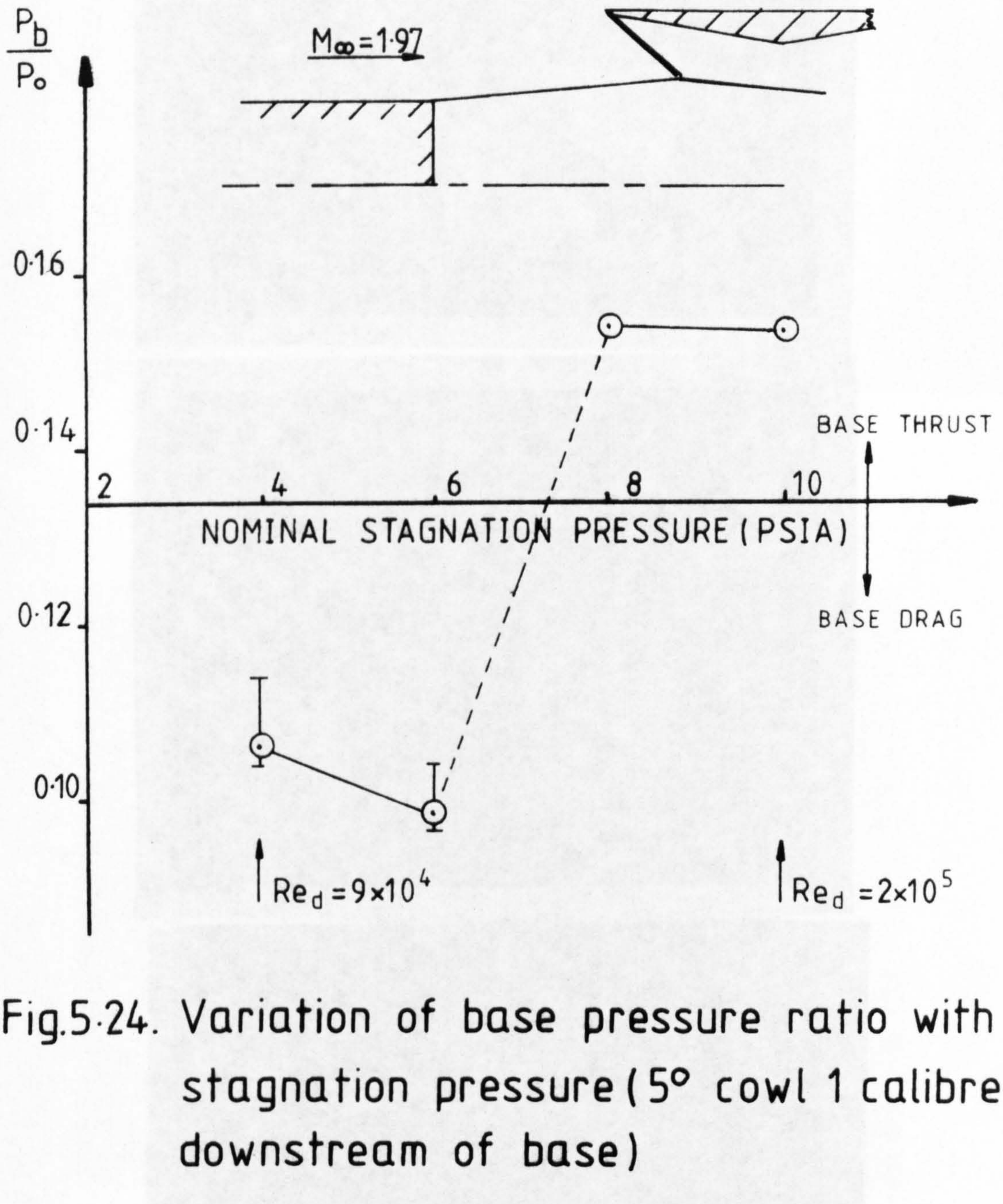

Fig.5·24. Variation of base pressure ratio with stagnation pressure (5° cowl 1 calibre downstream of base)

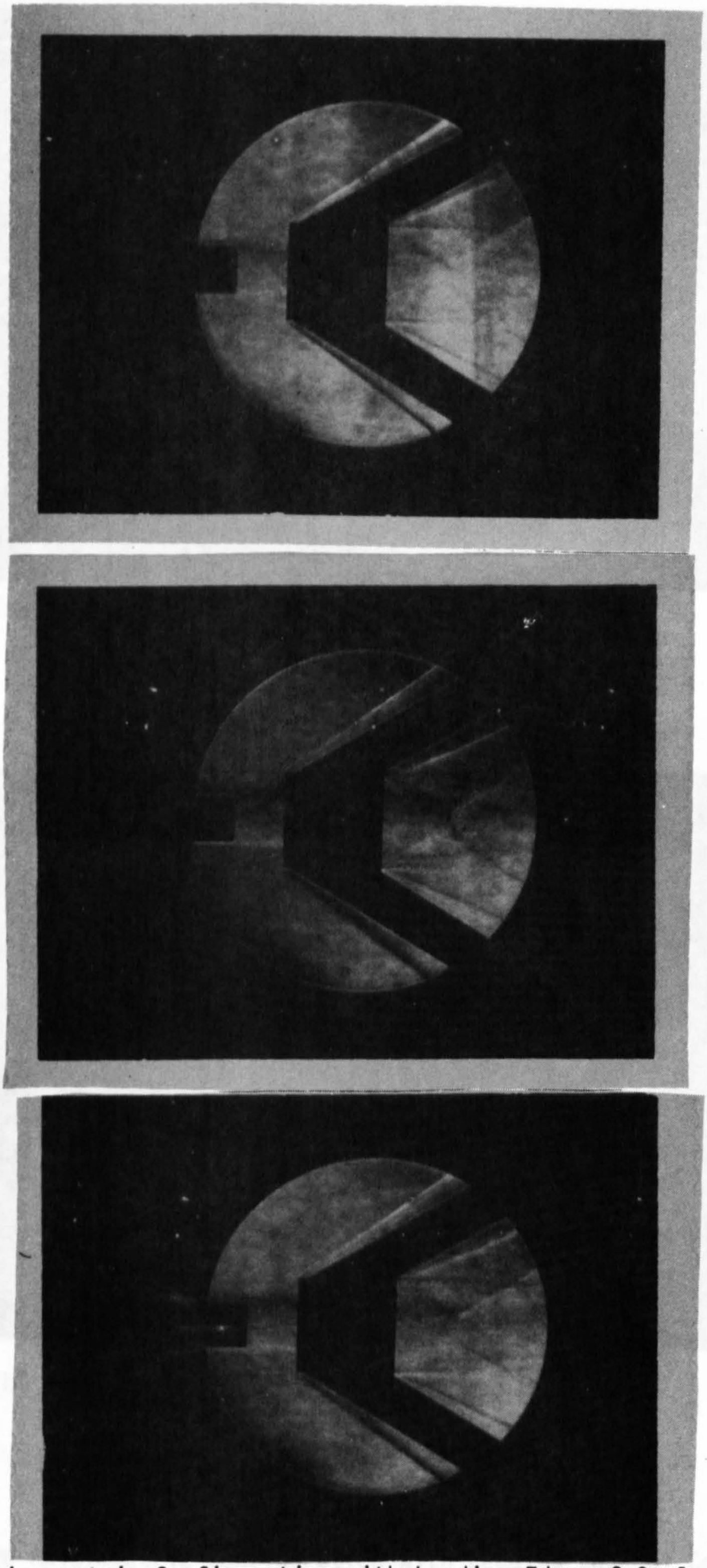

Fig. 5.25 Axisymmetric Configuration with Leading Edge of Cowl at 1 Calibre, $Re_d = 9.2 \times 10^4$, 8 μs exposure, in order of time, approximately 2 minutes between each exposure.

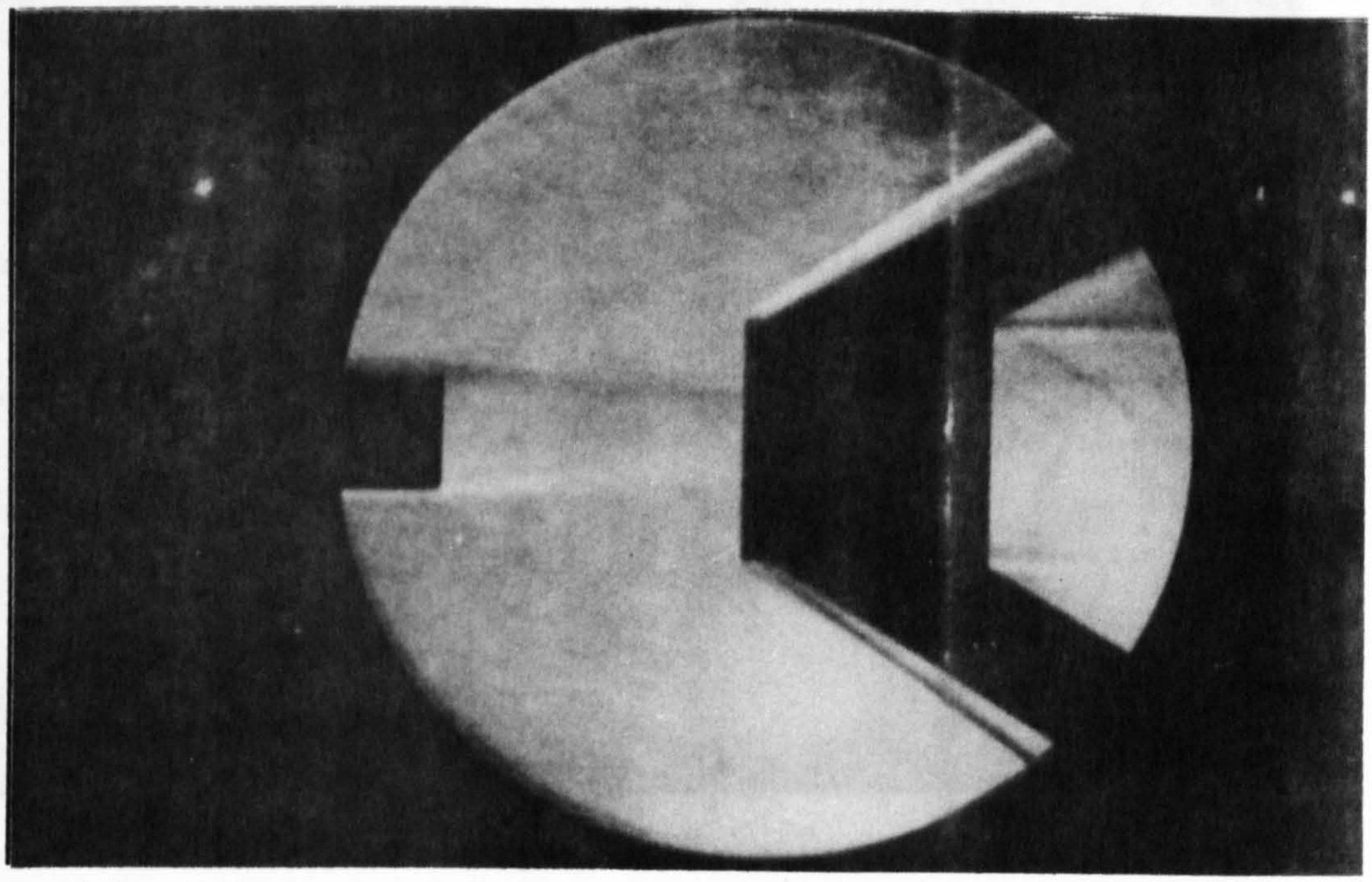

(a)

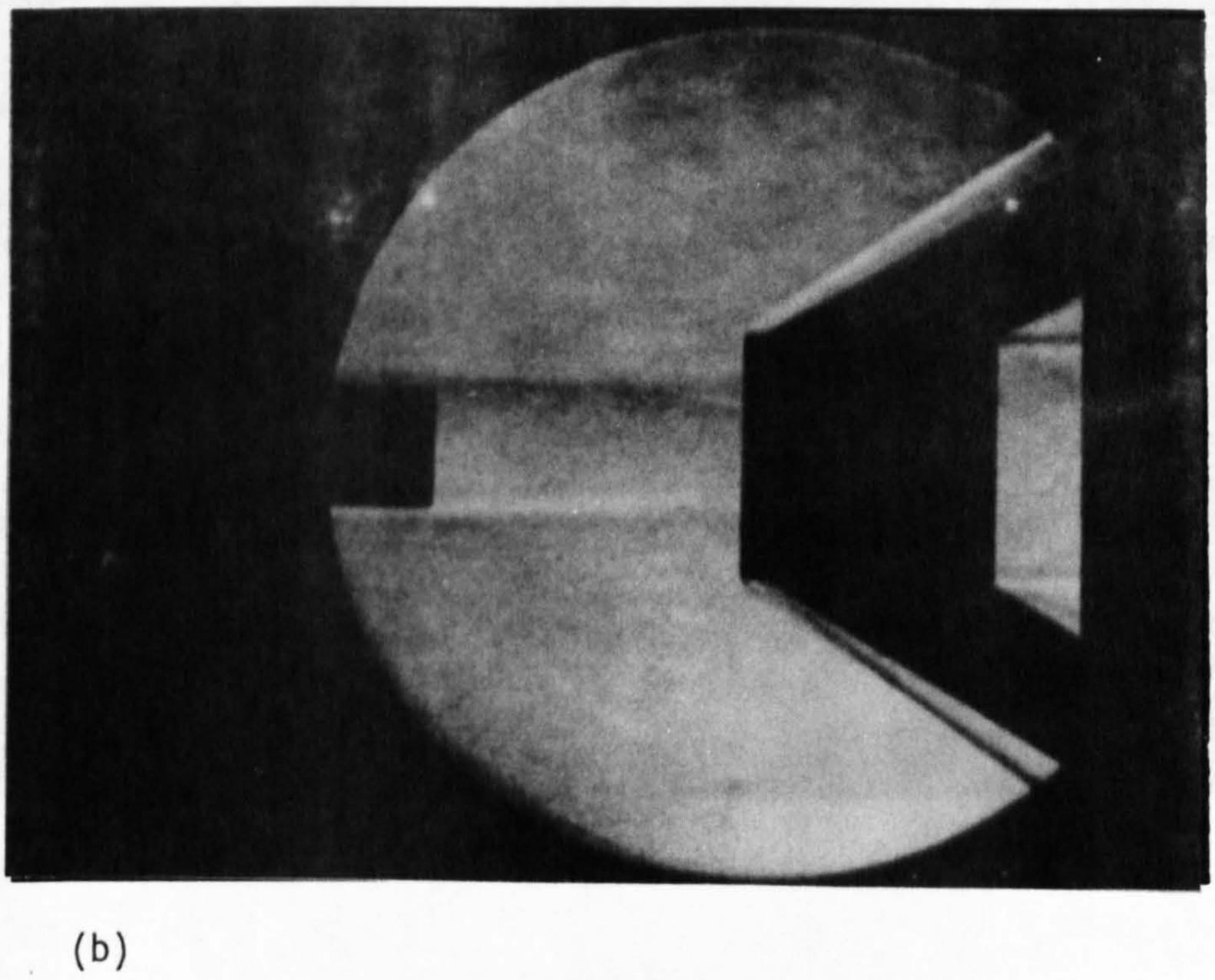

(b)

Fig. 5.26 Axisymmetric Configuration with Leading Edge of Cowl 2.5 Calibres Downstream of the Base Plane, $Re_d = 9.2 \times 10^4$, 10 ms exposure, in order of time.

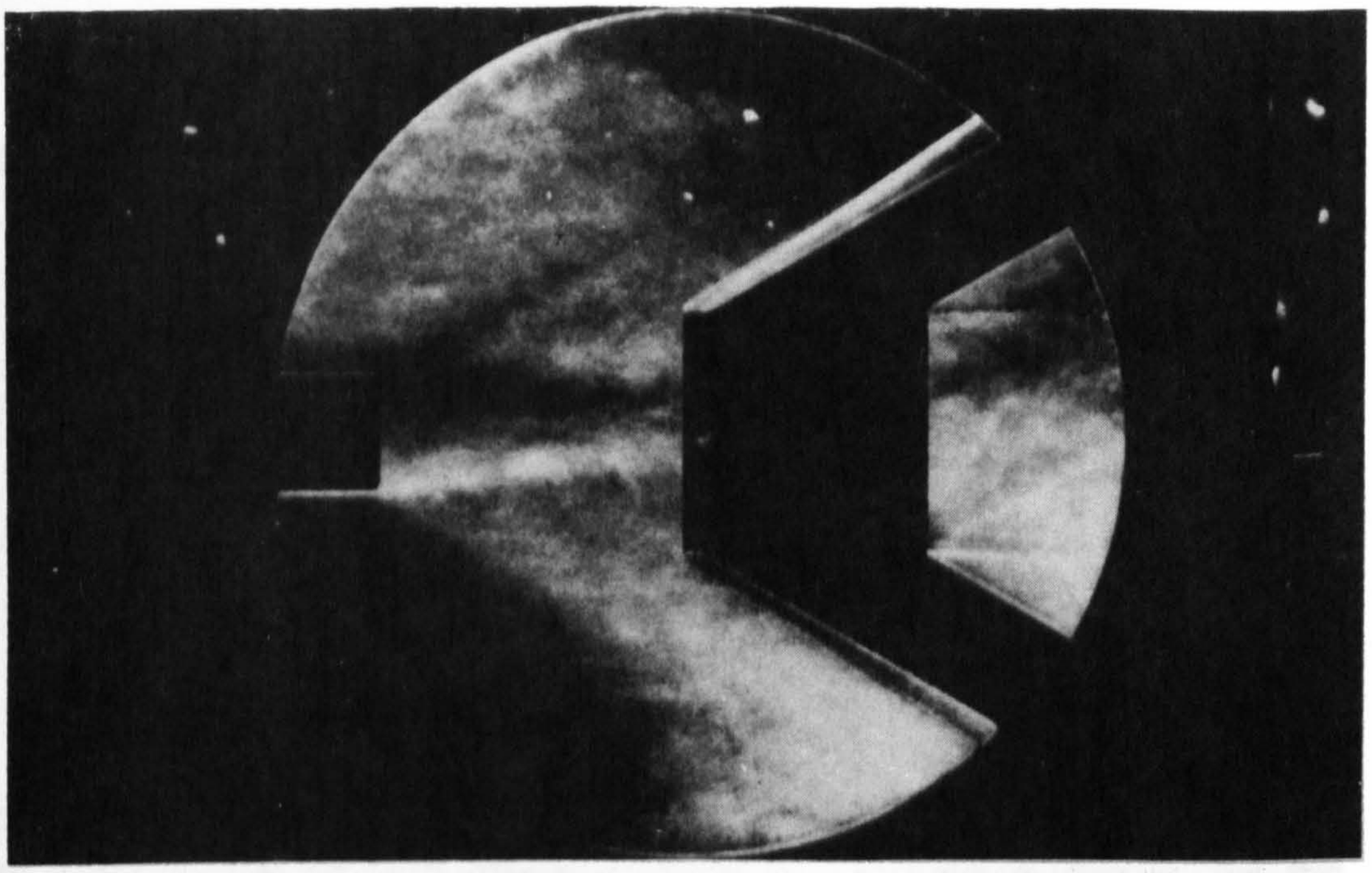

(a)

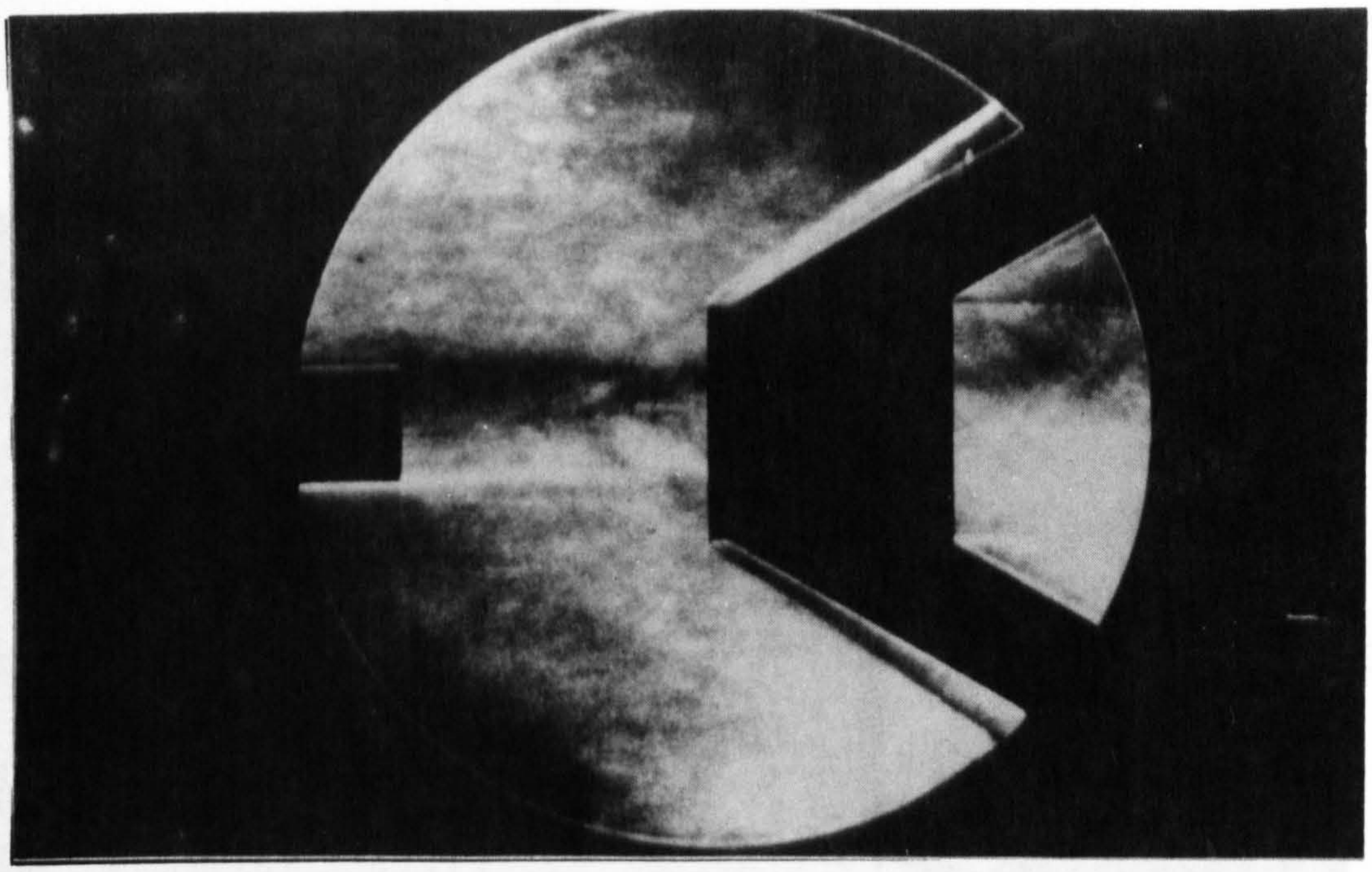

(b)

Fig. 5.27 Axisymmetric Configuration with Leading Edge of the Cowl 2.5 Calibres Downstream of the Base Plane, $Re_d = 9.2 \times 10^4$, 8 μs exposure in order of time, approximately 1 minute between exposures.

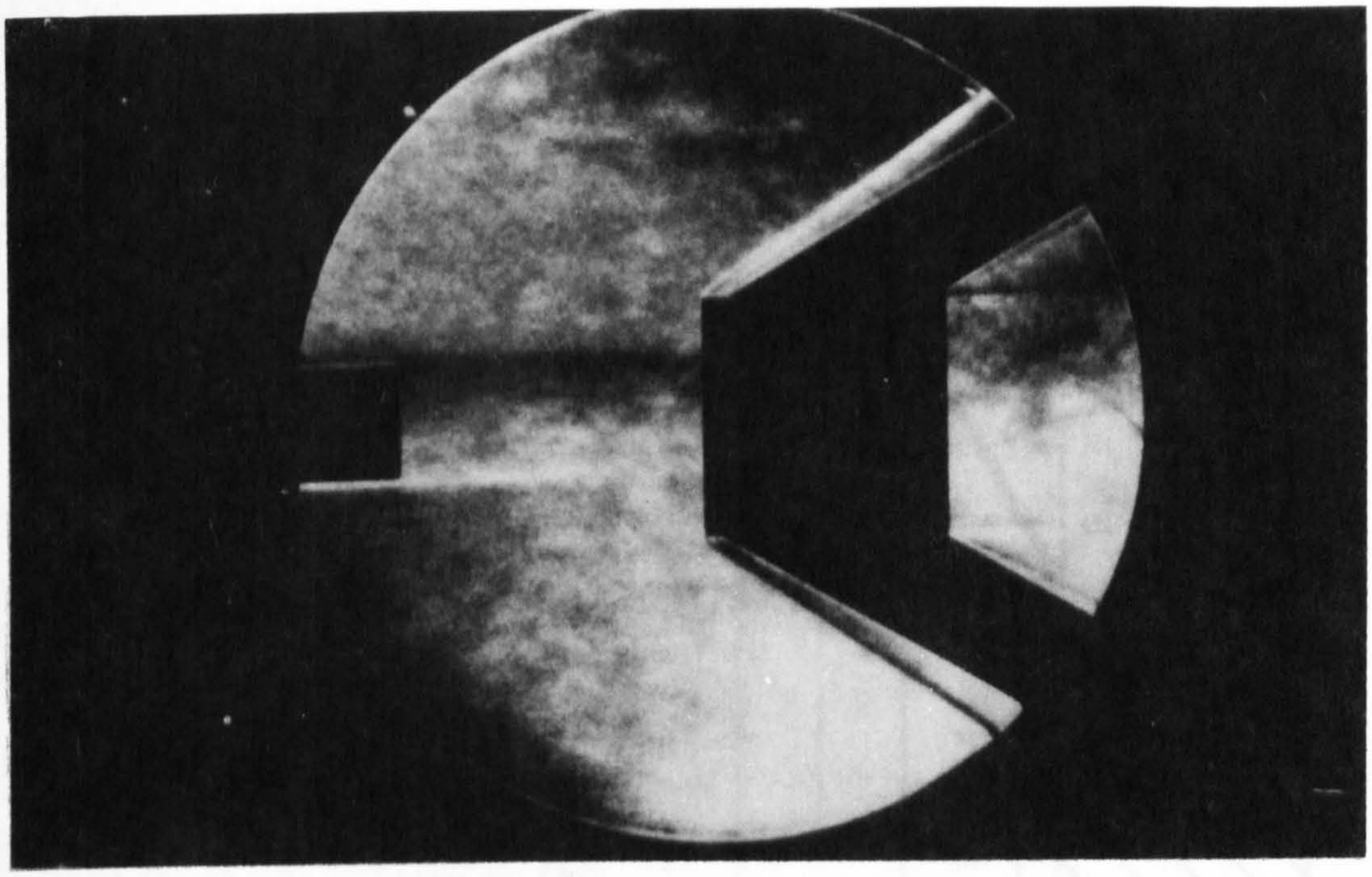

(c)

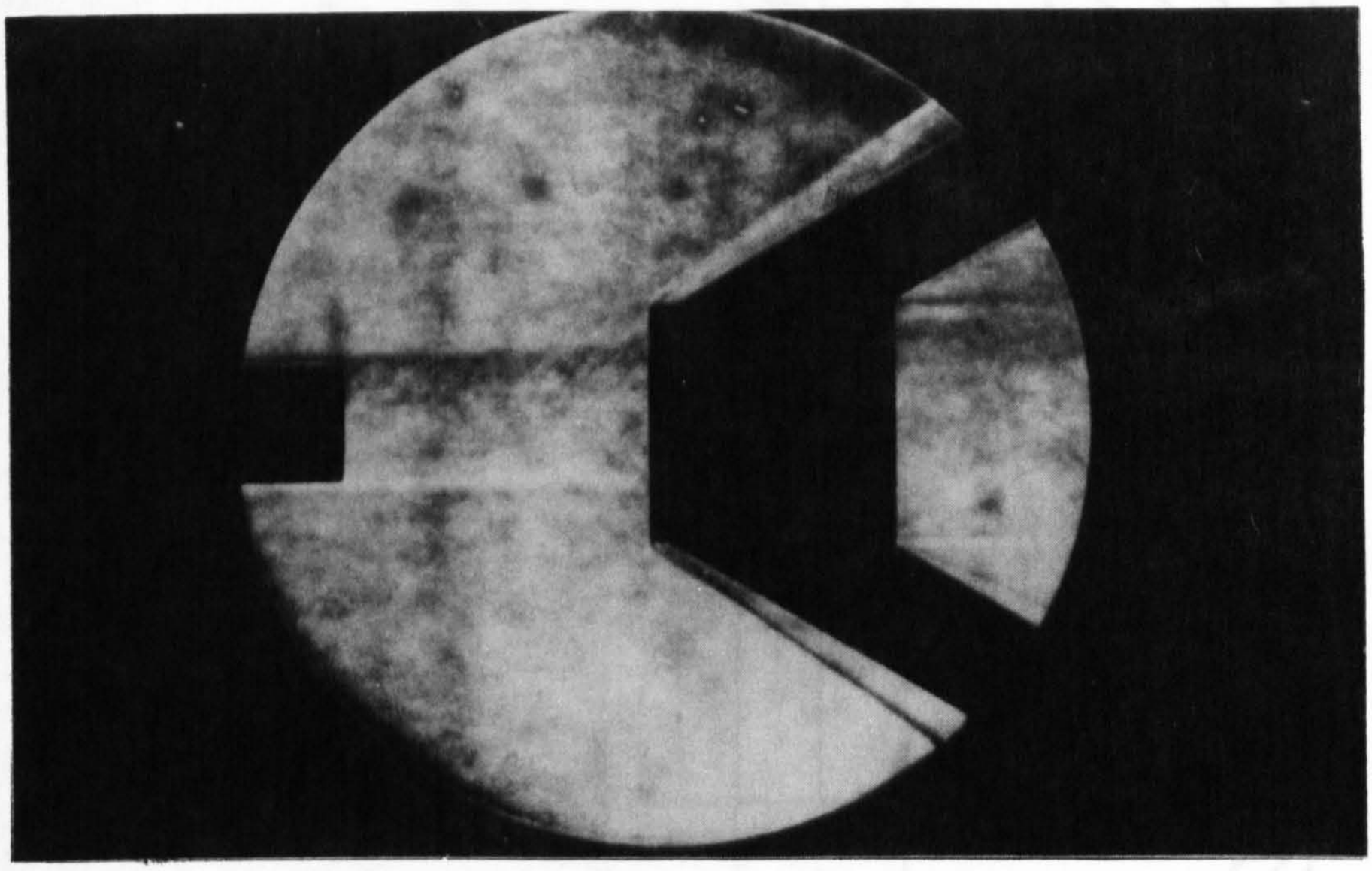

(d)

Fig. 5.27 (cont) Axisymmetric Configuration with Leading Edge of the Cowl 2.5 Calibres Downstream of the Base Plane, $Re_d = 9.2 \times 10^4$, 8 μs exposure in order of time, approximately 1 minute between exposures.

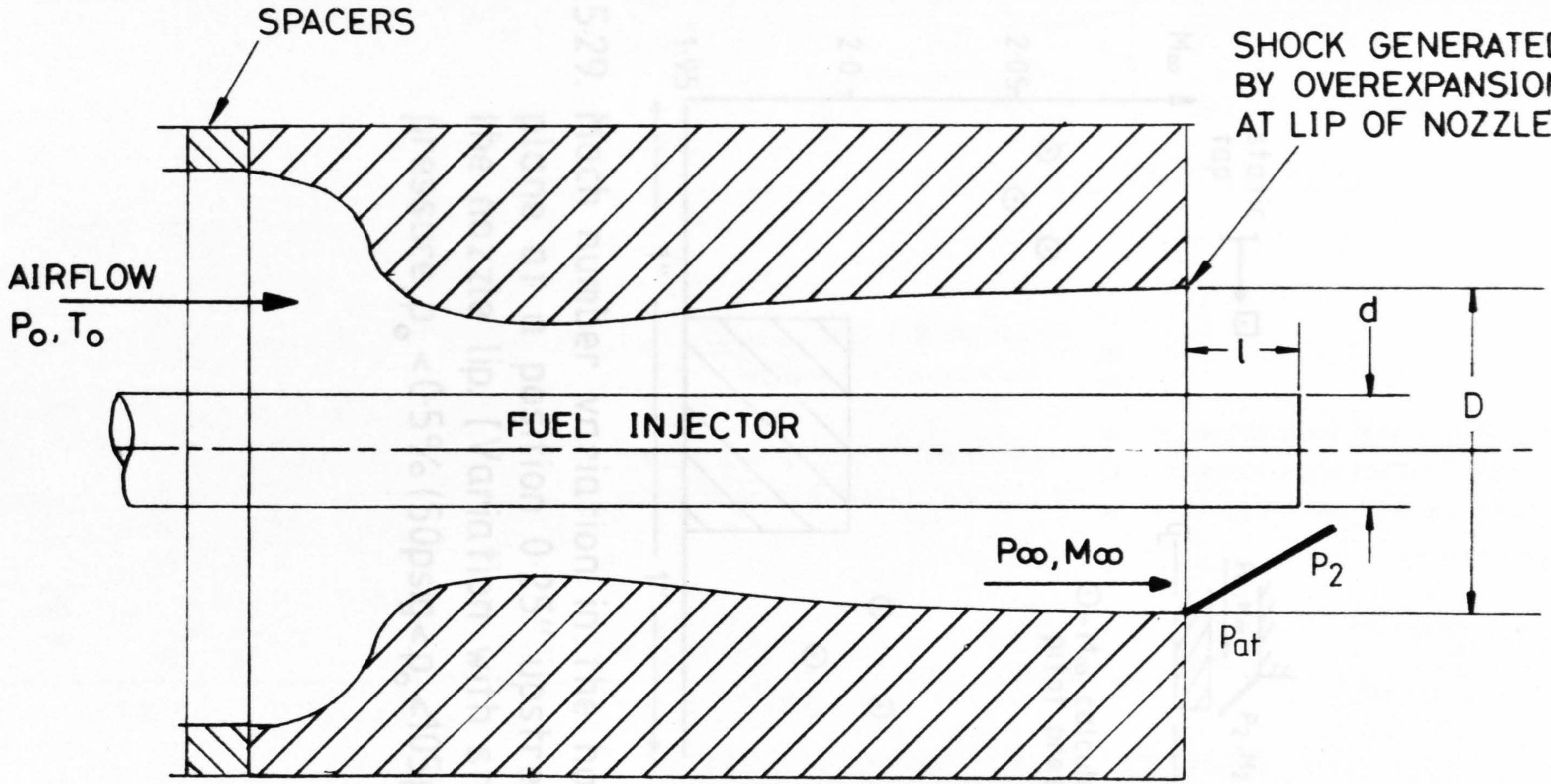

Fig.5.28. Open jet wind tunnel

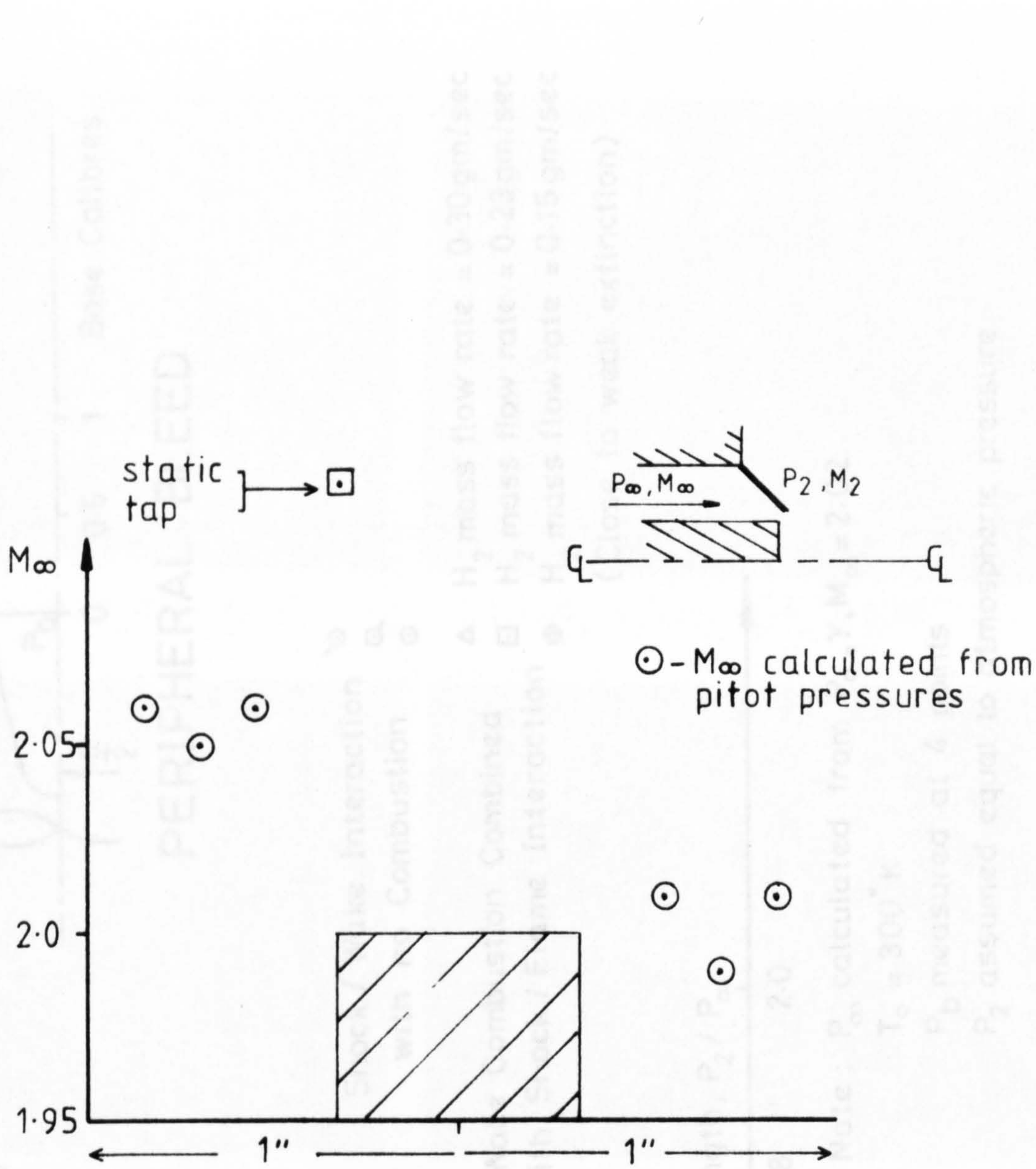

Fig.5·29. Mach number variation in the horizontal plane at a position 0·25" upstream of the nozzle lip. [Variation with stagnation pressure, p_o < 0·5% (50psig < p_o < 105psig)]

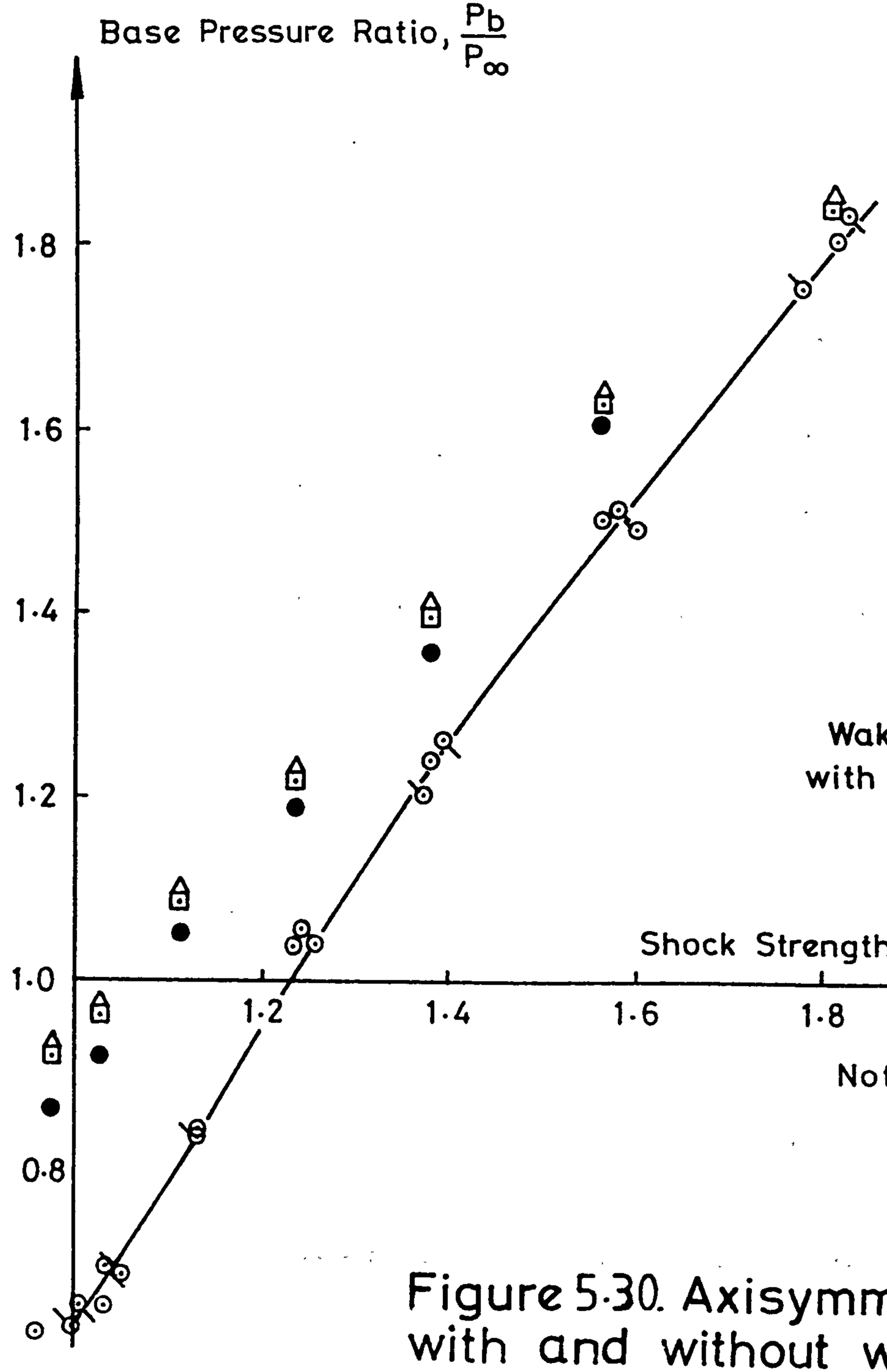

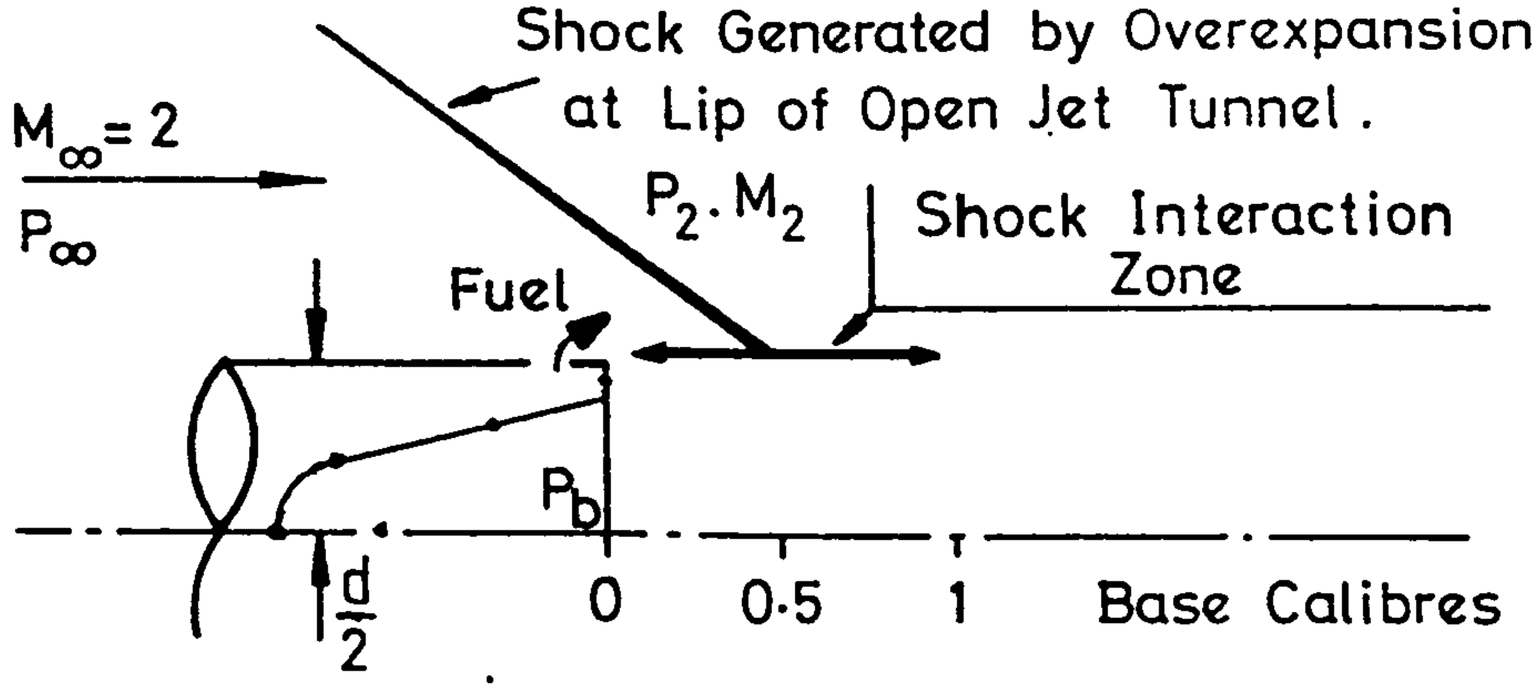

PERIPHERAL BLEED

Shock / Wake Interaction with no Combustion

Wake Combustion Combined with Shock / Flame Interaction

△ H_2 mass flow rate = 0·30 gm/sec
⊡ H_2 mass flow rate = 0·23 gm/sec
● H_2 mass flow rate = 0·15 gm/sec
(Close to weak extinction)

Note: P_∞ calculated from P_o, γ, $M_\infty = 2.02$
$T_o = 300^\circ K$
P_b measured at 4 points
P_2 assumed equal to atmospheric pressure.

Figure 5·30. Axisymmetric shock / wake interaction with and without wake combustion (l/D=0·21)

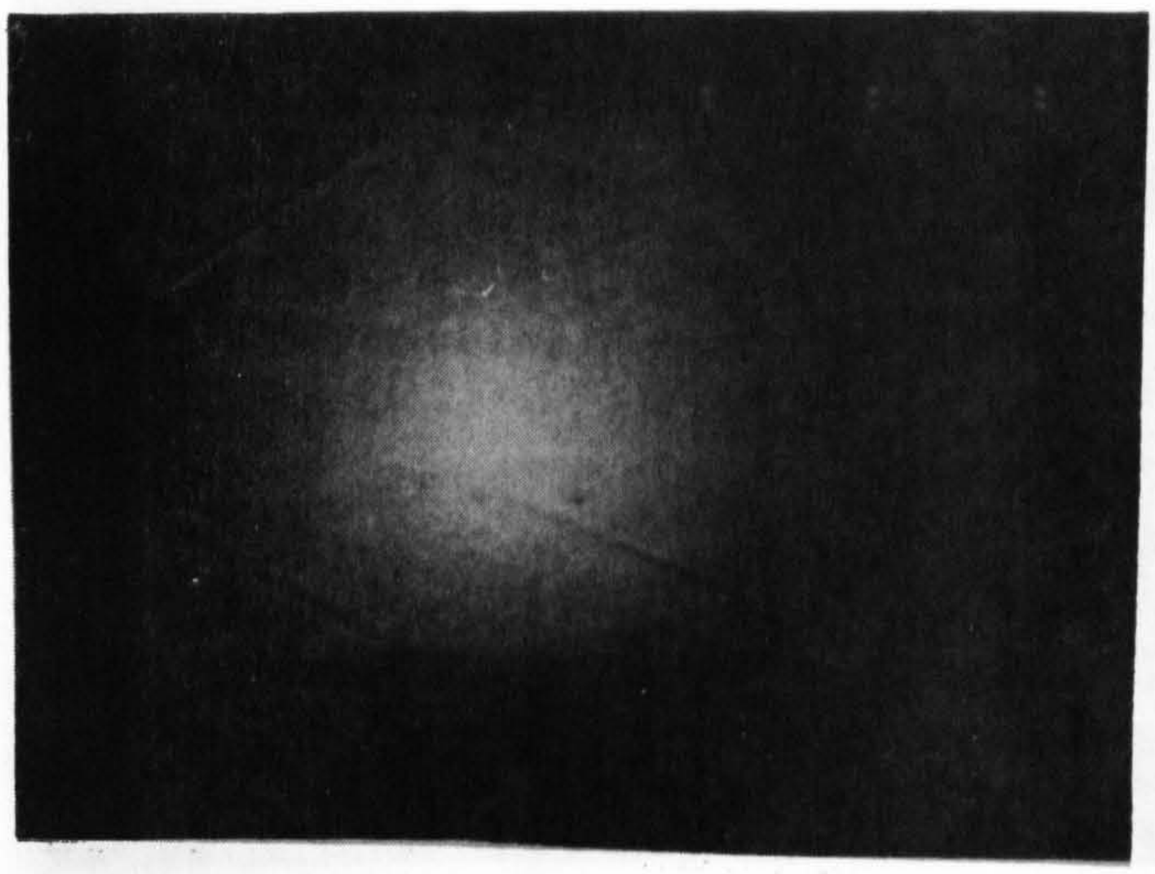

(a) $P_2/P_\infty = 1.03$, $P_b/P_\infty = 0.65$

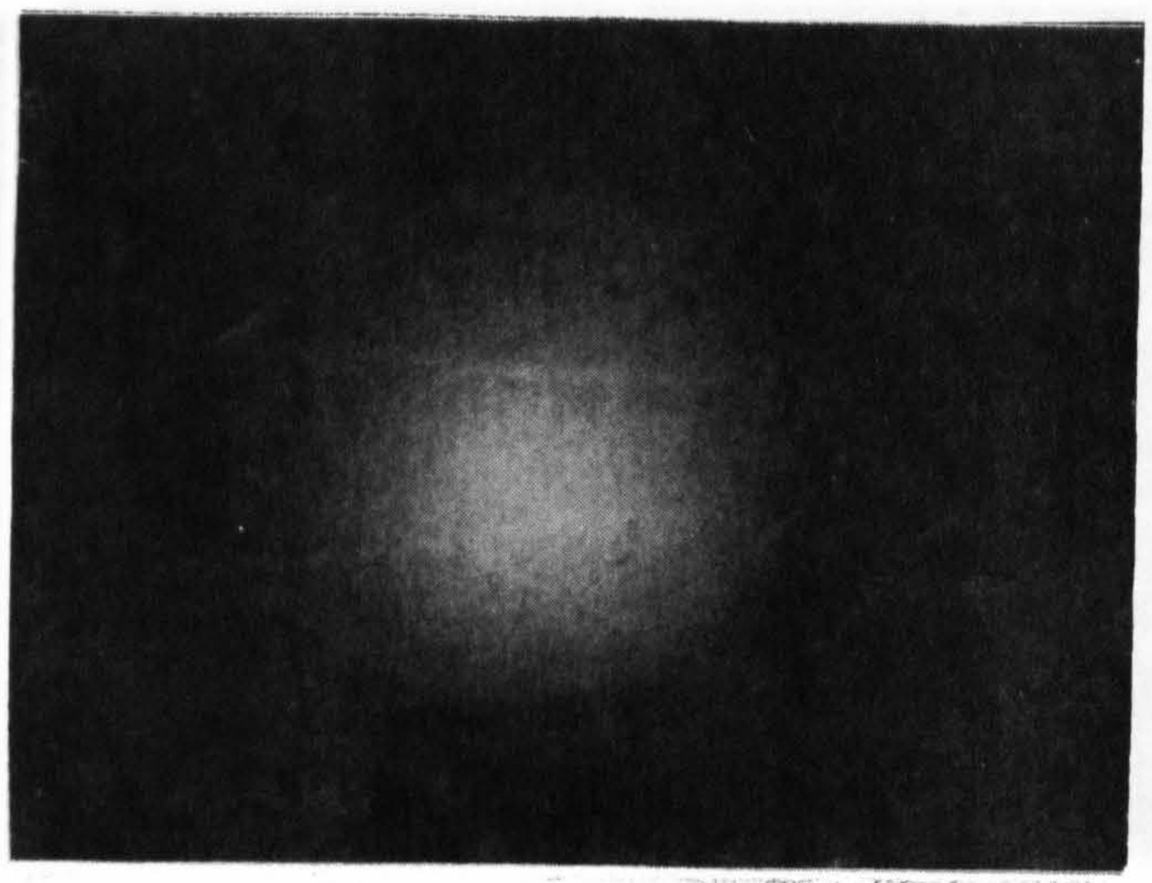

(b) $P_2/P_\infty = 1.13$, $P_b/P_\infty = 0.84$

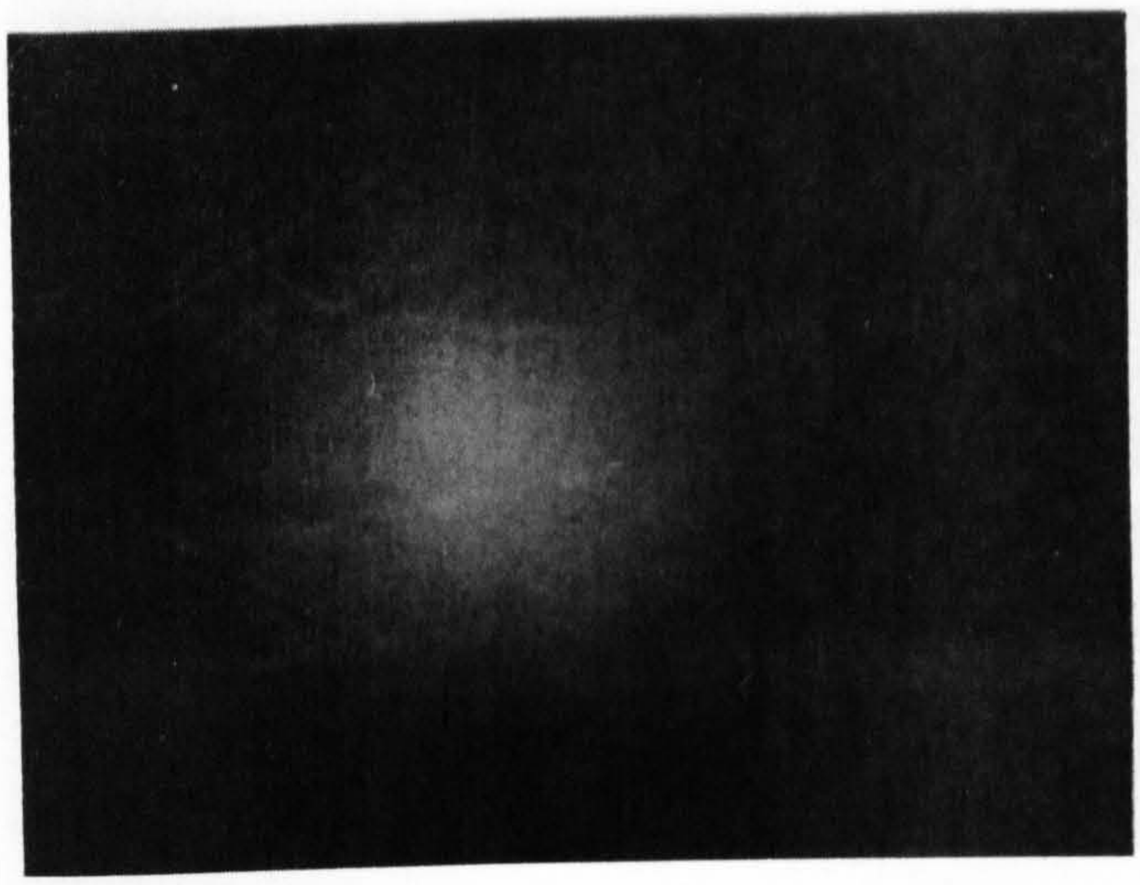

(c) $P_2/P_\infty = 1.24$, $P_b/P_\infty = 1.04$

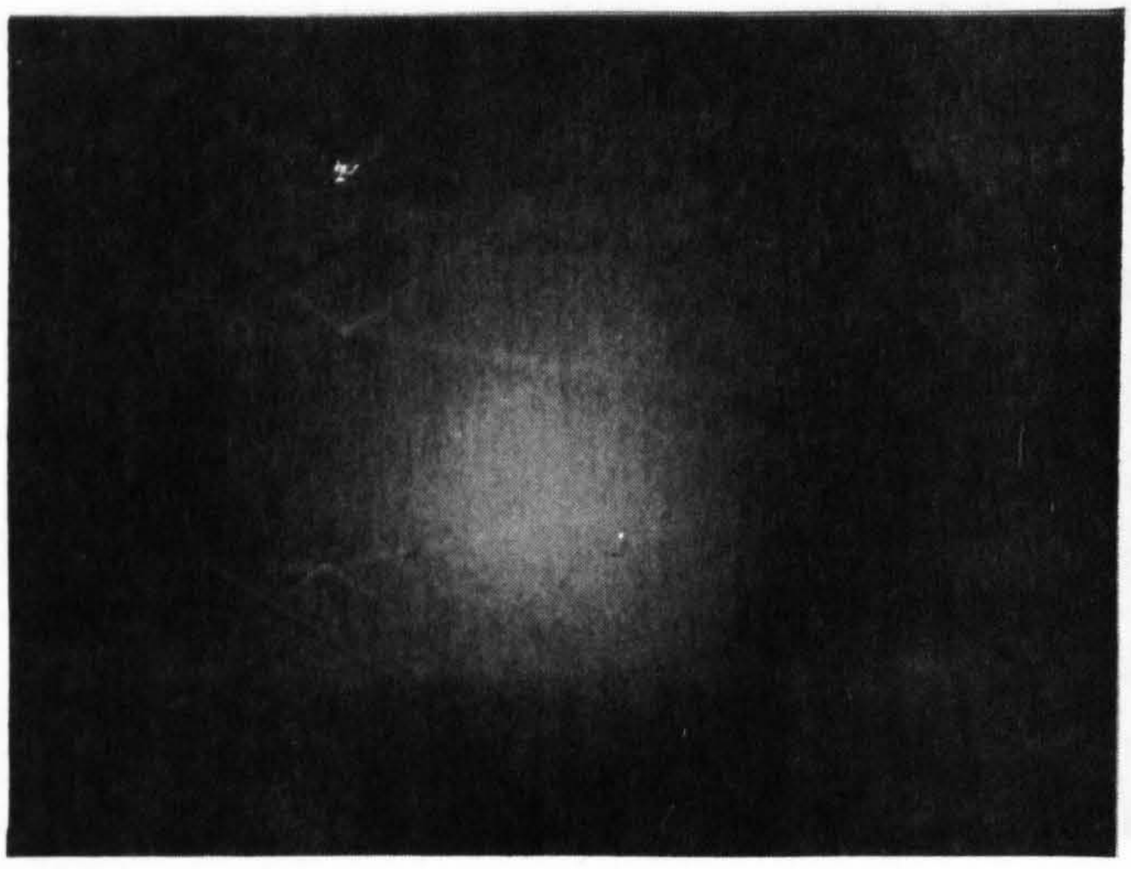

(d) $P_2/P_\infty = 1.39$, $P_b/P_\infty = 1.24$

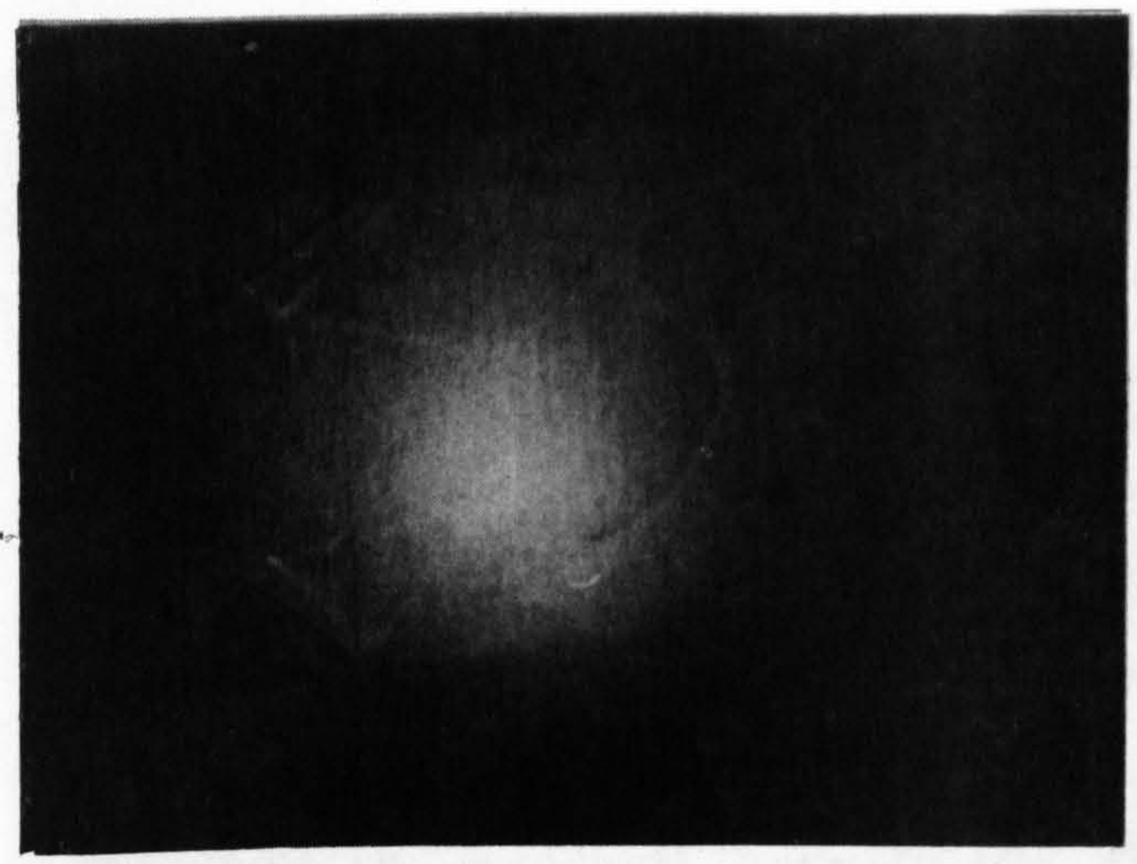

(e) $P_2/P_\infty = 1.57$, $P_b/P_\infty = 1.50$

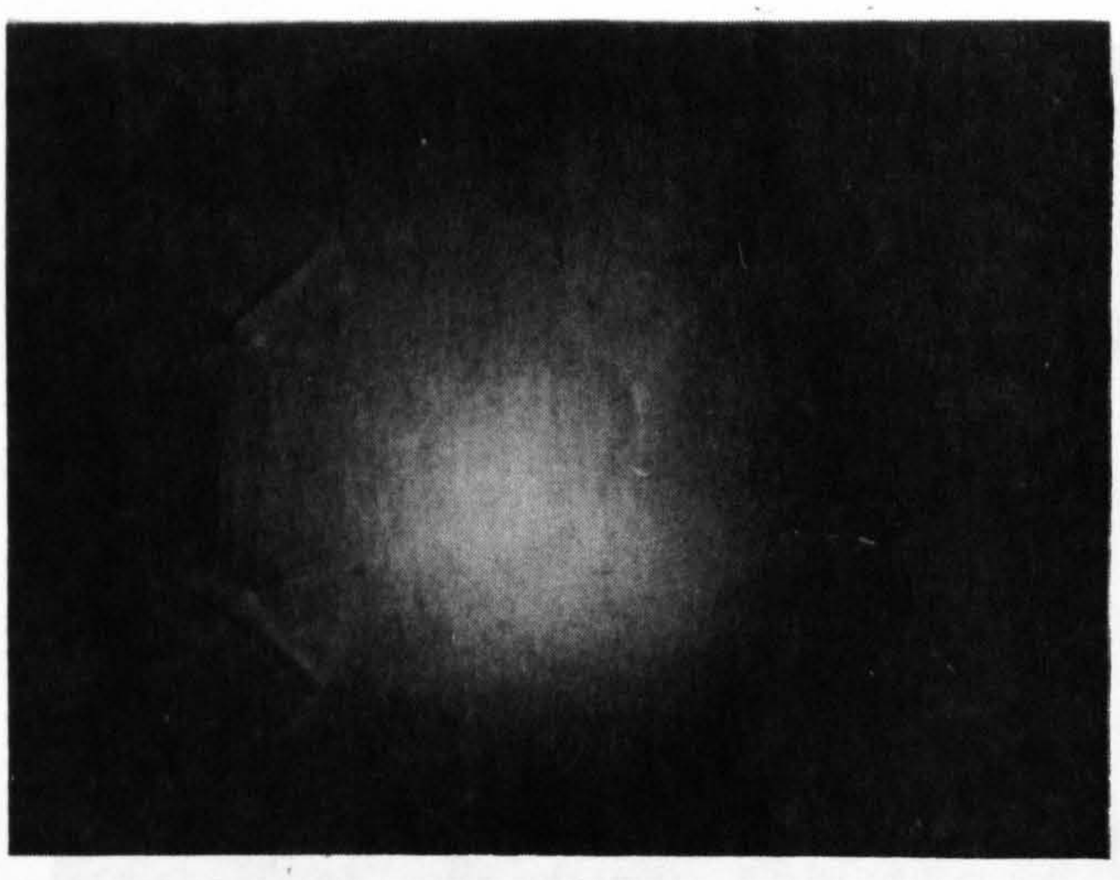

(f) $P_2/P_\infty = 1.82$, $P_b/P_\infty = 1.80$

Fig. 5.31 Shadowgraph Photographs. Recessed Base. No Bleed.

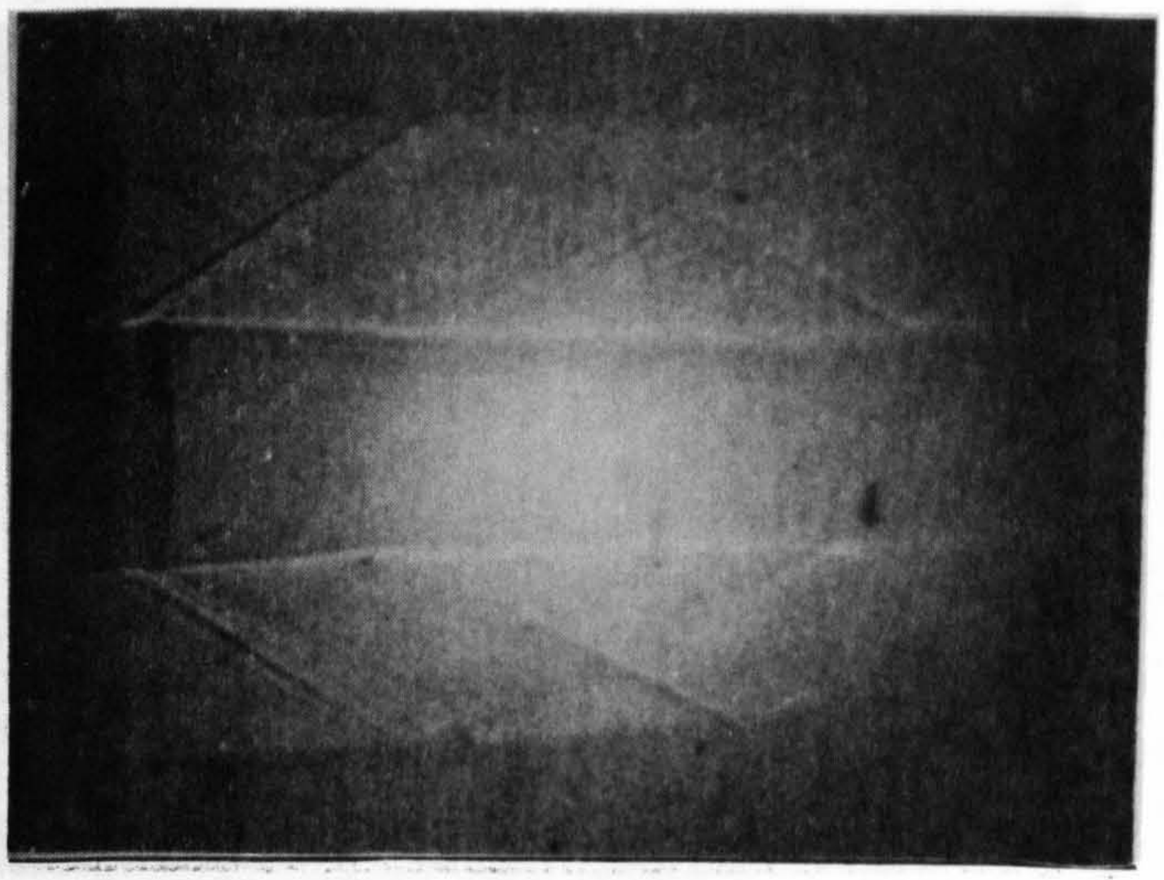

(a) P_2/P_∞ = 1.03, P_b/P_∞ = 0.92

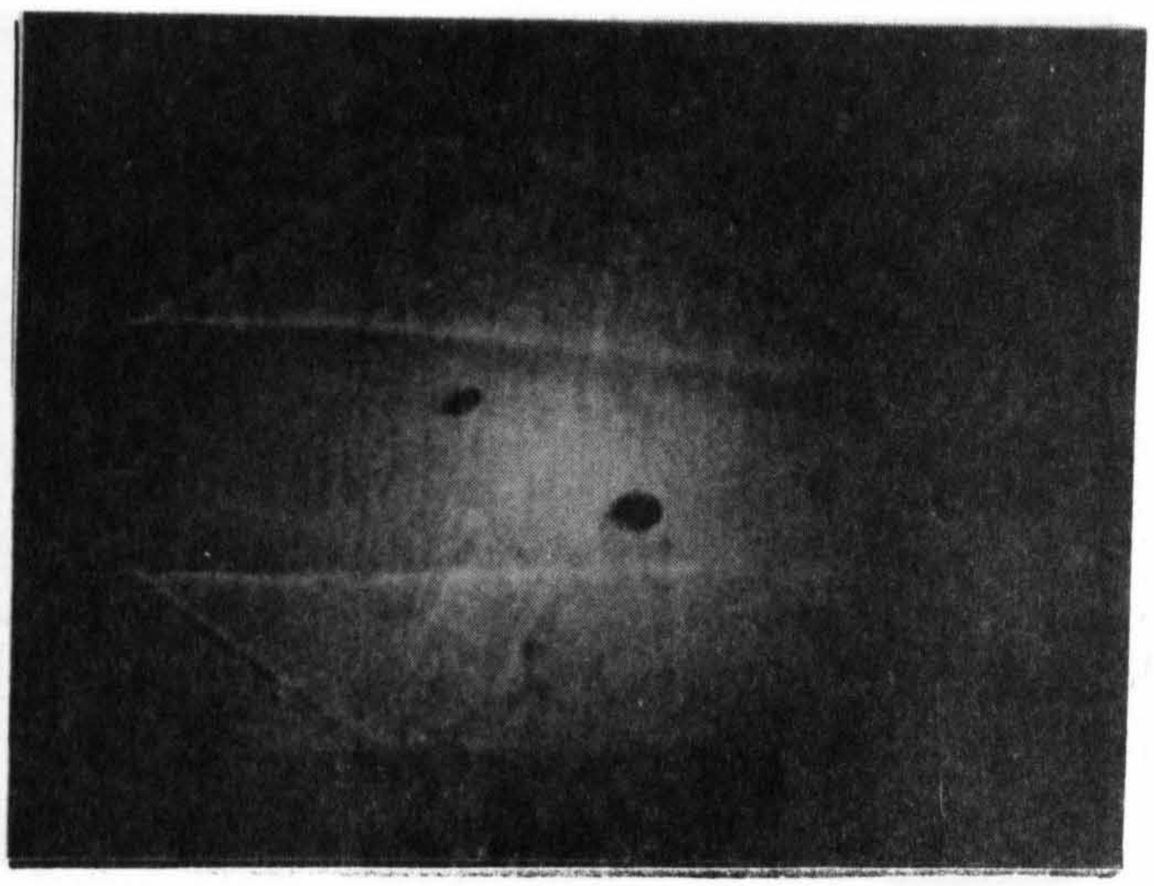

(b) P_2/P_∞ = 1.12, P_b/P_∞ = 1.05

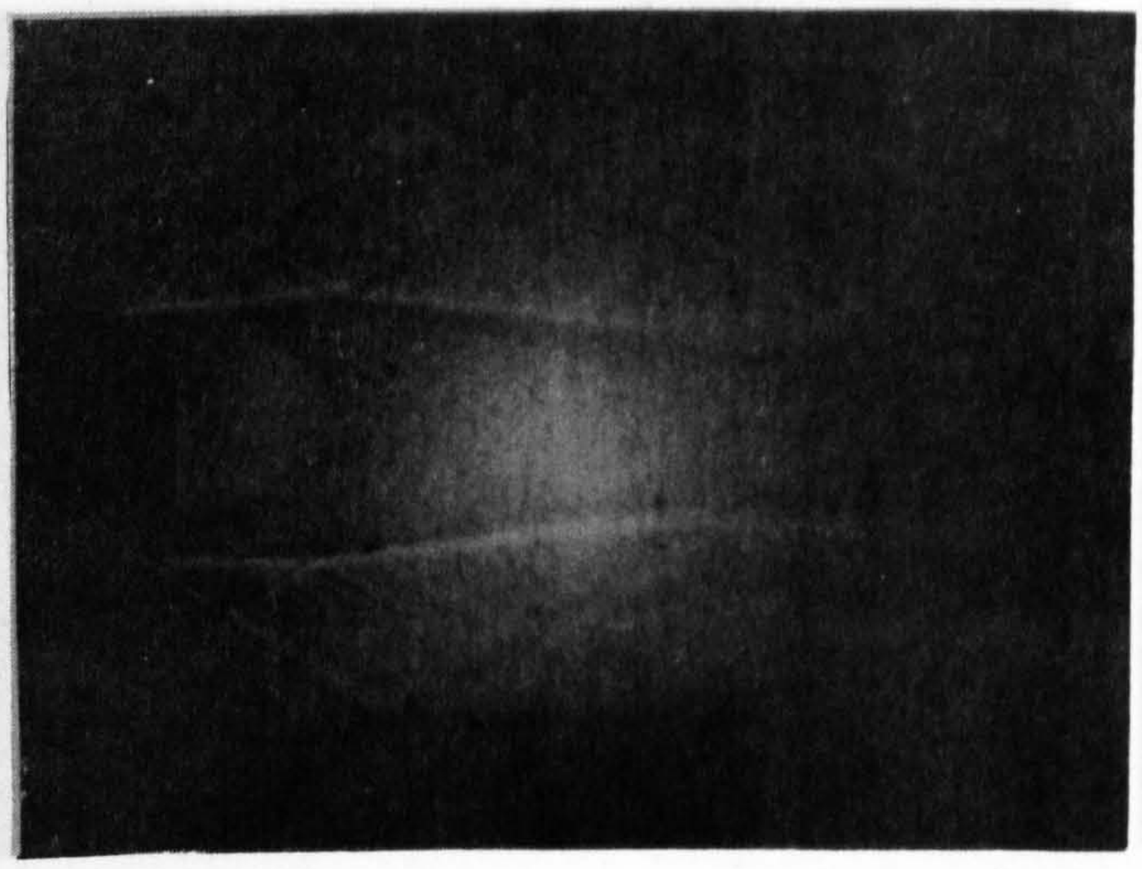

(c) P_2/P_∞ = 1.24, P_b/P_∞ = 1.19

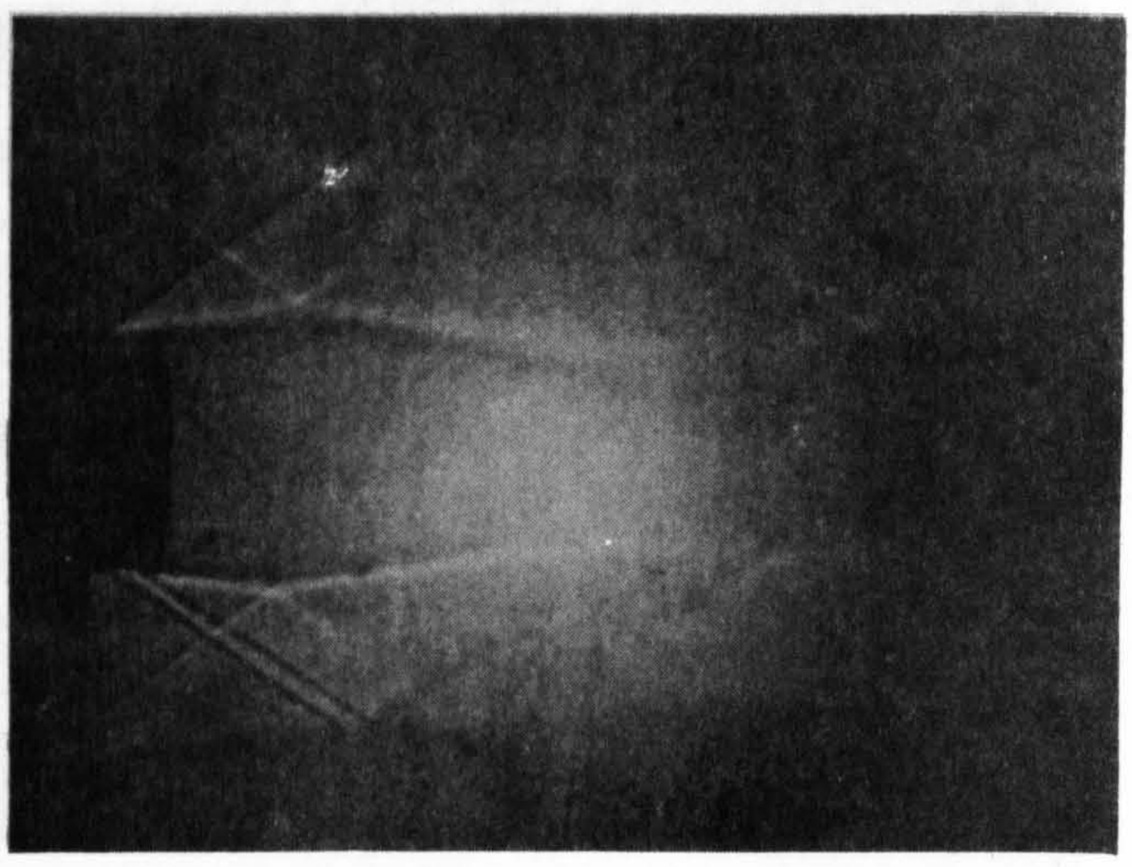

(d) P_2/P_∞ = 1.39, P_b/P_∞ = 1.36

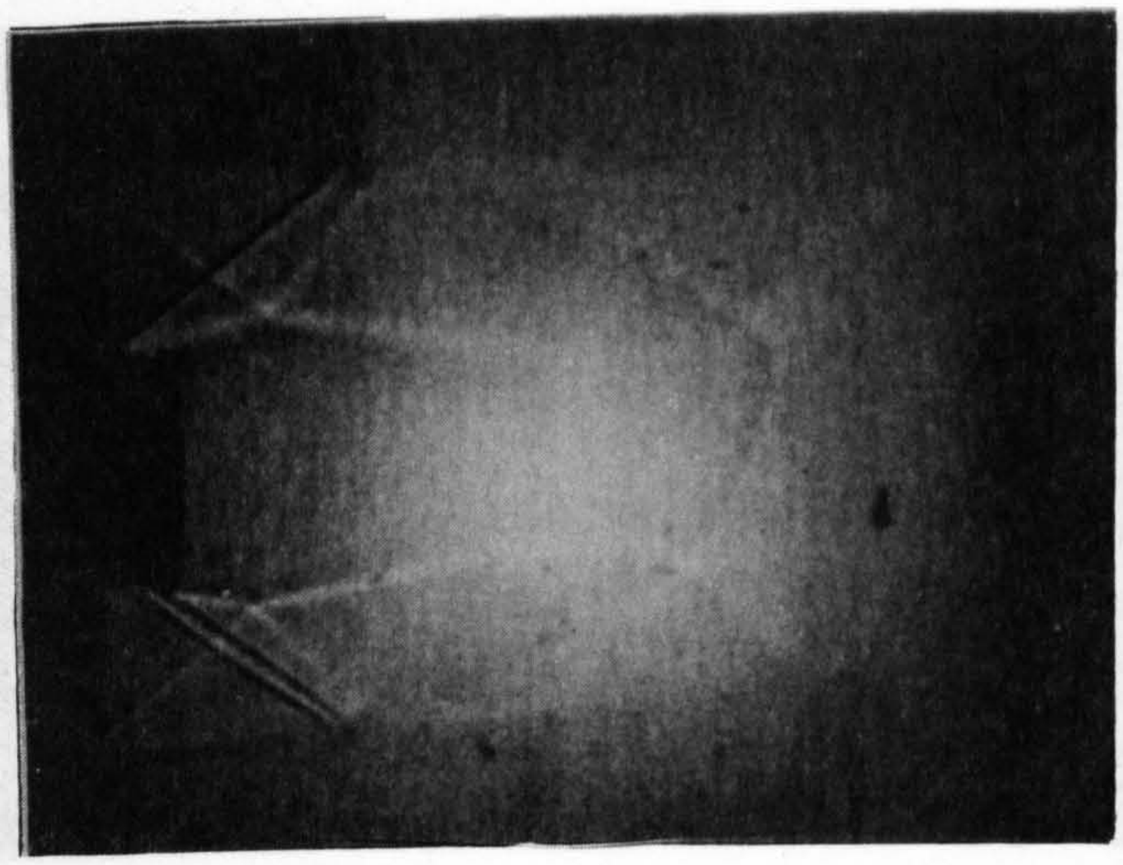

(e) P_2/P_∞ = 1.57, P_b/P_∞ = 1.60

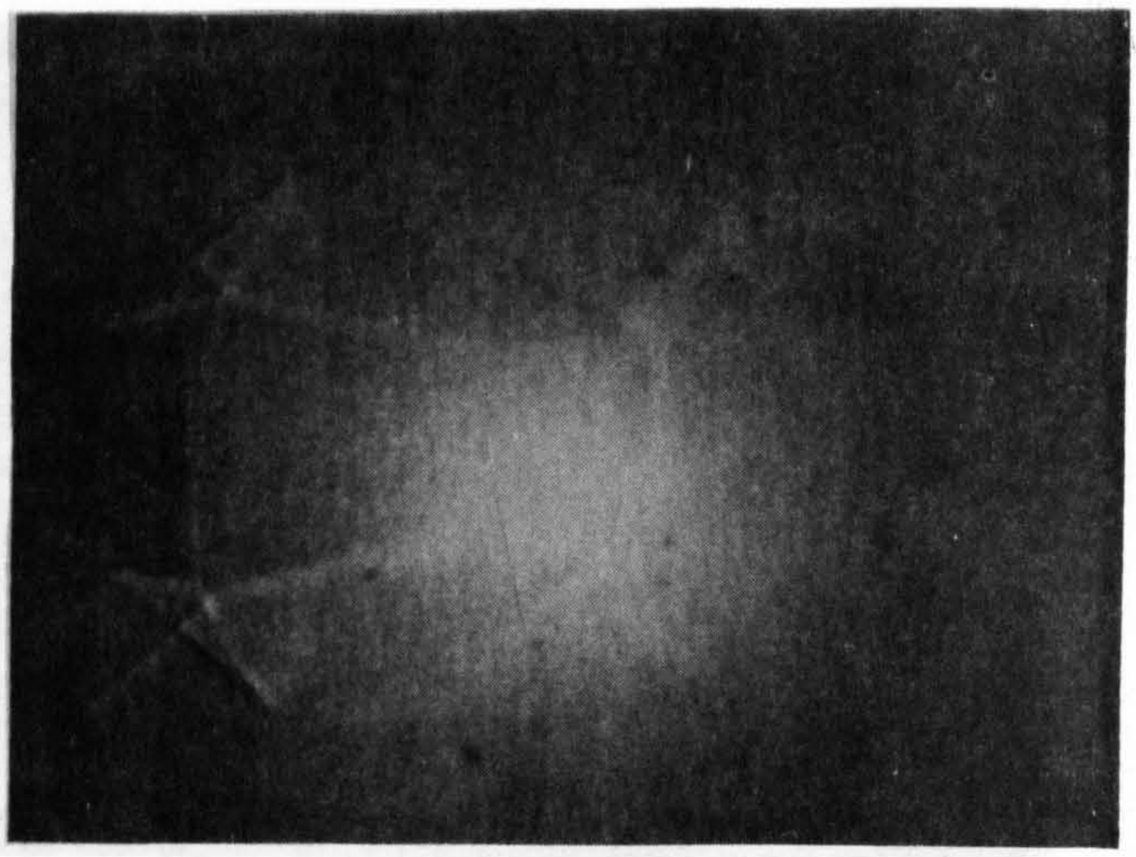

(f) P_2/P_∞ = 1.82, P_b/P_∞ = 1.84

Fig. 5.32 Shadowgraph Photographs. Recessed Base. H_2 Mass Flow Rate = 0.15 gm/sec.

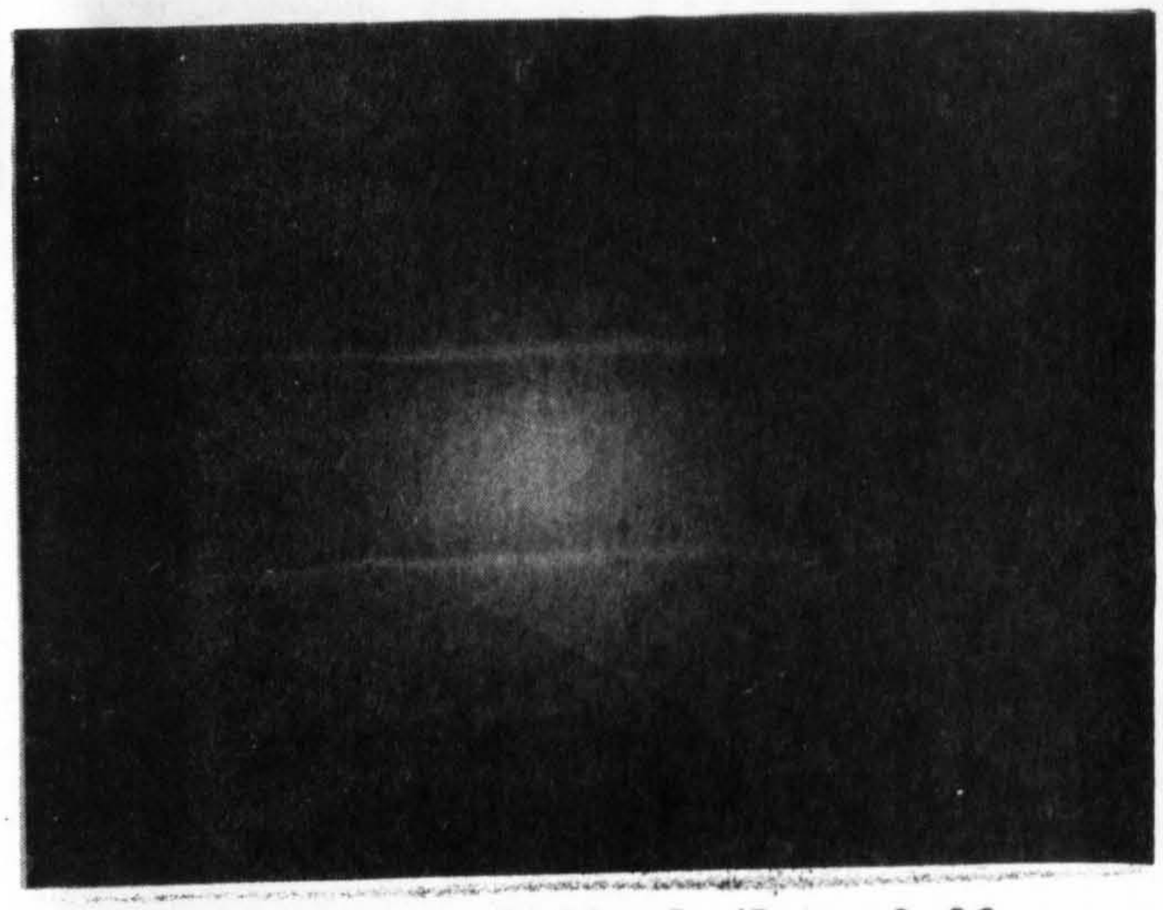

(a) $P_2/P_\infty = 1.03$, $P_b/P_\infty = 0.96$

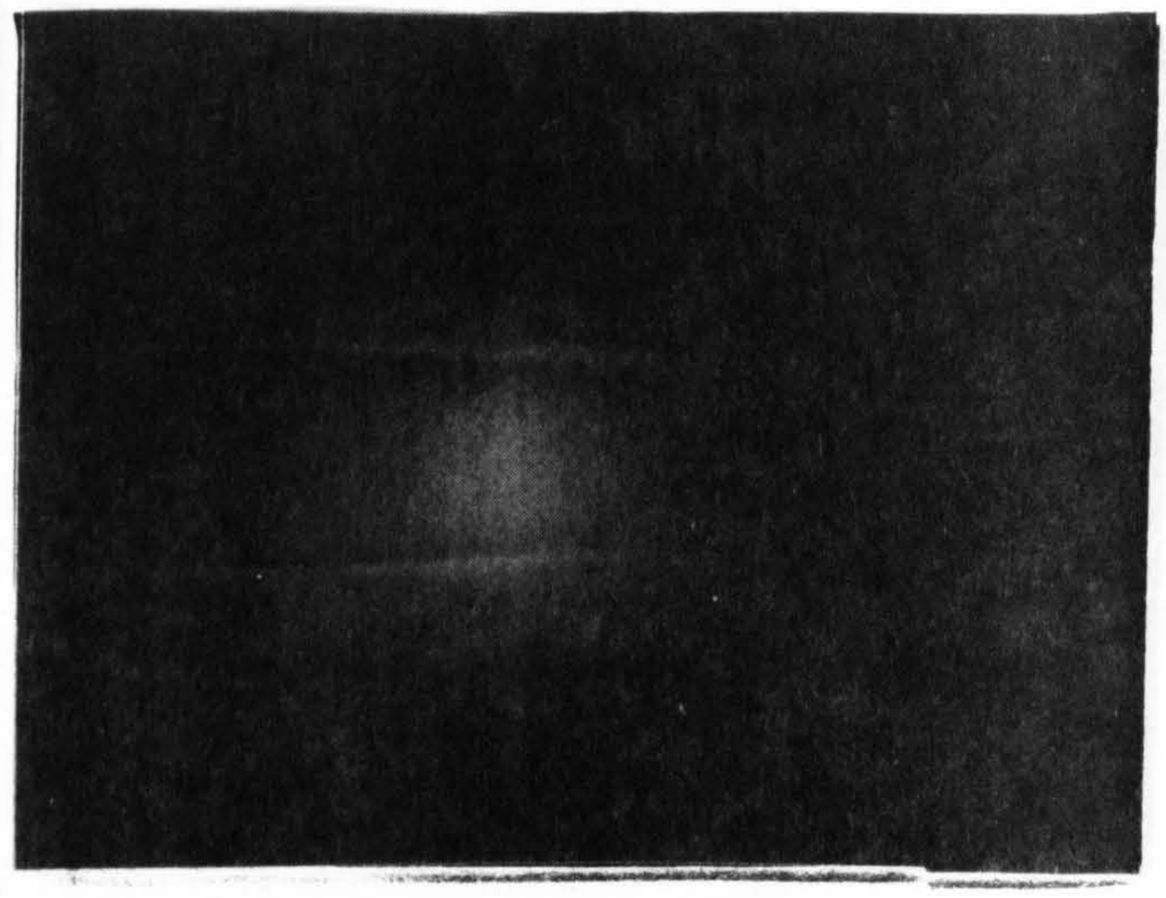

(b) $P_2/P_\infty = 1.12$, $P_b/P_\infty = 1.08$

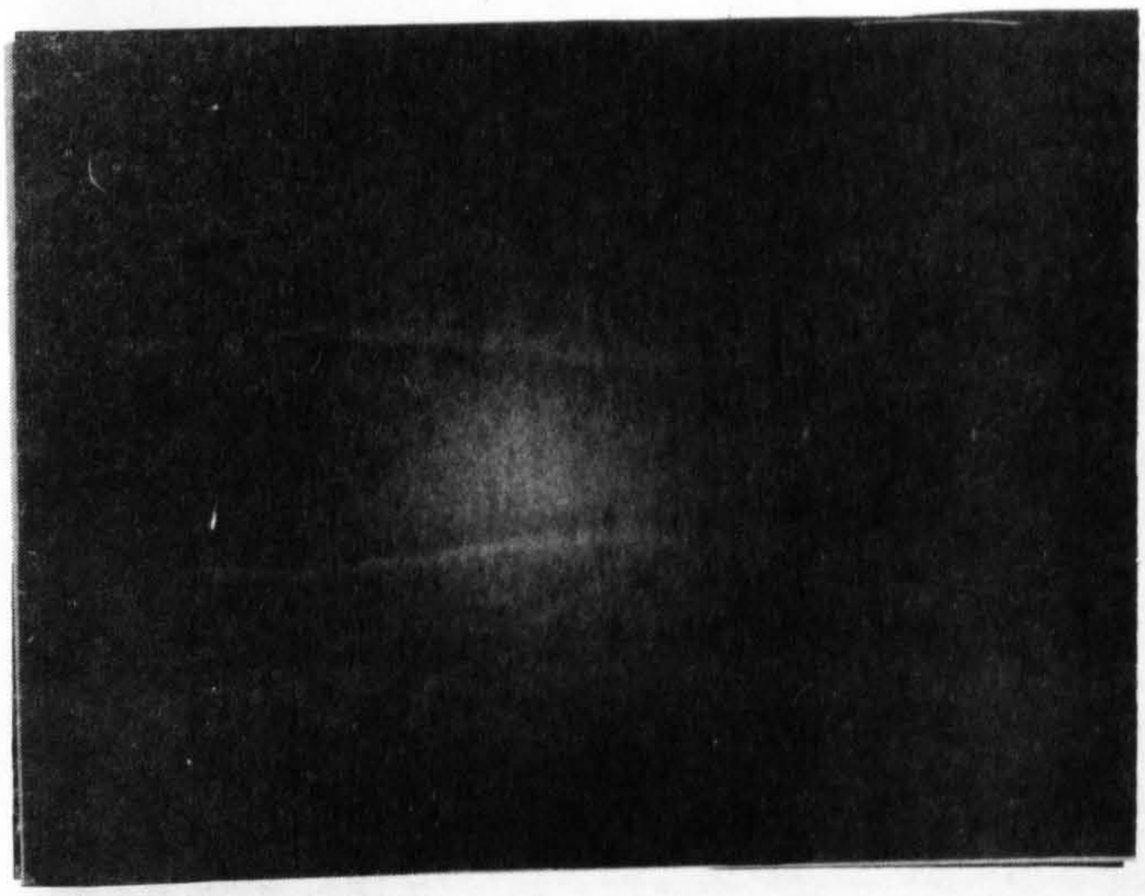

(c) $P_2/P_\infty = 1.24$, $P_b/P_\infty = 1.22$

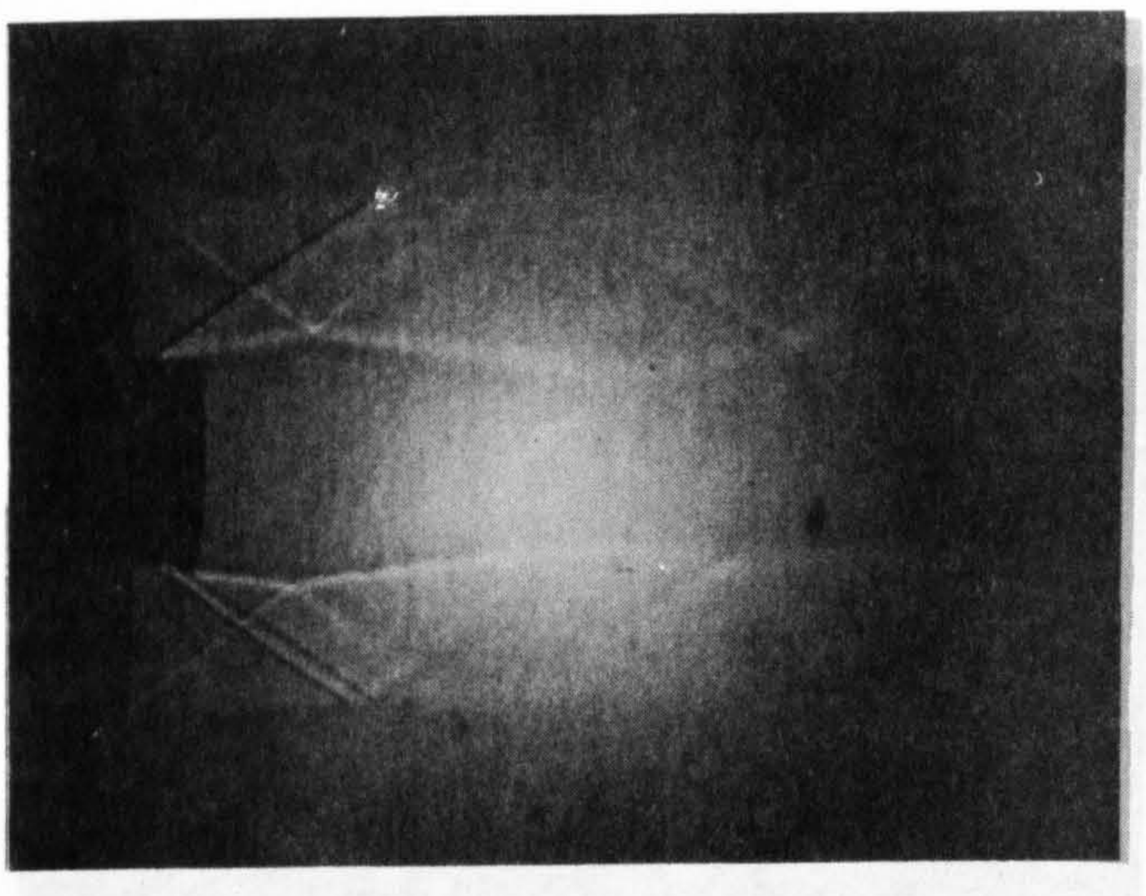

(d) $P_2/P_\infty = 1.39$, $P_b/P_\infty = 1.40$

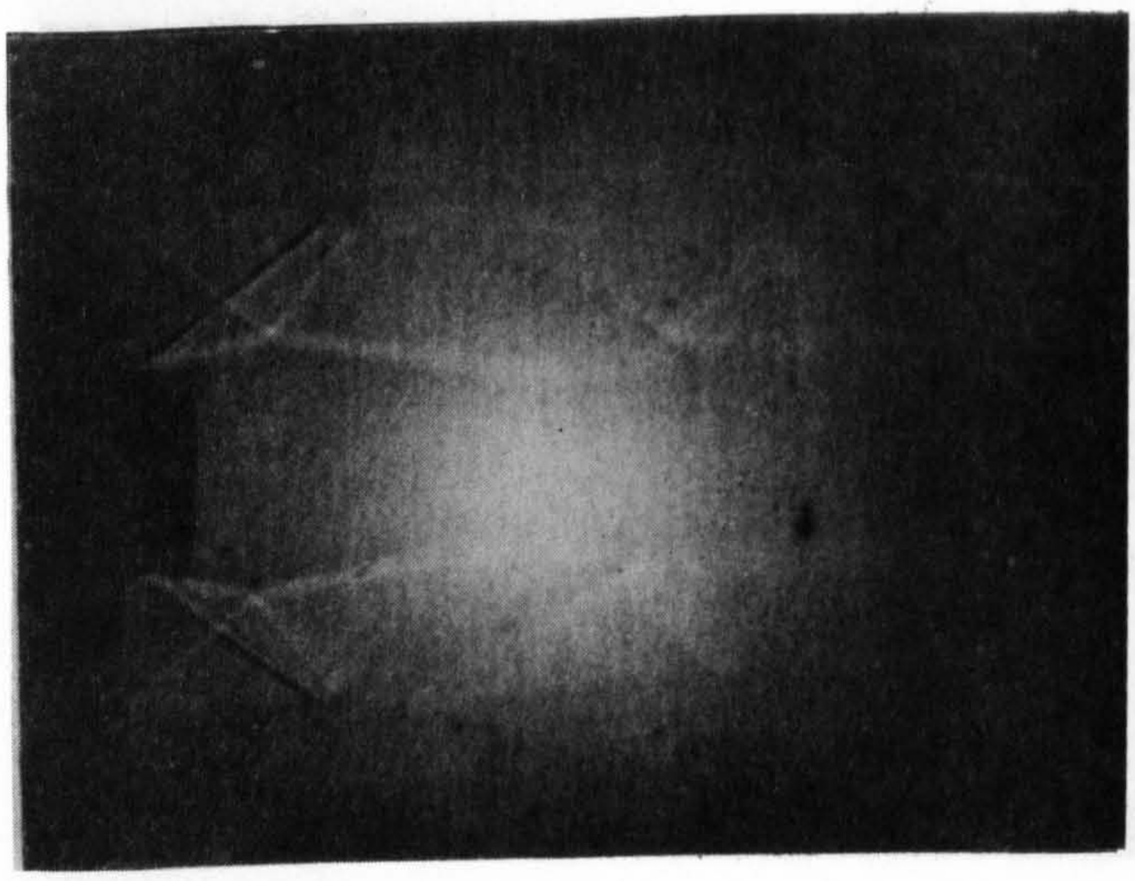

(e) $P_2/P_\infty = 1.57$, $P_b/P_\infty = 1.62$

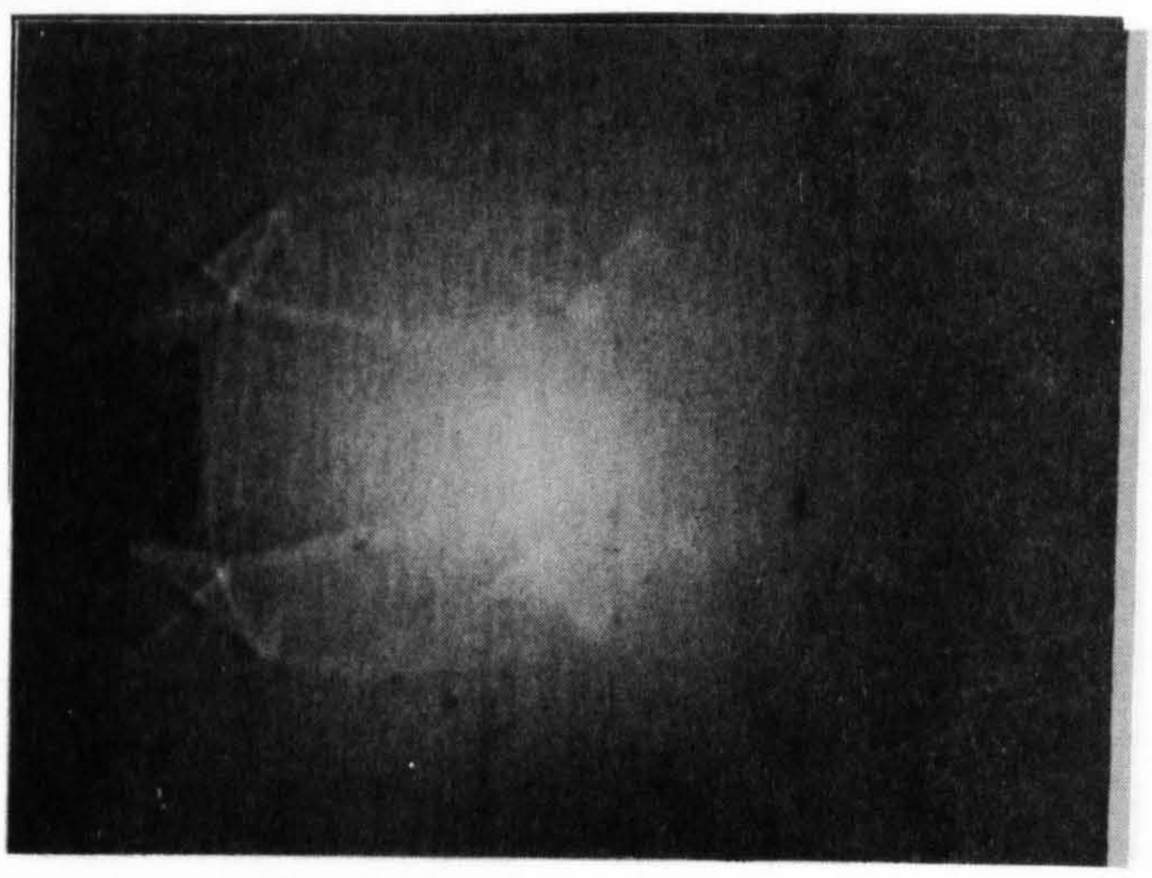

(f) $P_2/P_\infty = 1.82$, $P_b/P_\infty = 1.84$

Fig. 5.33 Shadowgraph Photographs - recessed base, H_2 mass flow rate = 0.23 gm/sec

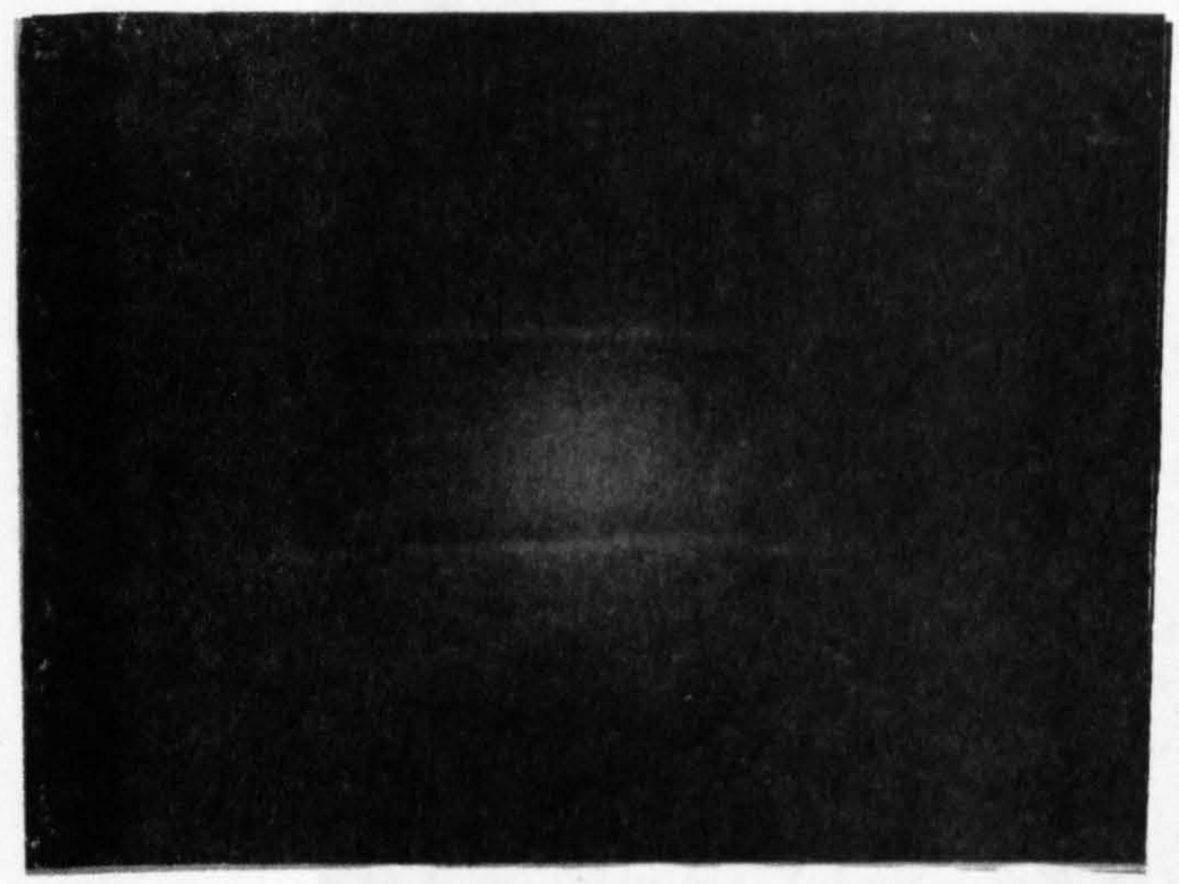

(a) $P_2/P_\infty = 1.03$, $P_b/P_\infty = 0.97$

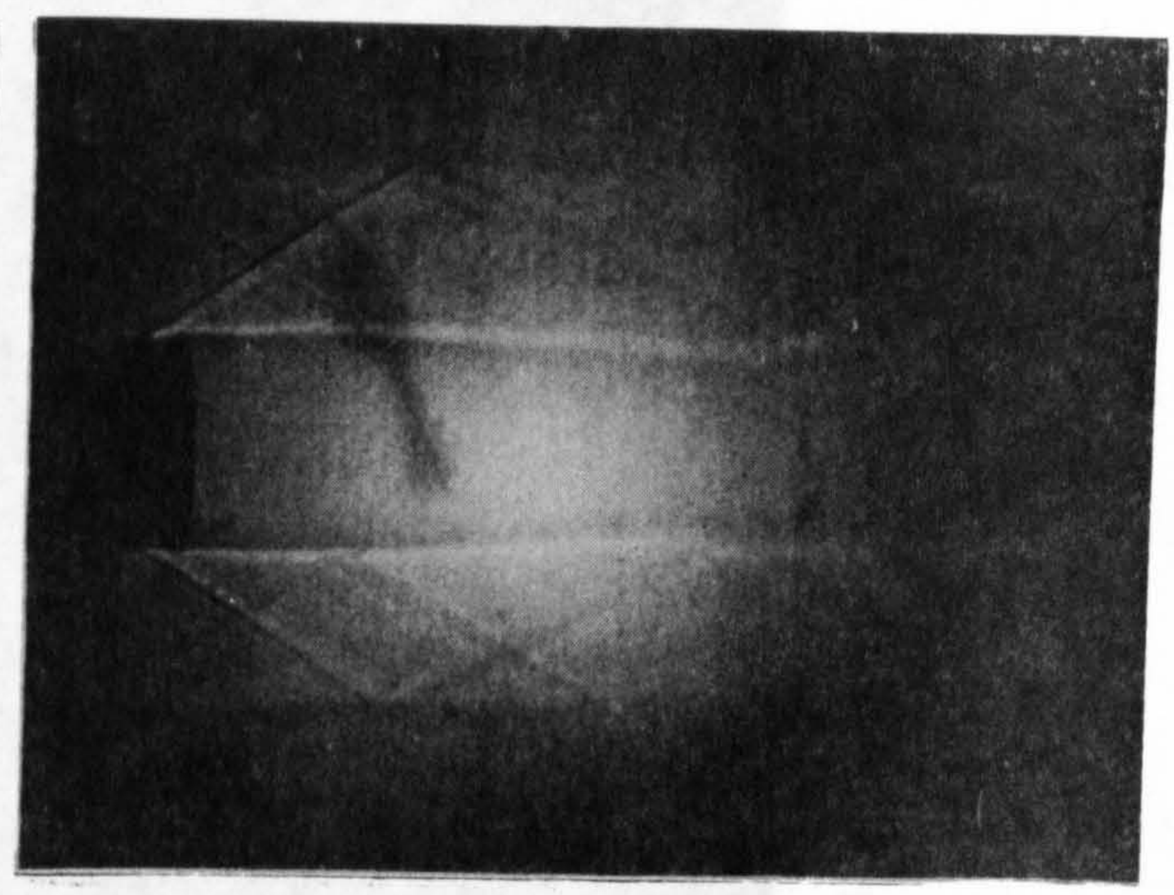

(b) $P_2/P_\infty = 1.12$, $P_b/P_\infty = 1.09$

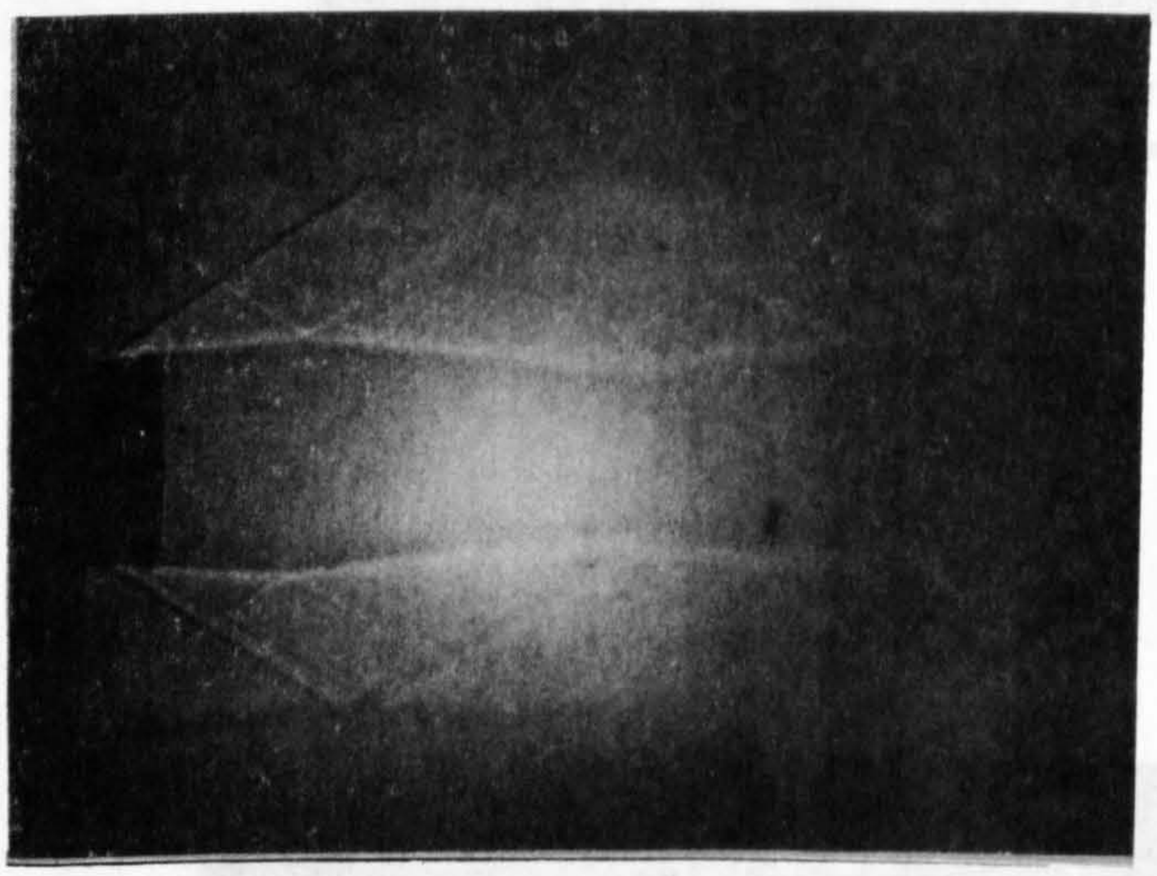

(c) $P_2/P_\infty = 1.24$, $P_b/P_\infty = 1.23$

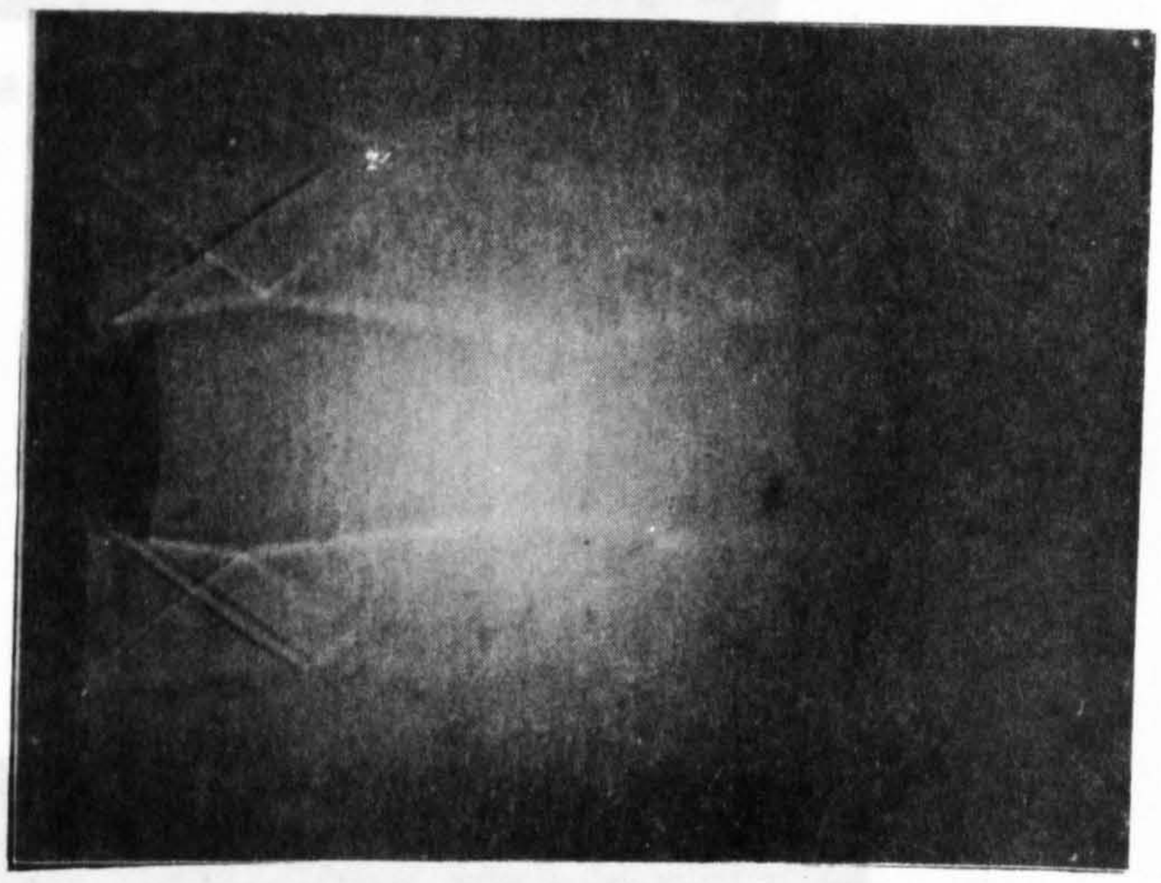

(d) $P_2/P_\infty = 1.39$, $P_b/P_\infty = 1.41$

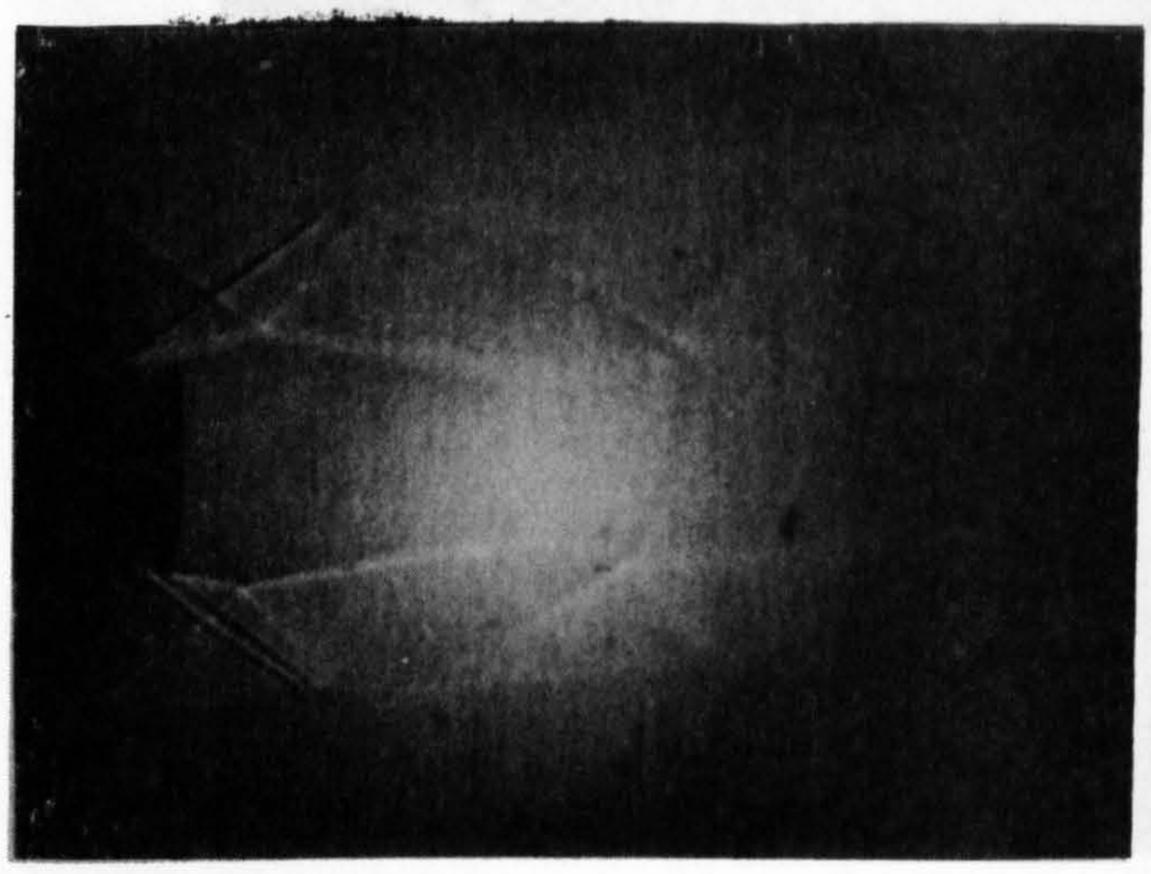

(e) $P_2/P_\infty = 1.57$, $P_b/P_\infty = 1.64$

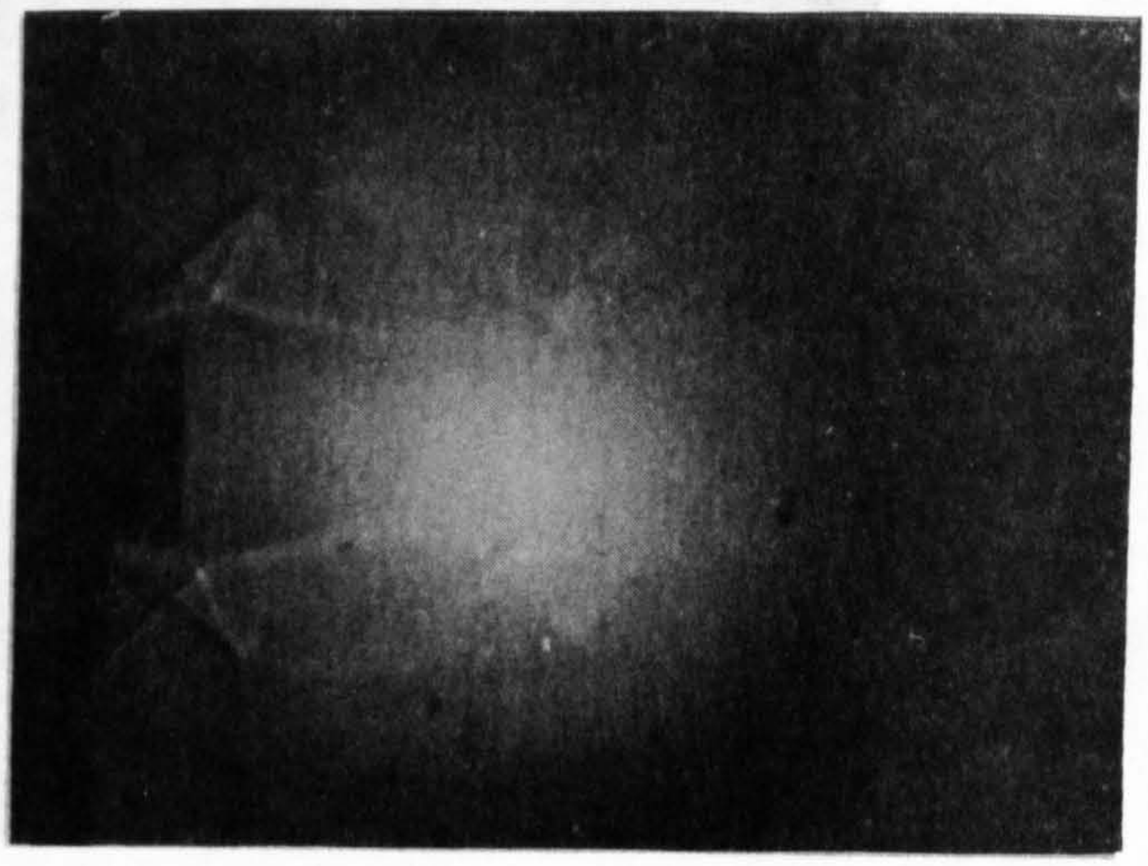

(f) $P_2/P_\infty = 1.82$, $P_b/P_\infty = 1.87$

Fig. 5.34 Shadowgraph Photographs - recessed base, H_2 mass flow rate = 0.3 gm/sec

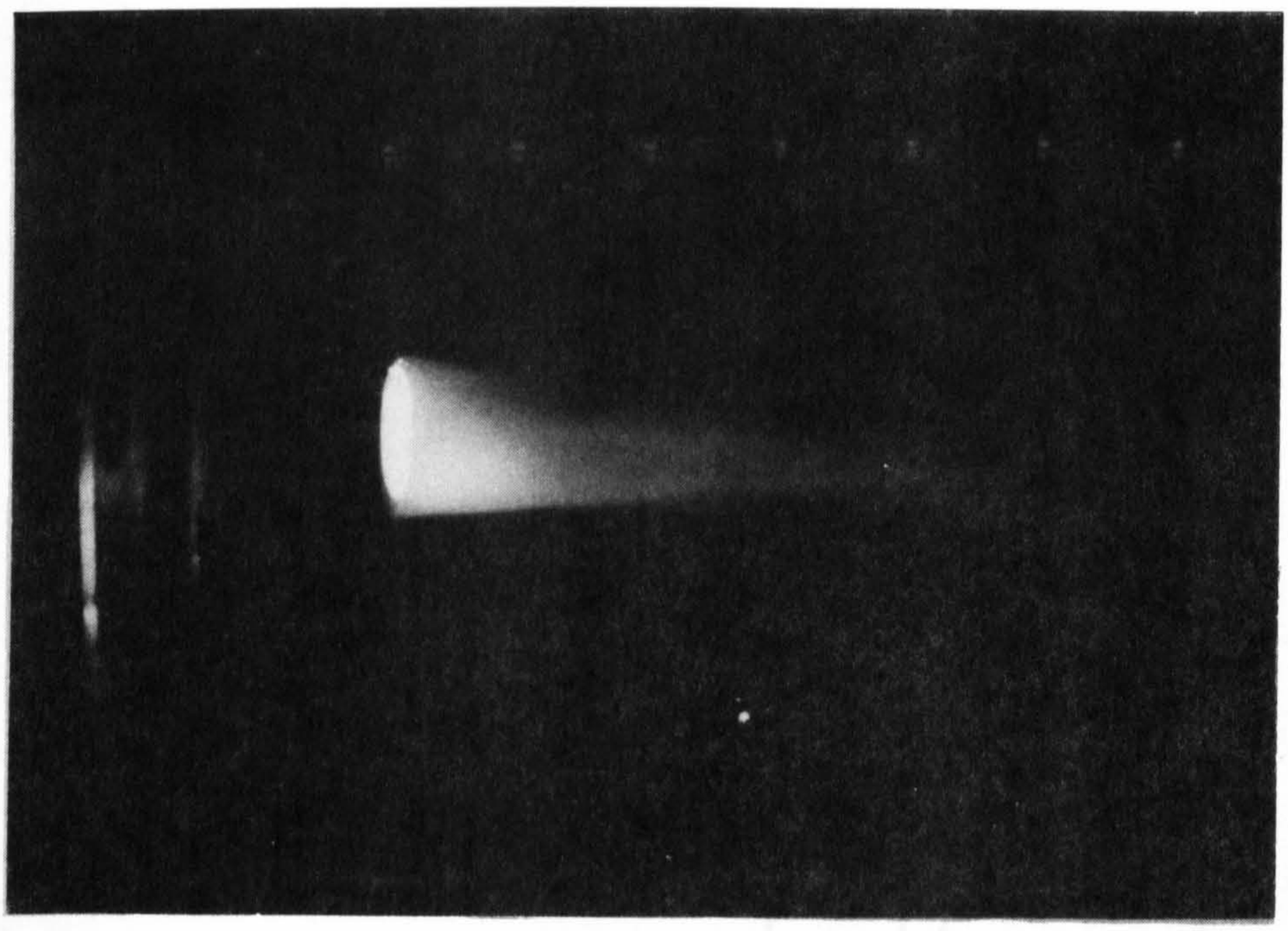

5.35 Direct Luminosity Photograph - recessed base,
Hydrogen mass flow rate = 0.3 gm/sec - P_2/P_∞ = 0.98

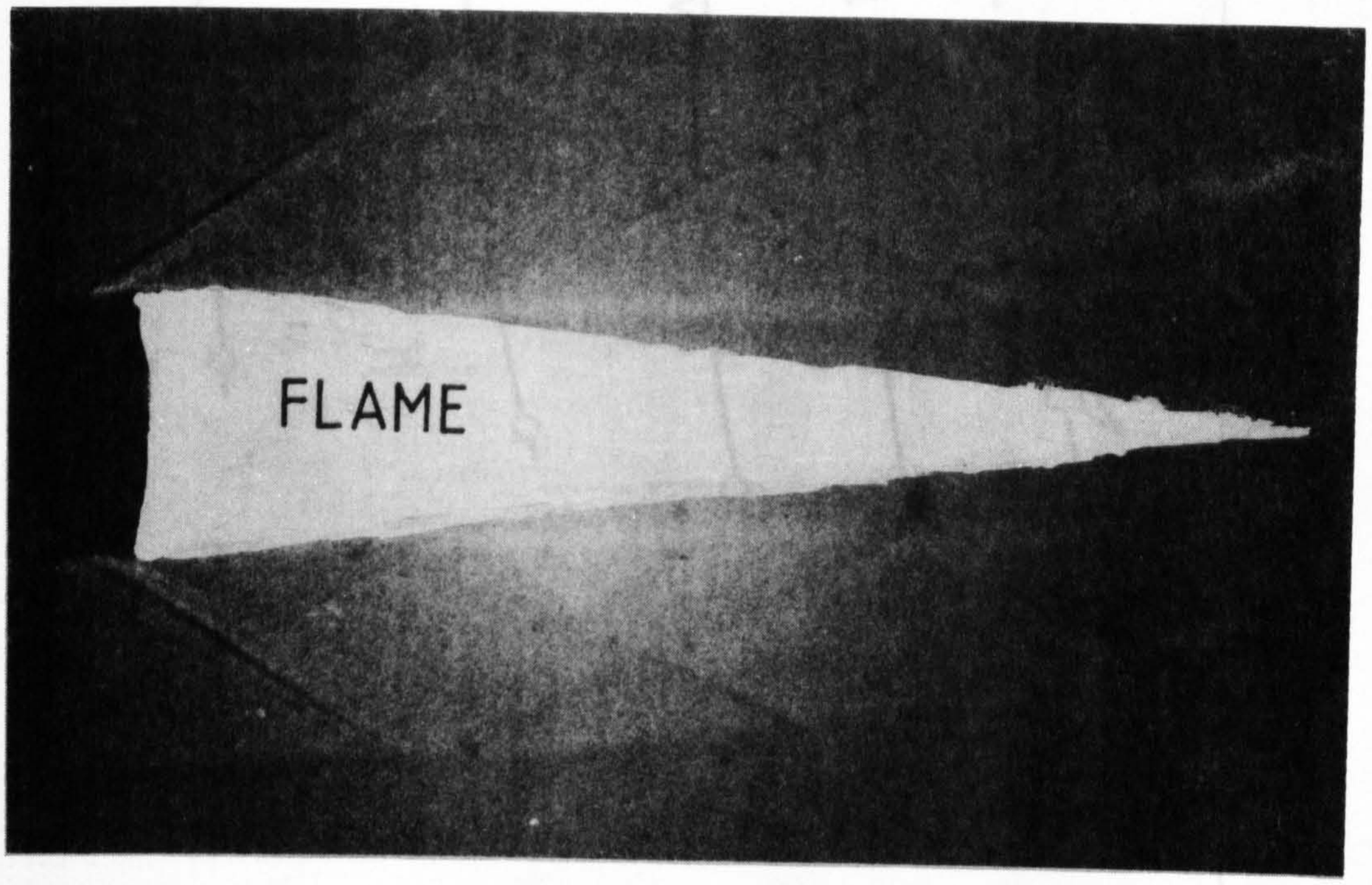

5.36 Shadowgraph Photograph - recessed base,
Hydrogen mass flow rate = 0.3 gm/sec - P_2/P_∞ = 0.98
showing flame superimposed (see fig. 5.35)

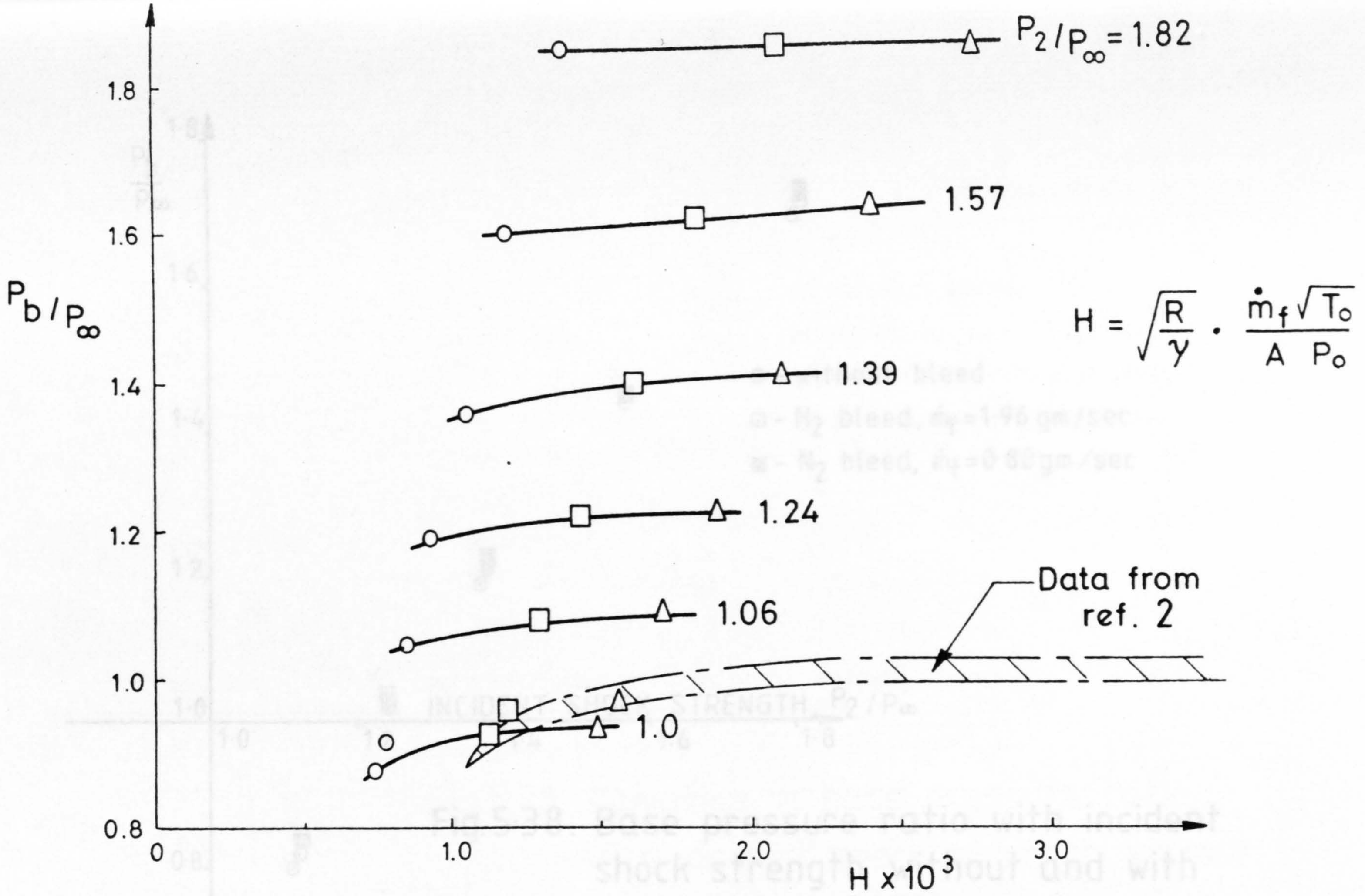

Figure 5.37. Base pressure ratio vs mass flow parameter for varying incident shock strength (P_2/P_∞)

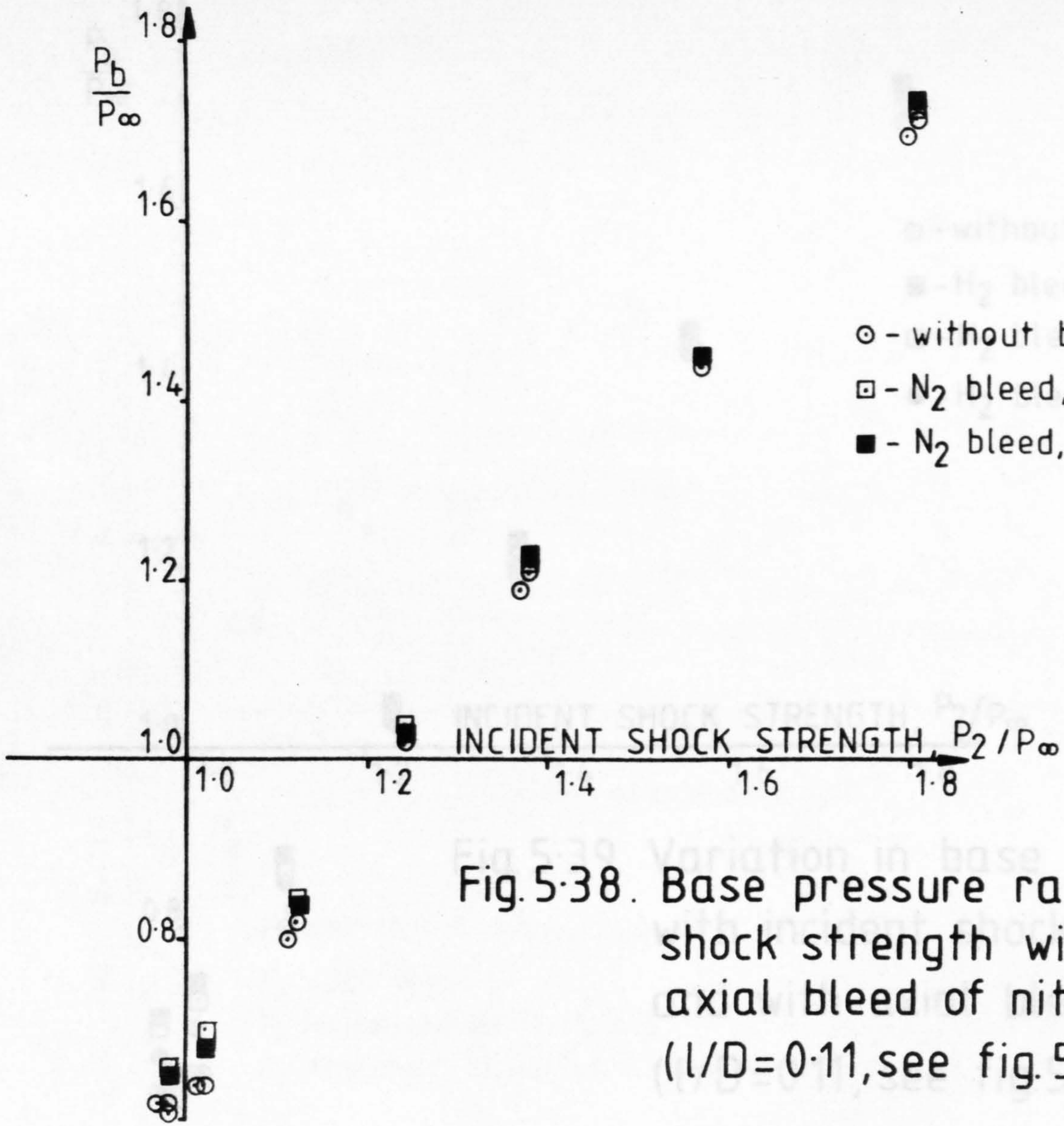

Fig. 5·38. Base pressure ratio with incident shock strength without and with axial bleed of nitrogen.
(l/D = 0·11, see fig. 5·28)

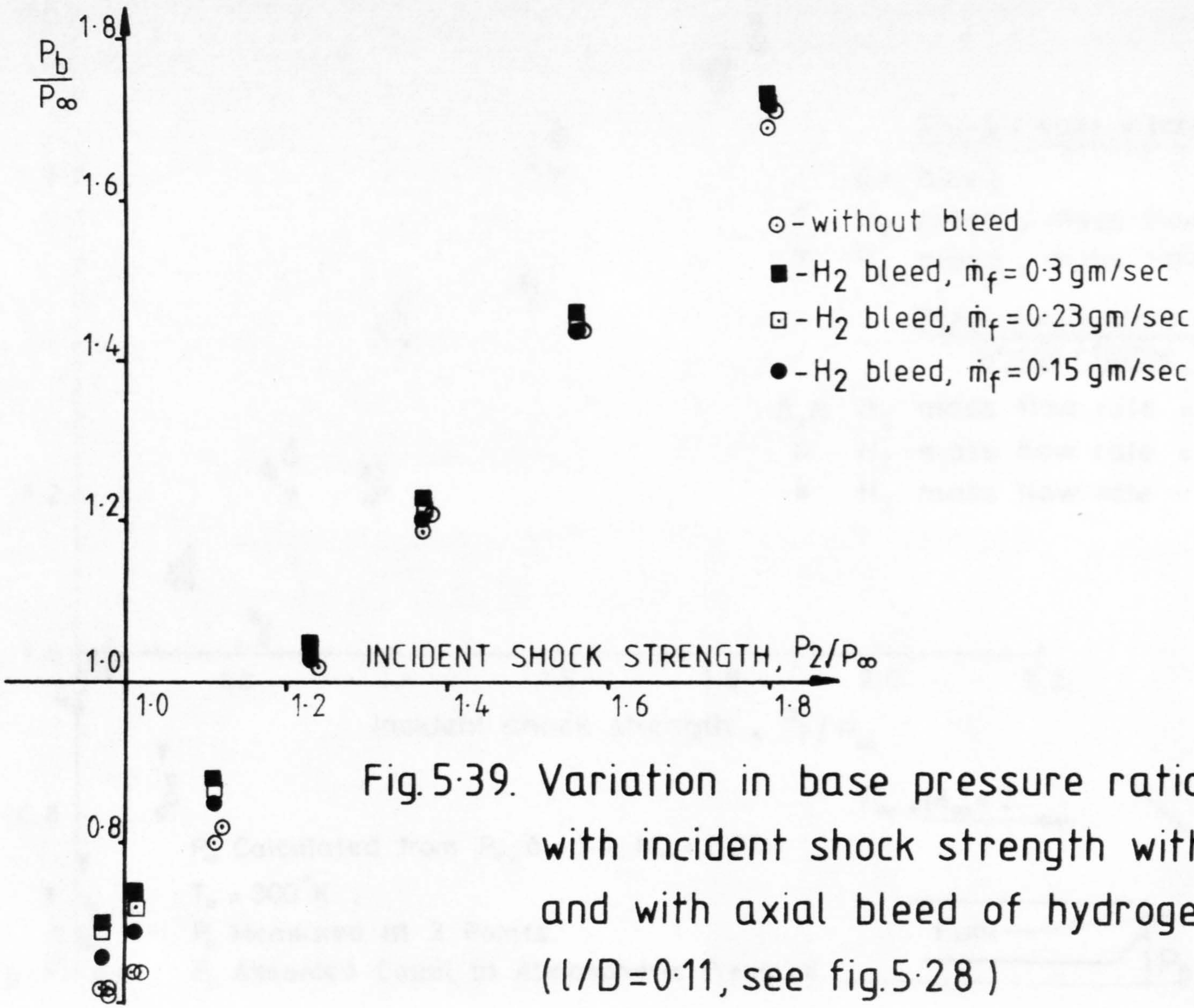

Fig. 5·39. Variation in base pressure ratio with incident shock strength without and with axial bleed of hydrogen. (l/D = 0·11, see fig. 5·28)

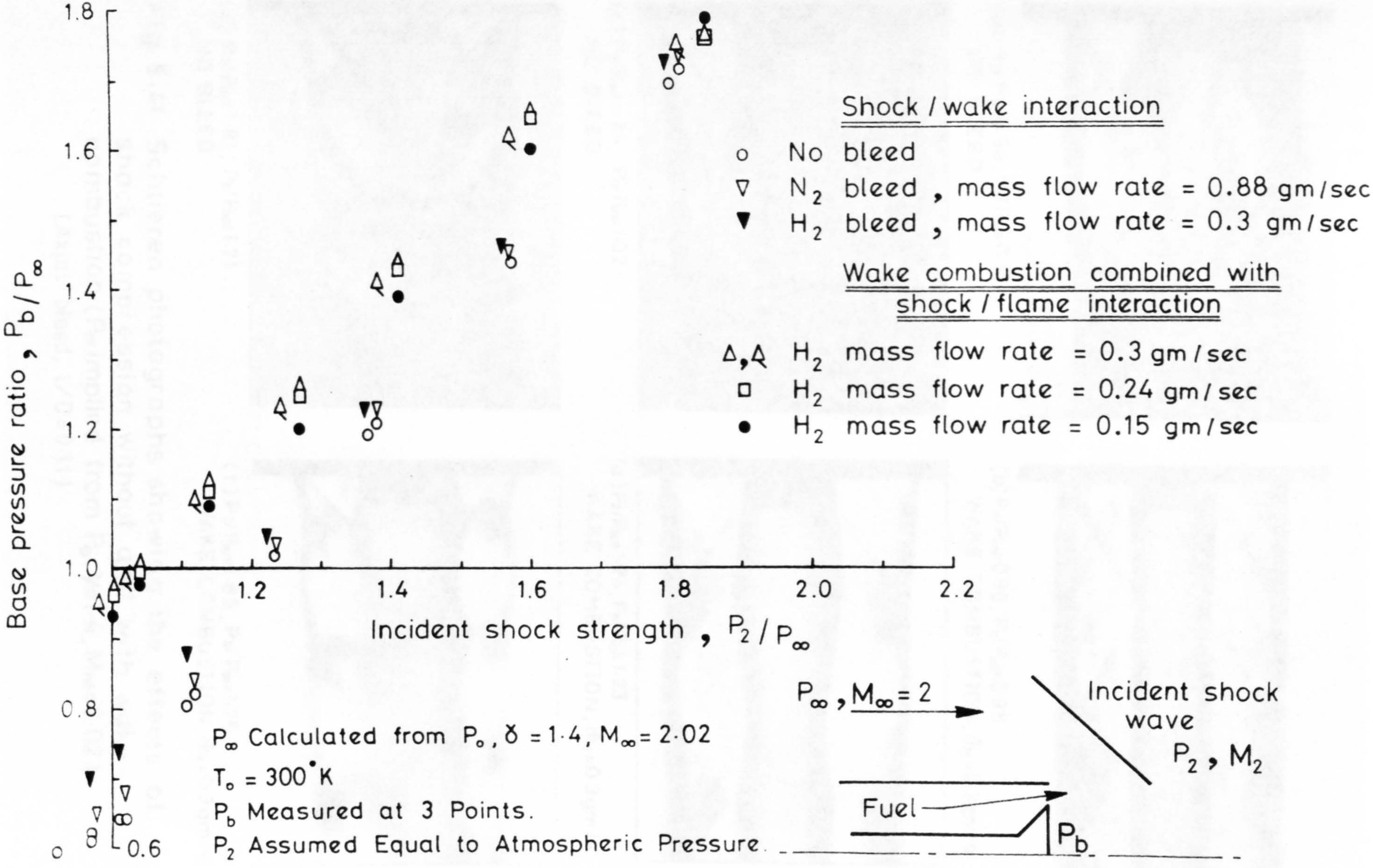

Fig. 5·40. Wake combustion combined with shock / flame interaction. (axial bleed) l/D=0·11 (see fig. 5·28)

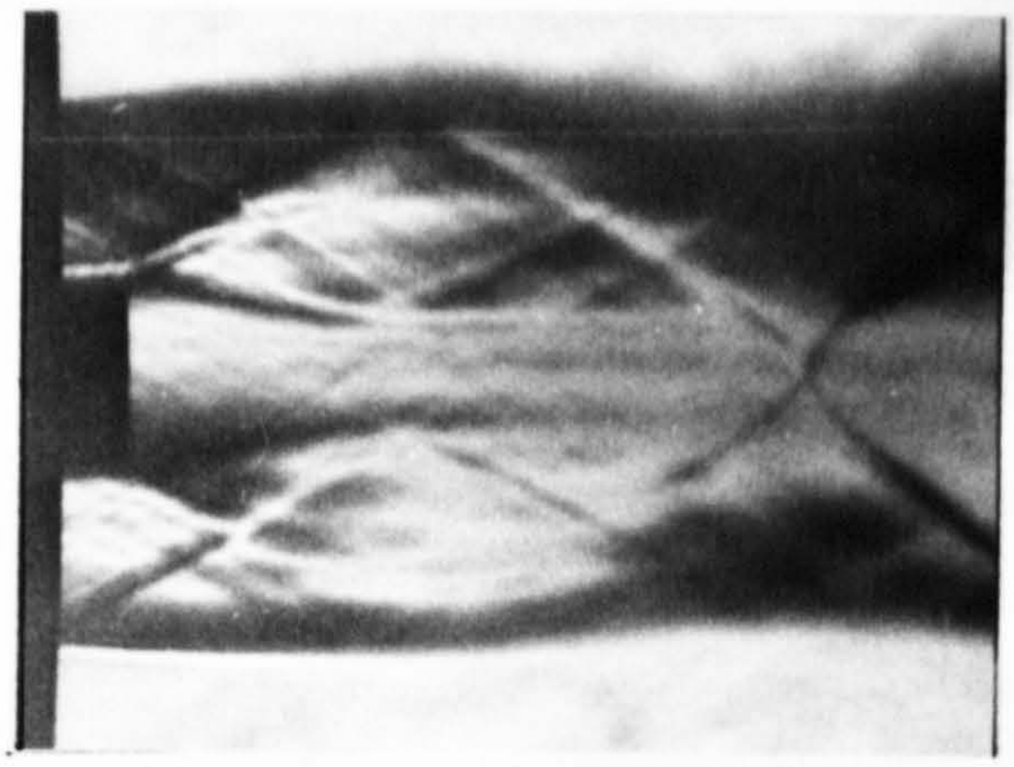

(a) $P_2/P_\infty = 0.98$, $P_b/P_\infty = 0.61$
NO BLEED

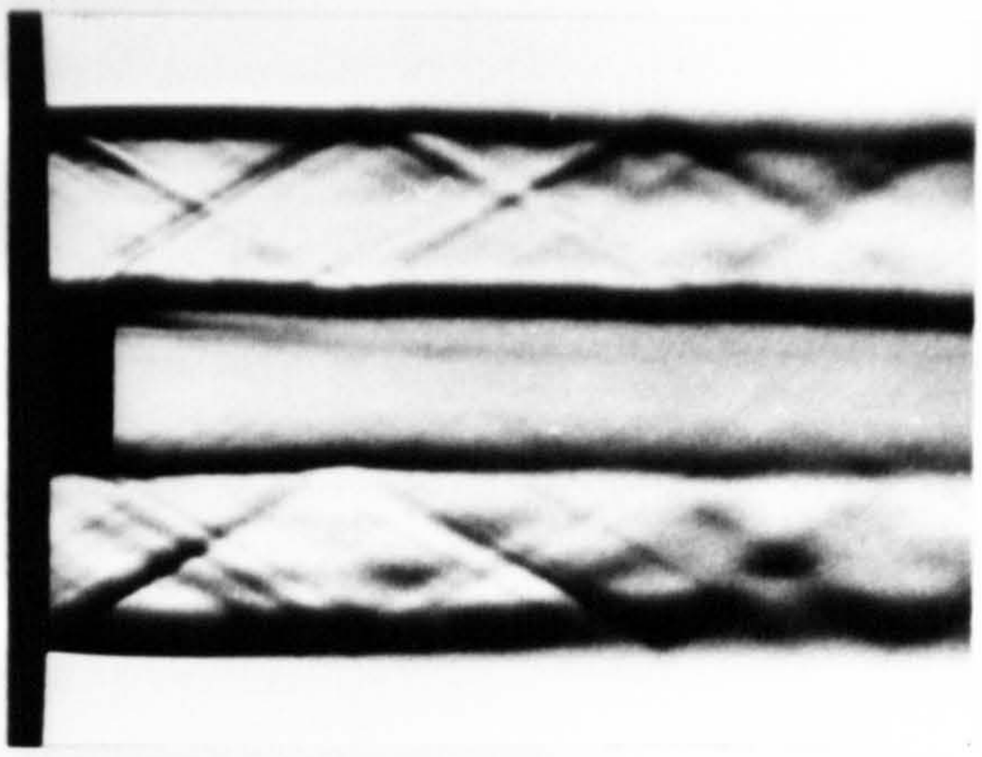

(b) $P_2/P_\infty = 0.98$, $P_b/P_\infty = 0.95$
WAKE COMBUSTION, $\dot{m}_f = 0.3$ gm/s

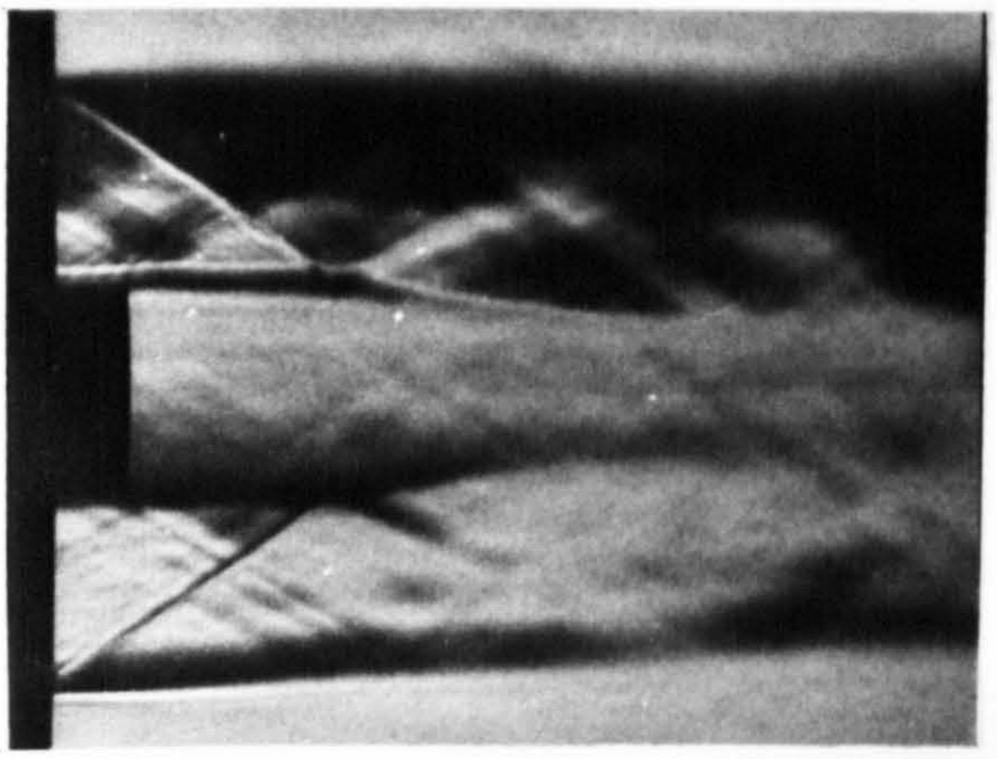

(c) $P_2/P_\infty = 1.24$, $P_b/P_\infty = 1.02$
NO BLEED

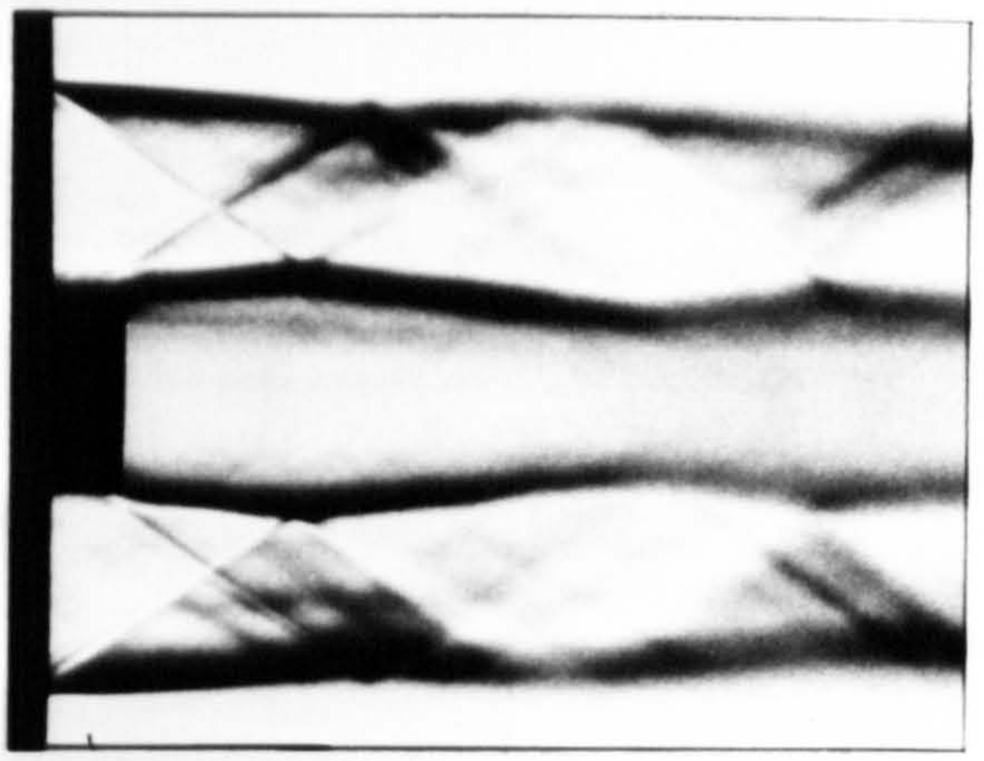

(d) $P_2/P_\infty = 1.24$, $P_b/P_\infty = 1.23$
WAKE COMBUSTION, $\dot{m}_f = 0.3$ gm/s

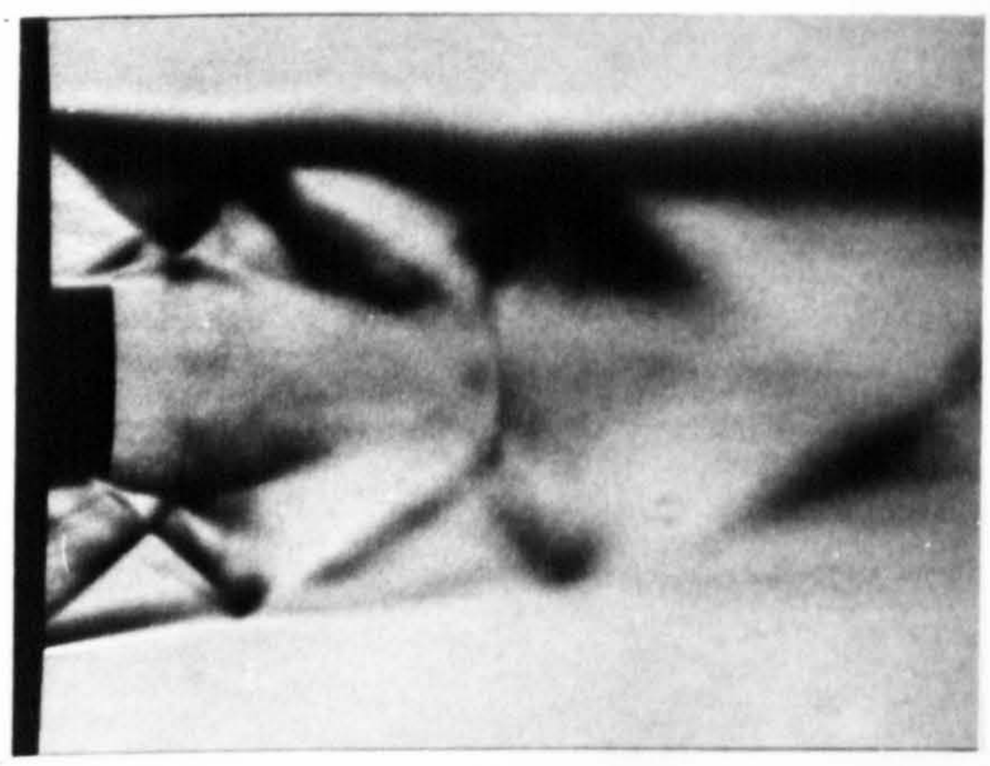

(e) $P_2/P_\infty = 1.81$, $P_b/P_\infty = 1.71$
NO BLEED

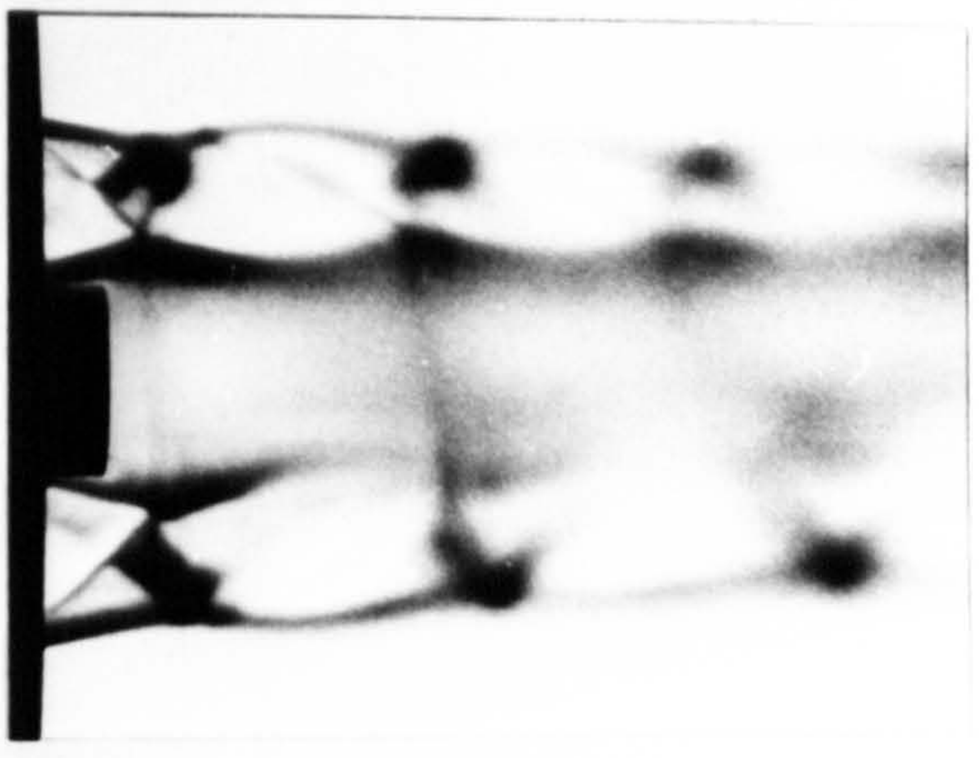

(f) $P_2/P_\infty = 1.85$, $P_b/P_\infty = 1.76$
WAKE COMBUSTION, $\dot{m}_f = 0.3$ gm/s

Fig. 5.41 Schlieren photographs showing the effects of shock compression without and with wake combustion (P_∞ implied from P_o, $\gamma = 1.4$, $M_\infty = 2.02$)
(Axial bleed, $l/D = 0.11$)

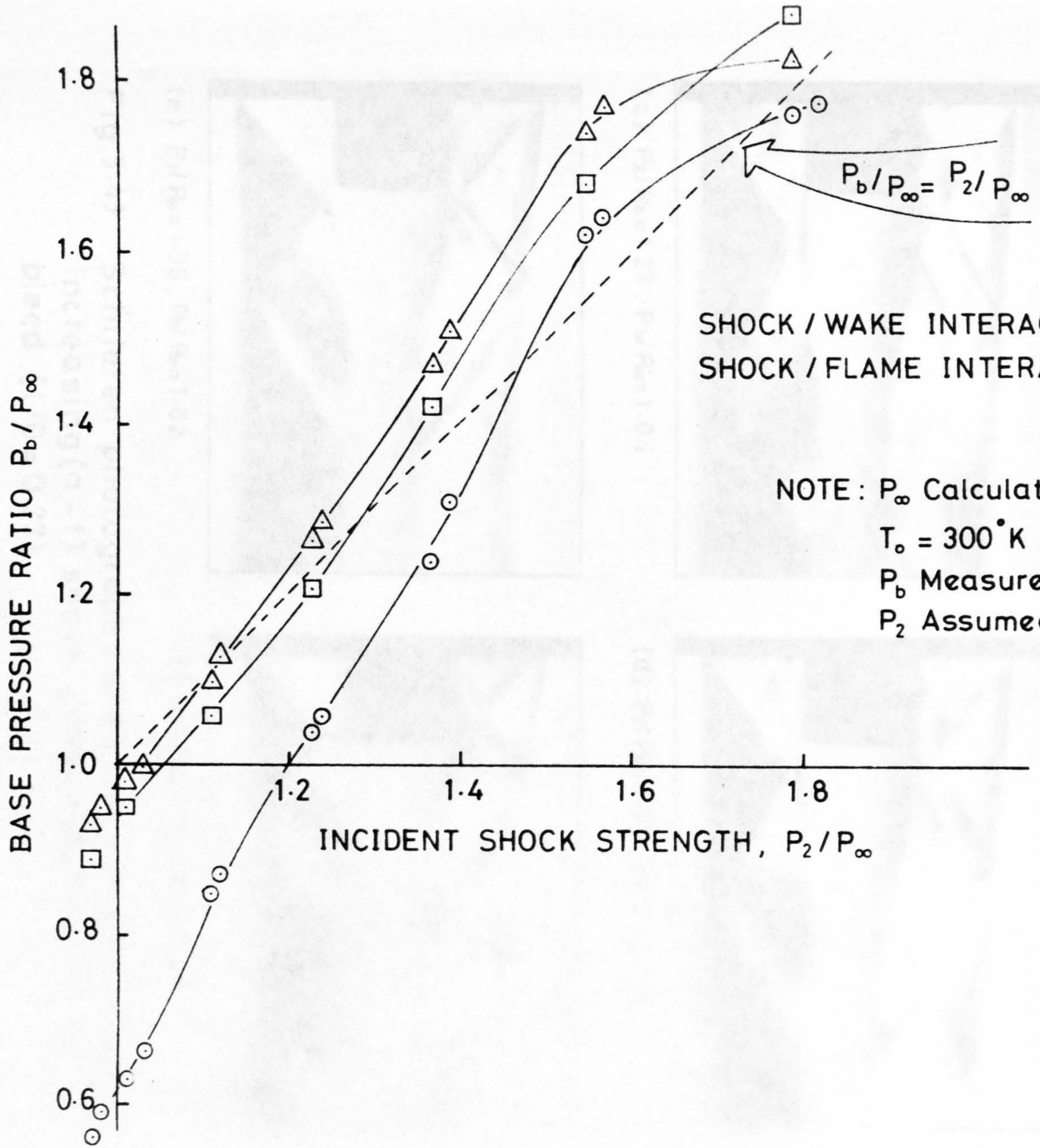

SHOCK / WAKE INTERACTION ⊙ NO BLEED

SHOCK / FLAME INTERACTION ⊡ H_2 mass flow rate = 0·15 gm/sec

△ H_2 mass flow rate = 0·30 gm/sec.

NOTE: P_∞ Calculated from P_o, $\delta = 1{\cdot}4$, $M_\infty = 2{\cdot}02$

$T_o = 300^\circ K$

P_b Measured at 3 Points.

P_2 Assumed Equal to Atmospheric Pressure.

Fig. 5·42 SHOCK / WAKE AND SHOCK / FLAME INTERACTION (AXIAL BLEED)

[l/D = 0·27 (See Fig 5·28)]

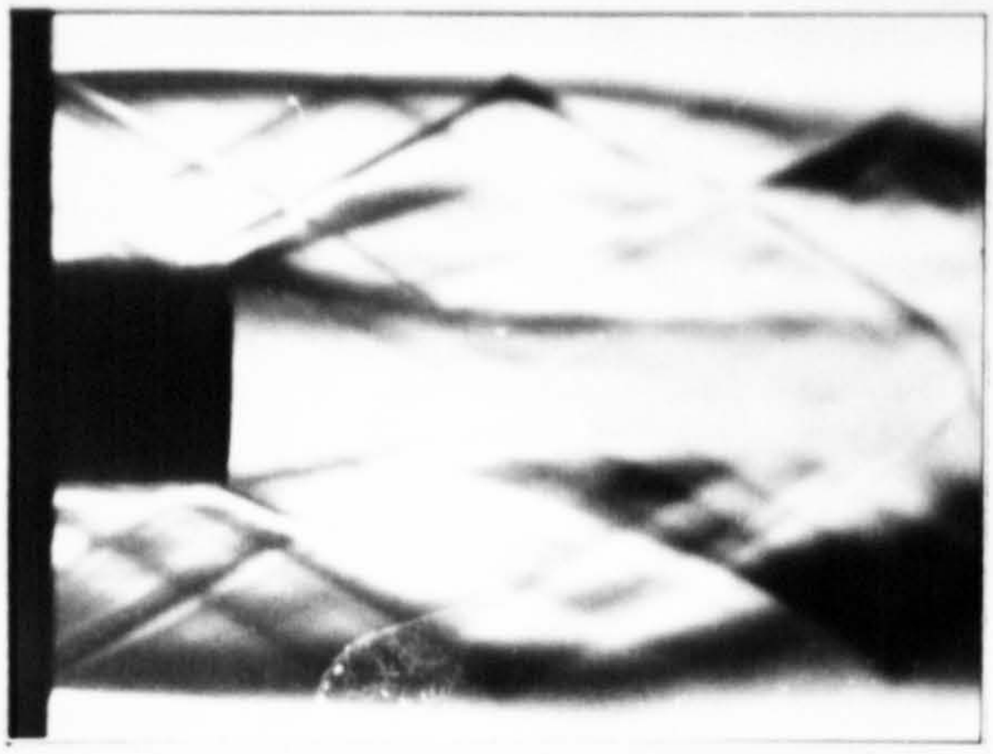

(a) $P_2/P_\infty = 1.01$, $P_b/P_\infty = 0.63$

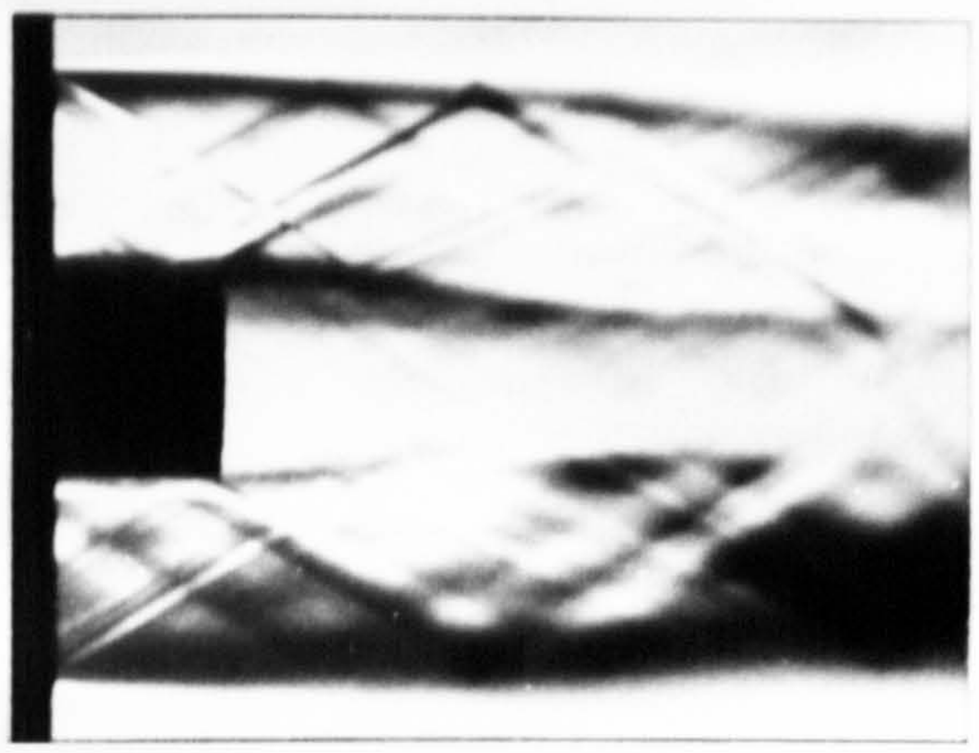

(b) $P_2/P_\infty = 1.11$, $P_b/P_\infty = 0.85$

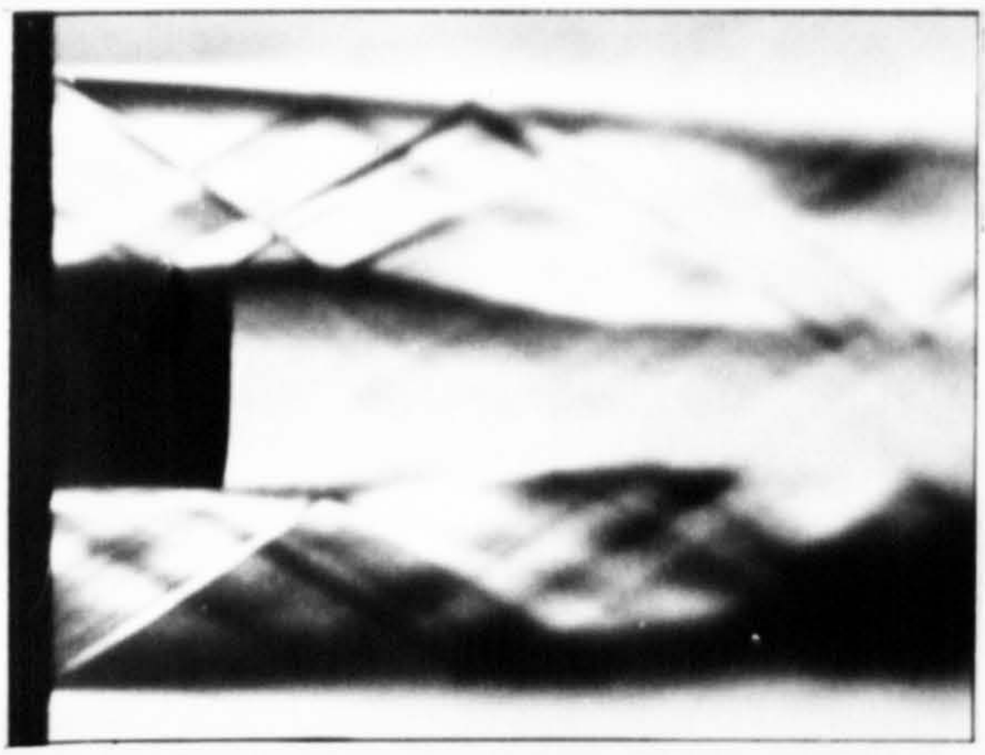

(c) $P_2/P_\infty = 1.23$, $P_b/P_\infty = 1.04$

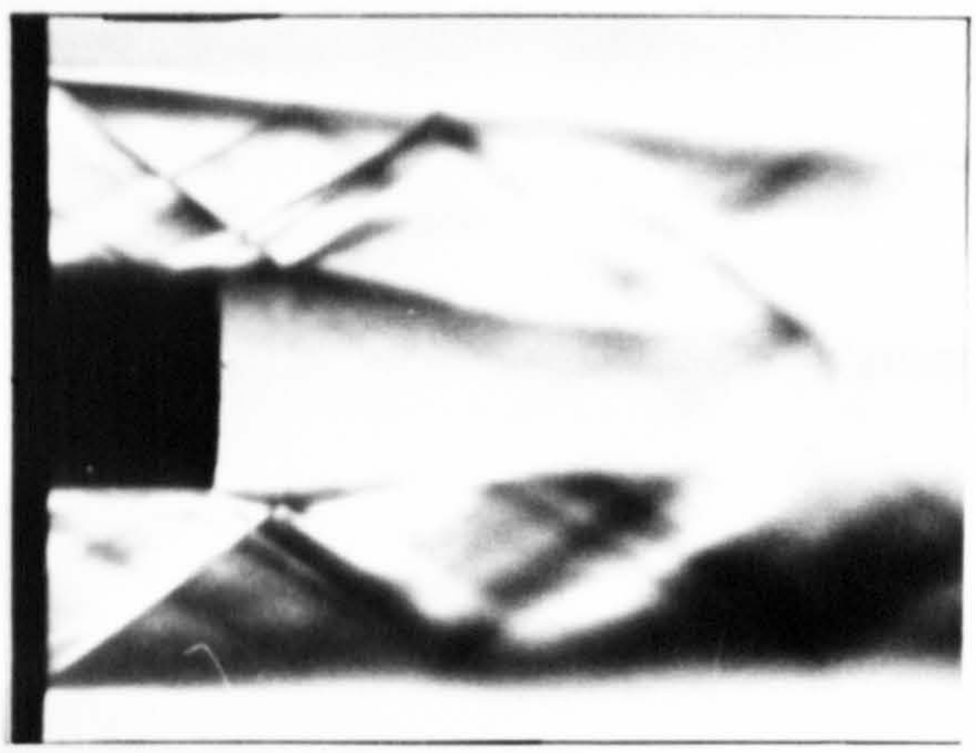

(d) $P_2/P_\infty = 1.37$, $P_b/P_\infty = 1.24$

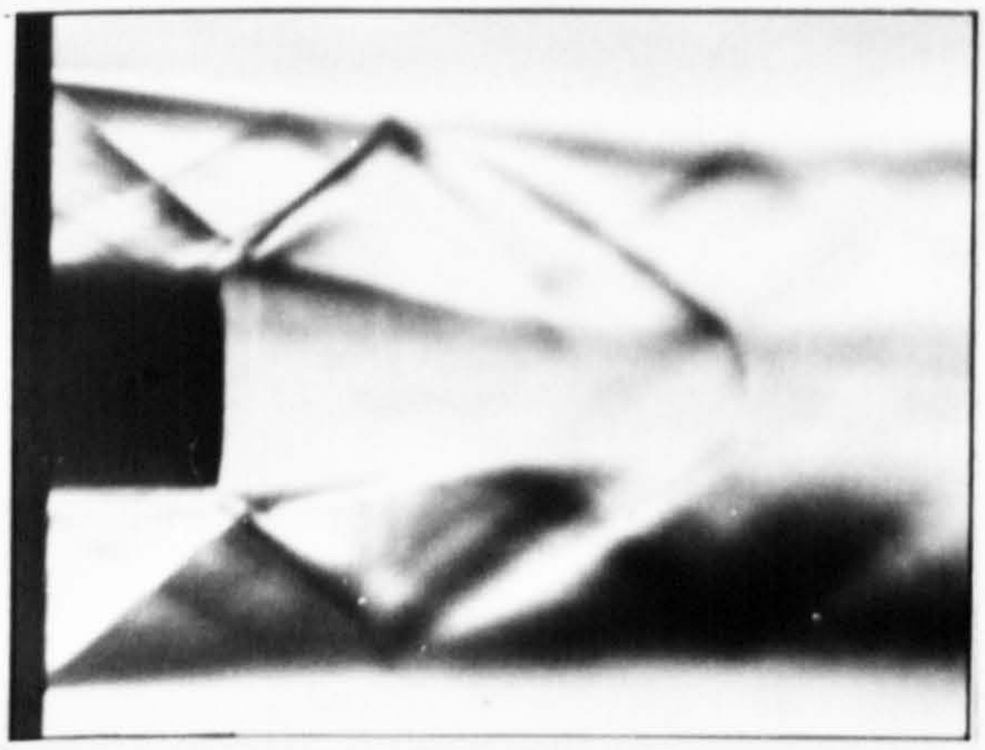

(e) $P_2/P_\infty = 1.55$, $P_b/P_\infty = 1.62$

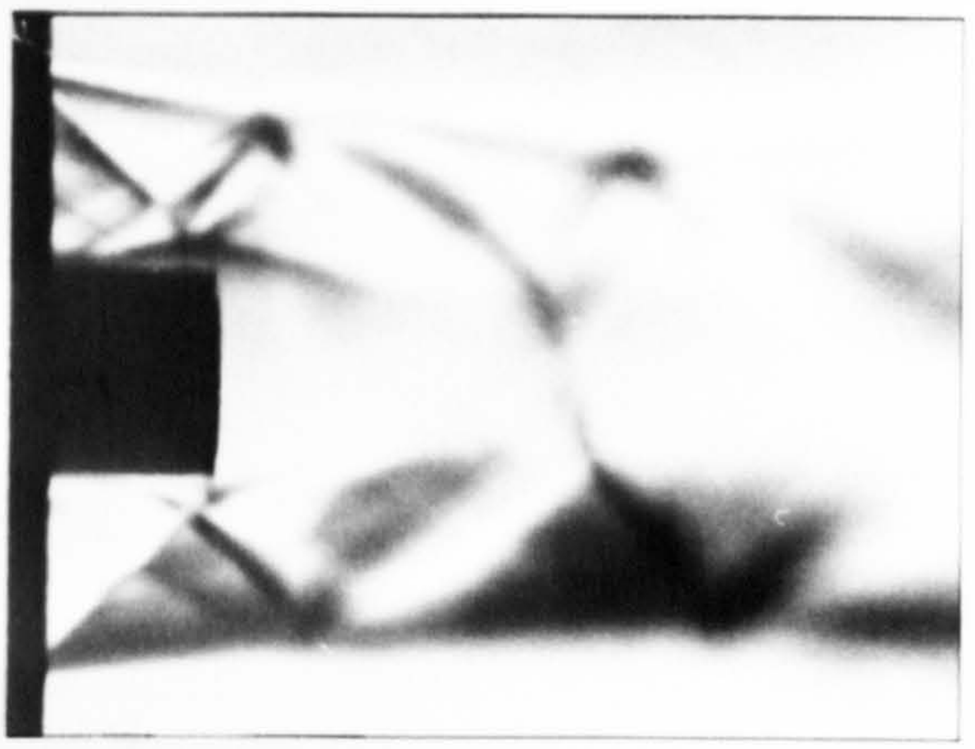

(f) $P_2/P_\infty = 1.79$, $P_b/P_\infty = 1.76$

Fig.5.43 Schlieren photographs showing the effects of increasing (a - f) shock compression with no bleed ($l/D = 0.27$)

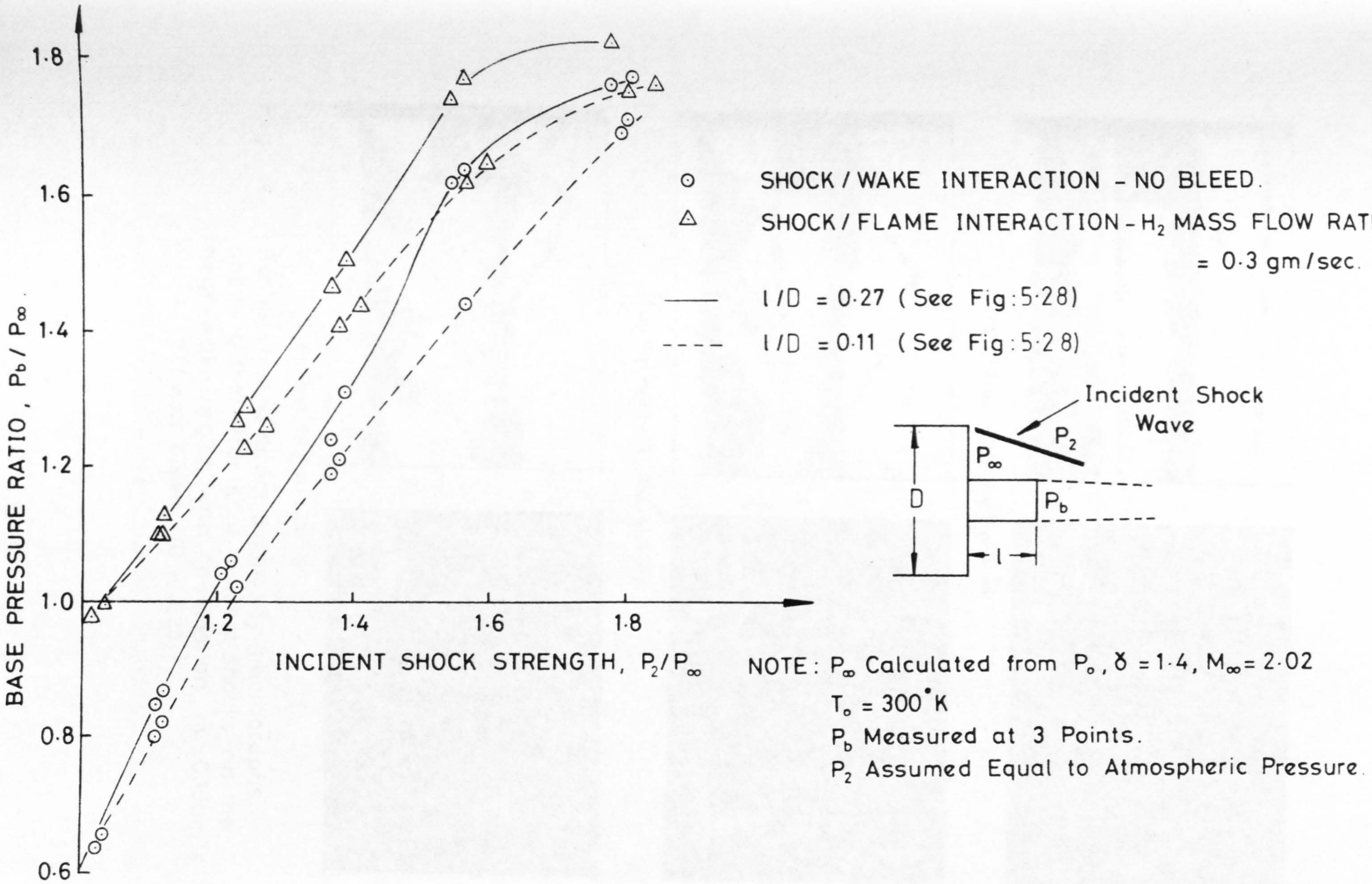

Fig. 5·44. COMPARISON OF BASE PRESSURE RATIO FOR TWO NOZZLE POSITIONS WITH SHOCK / WAKE AND SHOCK / FLAME (HIGH MASS FLOW RATE) INTERACTION (AXIAL BLEED).

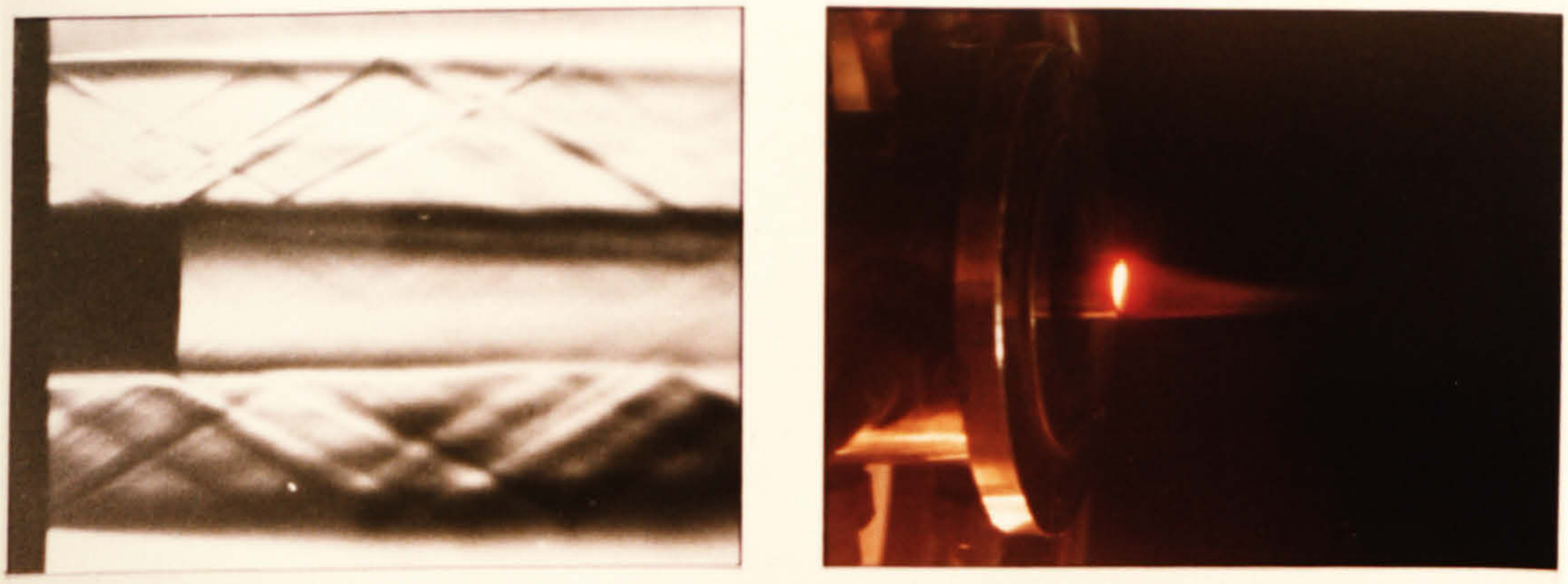

(a) $P_2/P_\infty = 1.01$, $P_b/P_\infty = 0.95$

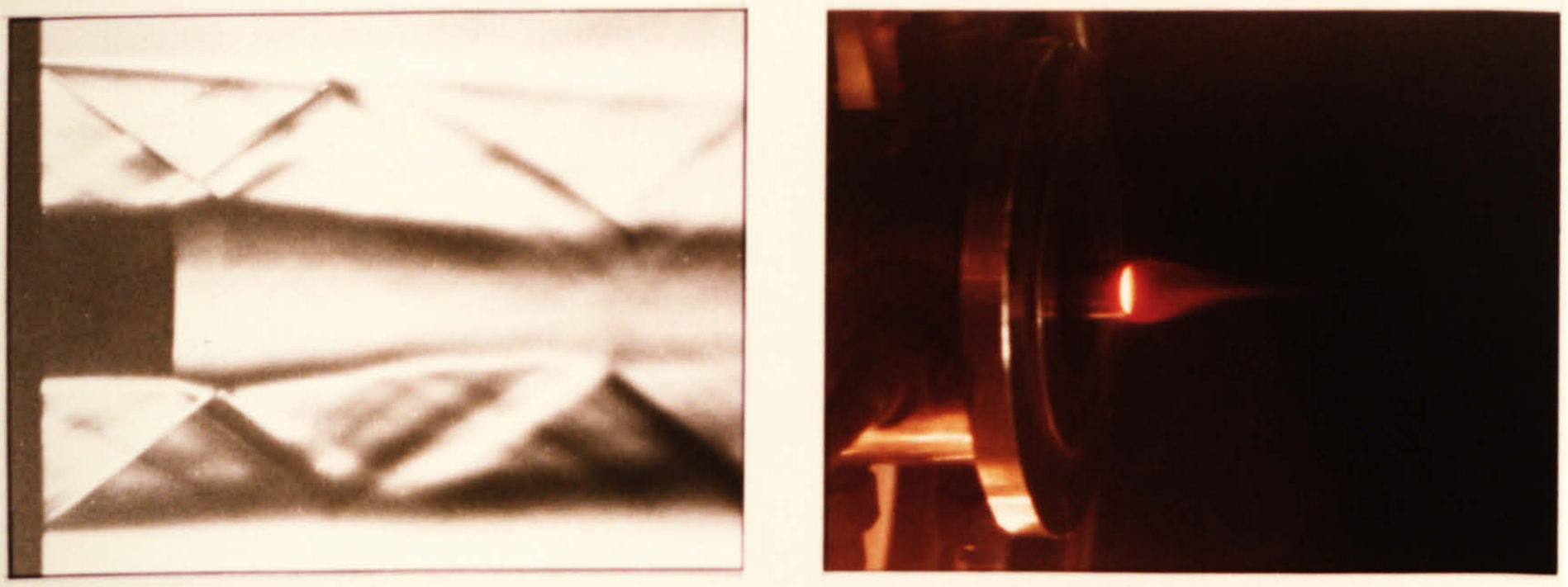

(b) $P_2/P_\infty = 1.37$, $P_b/P_\infty = 1.42$

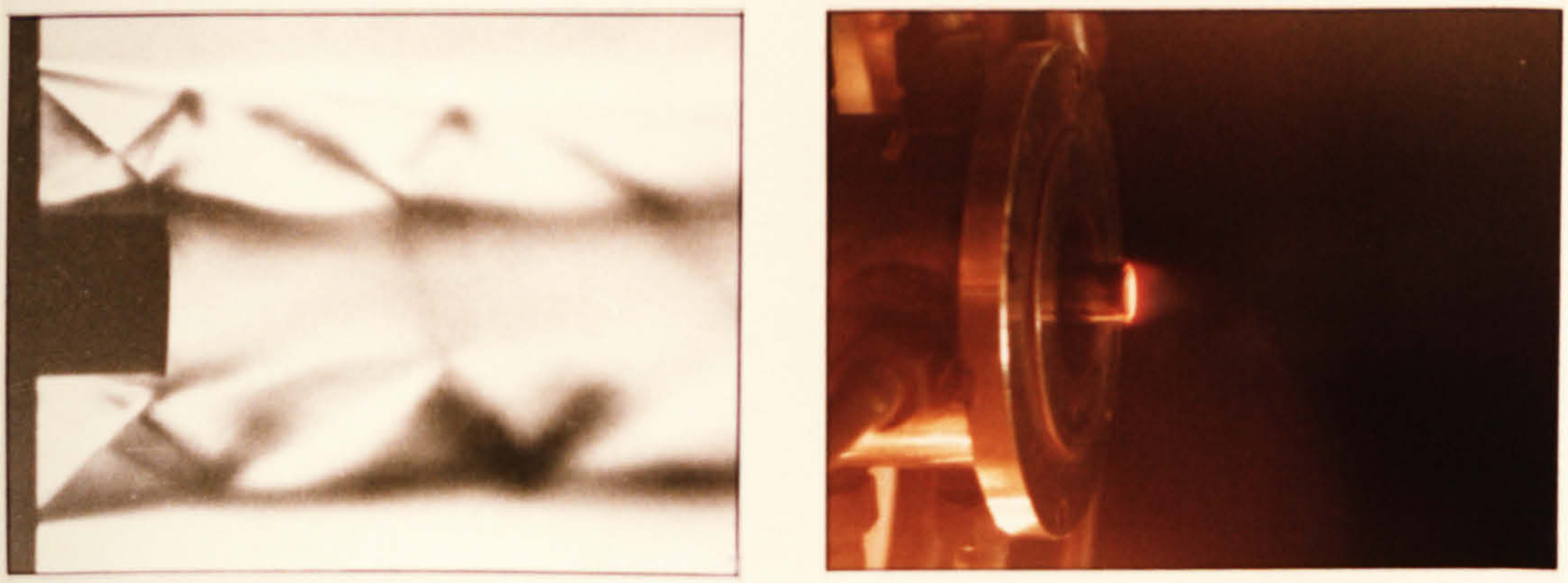

(c) $P_2/P_\infty = 1.79$, $P_b/P_\infty = 1.87$

Fig.5.45 Schlieren and direct luminosity photographs showing the effects of incident shocks on the near wake region with combustion, $\dot{m}_f = 0.15$ gm/s (Axial bleed, l/D = 0.27)

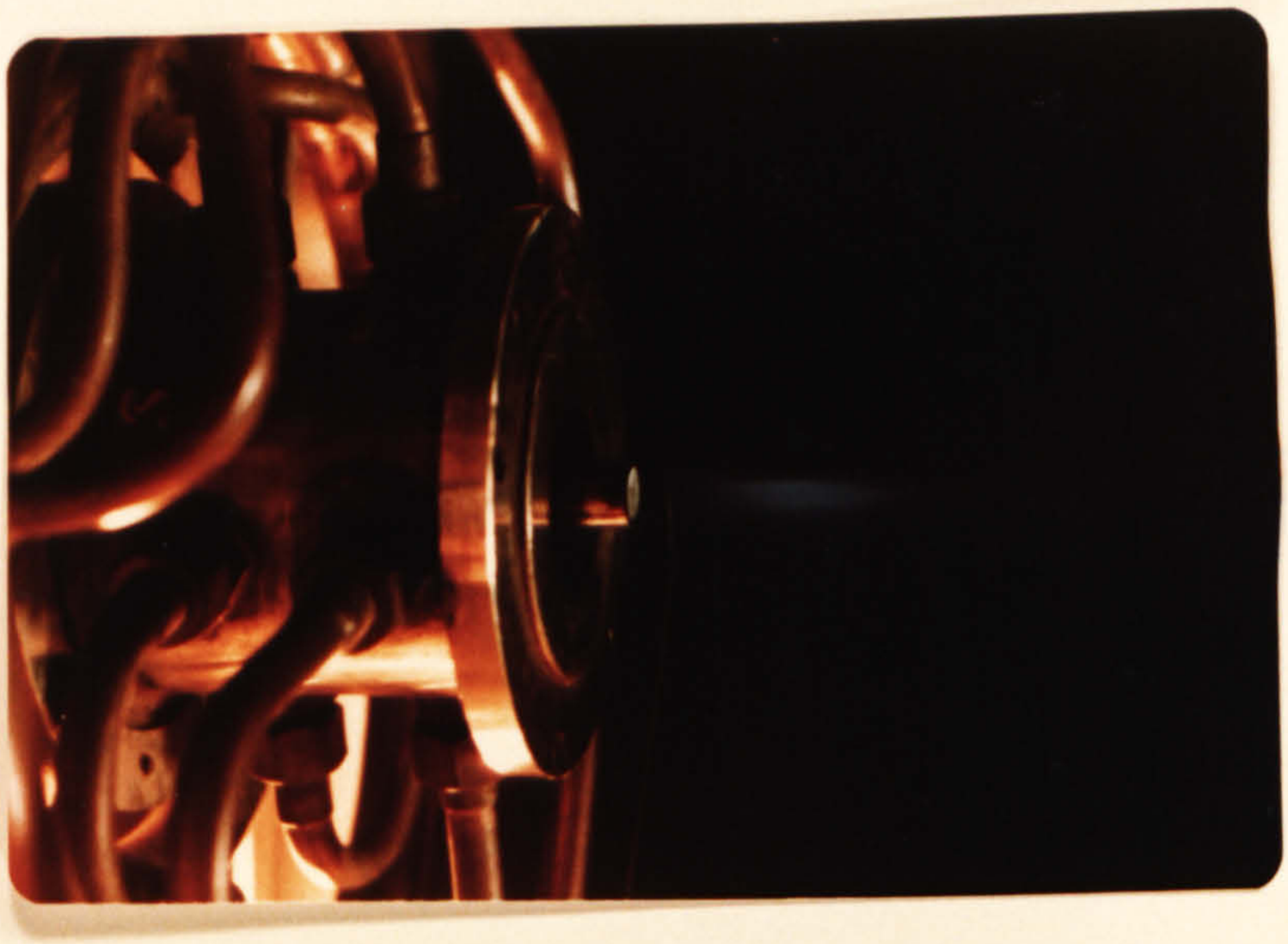

(a) Tungsten wire approximately 0·5 calibres downstream of base

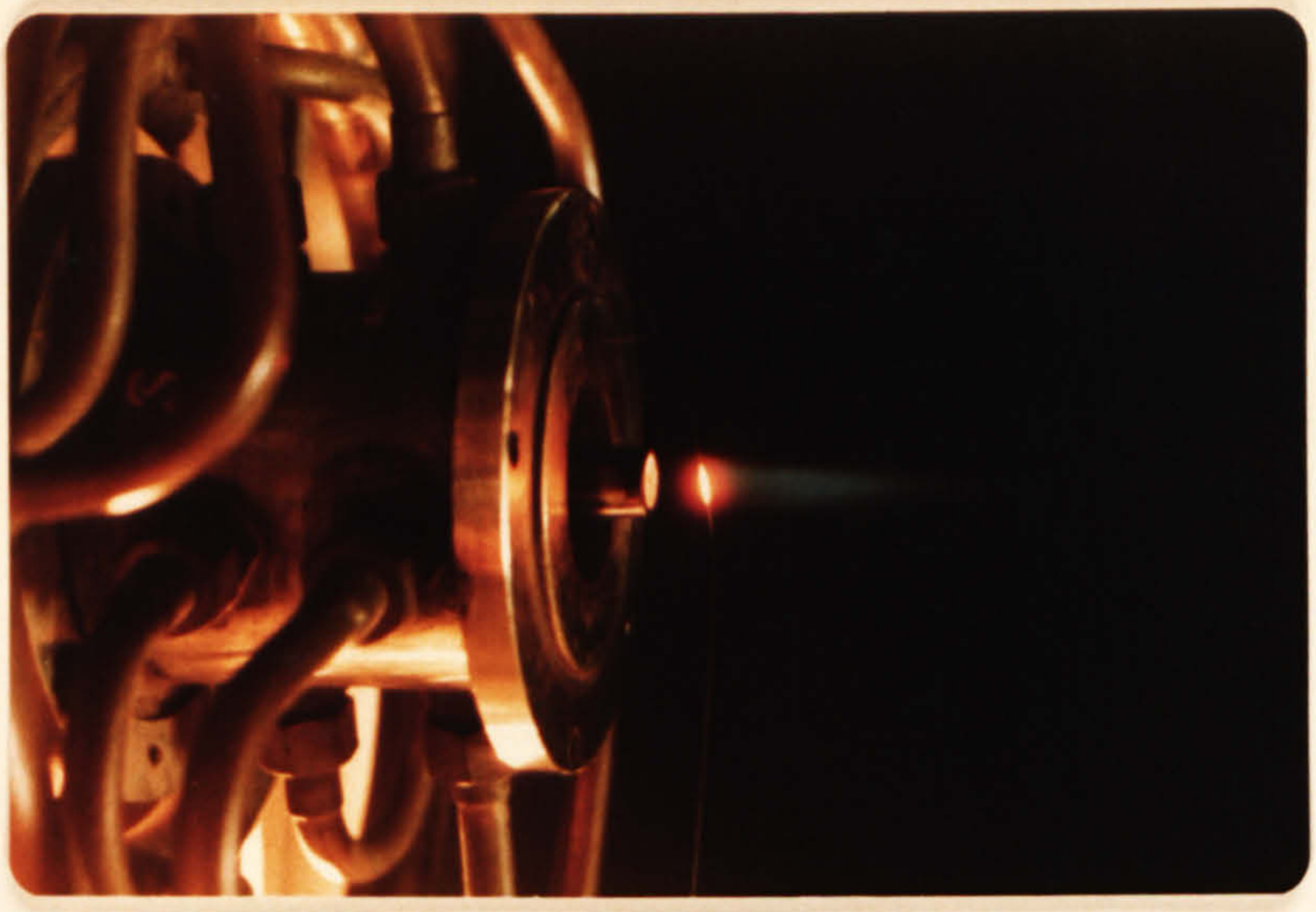

(b) Tungsten wire approximately 0·8 calibres downstream of base

Fig. 5·46. Wake probeing with 0·01" dia. tungsten wire ($\dot{m}_f$=0·3gm/sec)

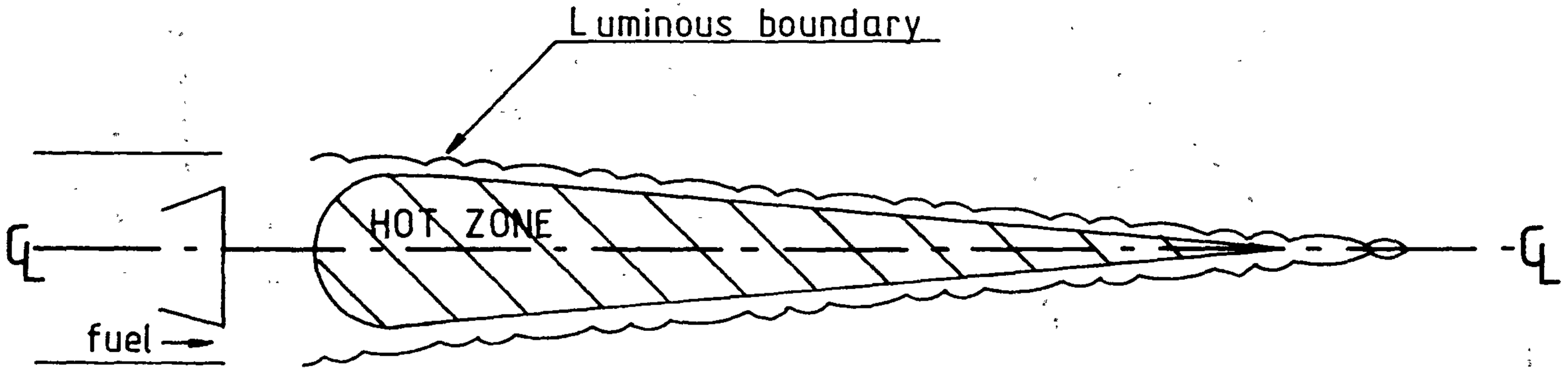

Fig. 5·47 `Hot´ area in wake as determined by tungsten probe

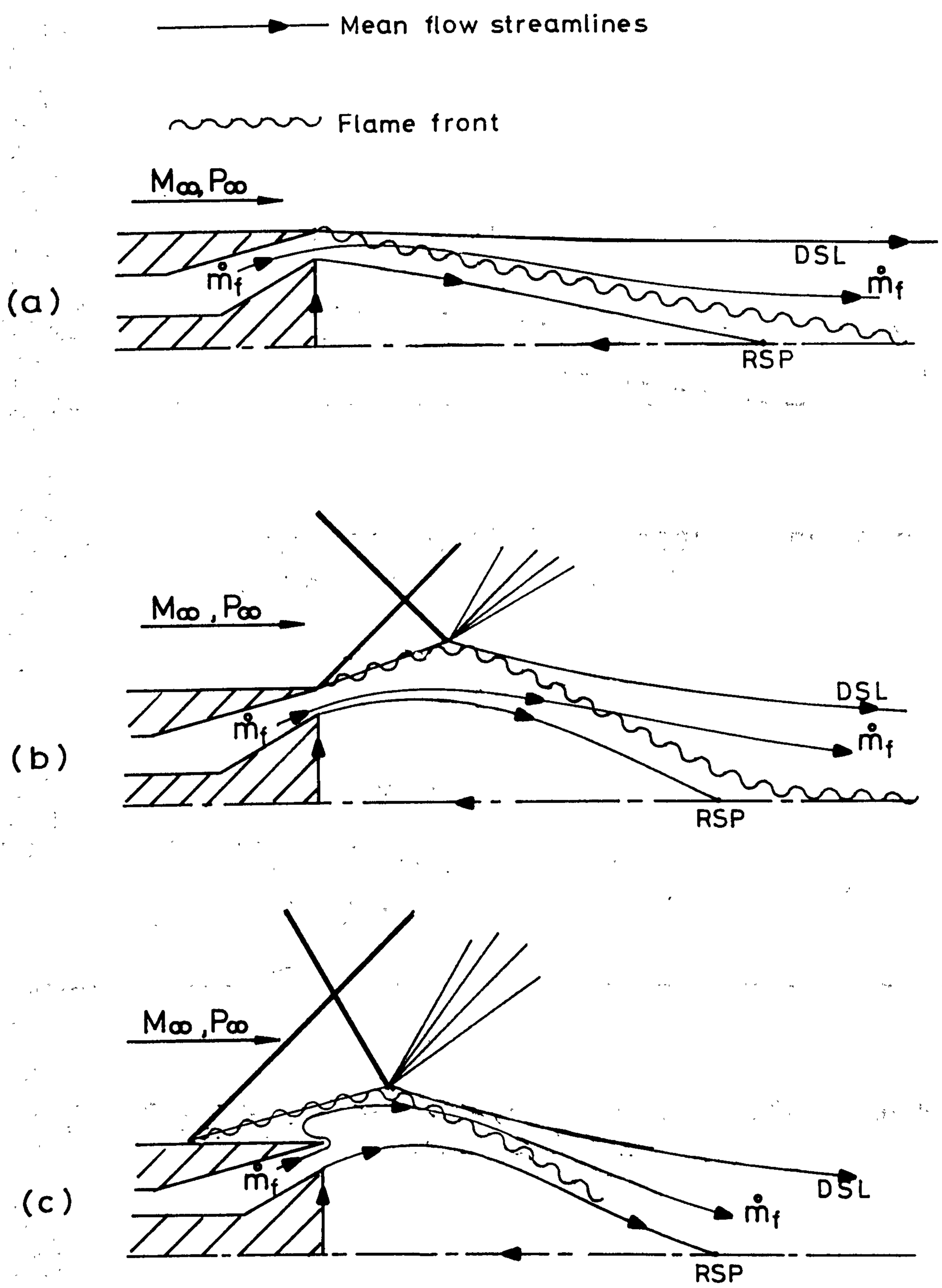

Fig.5·48. Hypothetical configuration of near wake flowfield with combustion (Axial bleed)
(Not to scale)

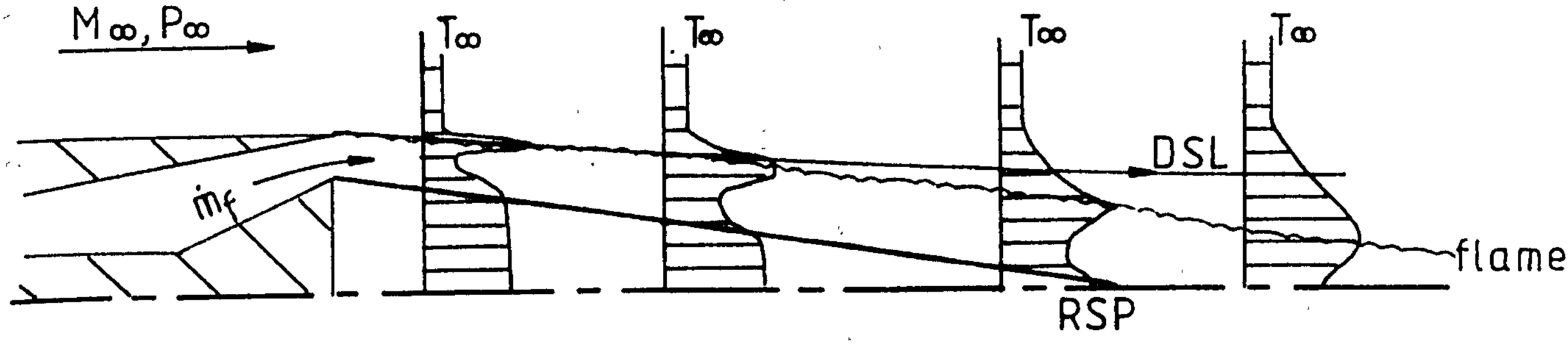

Fig. 5·49 Hypothesised static temperatures in near wake region with axial bleed

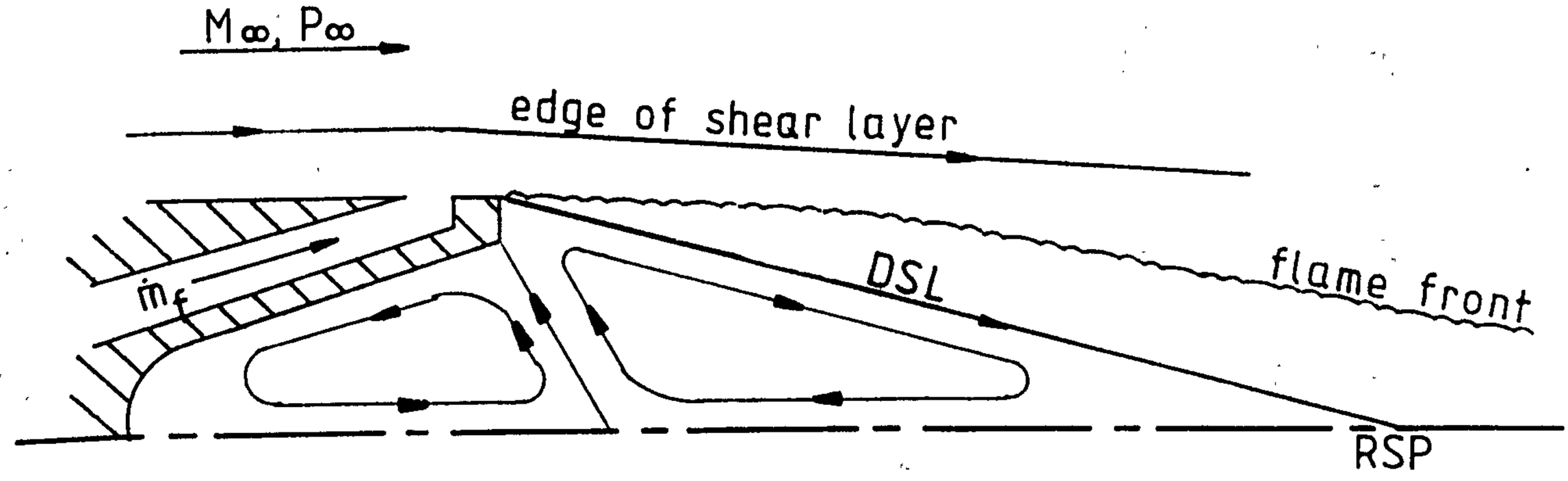

Fig. 5·50 Hypothesised near wake flowfield with peripheral bleed

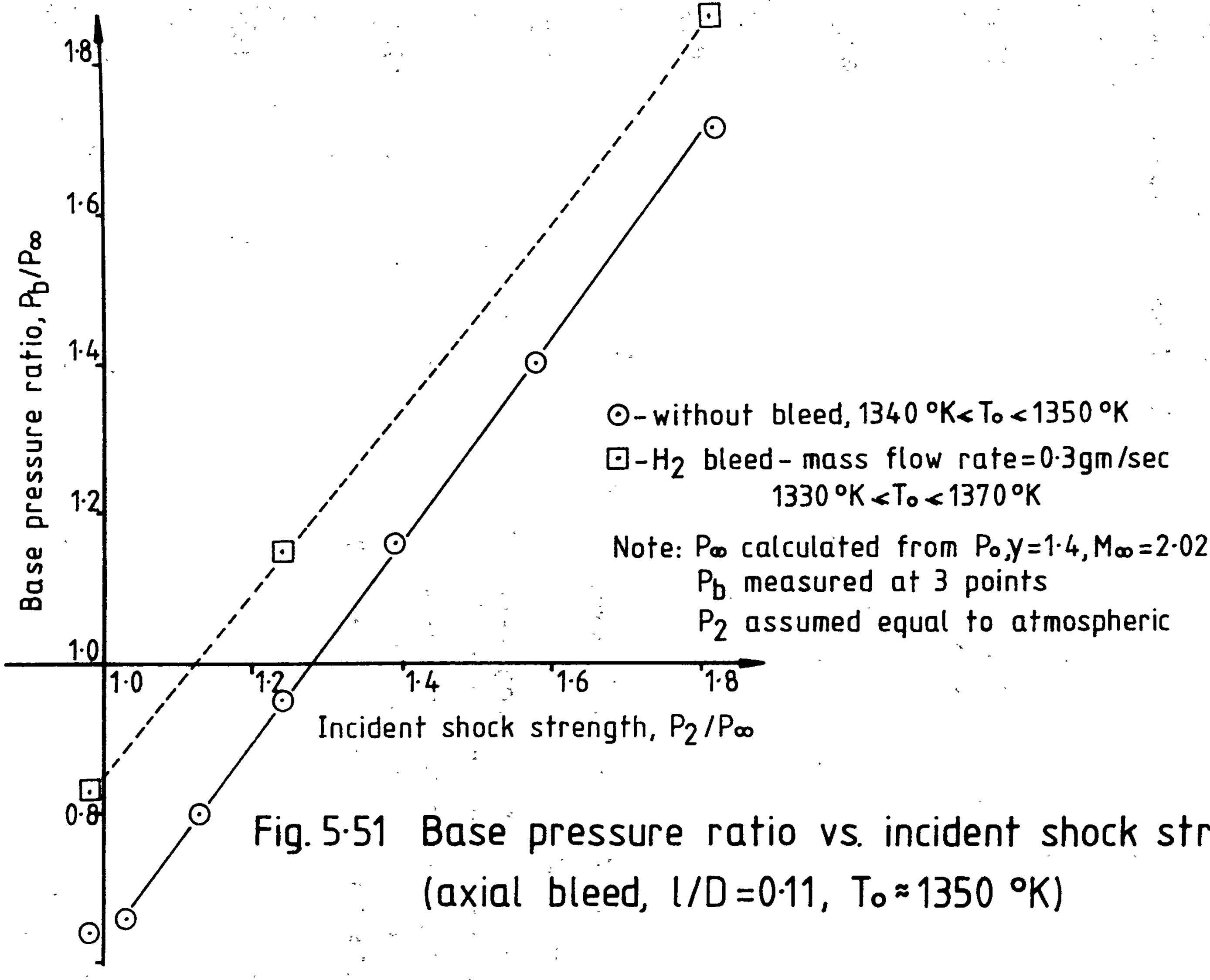

Fig. 5·51 Base pressure ratio vs. incident shock strength (axial bleed, l/D=0·11, $T_o \approx 1350$ °K)

Fig. 5·52 EFFECT OF SHOCK COMPRESSION ON BASE PRESSURE WITH AND WITHOUT WAKE COMBUSTION - Varying stagnation temperature (axial bleed, l/D=0·11)

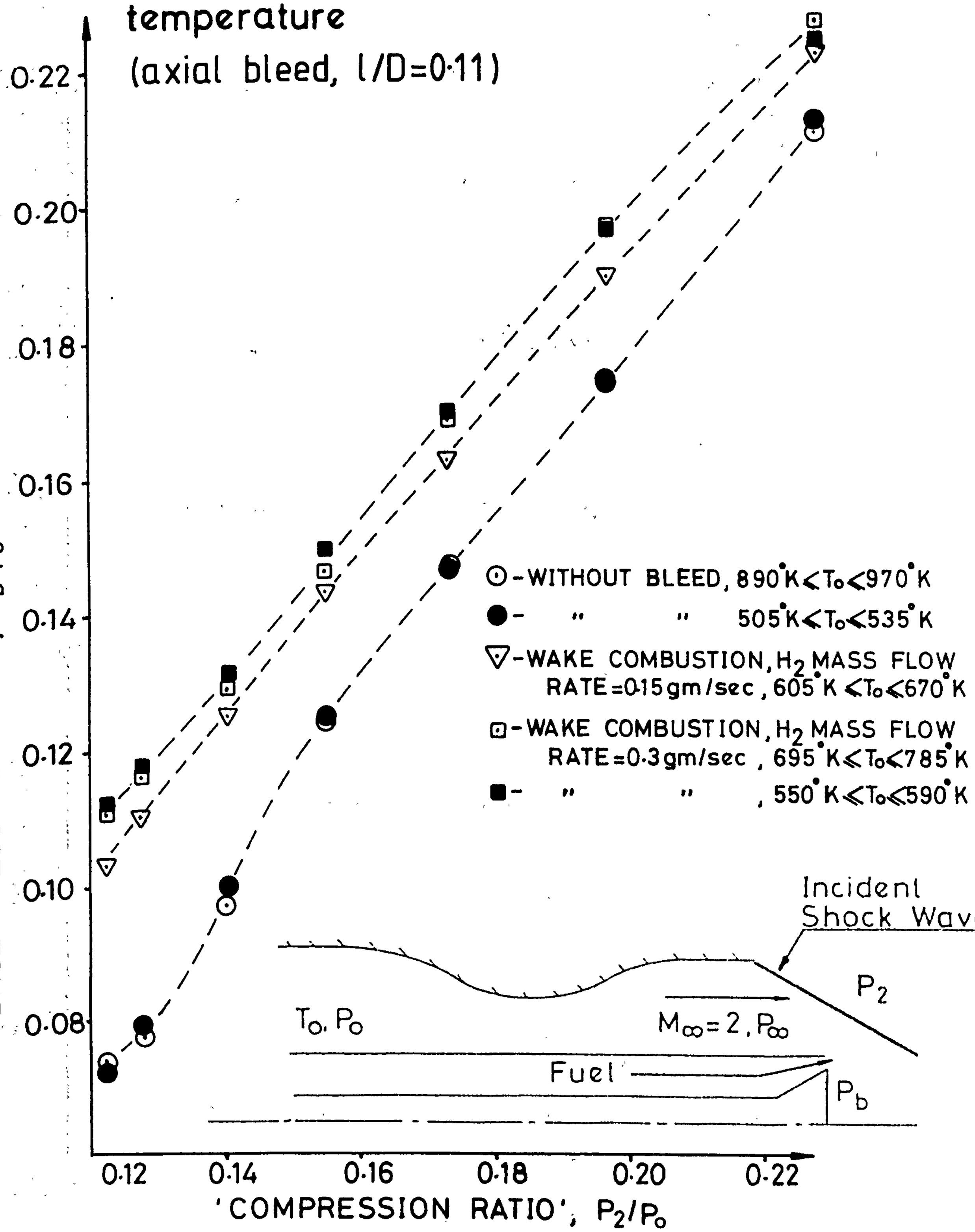

Fig. 5·53:

EFFECT OF STAGNATION TEMPERATURE ON BASE PRESSURE FOR CONSTANT COMPRESSION RATIO, P_2/P_o

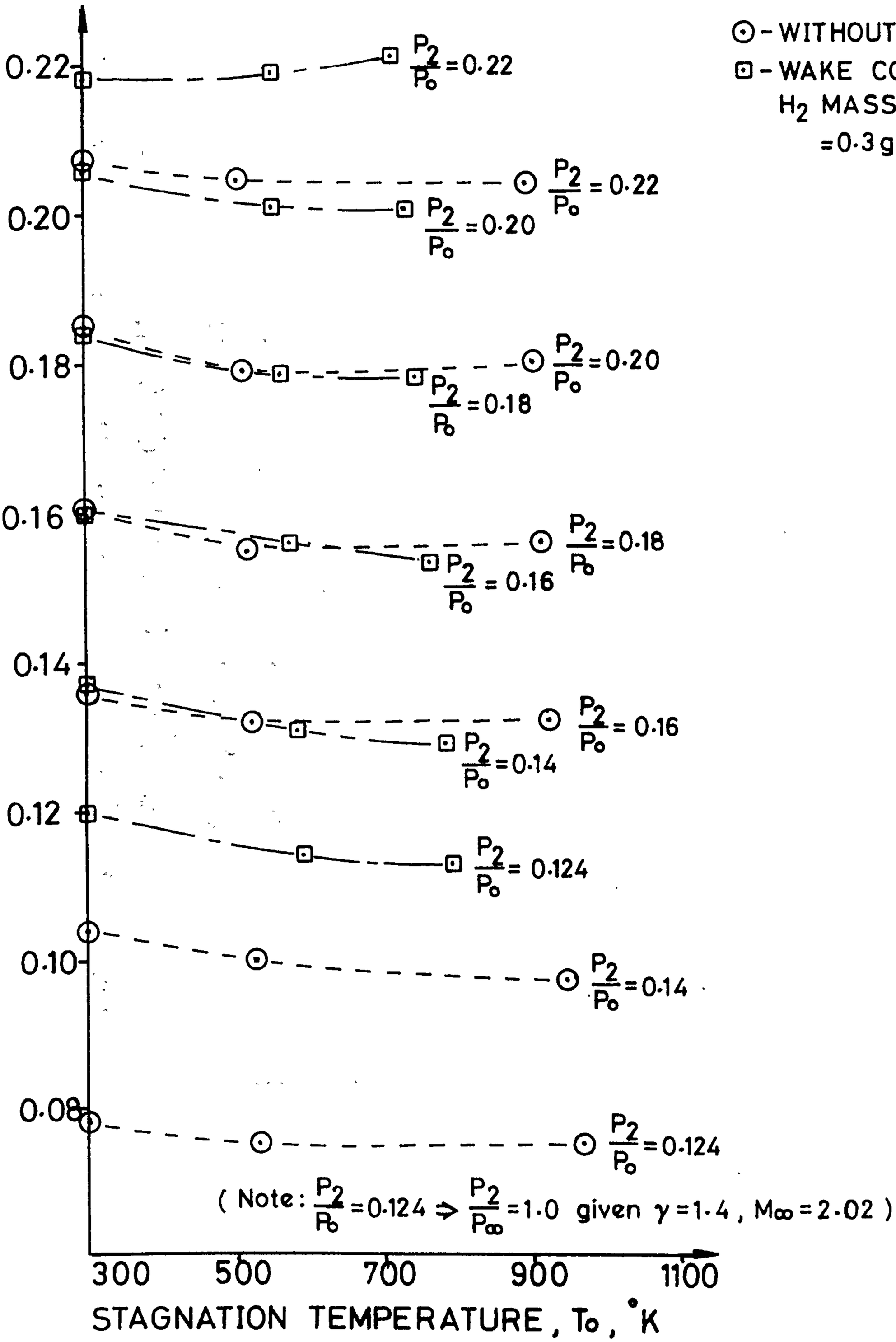

Fig. 5·54: Specific impulse, σ_o, with shock/flame interaction (Peripheral bleed, l/D = 0·21)

⊙ - H_2 mass flow rate = 0·15gm/sec

● - H_2 mass flow rate = 0·23gm/sec

⊡ - H_2 mass flow rate = 0·3gm/sec

$$\sigma_o = \frac{\text{base force rise}}{\text{hydrogen mass flow rate}}$$

1 lbf.sec/lbm = 9·81 N.sec/kgm.

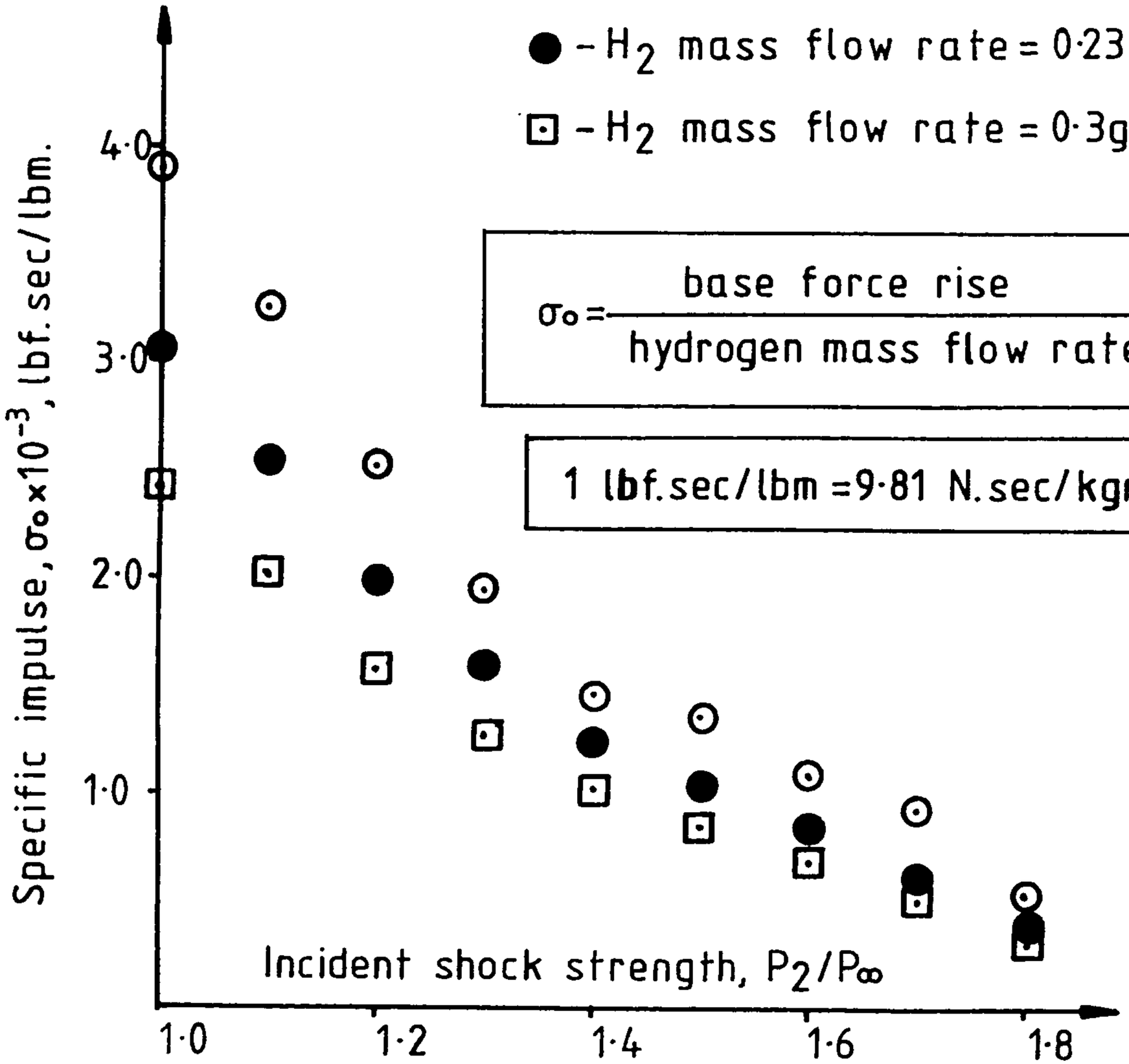

Fig. 5·55. Variation of specific impulse, σ_1, with incident shock strength. (Peripheral bleed, l/D=0·21)

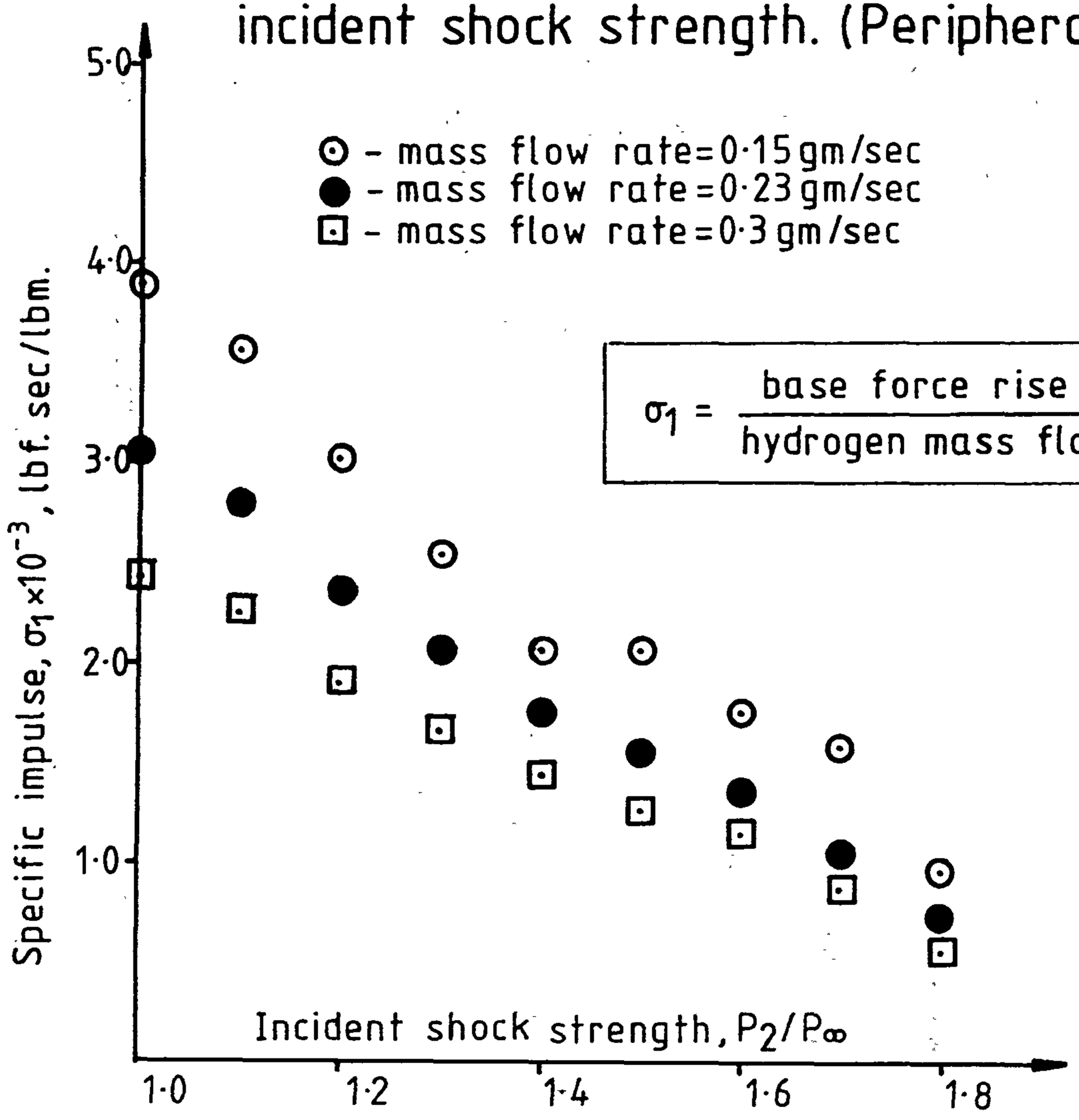

Fig. 5·56. Variation of specific impulse, σ_o, with incident shock strength. (Axial bleed, l/D=0·11)

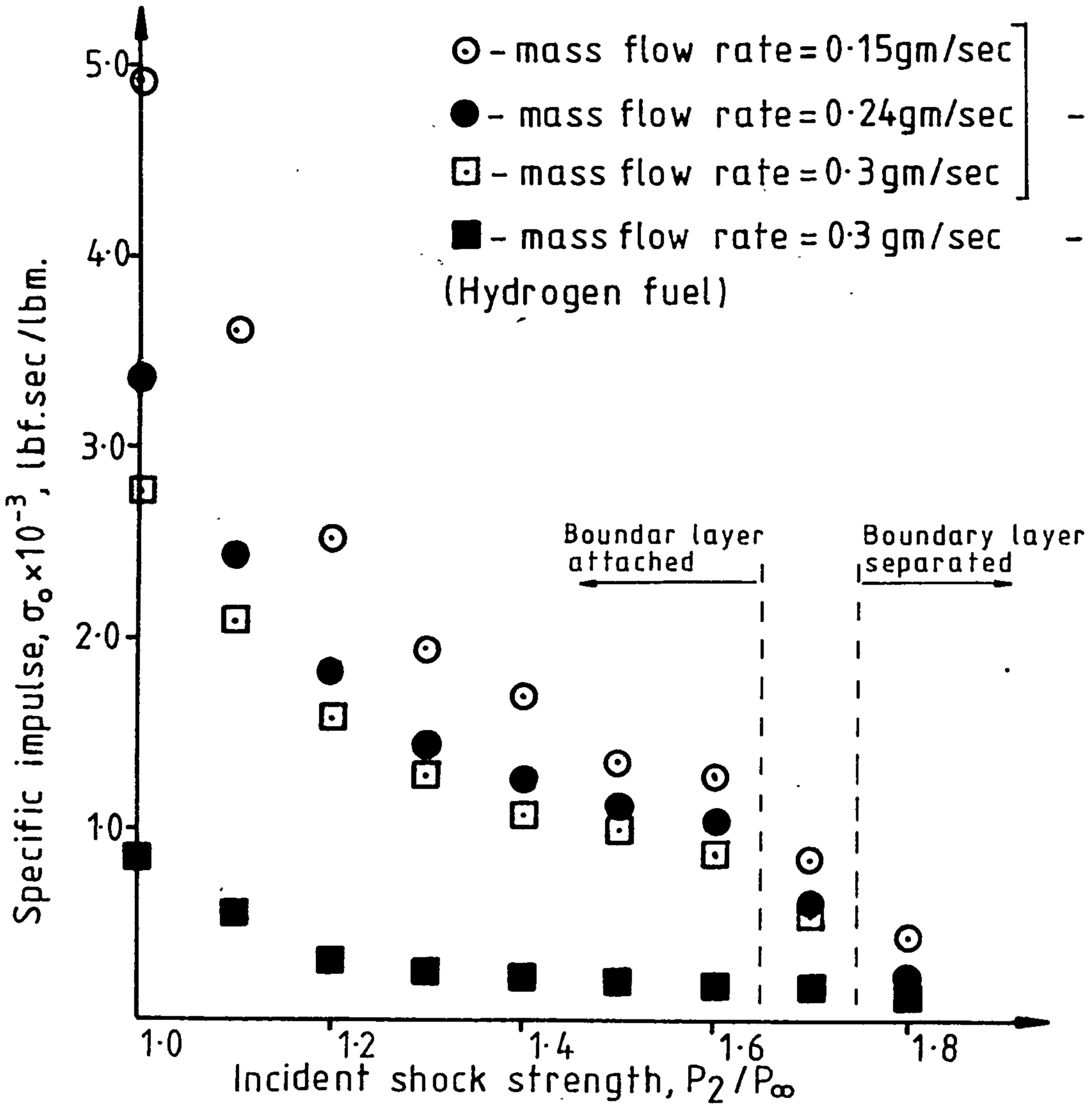

Fig. 5·57. Variation of specific impulse, σ_1, with incident shock strength. (Axial bleed, l/D = 0·11)

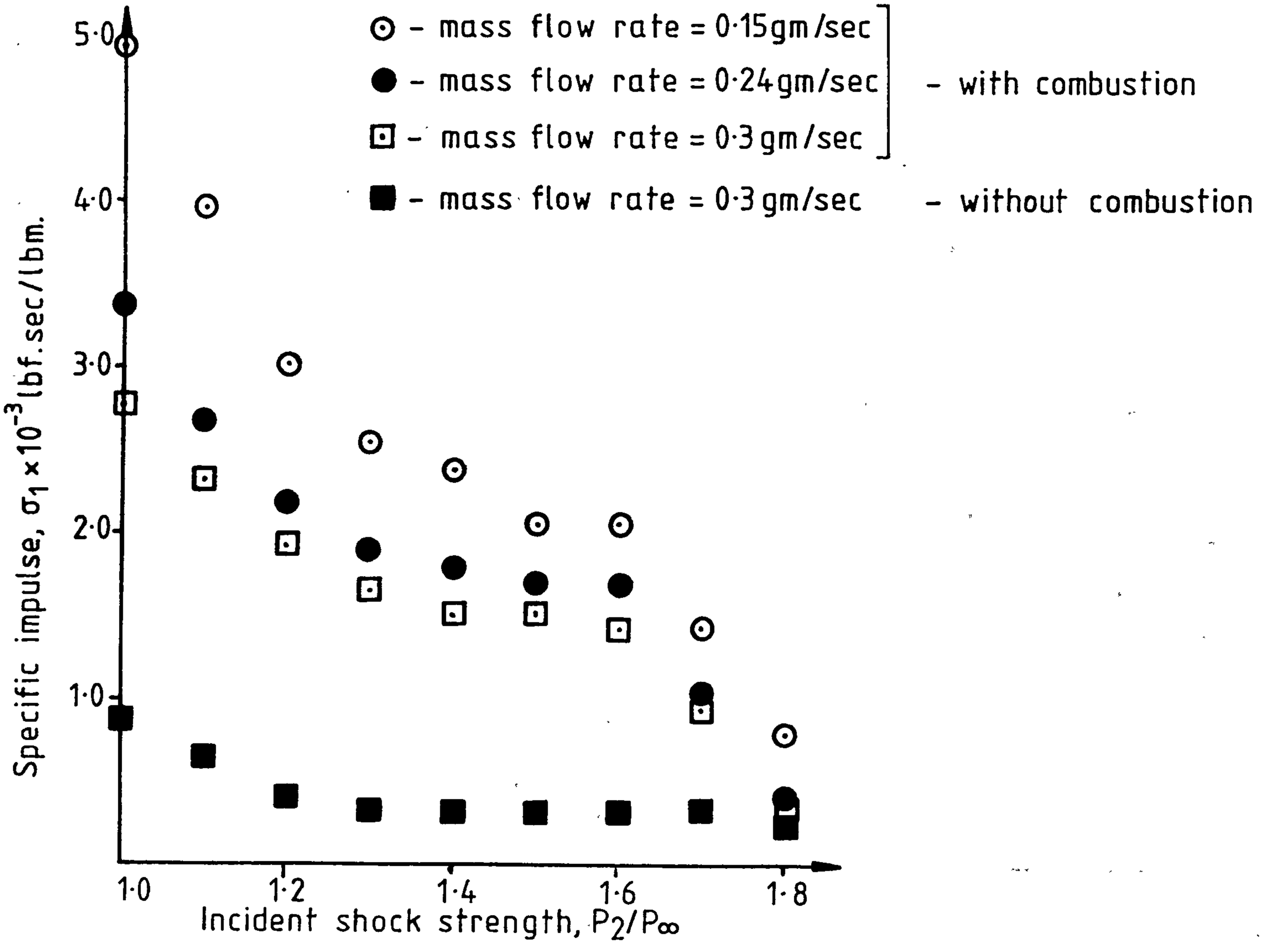

Fig. 5·58. Variation of specific impulses, σ_o and σ_1, with incident shock strength. (Axial bleed, l/D = 0·27)

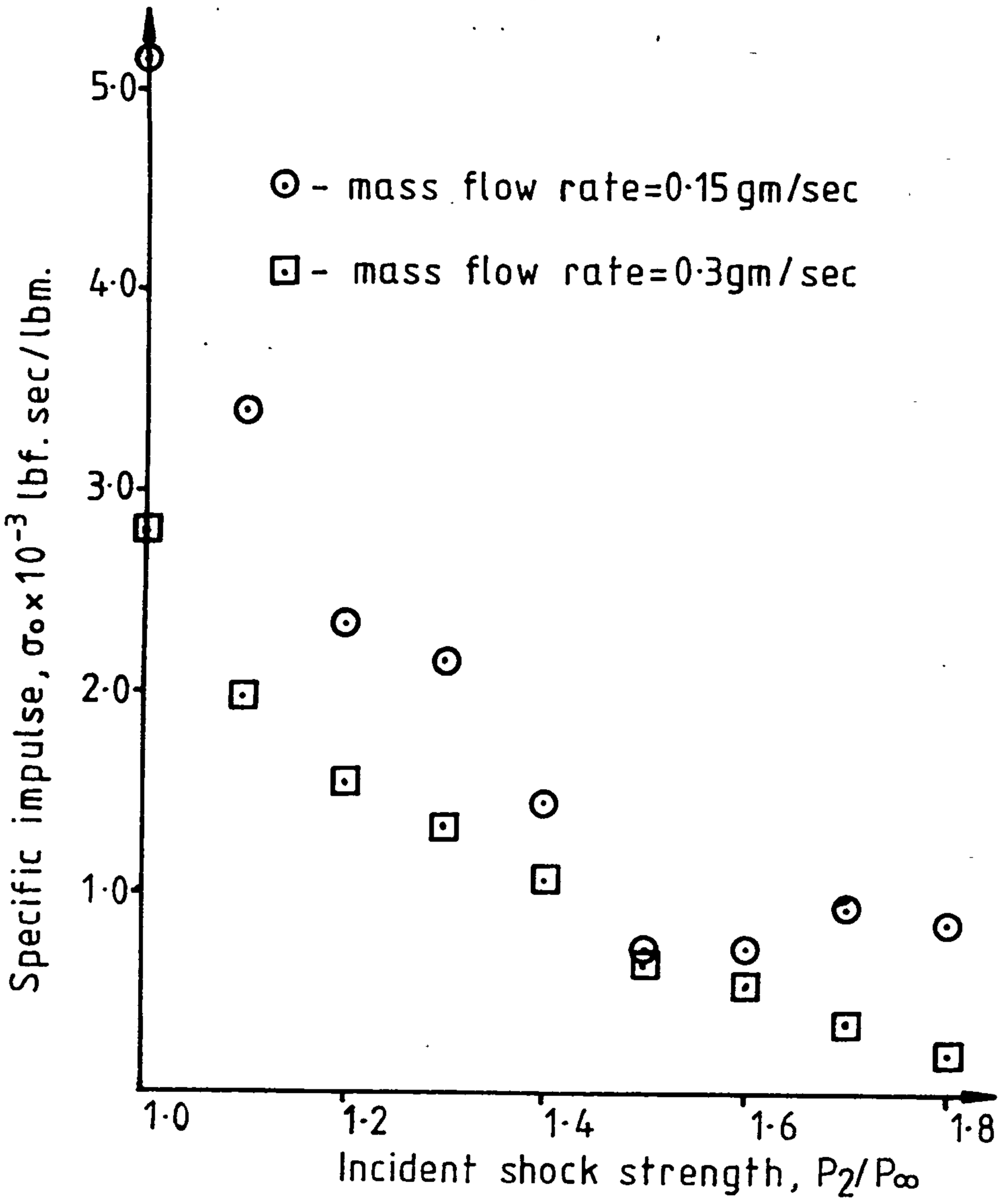

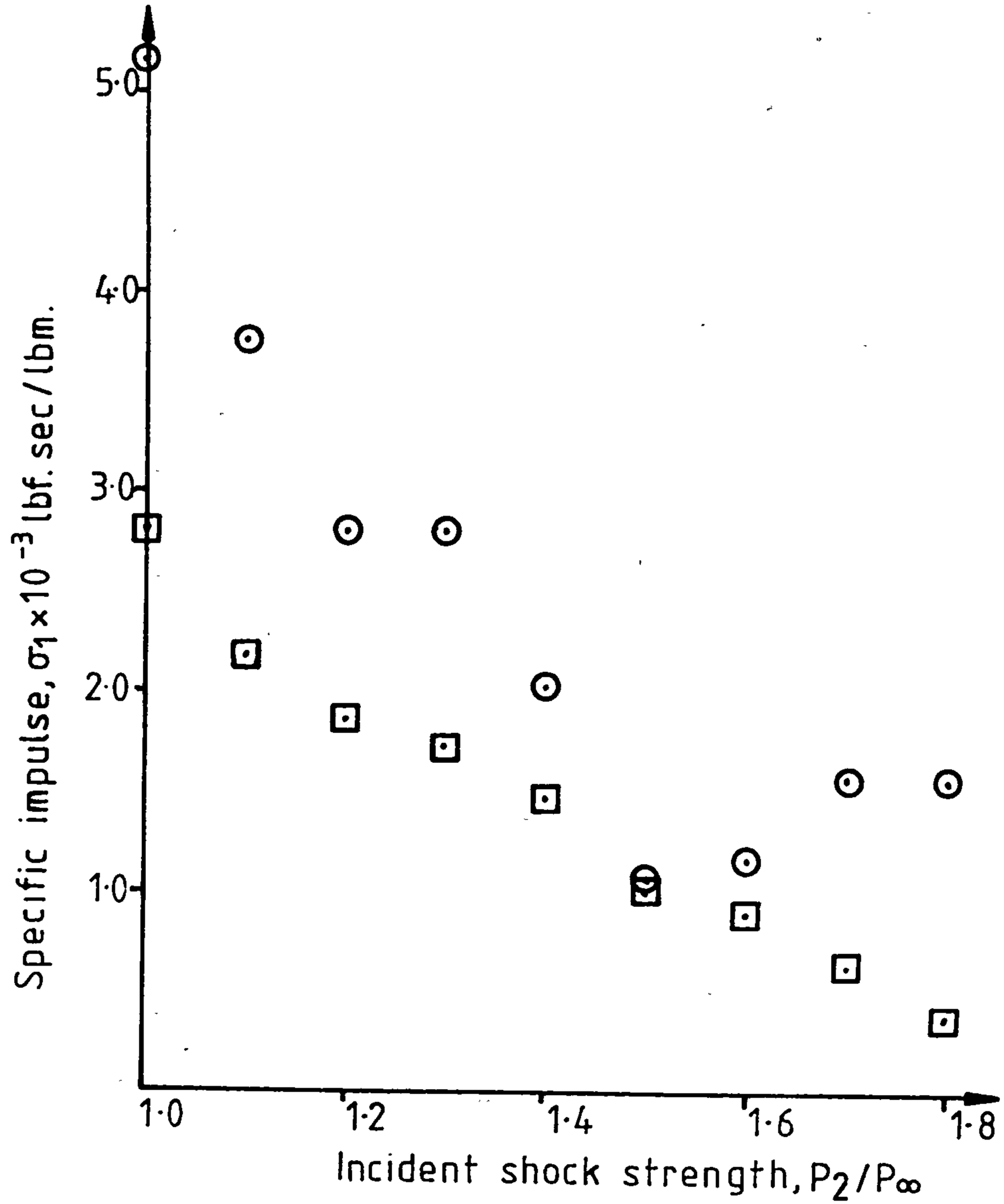

CHAPTER 6: CONCLUSIONS

1. It has been observed that there is a distinct cowl position which maximises the base pressure. This position appears to be roughly independent of Reynolds number, cowl angle and base geometry (for the two geometries tested).

2. The two-dimensional shock interference and delta wing tests with interaction upstream of the base plane show less dependence on shock generator position than does the cowl due to the greater distance between the leading edge shock and the trailing edge expansion. Clearly shock generator geometry is a significant factor in the determination of the base pressure.

3. It appears, in general, that with interaction in the optimum position that static pressurerise across the shock can be communicated in full to the base.

4. It has also been shown that favourable interference between the wake and the cowl can occur. For the cowl geometry tested the zone of favourable interference extends from cowl leading edge positions in excess of 0.6 calibres upstream of the base to 0.2 calibres upstream of the base. The region of minimum net drag does not correspond with the position of maximum base pressure.

5. The phenomenon of 'wake buzz' has been observed at the lower Reynolds numbers tested. This has been seen to be detrimental to performance in the cases where it has been observed but, in practice, at the higher Reynolds numbers expected for free flight conditions 'wake buzz' may not be significant.

6. The shock/wake and shock/flame experiments have demonstrated that substantial base thrust can be generated. It has been shown that the major factors affecting the base pressure are shock strength and interaction position.

7. It has also been observed that stagnation temperature does not appear to be a major factor in the determination of the base pressure under the influence of shock compression (in the range tested, $1000^{o}K \geq T_o \geq 300^{o}K$).

8. Both peripheral and axial bleed of fuel respond in a similar manner under the influence of shock/flame interaction. However, the weak extinction limits differ in the two cases, peripheral bleed having a greater weak extinction limit. While stable combustion was achieved in both cases, in the absence of further information, axial bleed is to be preferred since the undisturbed base pressures are greater than with peripheral bleed at the same mass flow rate and the flame may well be more robust to pressure perturbating in the flowfield.

9. One problem to overcome at high shock strength will be the onset of separation of the boundary layer approaching the base. The design shown in fig. 1.1 is intended to benefit both from favourable interference and from wake combustion on the rearward facing surfaces of the cowl or wings. It may be possible in practice to distribute the thrust

between the shock generators and the base of the projectile in such a manner as to avoid incipient separation.

10. The fuel specific impulse falls with increasing shock strength. Once the onset of incipient separation has occurred it is inefficient to add wake combustion (and may be detrimental due to heat transfer to the surface of the centrebody).

11. The separation shock generated at the base of the projectile when $P_b/P_\infty > 1$ can be used to advantage in the design of an engine geometry. The design shown in fig. 1.1 uses hardware to generate the secondary shock system. However, the experiments demonstrating favourable interference show that the secondary shock system can be generated by aerodynamic means without the complexity of a flared base.

12. Finally, it has been observed that silicon nitride is a suitable material for use in high temperature wake combustion experiments.

CHAPTER 7: RECOMMENDATIONS FOR FURTHER WORK

The most pressing requirement is for a model of the device shown in fig. 1.1 to be tested with wake combustion both on the base of the projectile and on the rear of the cowl. This could be done in the near future since a cowl model for testing in the Pebble Bed Heater is under construction.

Subject to the outcome of these tests it is necessary to increase the size of the model, since the scaling effects of combustion are not well understood and predictions of performance at full scale would therefore be dubious. This would require the use of a wind tunnel with a large working section prior to full scale tests.

Finally, hydrogen fuel is not likely to prove acceptable in a practical full scale device since, while the enthalpy release per unit mass is good, the enthalpy release per unit volume is poor. Some consideration should be given to the use of other fuels such as kerosene or pyrophorics.

ACKNOWLEDGEMENTS

I would like to thank my supervisor, Professor J.L. Stollery, for his constant encouragement and advice. Dr. L.H, Townend deserves special comment for his enthusiasm, interest and suggestions of which I was able to consider only a few in the time available. The members of the Supersonic Combustion Studies Group have also contributed to the sum of this report, but in particular, I would like to thank Professor J.F. Clarke for many helpful discussions and Dr. R.A. Cookson for allowing the use of the Pebble Bed Heater and his constant interest in the project. Further I should like to thank Professors H.H. Korst and J.A. Schetz for useful discussions.

For assistance with the 9" x 9" experiments I should like to thank the College of Aeronautics workshop staff, in particular the assistance of Stan Clarke, Malcolm Goodrige and Wayne Osborne has proved invaluable.

For assistance with the Pebble Bed Heater experiments I thank the staff of the S.M.E. drawing office and workshops. Don Banbury, Dick Kennewell, George Lipinski and Eddie Rolfe deserve special mention.

Finally, this report could not have been produced without the assistance of my wife, who has typed innumerable texts during the progress of the project including this report. Thank you, Sue.

This work was funded by the Ministry of Defence (Procurement Executive).

REFERENCES

1. Baker, W.T., Davis, T. and Matthews, S.E., "Reduction of Drag of a Projectile in a Supersonic Stream by the Combustion of Hydrogen in the Turbulent Wake", CM-673 Applied Physics Lab., The Johns Hopkins University, 1951.

2. Townend, L.H. and Reid, J., "Some Effects of Stable Combustion in Wakes Formed in a Supersonic Stream", in: Supersonic Flow, Chemical Processes and Radiative Transfer, ed: Olfe, D.B. and Zakkay, V., Pergamon Press, 1964.

3. Strahle, W.C., Hubbartt, J.E. and Walterick, R., "Base Burning Performance at Mach 3", AIAA Journal, Vol. 20, No. 7, 1982.

4. Strahle, W.C., "Theoretical Consideration of Combustion Effects on Base Pressure in Supersonic Flight", 12th Combustion (International) Symposium, Poitiers, France, 1968.

5. Mehta, G.K. and Strahle, W.C., "Analysis of Axially Symmetric External Burning Propulsion for Bluff-Base Bodies" AIAA Journal, Vol. 17, No. 3, 1979.

6. Smithey, W.J., "Projectile Thrust-Drag Optimization with External Burning", Ph.D. Thesis, Naval Postgraduate School, Monterey,Calif., 1974.

7. Schetz, J.A., Billig, F.S. and Favin, S. "Analysis of Base Drag Reduction by Base and/or External Burning", AIAA Journal, Vol. 19, No. 9, 1981.

8. Schadow, K.C. and Chieze, D.J., "Experimental Investigation of Combined Base Injection and External Burning", AIAA Journal, Vol. 16, No. 10, 1978.

9. Neale, D.H., Hubbartt, J.E., Strahle, W.C. and Wilson, W.W. "Effects of External Compression on an Axisymmetric Turbulent Near Wake", AIAA Journal, Vol. 16, No. 9, 1978.

10. Hubbartt, J.E., Strahle, W.C. and Neale, D.H., "Mach 3 Hydrogen External Base Burning", AIAA Journal, Vol. 19, No. 6, 1981.

11. Hawkins, R. and Trevett, E.G. "Changes in the Flow at the Base of a Bluff Body due to a Disturbance in its Wake", AGARD Report 539, 1966.

12. Hurdle, C., Private Communication, 1980.

13. Townend, L.H. and Cox, S.G., "Base Burning and Near Wake Combustion - Remarks on a Paper by W.C. Strahle" RAE T.M. Aero, 1081, 1968.

14. Townend, L.H., Research Proposals Document, M.O.D.(UK), 1978.

15. Townend, L.H. and Edwards, J.A., "Base Pressure Control and Ramjet Combustion Based on Shock-flame Interaction", Seventh International Symposium on Ballistics, The Hague, 1983.

16. Janes Defence Review, Vol. 1, No, 1, 1980.

17. Houghton & Brock, Aerodynamics for Engineering Students, Arnold 1970.

18. ESDU DATA SHEET 8002.

19. ESDU DATA SHEET 73016.

20. ESDU DATA SHEET BS.02.03.12.

21. ESDU DATA SHEET 75004.

22. Tanner, M. "Theoretical Prediction of Base Pressure for Steady Base Flow", Progress in Aerospace Sciences, Vol. 14, 1973.

23. Murthy, S.N.B. and Osborn, J.R. "Base Flow Phenomena with and without Injection", in: Aerodynamics of Base Combustion, Ed: S.N.B. Murthy, Progress in Astronautics and Aeronautics, Vol. 40, AIAA, 1976.

24. Murthy, S.N.B. and Osborn, J.R. "Base Combustion Effects on Base Pressure", In: Aerodynamics of Base Combustion, Ed: S.N.B. Murthy, Progress in Astronautics and Aeronautics, Vol. 40, AIAA, 1976.

25. Shvets, A.I. "Base Flow", Progress in Aerospace Sciences, Vol. 18, 1978.

26. Chang, P.K. "Separation of Flow", Pergamon Press, 1970.

27. Gabeaud, A. "Base Pressures at Supersonic Velocities", J. Aeronautical Science, Vol. 16, Oct 1949.

28. Gabeaud, A. "Base Pressures at Supersonic Velocities", J. Aeronautical Science, Vol. 17, Aug 1950.

29. von Karman, T. and Moore, N.B. "Resistance of Slender Bodies Moving with Supersonic Velocities, with Special Reference to Projectiles", Trans. ASME, Vol. 54, 1932.

30. Hill, F.K. "Base Pressures at Supersonic Velocities", J. Aeronautical Science, Vol. 17, 1950.

31. Cope, W.F. "The Effect of Reynolds Number on the Base Pressure of Projectiles", NPL Engrg. Div. 63/44, ARC, 1945.

32. Cope, W.F. "Flow Past Bodies of Revolution", In: Modern Developments in Fluid Dynamics". High Speed Flow. Vol. II ed: L. Howarth, Oxford, 1953.

33. Hankins, G.A. "Experiments of Reynolds Number Effect on Projectiles at Supersonic Speeds", 6th International Congress on Applied Mechanics, Paris, 1946.

34. Kurzweg, H.H. "Interrelationship Between Boundary Layer and Base Pressure", J. Aeronautical Science, Vol. 18, 1951.

35. Chapman, I.R., Wimbrow, W.R. and Kester, R.H. "Experimental Investigation of Base Pressure on Blunt Trailing-edge Wings at Supersonic Velocities", NACA TN 2611, 1952.

36. Weinbaum, S. "Rapid Expansion of a Supersonic Boundary Layer and its Application to the Near Wake", AIAAJ., Vol. 4, 1966.

37. Weinbaum, S. "On the Singular Points in the Laminar Two-dimensional Near Wake Flowfield", J. Fluid Mech., Vol. 33, 1968.

38. Platou, A.S., "Improved Projectile Boat-Tail", Journal of Spacecraft and Rockets, Vol. 12, No. 12, 1975.

39. Cortright, E.M. Jr. and Schroeder, A.M. "Preliminary Investigation of Effectiveness of Base Bleed in Reducing Drag of Blunt-base Bodies in Supersonic Stream", NACA R.M. E51A26, 1951.

40. Reid, J. and Hastings, R.C., "Experiments on the Axisymmetric Flow over Afterbodies and Bases at M = 2.0", ARC 21, 707, 1959.

41. Bowman, J.E. and Clayden, W.A., "Cylindrical Afterbodies in Supersonic Flow with Gas Ejection", AIAA Journal, Vol. 5, No. 8, 1967.

42. Bowman, J.E. and Clayden, W.A., "Boat-Tailed Afterbodies at M_∞ = 2.0 with Gas Ejection", AIAA Journal, Vol. 6, No. 10, 1968.

43. Smith, R.M., "A Review of Possible Sources of Fuel for use in the Base Flow Region of Supersonic Projectiles", Dept. of Mech. Eng., University of Surrey, Nov. 1979.

44. Korst, H.H., "A Theory for Base Pressure in Transonic and Supersonic Flow", Journal of Applied Mechanics, Vol. 23, 1956.

45. Collins, D.J., Lees, L. and Roshko, A., "Near Wake of a Hypersonic Blunt Body with Mass Addition", AIAA Journal, Vol. 8, No. 5, 1970.

46. Dixon, R.J. and Page, R.H., "Interdependence of Base Pressure and Base Heat Transfer", ARS Journal, Vol. 31, No. 12, 1961.

47. Korst, H.H. and Tripp, W., "The Pressure on a Blunt Trailing Edge Separating Two Supersonic Two-dimensional Air Streams of Different Mach Numbers, and Stagnation Pressures, but Identical Stagnation Temperature", Midwest Conf. on Solid and Fluid Mechanics, Univ. of Michigan, 1957.

48. Scanland, T.S. and Hebrank, W.H., "Drag Reduction Through Heat Addition to the Wake of Supersonic Missiles", Memo Rept. No. 596, Ballistics Research Labs., Aberdeen Proving Ground, 1952.

49. Ward, J.R. and Baltakis, F.P., "Development of Fumers for Small Calibre Amunition", In: Aerodynamics of Base Combustion, Ed: S.N.B. Murthy, Progress in Astronautics and Aeronautics, Vol. 40, AIAA, 1976.

50. Limendorf, I.A. and Trifiletti, R.A. "Gas Generators for Base Drag Reduction (Fumers)", In; Aerodynamics of Base Combustion, Ed: S.N.B. Murthy, Progress in Astronautics and Aeronautics, Vol. 40, AIAA, 1976.

51. Hudgins, H.E. Jr., "Range Increase of Projectiles by Heat and/or Mass Addition to Base or External Flow", In: Aerodynamics of Base Combustion, Ed: S.N.B. Murthy, Progress in Astronautics and Aeronautics, Vol. 40, AIAA, 1976.

52. Davis, L.R., "Experimental and Theoretical Determination of Flow Properties in a Reacting Near Wake", AIAA Journal, Vol. 6, No. 5, 1968.

53. Broadbent, E.G. and Townend, L.H. "Shockless Flows with Heat Addition in Two-Dimensions", RAE TR.69284, 1969.

54. Broadbent, E.G. "Axisymmetric Flow with Heat Addition to Simulate Base-Burning", RAE TR.70028, 1970.

55. Broadbent, E.G. "Some Shockless Axisymmetric Flows with Heat Addition", RAE TR.70080, 1970.

56. Broadbent, E.G. "Flowfield Calculations for Some Supersonic Sections with Ducted Heat Additions", RAE TR.71120, 1971.

57. Broadbent, E.G. "Some Unseparated Base Flows with Heat Addition", RAE TR.73094, 1973.

58. Channapragada, R.S. "Compressible Jet Spread Parameter for Mixing Zone Analysis", AIAA Journal, Vol. 3, No. 12, 1963.

59. Serafini, J.S. and Dorsch, R.G. and Fletcher, E.A. "Exploratory Investigation of Static and Base-Pressure Increases Resulting from Combustion of Aluminium Borohydride Adjacent to a Body of Revolution in a Supersonic Wind Tunnel", NACA RM E 57E15, 1957.

60. Crocco, L. and Lees, L. "A Mixing Theory for the Interaction Between Dissipative Flows and Nearly Isentropic Streams", J. Aeronautical Sci., Vol. 19, No. 10, 1952.

61. Alber, I.E. and Lees, L. "Integral Theory for Supersonic Turbulent and Base Flows", AIAA Journal, Vol. 6, No. 7, 1968.

62. Hubbartt, J.E. and Strahle, W.C. "External/Base Burning for Base Drag Reduction at Mach 3, AIAA Journal, Vol. 19, No. 11, 1981.

63. Rebuffet, P., "Effets de Supports sur l'ecoulement a l'arriere d'un Corps", NATO Report 302, 1959.

64. Miller, L.D. "A Study of Base Flows on Flared Afterbodies", M.Sc. Thesis, Cranfield Institute of Technology, 1980.

65. Courant, R. and Friedrichs, K.O. "Supersonic Flow and Shock Waves", Interscience, New York, 1948.

66. Ferri, A. "Application of the Method of Characteristics to Supersonic Rotational Flow", NACA TN 1135, 1946.

67. Antonov, A.N. "Effect of Dilation and Compression Waves on Base Pressure", Soviet Applied Mechanics, 1979.

68. Liepmann, H.W. and Roshko, A. "Elements of Gas Dynamics", John Wiley and Sons, New York, 1957.

69. Ames Research Staff, "Equations, Tables and Charts for Compressible Flow", NACA Report 1135, 1953.

70. Mager, A. "On the Model of the Free, Shock-Separated Turbulent Boundary Layer", Journal of Aeronautical Sciences, Vol. 23, No. 2, 1956.

71. Hoerner, S.F. "Fluid Dynamic Drag", Published by the Author, 1965.

72. Zucrow, M.J. and Hoffman, J.D. "Gas Dynamics", John Wiley and Sons, New York, 1976.

73. Cookson, R.A. "Design, Construction and Performance of a High Enthalpy Facility", CoA Report Aero No. 200, 1967.

74. Morel, J. "Effect of Base Cavities on the Aerodynamic Drag of an Axisymmetric Cylinder", Aero. Quart. Vol. 30, May 1979.

APPENDIX A1: THE METHOD OF TRAJECTORY CALCULATION

The equations of motion of a projectile;

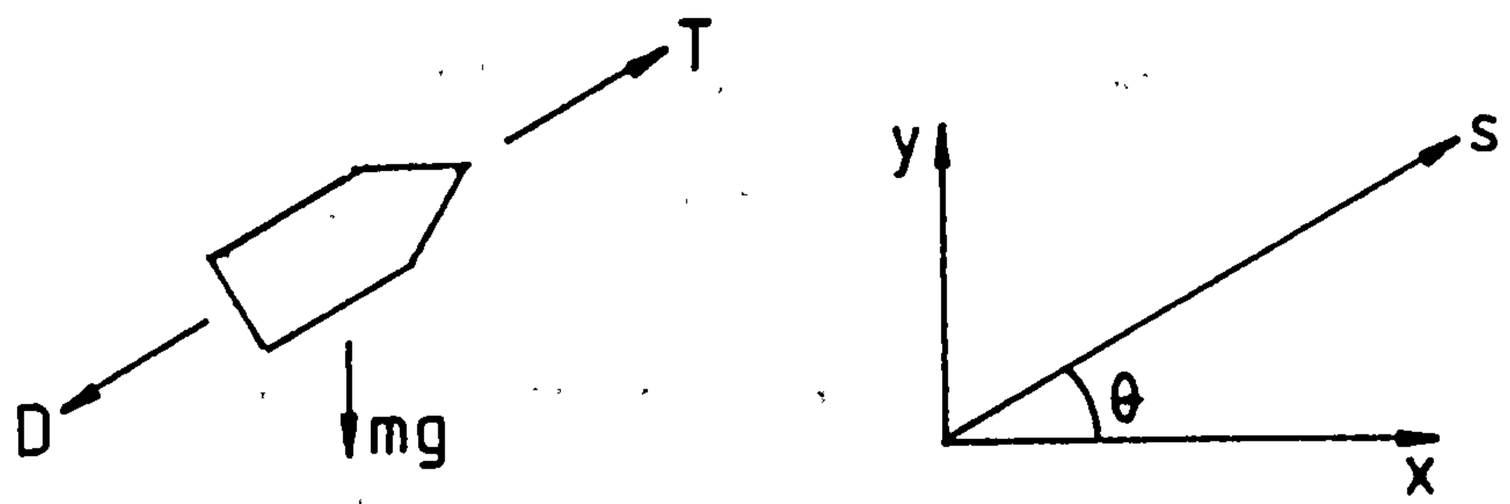

Fig. A.1.1

$$(T-D) - mg \sin\theta = m\ddot{s} \quad (1)$$

$$(T-D)\cos\theta = m\ddot{x} \quad (2)$$

$$(T-D)\sin\theta = m\ddot{y} + mg \quad (3)$$

where ($\dot{}$) refers to differentiation w.r.t. time, t.

Note $T = T(t)$ and $D = D(q,t)$ where q is the local velocity in the s - direction, also $m = m(t)$ as mass is burned to give thrust.

Rewrite (2) and (3) as:

$$\ddot{x} = \frac{1}{m}\cos\theta \ (T-D) \quad (4)$$

$$\ddot{y} = \frac{1}{m}\sin\theta \ (T-D) - g \quad (5)$$

Since $\theta = \tan^{-1}\frac{dy}{dx}$ we write (4) and (5) as

$$\ddot{x} = \frac{1}{m}\cos\left(\tan^{-1}\frac{dy}{dx}\right)(T-D) \quad (6)$$

$$\ddot{y} = \frac{1}{m}\sin\left(\tan^{-1}\frac{dy}{dx}\right)(T-D) - g \quad (7)$$

Also, as $D = D(q,t)$ and $q = \sqrt{\dot{x}^2 + \dot{y}^2}$ equations (6) and (7) are non-linear and coupled second order ordinary differential equations which are solved as an initial value problem with initial conditions

$$\text{at } t = 0 \quad x = 0, \quad y = 0 \quad \text{with } \frac{dy}{dx} \text{ given} \quad (8a)$$

$$\dot{x} = 0, \quad \dot{y} = 0$$

or at $t = 0$ $x = 0$ $y = 0$ with $\frac{dy}{dx}$ given (8b)

$\sqrt{\dot{x}^2 + \dot{y}^2}$ given

Equations (6) and (7) are discretised as follows:-

$$\frac{d^2x}{dt^2} \simeq \frac{1}{h^2}\left[x(t_{j+1}) - 2x(t_t) + x(t_{j-1})\right] \quad (9)$$

where h is the time-step, assumed constant, $h = t_{j+1} - t_j$

$x(t_j)$ is the value of x at time-step t_j etc.

A similar discritisation is used for $\frac{d^2y}{dt^2}$

Also $\cos\theta\,(t_j) = \cos\left\{\tan^{-1}\left[\frac{y(t_{j+1}) - y(t_{t-1})}{x(t_{j+1}) - x(t_{t-1})}\right]\right\}$ to retain the

same order of approximation as equation (9). However, this approximation will require an implicit scheme as both $x(t_{j+1})$ and $y(t_{j+1})$ are unknown at time t_{j+1}. (These are the variables for which we are solving.) We therefore write this term using a backward difference, trusting the stability and order of approximation will not provide difficulties, i.e.

$$\cos\theta\,(t_j) \simeq \cos\left\{\tan^{-1}\left[\frac{y(t_j) - y(t_{j-1})}{x(t_j) - x(t_{j-1})}\right]\right\} \quad (10)$$

A similar approximation to (10) is used for $\sin\theta\,(t_j)$. We also require $\frac{dx}{dt}$ and $\frac{dy}{dt}$ in the evaluation of D(q,t). Again a backward difference is used.

i.e. $\frac{dx}{dt} \simeq \frac{1}{h}\left(x(t_j) - x(t_{j-1})\right)$ (11)

etc.

The first of the initial conditions, (8a), requires no approximation, the second is approximated by introducing a fictitious point, t_{-1}. Then the $O(h^2)$ approximation $x(t_{-1}) = x(t_1)$ is introduced into equation (9) and thus $x(t_1)$ is found. Similarly for $y(t_1)$.

The second of the initial conditions, (8b) is usually given in the form M = given. If a is the speed of sound at x = 0, y = 0, then

$\dot{s} = aM$ (12)

But $\dot{y} = \dot{s}\sin\theta$ and $\dot{x} = \dot{s}\cos\theta$ so x and y at t = 0 can be evaluated. The introduction of a fictitious point then leads to the approximation for x

$$x_{-1} = x_1 - ha\ M(0) \cos 0\ (0) \tag{13}$$

with a similar approximation for y

For $j \geq 2$ the approximation takes the form

$$x(t_{j+1}) = 2x(t_j) - x(t_{j-1}) + \frac{h^2}{m}\left(T(t_j) - D(t_j)\right)\cos\left[\tan^{-1}\frac{y(t_j)-y(t_{j-1})}{x(t_j)-x(t_{j-1})}\right] \tag{14}$$

and

$$y(t_{j+1}) = 2y(t_j) - y(t_{j-1}) + \frac{h^2}{m}T(t_j)-D(t_j)\sin\left[\tan^{-1}\frac{y(t_j) - y(t_{j-1})}{x(t_j) - x(t_{j-1})}\right] - h^2 g \tag{15}$$

For $j < 2$ equation (13) is substituted into equation (14) to evaluate x (1). A similar substitution is made in equation (15).

Note that D is evaluated from the drag coefficient distribution shown in fig. A.1.2 by $D(t_j) = \frac{1}{2}\rho(t_j)(g(t_j))\ AC_D$. The values of $\rho(t_j)$ are obtained using Internation Standard Atmospheres[17].

APPENDIX A2: Calculation of drag of Firos 25 122 mm calibre missile at M = 2.5.

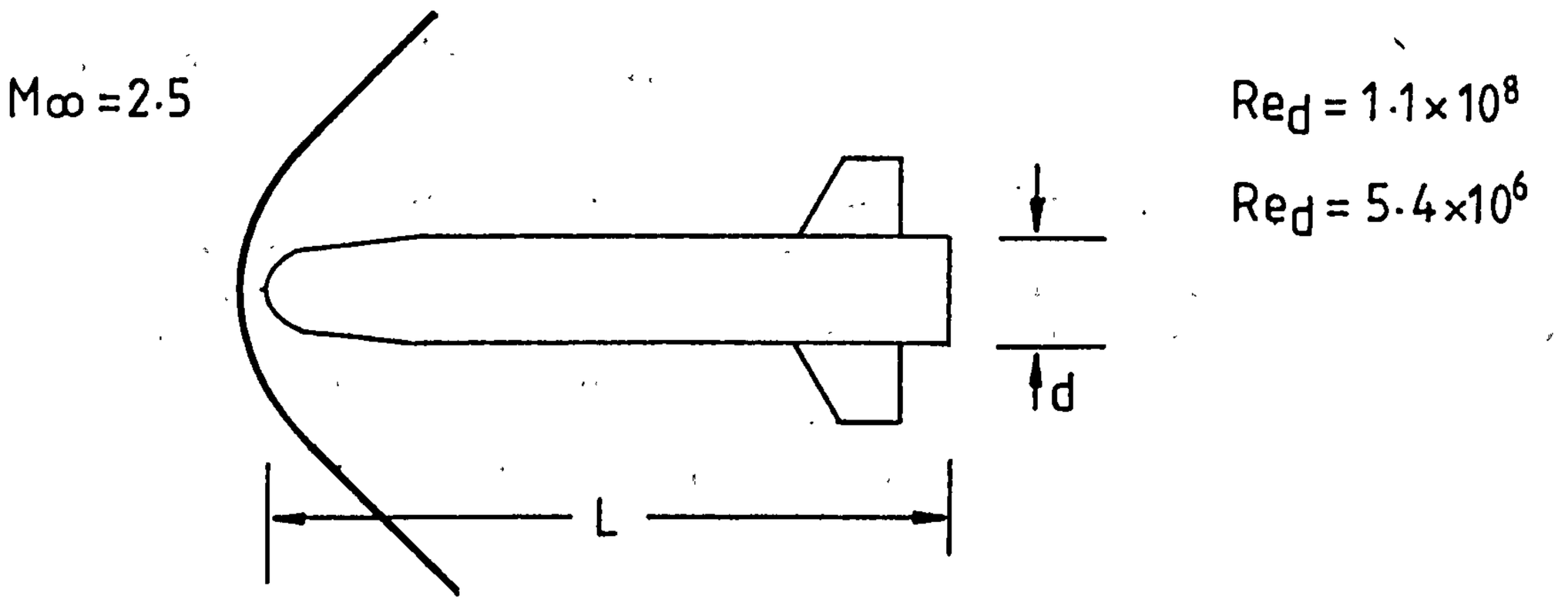

Fig. A.2.1

In general there are three components of drag at supersonic speeds:

a) Wave drag, or form drag (not very dependent on Reynolds number, highly dependent on Mach number).

b) Skin friction drag (dependent on both Reynolds number and Mach number)

c) Base drag (dependent on both Reynolds number and Mach number but for Reynolds numbers sufficiently high that the boundary layer on the body is turbulent then base drag may be taken to be independent of Reynolds number).

Assuming that the drag due to the fins may be calculated independently of the body then the body drag components are calculated as follows:-

a) Wave drag, C_{DW} = 0.10 from ref. 18.

b) Skin friction drag $C_{Df} = 1.05C_F$ x S/Base Area where C_F is the mean skin friction coefficient and S is the wetted area. From ref. 19 $C_F = 1.4 \times 10^{-3}$ i.e. $C_{DF} = 0.12$ assuming the projectile is aerodynamically smooth.

c) Base drag, C_{Db} = 0.12 from ref. 20.

In a similar manner the drag due to the fins is estimated. Using ref. 21 to calculate the wave drag coefficient based on base area is found to be $C_{D_{FIN}} = 2.8 \times 10^{-2}$

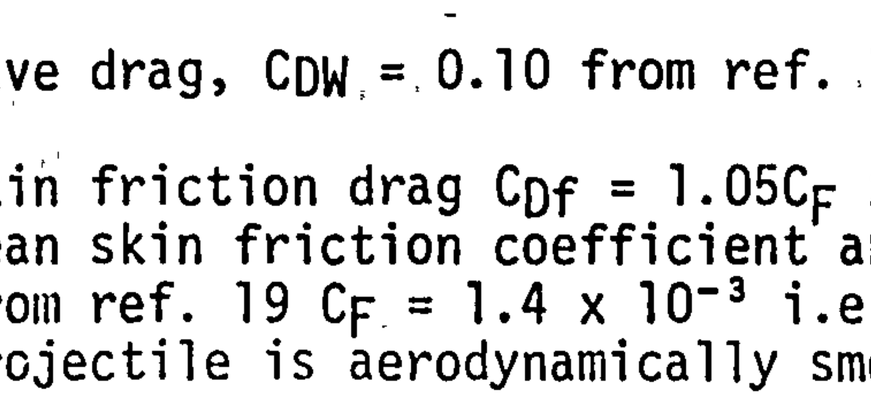

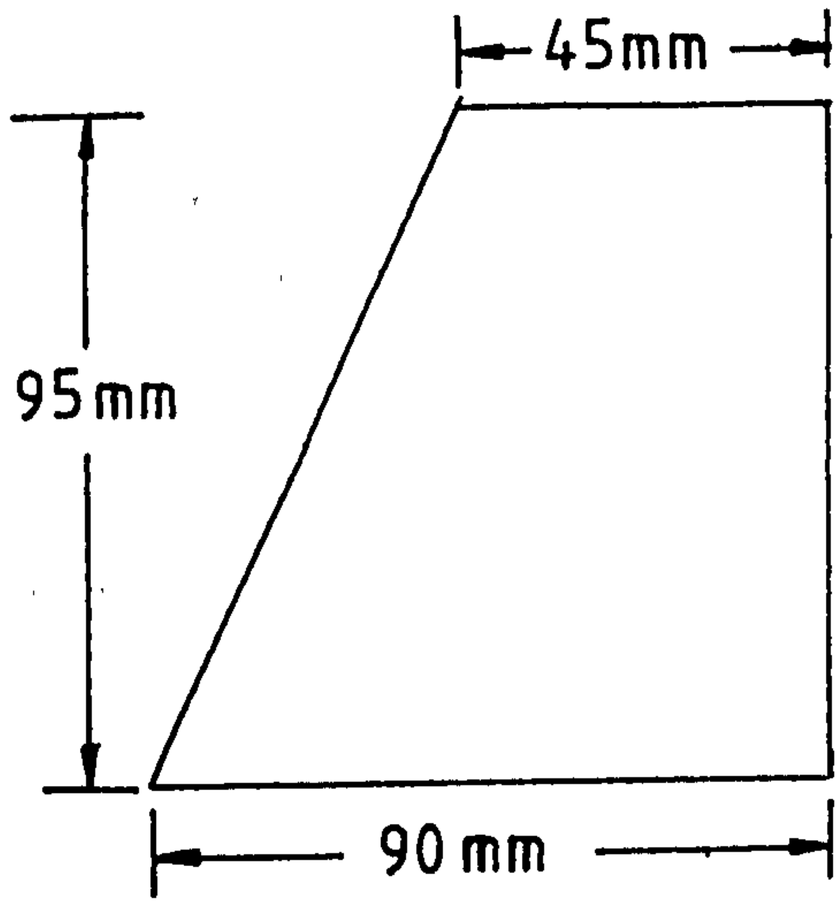

The total drag coefficient for the projectile is thus found to be

$$C_D = C_{DW} + C_{DF} + C_{Db} + C_{D_{FIN}} = 0.37$$

It is interesting to examine the question "Can the base pressure be raised sufficiently to overcome the total drag of the vehicle?" Since the base pressure must be raised to the free stream static pressure to overcome the base drag alone it is clearly necessary for the base pressure to be greater than the free stream static pressure.

The drag coefficient is defined by

$$C_D = \frac{D}{\frac{1}{2} \gamma P_\infty M^2_\infty A}$$

where D is the drag force, P_∞ is free-stream static pressure, γ is the ratio of specific heats, M_∞ is free stream (or projectile) Mach number and A is the base area.

Thus $D = \frac{1}{2} \gamma P_\infty M_\infty^2 A C_D$

Now to overcome this drag force we require a base pressure P_b such that

$$(P_b - P_\infty) A = D = \tfrac{1}{2} \gamma P_\infty M_\infty^2 A (C_D - C_{Db})$$

so $$\frac{P_b}{P_\infty} = 1 + \tfrac{1}{2} \gamma M_\infty^2 (C_D - C_{Db}) = 2.09$$

It is also of interest to compute the necewsary base pressure ratio for a vehicle such as MLRS (fig. A.2.3).

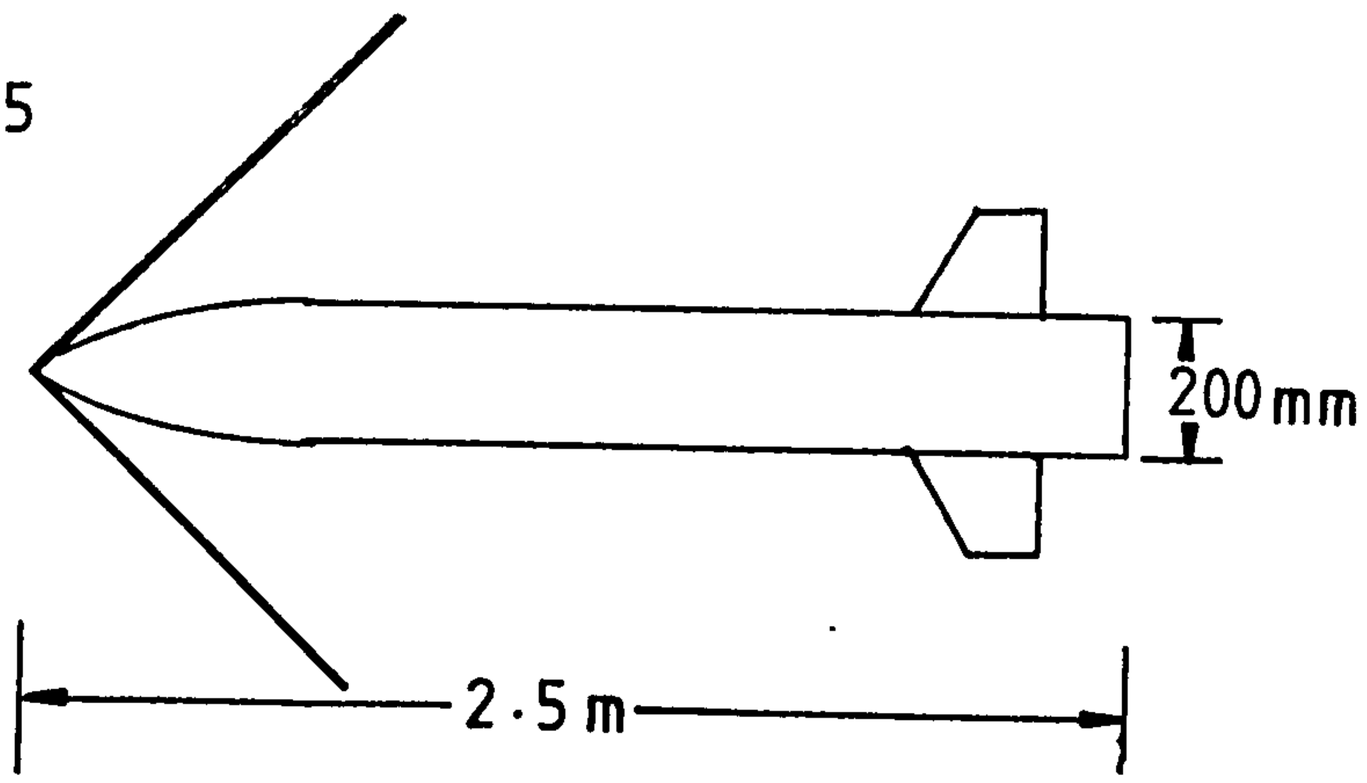

Fig. A.2.3

The total drag coefficient for this vehicle is $C_D = 0.32$ and $C_D - C_{Db} = 0.20$ so we require

$$\frac{P_b}{P_\infty} = 1.875$$ to overcome the vehicle drag.

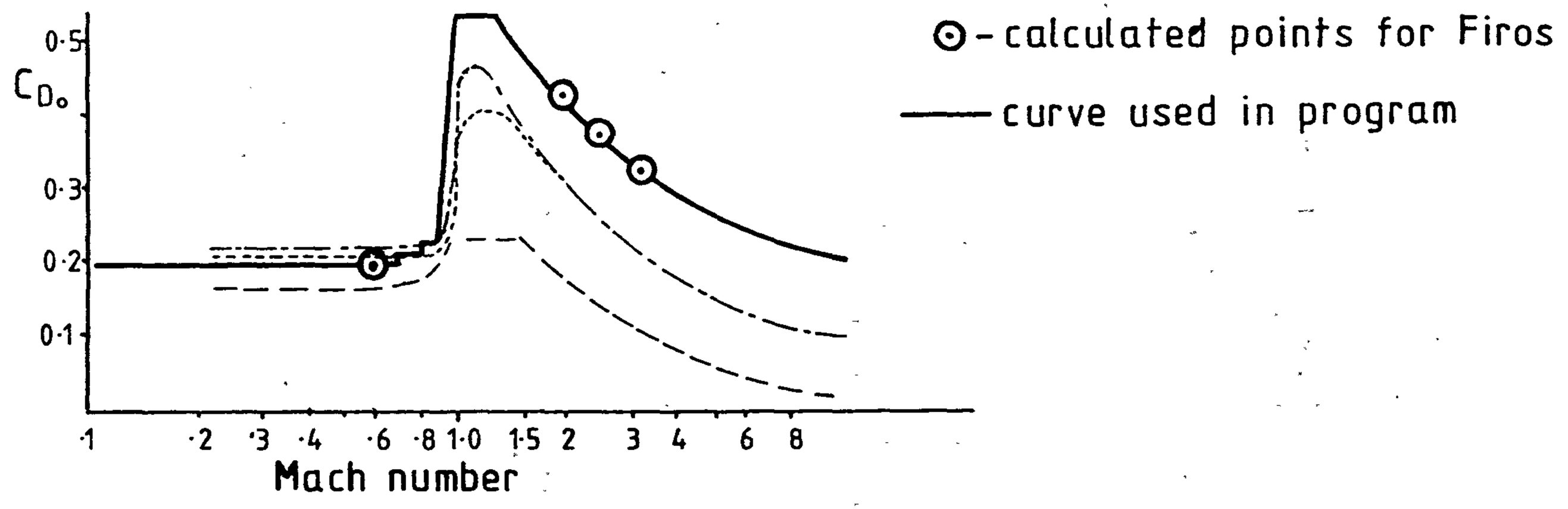

Fig. A.1.2: Drag coefficient of smooth projectiles (Hoerner[71])

APPENDIX B: CALCULATION OF MACH NUMBER VARIATION WITH TEMPERATURE

From ref. 68 one can write the area ratio in the nozzle as

$$\frac{A_*}{A_\infty} = \left(\frac{\gamma+1}{2} \right)^{\frac{\gamma+1}{2(\gamma-1)}} M_\infty \left(1 + \frac{\gamma-1}{2} M_\infty^2 \right)^{-\frac{\gamma+1}{2(\gamma-1)}} \qquad \text{B.1}$$

where A^* is the throat area, A_∞ is the area of the working section and M_∞ is the Mach number in the working section.

For $T_0 = 300^0K$, $M_\infty = 2.02$, $T_\infty = 165^0K$ and from ref. 72, $\gamma = 1.3977$ then,

$$\frac{A_*}{A_\infty} = 0.5821 = A \qquad \text{B.2}$$

Assuming that $\frac{A_*}{A_\infty}$ remains constant with varying stagnation temperature, then A in equation B.2 is a constant. (This is equivalent to the assumption that the variation in the displacement thickness of the boundary layer on the nozzle wall is negligible.) Equation C.1 may then be written as

$$M_\infty = A \left(\frac{\gamma+1}{2} \right)^{\frac{\gamma+1}{2(\gamma-1)}} \left(1 + \frac{\gamma-1}{2} M_\infty^2 \right)^{-\frac{\gamma+1}{2(\gamma-1)}} \qquad \text{B.3}$$

Equation B.3 is then solved iteratively by the method of bisection. Numeric values of the solution of equation B.3 for $\gamma = \gamma(T)$ are given in table B.1. Values of stagnation temperature T_0 are then found using

$$T_0 = T_\infty \left(1 + \frac{\gamma-1}{2} M_\infty^2 \right) \qquad \text{B.4}$$

Figures B.2 and B.3 show respectively the variation of Mach number and γ with stagnation temperature.

T_∞	γ	M_∞	T_0
150	1.397	2.020	271
200	1.400	2.022	364
250	1.401	2.022	455
300	1.400	2.022	545
400	1.395	2.019	722
500	1.387	2.014	892
600	1.376	2.008	1055
700	1.365	2.002	1212
800	1.354	1.996	1364
900	1.344	1.990	1513
1000	1.336	1.986	1663

Table B.1. Calculated values of Mach number and stagnation temperature for varying static temperature (assuming constant area ratio).

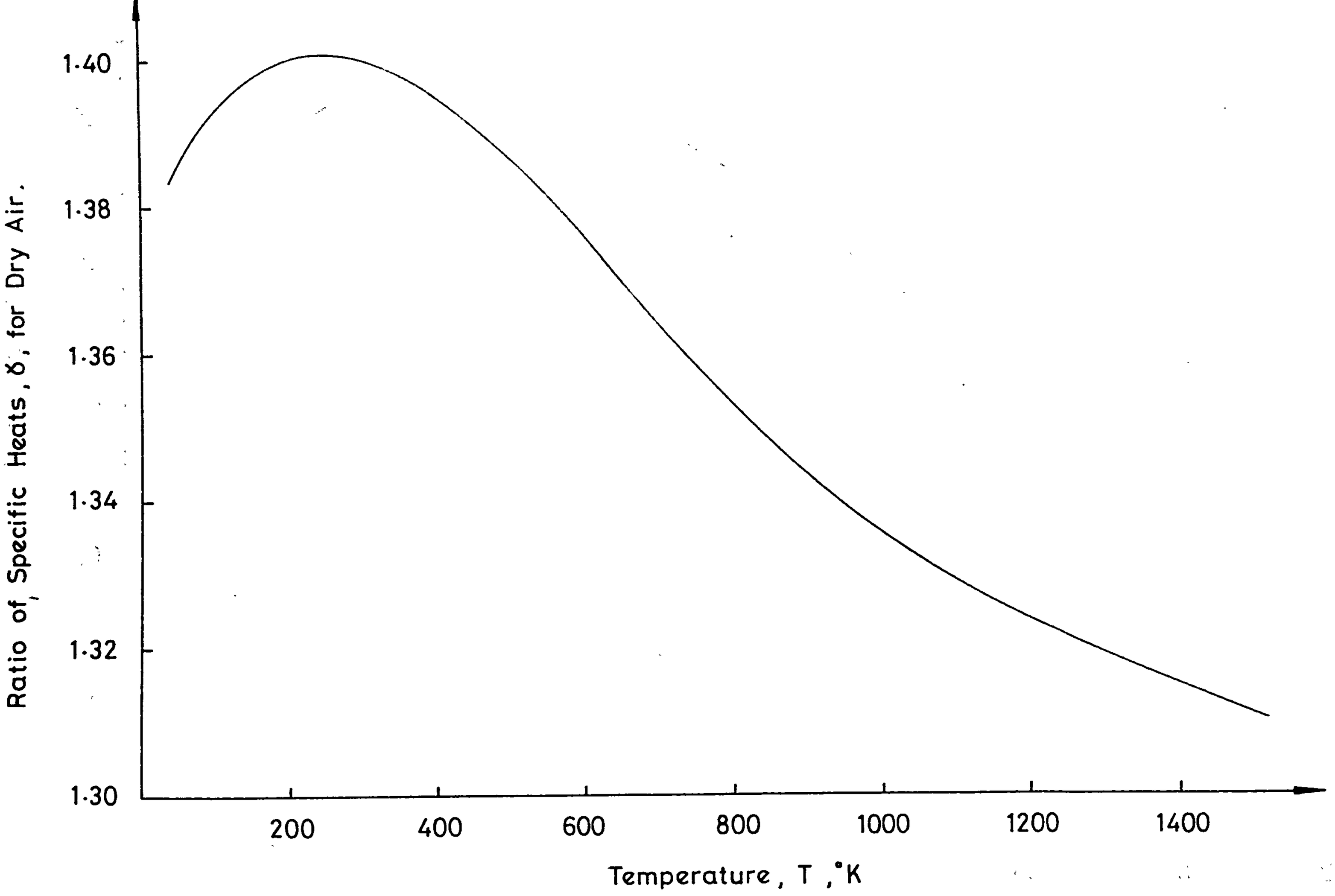

Fig. B.1. Variation of δ with Temperature [Data from Zucrow & Hoffman[72]].

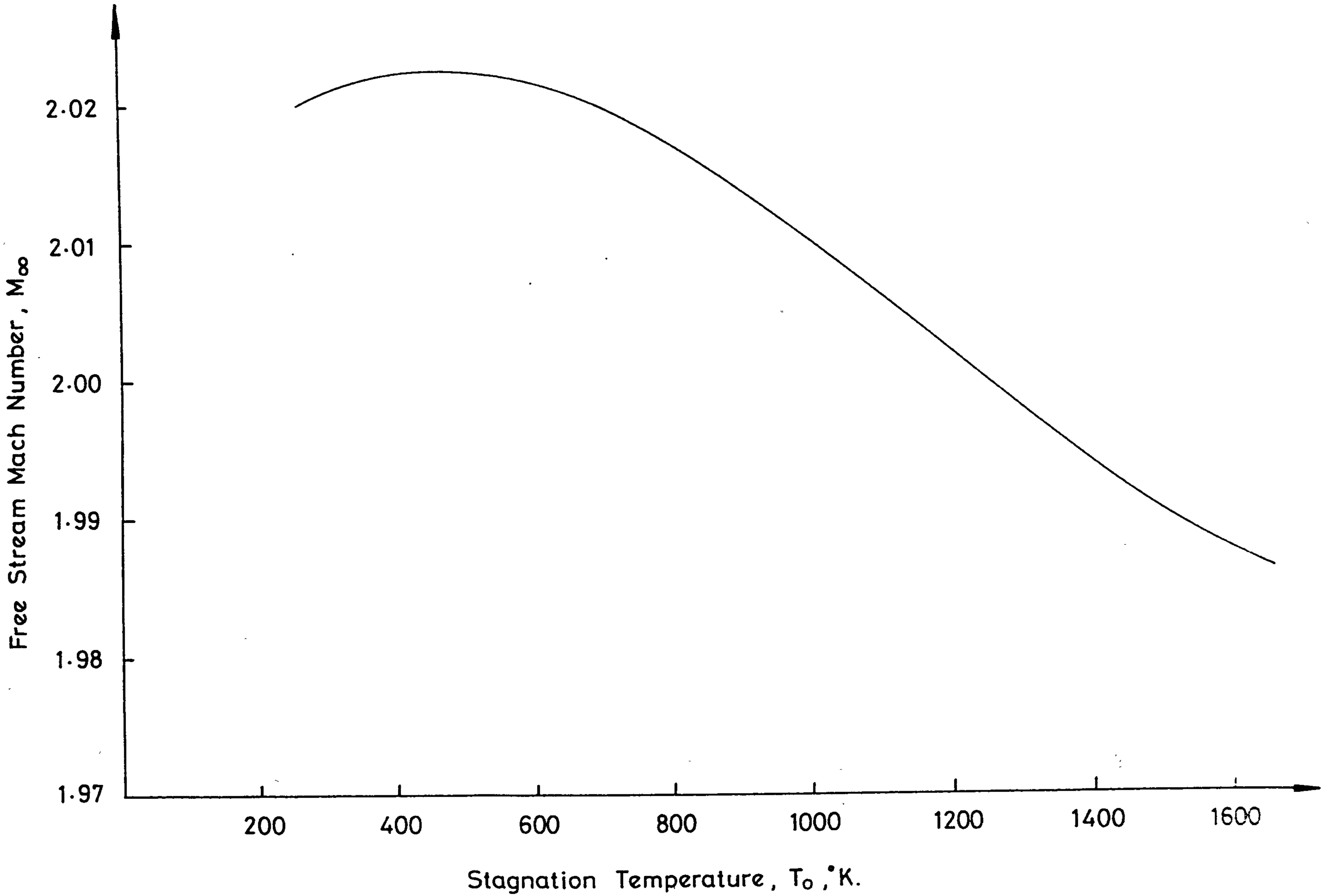

Fig. B.2. Variation of Mach Number with Stagnation Temperature

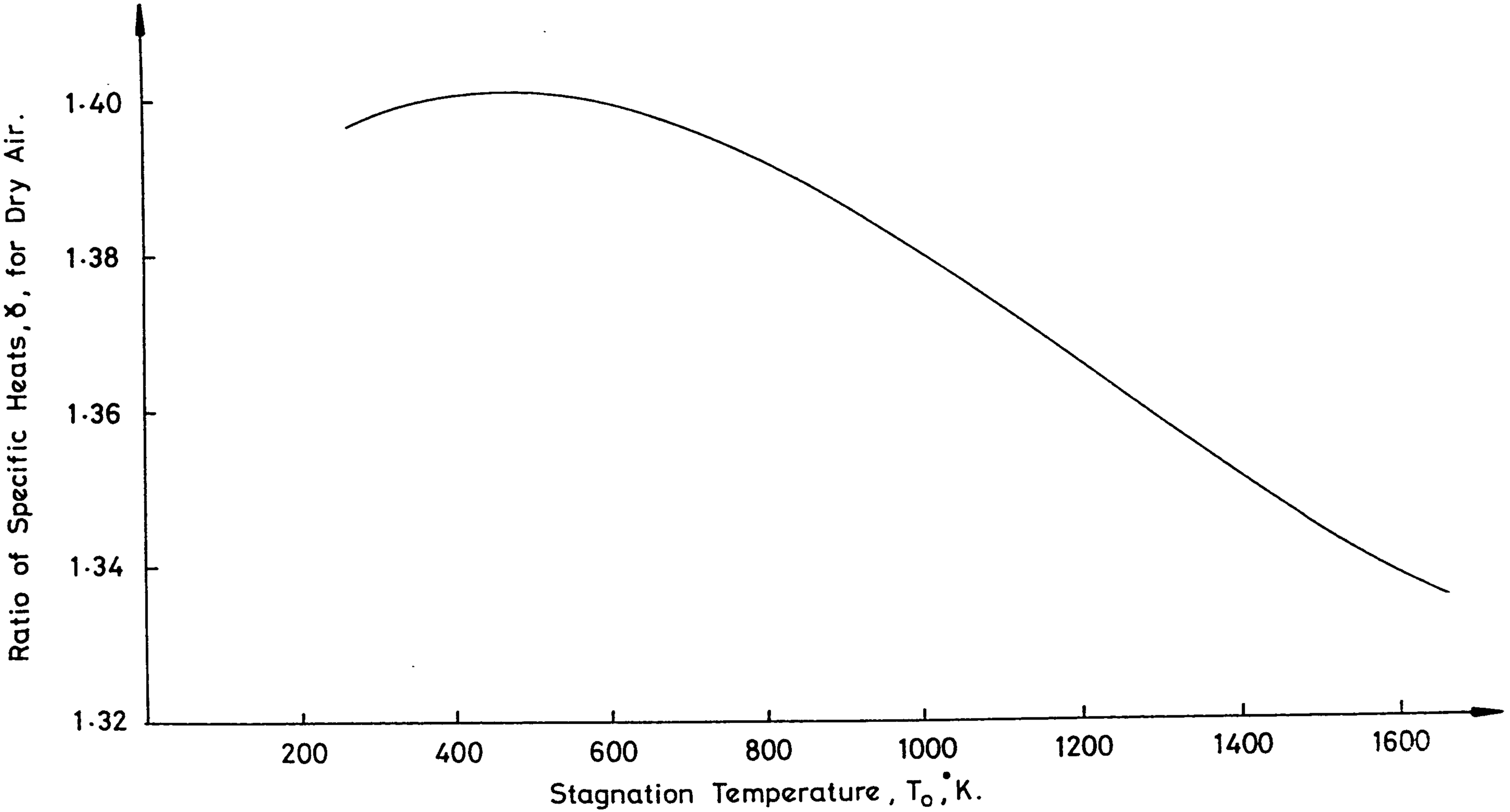

Fig. B.3. Variation of δ with Stagnation Temperature.